2008

# Designs and applications of surface acoustic wave sensors for biological and chemical sensing and sample handling

Stefan Cular
*University of South Florida*

Follow this and additional works at: http://scholarcommons.usf.edu/etd

Part of the American Studies Commons

Designs and Applications of Surface Acoustic Wave Sensors for Biological and

Chemical Sensing and Sample Handling


by


Stefan Cular


A dissertation submitted in partial fulfillment
of the requirements for the degree of
Doctor of Philosophy
Department of Chemical Engineering
College of Engineering
University of South Florida


Co-Major Professor: Venkat R. Bhethanabotla, Ph.D.
Co-Major Professor: Darren W. Branch, Ph.D.
William E. Lee III, Ph.D.
Thomas Weller, Ph.D.
Babu Joseph, Ph.D.
Patricia Kruk, Ph.D.
Joel A. Strom, M.D.


Date of Approval:
February 15, 2008


Keywords: SAW, Micro-fluidics, Acoustic Streaming, Nonspecific Protein Removal

Note to Reader

Note to Reader: The original of this document contains color that is necessary for understanding the data. The original dissertation is on file with the USF library in Tampa, Florida.

Dedication

I dedicate this work to my family and friends that have made it possible through guidance and support. The values they instilled in me have shaped me into what I am. *Semper Paratus*

Acknowledgments

Table of Contents

List of Tables

List of Figures

List of Acronyms and Variables

| | |
|---|---|
| 3-GPDMS | (3-glycidoxypropyl)dimethylethoxysilane |
| $A$ | Area; Molar Refractivity |
| AFM | Atomic Force Microscopy |
| Alexa-488 | Alexa Fluor 488 Fluorescent Dye |
| Alexa-594 | Alexa Fluor 594 Fluorescent Dye |
| Amp | Amplifier |
| BAW | Bulk Acoustic Wave |
| BSA | Bovine Serum Albumin |
| CCD | Charged Coupled Device |
| $c_i$ | SAW Film Coupling Parameter |
| d | Thickness of Film |
| DAQ | Data Acquisition |
| DSF | Double Split Finger |
| $E^{(i)}$ | Young's Modulus for $i^{th}$ Component |
| ELISA | Enzyme Linked Immunosorbent Assay |
| $f$ | Frequency |
| FE | Finite Element |
| FEM | Finite Element Method |

| | |
|---|---|
| G | Bulk Modulus |
| GPIB | General Purpose Interface Bus |
| $h$ | Height of Film |
| IDT | Interdigital Transducer |
| IF | Intermediate Frequency |
| IgG | Immunoglobulin G |
| IL-6 | Interleukin-6 |
| K | Bulk Modulus |
| $k_0$ | Wave Number |
| $LiNbO_3$ | Lithium Niobate |
| $LiTaO_3$ | Lithium Tantalate |
| $M_i$ | Generalized Modulus for $i^{th}$ Component |
| $M_w$ | Molecular Weight |
| $n$ | Index of Refraction |
| NSB | Nonspecifically Bound Protein |
| PBS | Phosphate Buffered Saline |
| PC | Personal Computer |
| PCA | Principal Component Analysis |
| PIB | Polyisobutylene |
| PR-DSF | Pruned Double Split Finger |
| PS | Polystyrene |
| $R$ | Motional Resistance |
| RF | Radio Frequency |

| | |
|---|---|
| SAW | Surface Acoustic Wave |
| SH | Shear-horizontal |
| $S_i$ | Strain |
| SMA | Subminiture Version A |
| SPR | Surface Plasmon Resonance |
| SPUDT | Single-phase Unidirectional Transducer |
| $T_i$ | Stress of the ith Component |
| $T_k$ | Matrix of Principal Component Scores |
| TTE | Triple Transit Effects |
| U-DSF | Unidirectional Double Split Finger |
| $u_i$ | Displacement Gradient |
| UV | Ultraviolet |
| $V_k$ | Matrix of Eigenvectors |
| VNA | Vector Network Analyzer |
| $Z_i$ | Impedance of ith Component |
| $\alpha$ | Attenuation Component of SAW Response |
| $\beta_i$ | Complex Propagation Factor for i[th] Component |
| $\gamma$ | Complex Response |
| $\Delta$ | Phase Shift (Difference) |
| $\delta^l$ | Decay Length into Liquid |
| $\varepsilon$ | Unexplained Variance |
| $\eta^l$ | Viscosity of Liquid |
| $\lambda$ | Lamé Constant |

| | |
|---|---|
| $\lambda$ | Wavelength |
| $\mu$ | Lamé Constant |
| $\nu$ | Velocity Component of SAW Response |
| $\nu_0$ | Original Velocity |
| $\rho$ | Density |
| $\rho^1$ | Density of Liquid |
| $\Psi$ | Amplitude Ratio |
| $\omega$ | Angular Velocity |

Designs and Applications of Surface Acoustic Wave Sensors for Biological and

Chemical Sensing and Sample Handling


Stefan Cular

ABSTRACT


Acoustic wave sensors have proven useful in many fields as primarily mass sensitive devices capable of responding to small environmental perturbations. The focus of this dissertation is the development of a new type of surface acoustic wave device with application to material property measurement, and biological and chemical sensing. This device is a combination of three independent acoustic wave devices with these waves propagated across the same area, while retaining independence of actuation and sensor function. The development of a complete sensor system, and its use and operation are presented for several example cases of chemical and biomarker sensing, and sample manipulation. These include experimental and theoretical studies for organic vapor sensing, biological moiety sensing, acoustic streaming to remove loosely bound material, and optimization of designs for these applications.

Chapter 1

Introduction

Acoustic wave sensor systems rely on many components to function as biological and chemical sensing instruments. These devices, although complex, have been used successfully for many years for the sensing of chemical species and measurement of material properties. More recent work has utilized them in sensing of biological species. In this dissertation, new designs and supporting systems that improve the standards for sensing systems are presented. The total work is described initially as individual components from underlying principles through development of the complete system and optimization studies as a series of independent papers.

## 1.1 Motivation and Objectives

This work is motivated by the wide desirability of reliable sensor systems in medical diagnostics and in chemical sensing. In particular, alleviating the need for sample handling and manipulation necessary in current biological sensor technologies is an important motivation for this work.

Acoustic wave devices have admirable characteristics that make them useful in sensor systems including for medical diagnostics. These sensors are highly portable, configurable to many applications, and have high sensitivity [1, 2]. Acoustic wave sensors can additionally be utilized as actuators to remove loosely bound material from their surface [3-6].

The work presented here is focused on the development of a surface acoustic wave sensor design and technique to permit rapid analysis of biological samples containing multiple analytes while reducing unwanted effects commonly seen in current assay technologies. At the core of this research is the use of a hexagonal shaped transducer for producing acoustic waves to manipulate sensing films as well as for enhancing sensing. Functionality to manipulate the sensing film is part of the design, while simultaneously monitoring it for perturbations from analytes [7]. Such a concept fits with the current trend to reverse the stereotypical event of having to take a sample to a laboratory with taking the laboratory to the material needing analysis [8, 9]. For the end-user applications of early biomarker detection described here, the importance of having a device capable of operating autonomously from analytical instruments is paramount.

The outcome of this dissertation work is the demonstration of the feasibility of acoustic waves to simultaneously manipulate and sense an analyte-specific film for biomarkers. Objectives for this research are:

1.     Development of a hexagonal surface acoustic wave sensor capable of simultaneously manipulating an analyte specific film and sensing the perturbations to the film when exposed to the analyte.

2.      Development of sensor electronics and testbed for testing acoustic wave sensors without analytical instruments.

3.      Calibration of the sensor for simple as well as complex test systems representative of real biologic fluid samples.

4.      Development of models for sensor analysis through analytical and finite element methods.

1.2    Organization of the Dissertation

This dissertation is organized such that chapter 2 contains general and common supporting information for chapters 3-8, which have been prepared as separate manuscripts.  The details of each of these chapters are as follows:

1.      Chapter 2 discusses in general terms what a sensor is and does.  Specific details of acoustic wave sensors with an emphasis on surface acoustic wave sensors follow.  Background information that describes the physics of sensor operation is presented as a brief overview.  For a more thorough understanding of acoustic wave sensors one should consult one of a number of excellent books referenced throughout chapter 2.  Additionally, chapter 2 has common materials and methods used throughout this dissertation research.

2.      Chapter 3 discusses a new design of surface acoustic wave sensor that has three crossing acoustic delay paths.  The crossing of the delay paths allows for the

measurement of multiple properties as verified through the use of principal component analysis on polymer / organic-vapor sorption experiments.

3.    Chapter 4 describes the use of acoustic streaming to remove nonspecifically bound material from the surface of sensors.  In this experimental study, fluorescently labeled proteins are used to both specifically and nonspecifically bind to a sensor surface.  The fluorescence intensity is measured using an inverted fluorescent microscope, and is qualitatively correlated with removal phenomena.

4.    Chapter 5 describes the optimization of polystyrene waveguide thickness for surface acoustic waves, specifically for shear-horizontal waves that created Love-waves when an appropriate waveguide is applied to the surface.  In this work, experimental and finite elements simulation data are compared.  The simulations used in this work allowed for the direct calculation of sensitivity data that were used to compare three different interdigital transducer designs.

5.    Chapter 6 describes a shear-horizontal surface acoustic wave sensor utilized for the sensing of interleukin-6 in phosphate buffered saline pH 7.4.  In this chapter, the need for biosensors is presented in terms specific for interleukin-6.  Additionally senor sensitivity is shown through a saturation curve including interleukin-6 concentrations that are physiologically relevant.

6.    Chapter 7 describes the use of a surface acoustic wave sensor and actuator that simultaneously allows measurements from surface perturbations and stimulates the same surface with high intensity waves to remove loosely bound material.

7.    Chapter 8 expands upon the designs presented in chapter 5 using finite element simulations.  Particular to this chapter is a new design approach to increase

sensitivity and decrease sensor power consumption. The designs simulated take the best of all previously used concepts for efficient surface acoustic wave transmission, and present an optimal design with a low energy loss and high mass sensitivity.

8.        Chapter 9 summarizes contributions of this dissertation, and provides recommendations for future work to further advance the field of acoustic wave sensors.

9.        The appendices of this dissertation contain extensive details required to reproduce presented in this dissertation. Codes for finite element simulations and data analysis, designs of fixtures, designs of surface acoustic wave devices, and analytical models are all presented.

Chapter 2

Sensors

Sensors are common to everyday life, and are developed to make lives better. Some of the more common sensor types that come to mind are tactile sensors such as touch pads on computers and touch screens. These devices take an input from the environment, the pressing by a finger, and convert it into an electrical signal that is then processed to perform an operation by the computer. This complete system is a sensor system.

The work described in this dissertation crosses multiple fields of study which will be briefly described in this chapter to permit understanding of the work accomplished. The topics described cover a biosensor pertinent for biomarker detection, acoustic waves in viscoelastic media, and the design aspects of the hexagonal surface acoustic wave sensor developed as part of this dissertation work.

2.1   Sensors Generalized

The role of a sensor is to measure a particular analyte and produce a signal that is then interpreted by the rest of the system. Sensors can be thought of as consisting of three components, as shown in Figure 1: detection element, transducer and signal

processor. As an analyte comes in contact with the detection element a change occurs with the detection element that is converted by the transducer into a signal that is finally processed by the signal processor. Following this general idea of a sensor, one can consider the nose as a sensor. A particular smell (analyte) creates changes in the olfactory membrane (detection element). Nerve cells (transducers) then convert the changes into a signal that is carried to the brain (signal processor) for recognition.[1, 8, 9]

| Analyte | Detection Element | Transducer | → | Signal Processing |
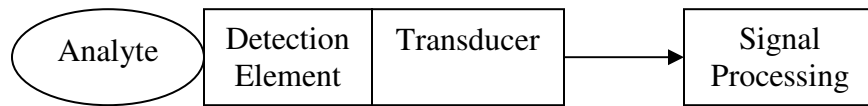
Figure 1  Schematic layout of a sensor.

Each of the components in the schematic of Figure 1 can have many different aspects. The detection element is the most important component for a selective sensor system. Particularly, this element should only respond a specific analyte or a group of analytes with similar properties. For the work contained in this dissertation, detection elements used are polymers for chemical vapor sensing and anti-bodies for protein analyte sensing [7, 10, 11].

For a biosensor to be functional, the sensor must have a selective detection element that is specific to a particular analyte in a sample. Such analytes for this project include biomarkers for cardiac trauma. The biomarkers within this project are specific proteins that have been identified to be found in elevated concentrations as a result of the illnesses. Particularly, interleukin-6 is a common biomarker that has been shown to reach

significantly high levels in people that have experienced injuries including a cardiac trauma.

The transducer component can be any of many different devices that have been found in traditional analytical techniques such as photometric transducers in spectrum analyzers. Transducers commonly fit into four categories: electrochemical, optical, piezo-electric and thermal transducers. Fortunately, all of the transducers utilize similar techniques to attach the detection element to the transducer [9].

Utilizing the transducer, of a sensor system, the signal processing component can be anything from a simple circuit and meter to a full computer controlled data acquisition system. Following the schematic in Figure 1 all of the components need to be integrated in a compatible fashion  The signal processing component offers the greatest diversity; hence, in the schematic it is not directly connected to the transducer [1, 9]. As the components are integrated from laboratory bench top to handheld devices, considerable work is necessary to develop easy to use interfaces.

2.1.1   Biosensors for Biomarkers

Within the scope of this work, a biosensor is defined as the interface from a biological system to an electronic system [12]. Biosensors are typically named for the materials and or equipment used. These devices come in all different types, some requiring labeling with fluorescent dyes, isotopes, or other detectable materials and some that are label free. Many biosensors require a basic visual inspection to a large analytical

instrument in order to make a determination as described in Table 1 [12-14]. Additionally, a qualitative comparison of the speed of response and accuracy of the systems is provided in the table.

Table 1  Typical detection methods used in biosensors.

| Detection | Probe Labeling | Data Acquisition | Real time | Resolution |
|---|---|---|---|---|
| ELISA (Enzyme linked immunosorbent assay) | Enzyme-linked antibodies | CCD (charged coupled device) imaging | No | Low |
| Isotropic labeling | Radio isotope-labeled analyte | X-ray film or phosphorimager | No | High |
| Sandwich immunoassay | Fluorescently labeled antibodies | Laser scanning | No | High |
| SPR (surface plasma resonance) | Not necessary | Refractive index change | Yes | Low |
| Non-contact AFM (atomic force microscopy) | Not necessary | Surface topological change | No | High |
| Planar waveguide | Fluorescently labeled antibodies | CCD imaging | Yes | High |
| Seldi (surface-enhanced laser desorption/ionization) | Not necessary | Mass spectrometry | No | Low |
| Electro-chemical | Metal-coupled analyte | Conductivity measurement | Yes | Medium |
| Acoustic wave | Not necessary | Integrated circuit | Yes | High |

Further analysis of sensor types is far more quantitative.  Parameters such as proportional signal response, hysteresis, response time, signal to noise ratios, selectivity and sensitivity all need to be considered to determine which sensor is the most suitable for a particular application [1, 8].

## 2.2    Acoustic Wave Sensors

Acoustic wave sensors can be found in a multitude of designs specific for their respective application.  Perhaps the most common acoustic wave sensor is the quartz crystal microbalance.  This device has been used for many years for deposition monitoring, and thin film characterization [1, 15, 16].  Although not the topic of this dissertation, the quartz crystal microbalance shares with the surface acoustic waves the same fundamental principles that uses piezoelectricity to convert electric and mechanical signals [1].  These principles are described in this chapter within the context of developing a basic understanding of surface acoustic wave sensors.

## 2.2.1    Acoustic Wave Device History

Approximately 120 years ago the Curie brothers discovered piezoelectricity, which is the coupling between elastic deformation and electric polarization that exists in certain crystals such as quartz, lithium niobate, and sapphire, just to name a few.  Shortly thereafter, Lord Rayleigh, in 1885, demonstrated surface acoustic waves, but it was not until the middle of the $20^{TH}$ century that these two findings were combined.  The key that was missing until this time was the invention of interdigital transducers (IDT) by White and Voltmer in 1965.  Having the basic concepts of the IDT available allowed for many designs to perform signal processing, and thus the beginning of surface acoustic wave (SAW) signal processing occurred.  Over time, SAW sensors were realized [17].

Acoustic wave devices are particularly useful in gas and liquid sensing environments due to the relative ease of use and low detection limits ($3x10^{-15}$ g according to Wohltjen (1984)) [1]. There is a problem that plagues acoustic sensors: substrate crystals that lend themselves to better sensors often have temperature coefficients that are very high, and require additional means to compensate the signal for temperature changes. Lithium niobate, for example, has excellent properties such as a coupling constant of 0.045 which is many times greater than the traditionally used quartz, but has a temperature coefficient of 19 ppm/$^o$C leading to the necessity of more advanced data acquisition schemes [2].

SAW devices are extremely common today; they are used in many forms of electronics such as band pass filters. "Every modern television receiver contains at least one SAW filter…" [17]. Due to the commercial value of filters, they have been developed to a very high level of sophistication for the removal of ideal sensor behaviors. As a result, it is necessary to fabricate in house SAW sensors that do not incorporate advanced designs to remove the effects of mass loading [18]. These sensors do the inverse and amplify the resulting response to a specific analyte. The resulting response of a SAW sensor can be from either an increase in the mass or a change in electric properties in the wave's path which are governed by the devices characteristics [1].

## 2.2.2 Surface Acoustic Wave Device Theory and Principles

SAW filter design is a technology that has predominately belonged to the communications industry. In recent history, this industry has developed advanced designs through an iterative process to eliminate the effects that are used to make good sensors [1]. For this reason it is important to continue the development of SAW devices for sensor applications that were not considered by communication companies. The basic SAW device as shown in Figure 2 consists of a pair of IDTs for input and output transduction, and a delay path for the acoustic wave to propagate. The delay path in sensor applications is coated with a sensing film that perturbs the propagating wave when it is exposed to a specific analyte [2]. The design and layout of the IDTs determines the signature response of the SAW devices [1, 18].

Input signal    Input IDT's    Delay path    Output IDT's    Outut signal

Substrate
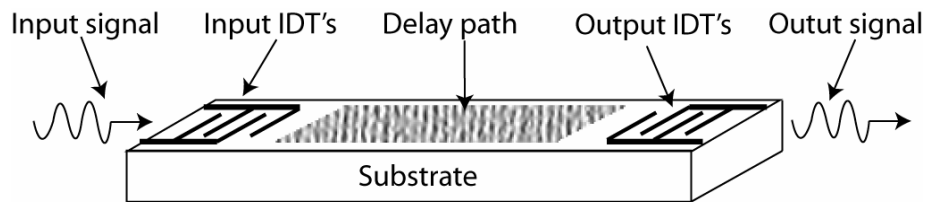
Figure 2  Surface acoustic wave sensor layout including input/output signals and IDTs and sensing film.

2.3    Common Materials and Methods

2.3.1    IDT Designs

Three designs of SAW device IDTs were fabricated and tested in this research. These designs intended for sensor applications are schematically shown in Figure 3. The first design is a standard double split finger IDT structure consisting of 60 finger pairs, delay path of 197 λ, and a wavelength of 32 μm. Such a design provides a narrow pass band response that is desirable for a sensor; however, due to the large number of fingers, the device displayed a significant amount of internal reflections. Subsequent and current designs have reduced the number of finger pairs by half, but have maintained the same delay path length and wavelength to allow for easier comparisons.

Of the three designs illustrated in Figure 3, two of them are direct comparisons to the original 60 finger pair design. First, the pruned IDT design is an interesting modification that has the same length IDT; however, every other finger pair set has been removed. As expected, the response from this design shows much less internal reflection, yet it maintains the desirable narrow pass band. The second direct modification was to remove half of the finger pairs. This design also met expectations with less internal reflections and a wider pass band. Unfortunately, this design shows a triple transit effect that can hinder a sensors signal to noise ratio [19]. The final design as shown in the figure is an advanced design that utilizes non-uniform IDT widths to reduce unwanted effects and better guide the SAW. All of these newer designs have additional features that include aperturization and gratings to further guide the SAW for brevity, these

features provide small improvements to wave propagations from the input to output port [18, 19].
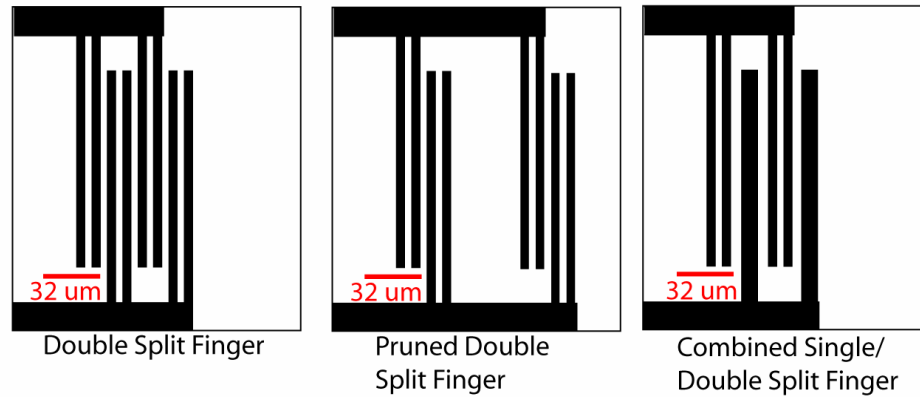


Figure 3  Illustrations of three IDT device designs tested in this work.  From left to right, the double split finger (DSF) design, pruned double split finger (PR-DSF), and unidirectional design (U-DSF).

2.3.2   Acoustic Wave Guiding Layers

Aside from the typical SAW sensor illustrated in Figure 2, the sensor used in this research has two additional features to enhance the sensitivity and resolution of the sensor.  The first added component is a guiding layer to trap energy of the SAW near the surface to make the sensor more sensitive to surface perturbations.  Even though SAW sensors are inherently capable of detecting analytes in solution concentrations on the order of ppb by mass, through use of higher frequency (>300 MHz) these higher frequency devices have smaller sensing regions that actually are too small to be feasible

14

for a sensor application [20]. For this reason, additional measures such as a adding a guiding layer need to be taken to enhance the sensitivity of the lower frequency (100-200 MHz) devices to reach sensitivities to on the order of 100 ppb by mass [21]. By applying an appropriate guiding layer, energy of the SAW is trapped within the layer to act as an amplifier to the surface perturbations [20, 22]. Layers that are ideal need to have a lower density and lower acoustic velocity than the piezoelectric substrate. Materials that have been utilized in past include polymers such as poly-methyl-metharcylate [21] and Novolac [20] and oxides including silicon dioxide [23] and silicon monoxide [24].

### 2.3.3    Acoustic Streaming

The second additional feature of the sensor is the use of acoustic energy to remove bound material from the sensing film. It has been shown that a Rayleigh wave launches energy longitudinally into the medium above substrate in which the wave is traveling [25, 26]. This phenomenon is termed acoustic streaming. And until recently is now being exploited in fluidic applications [4, 27-29]. Typically for SAW sensors, the Rayleigh wave is only used in gaseous environments because attenuation of the wave from the loss of this energy into a liquid sample. What was chosen in this research was to increase the input energy into the SAW device to not let the wave become attenuated. This has the effect of cleaning loosely bound material from the surface at lower energies and potentially removing more strongly bound material with higher energy inputs [3, 5, 27].

15

### 2.3.4 Device Fabrication

The SAW devices were fabricated using a single step photolithographic pattern process to prepare the wafers for metallization and liftoff processes. Included in the lithographic processing are specialized steps to enable safe and reliable fabrication such as controlled discharges from the pyroelectric crystals after thermal treatments. Due to the unique nature of the crystals used in this work these specialized processing steps were developed within the capabilities of the existing facilities. Since the processing techniques were developed and optimized, all current devices are fabricated using these recipes. The processing recipes can be found in 9.2.8Appendix E.

### 2.3.5 Device Testing and Characterization

SAW device testing and characterization was done immediately after the fabrication processing was completed. First tests include visual analysis and conductivity measurements of the IDTs to insure that the necessary processing was complete. Following the basic inspections and testing, devices were probed directly on wafer using the custom wafer probing fixture shown in Figure 4b. The measurements taken while using the probing fixture include the transmission and reflection scatter parameters and time domain measurements.

(a)                                    (b)
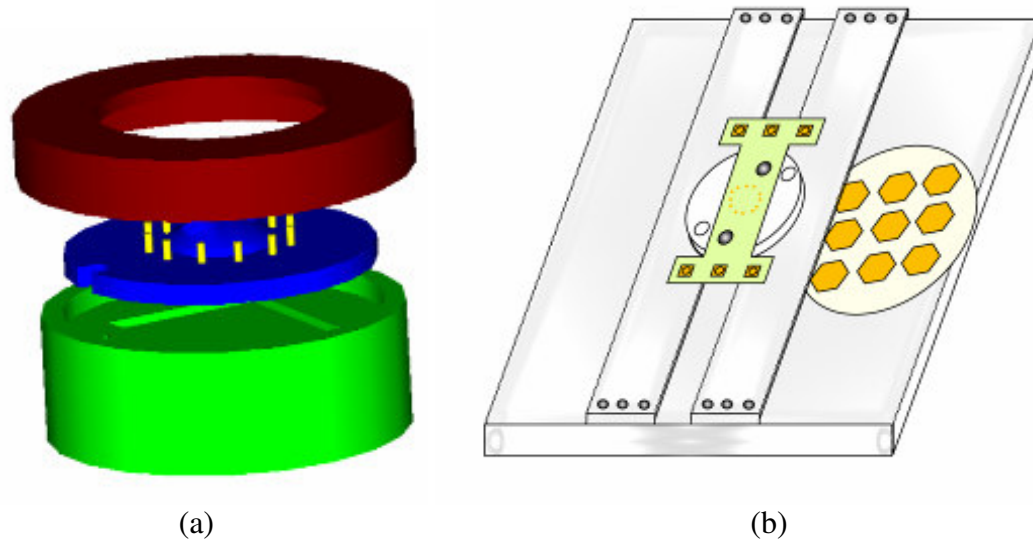
Figure 4  (a) 3d rendering of micro-fluidic test fixture for diced hexagonal SAW devices.

(b) 3d illustration of whole wafer micro-fluidic test fixture for the hexagonal SAW

devices.

2.3.6   Micro-fluidic Testbed and Fixture

To facilitate easy testing of liquid phase biological samples, a micro-fluidic test

fixture has been configured as illustrated in Figure 5.   The sensitivity required for

detection of many biological markers is on the order of a few nano-grams, which is

obtainable by many sensors; however, due to the high operating frequencies possible of

SAW devices, they are the most sensitive [30-32].  The challenge associated with this

type of mass sensitivity becomes largely a fixture and test parameter issue as any

variation in fluid flow or pressure will cause a significant sensor response [33].   To

address this issue, a precision syringe pump manufactured by Harvard Apparatus was used which unlike peristaltic pumps provides a smooth continuous flow with no pulses. The equipment shown in the illustration is highly adaptable for all of  required fluid requirements from nano-liters to milli-liters [34].   Additionally, making the configurability and operation of the testbed simple is a LabView virtual instrument interface that controls and records all electronic operations including flow rate, flow direction, and valve sample selection.
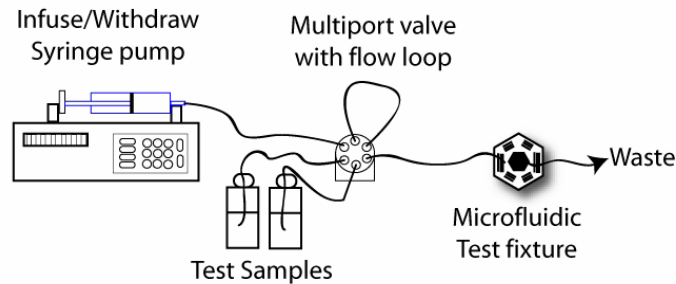


Figure 5   Schematic of micro-fluidic testbed for liquid phase sampling of biologic samples.

Due to the design of the hexagonal SAW a typical fluidic fixture is not feasible, so an in house design has been designed and fabricated.  The test fixtures have been constructed of acetal and Lexan, which have low moisture absorption, high strength, no centerline porosity and are easily machined.  A "pill box" design as shown in Figure 4(a) was utilized for even distribution of clamping force (attained with fine threading on both the sealing ring and fixture body), with spring-loaded pogo pins contacting the bonding

pads of the device. Fluid inlet/outlet to the central region is permitted via suitable plumbing fitting to facilitate liquid phase operation. The conical region in the middle (blue) piece is introduced to increase surface area available for the fluid inlet/outlet fittings.

Figure 4(b) is a whole wafer probing apparatus that was designed for the purpose of being able to test SAW device designs without the need to dice the wafers. The construction consists of metal base plate with two arms spanning the width of the base plate with a recess just greater than that of a typical wafer. The probing is accomplished with an acetal piece similar to the one used in the "pill box" designed; however, this piece has micro-fluidic channels and chamber as well as an attached circuit board with SMA connectors for simple connections to all analytical instruments.

## 2.3.7    Hexagonal SAW Device Operation

Initial characterization of the sensors was done using an HP 8753ES S-parameter Network Analyzer (VNA). Although the instrument can provide a complete data set within a few seconds, it is impractical to consider an analytical tool to be used outside of the laboratory. As a solution, circuitry as depicted in the schematic Figure 6 has been developed. This circuit is constructed such that a single waveform is split into three signals, sent through the three delay paths of the hex-a-saw, and finally is measured with commercial integrated circuits (Analog RF/IF gain and phase detector [35]), providing independent phase and magnitude measurements that can be easily recorded with a Data

Acquisition System. The unique part of this configuration is the use of a power amplifier capable of providing enough RF power (few milliWatts) to the SAW to remove proteins from the surface. Note that the configuration as shown in the figure uses two sets of IDT's to more uniformly deliver the RF power to the sensor's film.
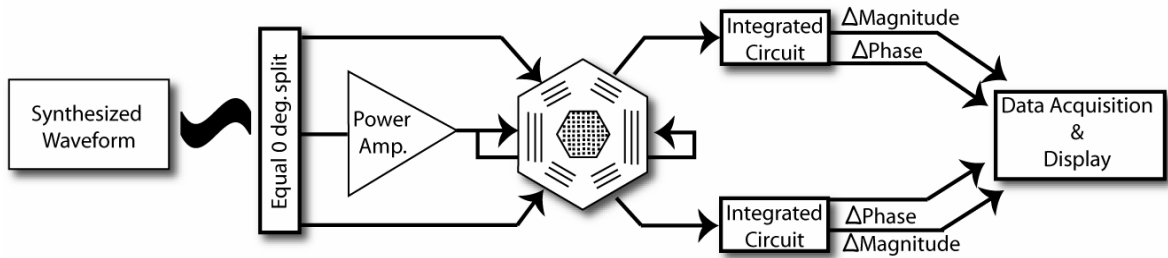


Figure 6 Schematic of hex-a-saw configured to simultaneously clean the surface and monitor with two delay paths for enhanced sensor response.

The decision to monitor the phase and magnitude was made in light of the necessity for this project to have stable measurements. Typically, this type of measurement is done with large analytical tools, and has been shown by several researchers to be as good as or better than measurements utilizing a feedback loop. The more traditional approach of using a feedback loop oscillator circuit with the SAW delay-line being the limiting factor to the frequency has been used extensively and is well known; however, this method is somewhat limited by interference from a number of sources including the RF amplifier. Another drawback to the oscillator configuration is only frequency-shift data can be easily collected [1], so less of an image of the sensing film interactions is perceived.

20

Chapter 3

Hexagonal Surface Acoustic Wave Devices for Enhanced Sensing and Materials

Characterization


The design, fabrication and testing of a hexagonal surface acoustic wave (SAW) array device fabricated in Y-cut Z-propagating lithium niobate is presented for non-destructive evaluation of thin organic films. Propagation along the Y-axis generates a Rayleigh mode wave where off-axis propagation excites a mixture of other SAWs. This approach permits rapid and simultaneous extraction of multiple film parameters (film material density or thickness, Lamé and shear moduli, sheet conductivity) of a thin film material to achieve a more complete characterization than when a single SAW device is utilized. In sensor applications, this capability translates to better discrimination of the analyte and possibly more accurate quantification. The devices are based on a double split finger delay-line design with a line width of 4 μm and a delay path of 197 λ. The individual delay paths of each hexagonal device intersect in the center of the die producing a single region for sensor analysis. Additionally, the central region where the acoustic waves intersect is shorted to reduce the number of modes of waves traversing the surface. Vapor sensing tests were conducted by exposing a poly(isobutylene)-coated device to various concentrations of benzene, chloroform, and n-hexane in the range of 0.8 to 16.6 volume percent. Measured attenuation and phase angle shifts at a fixed, near-

center frequency revealed significant, signature-type differences for the three delay-paths at each exposure concentration. These responses can be exploited in constructing better sensors and sensor arrays utilizing these hexagonal SAW devices.

3.1 Introduction

For many years, SAW devices have been used both individually and in arrays as sensors and for materials characterization in a variety of applications ranging from gases/vapors to biological systems [1, 36, 37]. Within this broad range of uses for SAW devices, is the need for non-destructive testing of thin films. Current technology is based on using dual delay-line configuration with one delay-line used as a reference to compensate for environmental changes [1, 38-40]. For basic sensor applications, this technique is sufficient; however, it is possible to design simple devices that can achieve better sensor characteristics as well as materials characterization possibilities utilizing simple device response models derived from perturbation theories [1, 41]. The hexagonal SAW device presented in this work is one such example that affords the possibility of extraction of multiple film parameters from responses of the multiple delay-lines that probe a common region. It is hoped that this and similar devices can serve as *in-situ* characterization tools in thin film physical and chemical deposition equipment, and perform better than the ubiquitous quartz crystal microbalance, which yields film thickness information only. It is conceivable that under specifically optimized

conditions, devices or arrays of devices presented here can be relied on to monitor deposition processes in such equipment.

In sensor applications, multiple parameters extracted from the film can thought of as multiple calibration curves and allow for a more unique characterization of the type and concentration of the analyte being sensed. Combined with the array concept, significantly more information can be obtained to better characterize the analyte. Also, many acoustic wave devices are specific to the phase in which they operate; for example, the successful Rayleigh wave device for vapor sensing is useless in the liquid phase due to excessive attenuation [4, 42]. The multiple directions in which the waves are launched in the hexagonal device of this device work are different in character, and may allow for a common device to be functional in both gas and liquid phases. In recent work, it was shown that Rayleigh wave devices can be utilized in acoustic cleaning of nonspecifically bound proteins in biosensor applications [3]. With the possibility of launching shear-horizontal SAW waves in one direction and Rayleigh waves in another, the hexagonal device may well serve as a better biosensor element for liquid phase applications. Such investigations are underway in laboratory, with designs implemented in more suitable piezoelectric materials, than the lithium niobate utilized in this work.

The results of vapor sorption by poly(isobutylene) (PIB) of this work can be interpreted by known sensor response models for SAW device perturbation by viscoelastic films [41]. The response of a typical SAW sensor to an external perturbation from a viscoelastic film can be expressed by:

$$\frac{\Delta\gamma}{k_o} = \frac{\Delta\alpha}{k_o} - j\frac{\Delta v}{v_o} = \sum_{i=1}^{3} \frac{c_i \beta_i M_i}{\omega} \tanh(j\beta_i h) \tag{1}$$

$$R = \frac{A f v_o \rho h}{|G|} \tag{2}$$

which is independent of type of wave. For many determinations, it is convenient to assume that the material properties contained in the $\beta$ and $M$ terms remain constant [37, 41].

For a thorough derivation and discussion of the use of these equations, see the work of Martin *et al* [1, 41]. Simplifications to this equation can be made by assuming the film to be acoustically thin, and not displaying viscoelastic properties. Roughly, when $R<<1$ in equation the previous equations the polymer film is considered to behave as an acoustically thin film; whereas, when $R \geq 1$ the film behaves as an acoustically thick film [1, 41]. Using the relations above, for a typical 100 MHz SAW sensor the determination of an acoustically thin or thick can be made using Figure 7.
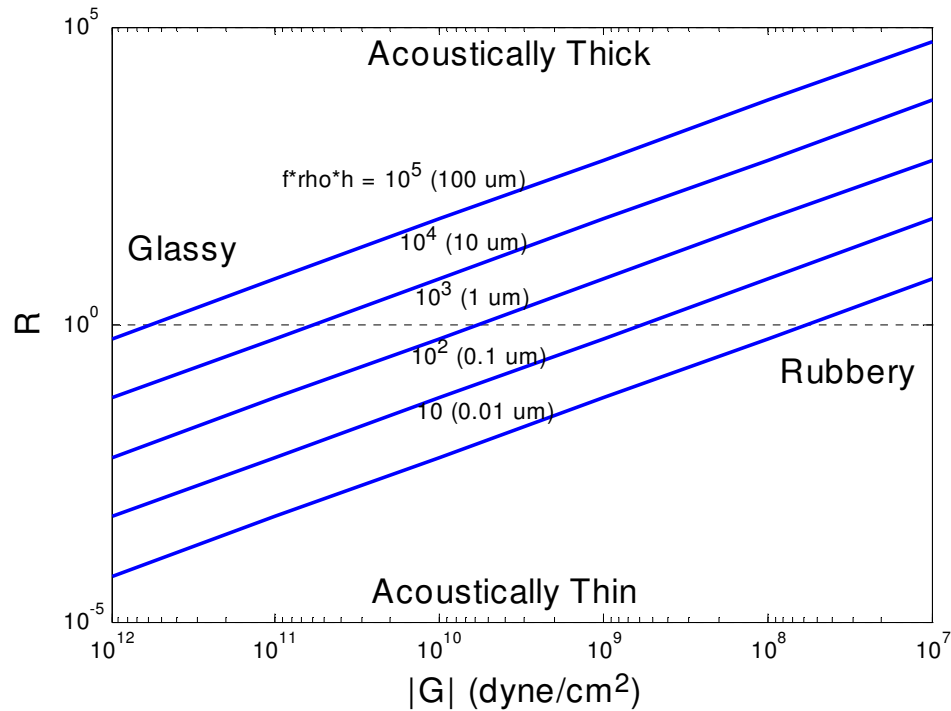
Figure 7 Calculated values of a typical 100 MHz SAW sensor with a polymer film to determine if it is acoustically thin or thick.

One challenge associated with new applications is the interpretation of the device-response. Often, SAW devices are used in arrays and when each device produces a complex response, the use of data analysis techniques is necessary. In this work, a chemometric technique was applied to the responses of the hexagonal SAW sensor. Within chemometrics there are many different techniques that can be used to analyze and build models from multivariate data [43, 44]. Principal component analysis (PCA) is perhaps one of the most common and robust methods for building linear multivariate models from complex data sets. Commonly, PCA is used for chromatography and other analytical techniques that involve spectral type data [43].

Techniques such as PCA are needed when sensor responses are not accurately predictable due to complexity in modeling and the unknown nature of the physical phenomena. The advantage of PCA over other techniques is its ability to map the sensor response to a unique set of basis vectors that span the significant space of the data matrix, $A$, without prior knowledge [44]. Empirically, the data can be described by:

$$A = T_k V_k^T + \varepsilon \tag{3}$$

where $T_k$ is an $n$ x $k$ matrix of principle component scores, $V_k$ is an $m$ x $k$ matrix of eigenvectors, and $\varepsilon$ is the unexplained variance. Based on this model, it is expected that each independent variation in the data will produce a principle component in the form of a nonzero eigenvector. The importance of the principle components will be ordered such that the first component will be the first column in $V_k$, which will be the principal component explaining the maximum variation. It is common to begin with >50 variants and reduce the data to only two principle components accounting for >99% of the variance in the data.

Since PCA can reduce data significantly, it is crucial that the data first be of high quality, and preprocessing be done to normalize/scale the data. There are many transformations that can be used on data to normalize them. Two of the easiest and most fundamental are mean centering and variance scaling [45].

3.2    Materials and Methods

3.2.1    Hexagonal Device Design

Several IDT designs have been tested on the route to devices having linear phase, low noise, and low insertion loss.  All of the devices designed and tested have been laid out using a standardized bonding pad design to increase the ease of probing while on wafer.  The overall die size is a 20 millimeter square.  Rotated about the center of the die are three identical bi-directional SAW delay paths consisting of an aperture of 47 $\lambda$, a delay path of 197 $\lambda$, a minimum feature size of 4 $\mu$m, with the delay path shorted.  See Figure 8 for an illustration of the hexagonal SAW layout.  The first patterns tested consisted of a standard double split finger design with 60 finger pairs, designed to have a narrow passband.  Subsequent and current designs have considerably fewer fingers.  The first technique to improve the SAW filter sensor characteristics was to remove fingers.  In the second techniques, the 60 pairs were reduced by pruning to create a ladder structure. The final design used employs a weighting technique of using one finger followed by a split finger to make up the pair [18, 19].  These three major designs are shown in Figure 3.  A standard metallization procedure of 100 nm chromium followed by 700 nm gold was used for all of the devices.

3.2.2   Electronic Characterization Methods

The hexagonal SAW devices were tested using an Agilent 8753ES S-parameter Network Analyzer connected to Mini-Circuits ZASWA-2-50DR switches.  The switches were configured to allow measurement of all three delay paths without the movement of the probing fixture or cables.  The fixture consists of a custom fabricated acetal housing holding spring pins (Ostby Barton Pylon) in a mating pattern to the bonding pads of the devices.  Due to the nature of the SAW devices, the hexagonal pattern resulted in the ground and signal pins to alternating, providing better than average signal properties when compared to other in house designed SAW's and fixtures.
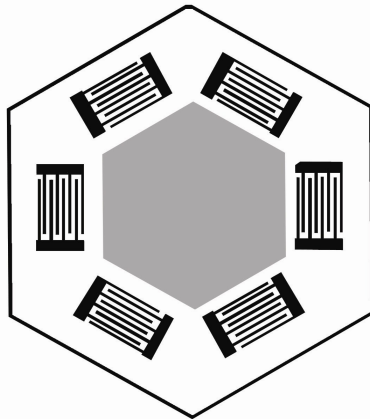


Figure 8  Hexagonal SAW device schematic.

Measurement of the wave velocity was achieved using the VNA's built in transform function.  This function is a Fast Fourier transform (FFT) that takes the standard $S_{21}$ parameter and converts it to the time domain which shows the fundamental and higher harmonics of the SAW device.  While in this measurement domain, the

maximum value on the plot is selected; this corresponds to the fundamental frequency of the SAW device. Further analysis such as applying gating to see the effects of bulk acoustic waves, triple transient effects, and internal IDT reflections of the different SAW devices was done while using the transform function.

The decision to monitor the phase and magnitude was made in light of the necessity for this project to have stable measurements. Typically, this type of measurement is done with large analytical tools, and has been shown by several researchers to be as good or better than measurements utilizing a feedback loop [21, 46, 47] Rugemer et al., 1999). The more traditional approach of using a feedback loop oscillator circuit with the SAW delay-line being the limiting factor to the frequency has been used extensively and is well known; however, this method is somewhat limited by interference from a number of sources including the RF amplifier. Another drawback to the oscillator configuration is only frequency-shift data can be easily collected [1], so less of an image of the sensing film interactions is perceived. Additionally, the oscillator circuit must maintain oscillation conditions; where as phase measurements can be made successfully under non-oscillatory conditions.

3.2.3   Polymer Solvent Experiments

The polymer poly(isobutylene) (PIB) was used for preliminary testing of the functionality of the hexagonal SAW devices. Tape was used to mask off the IDTs to prevent excess attenuation. A 0.5 weight percent PIB chloroform solution was used with

a Badger® airbrush to apply thin films from 200-600 nm onto the SAW delay path. Following the coating, the polymer was annealed for 20 minutes.

The hexagonal SAW was connected to a homebuilt organic vapor dilution system capable of delivering four different organic vapors with computer controlled accuracy. This dilution setup is described in detail by Upadhyayula, *et al* [48]. In this work the solvents benzene, chloroform, and hexane were used. The programmed exposure pattern consisted of a 1200 second purge followed by 600 second exposures and 600 second purges in increasing concentrations of solvent. The volume percentages of the solvent vapor in nitrogen are given in Table 2

Table 2  Concentration (volume percent) of solvents in nitrogen carrier stream.

| Stage | Benzene | Chloroform | Hexane |
|-------|---------|------------|--------|
| 1 | 0.8 | 1.9 | 1.4 |
| 2 | 1.6 | 3.8 | 2.8 |
| 3 | 2.4 | 5.6 | 4.2 |
| 4 | 3.2 | 7.4 | 5.5 |
| 5 | 4.0 | 9.0 | 6.8 |
| 6 | 4.8 | 10.7 | 8.0 |
| 7 | 5.5 | 12.2 | 9.2 |
| 8 | 6.3 | 13.7 | 10.4 |
| 9 | 7.0 | 15.2 | 11.5 |
| 10 | 7.7 | 16.6 | 12.7 |

3.3    Results

The three delay paths of the hexagonal SAW devices were first characterized in the VNA and followed by the vapor sorption experiments.

3.3.1   Characterization of Devices

For SAW device characterization, the primary analysis is the transmission s-parameter ($S_{21}$).  From this measurement, the amount of power transmitted through the delay line band pass filter SAW is plotted against a frequency sweep.  Further benefit from analysis was found by applying gating to the response to see the effects from triple transit and bulk effects.  Gating was applied to remove faster and slower effects from around the fundamental harmonic while monitoring the time domain.

Table 3   Theoretical Rayleigh wave and measured velocities of the three shorted delay paths of the hexagonal SAW device on lithium niobate.

| Orientation Euler Angle ($\varphi$, $\theta$, $\psi$) | Theoretical (m/s) | Measured (m/s) |
| --- | --- | --- |
| (0,90,91) | 3542.06 | 3593.30 |
| (0,90,151) | 3646.81 | 3721.85 |
| (0,90,31) | 3622.59 | 3620.73 |

The resulting typical $S_{21}$ responses after applying gating to remove these unwanted effects are shown in Figure 9.  Calculations for velocity were made while performing the analysis for gating while in the time domain.  As shown in Table 3 the measured values for the different delay paths correspond well to the theoretical velocities calculated by the Campbell and Jones method for the lithium niobate substrate.

31
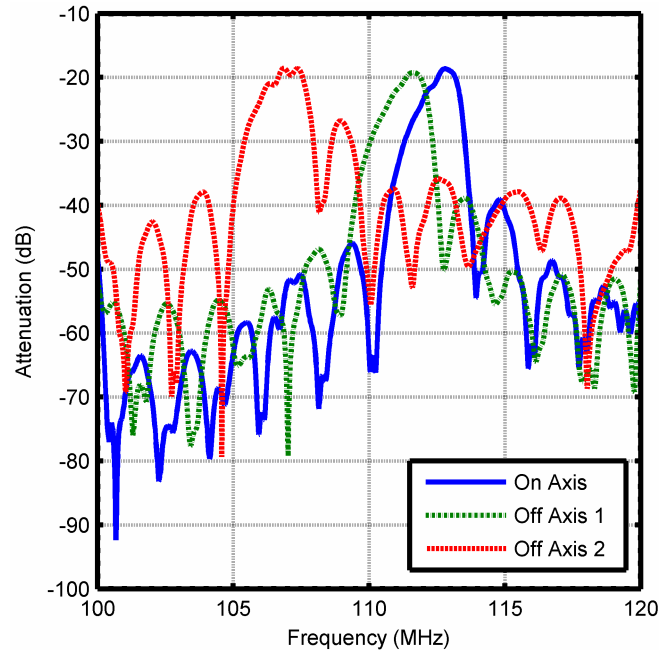
Figure 9  $S_{21}$ measurement of the three delay paths with gating applied having gating start and stop values of 1.218 μs and 3.878 μs.

SAW filter design has been a technology dominated by he communications industry.  For many years, the industry has developed advanced designs through an iterative process to eliminate the effects that are used to make good sensors.  For this reason it is important to continue the development of SAW devices for sensor applications.  As shown in Figure 10, are four generation of SAW patterns that have been tested in the hex-a-saw configuration.  The first design tested was a standard double split finger IDT structure consisting of 60 finger pairs, delay path of 197 λ, and a wavelength of 32 μm.  Such a design provided a narrow pass band response that is desirable for a sensor; however, due to the large number of fingers, the device displayed a significant amount of internal reflections.  Subsequent and current designs have reduced the number

of finger pairs by half, but have maintain the same delay path length, and wavelength to allow for easier comparisons.



(a)                                                          (b)

(c)                                                          (d)
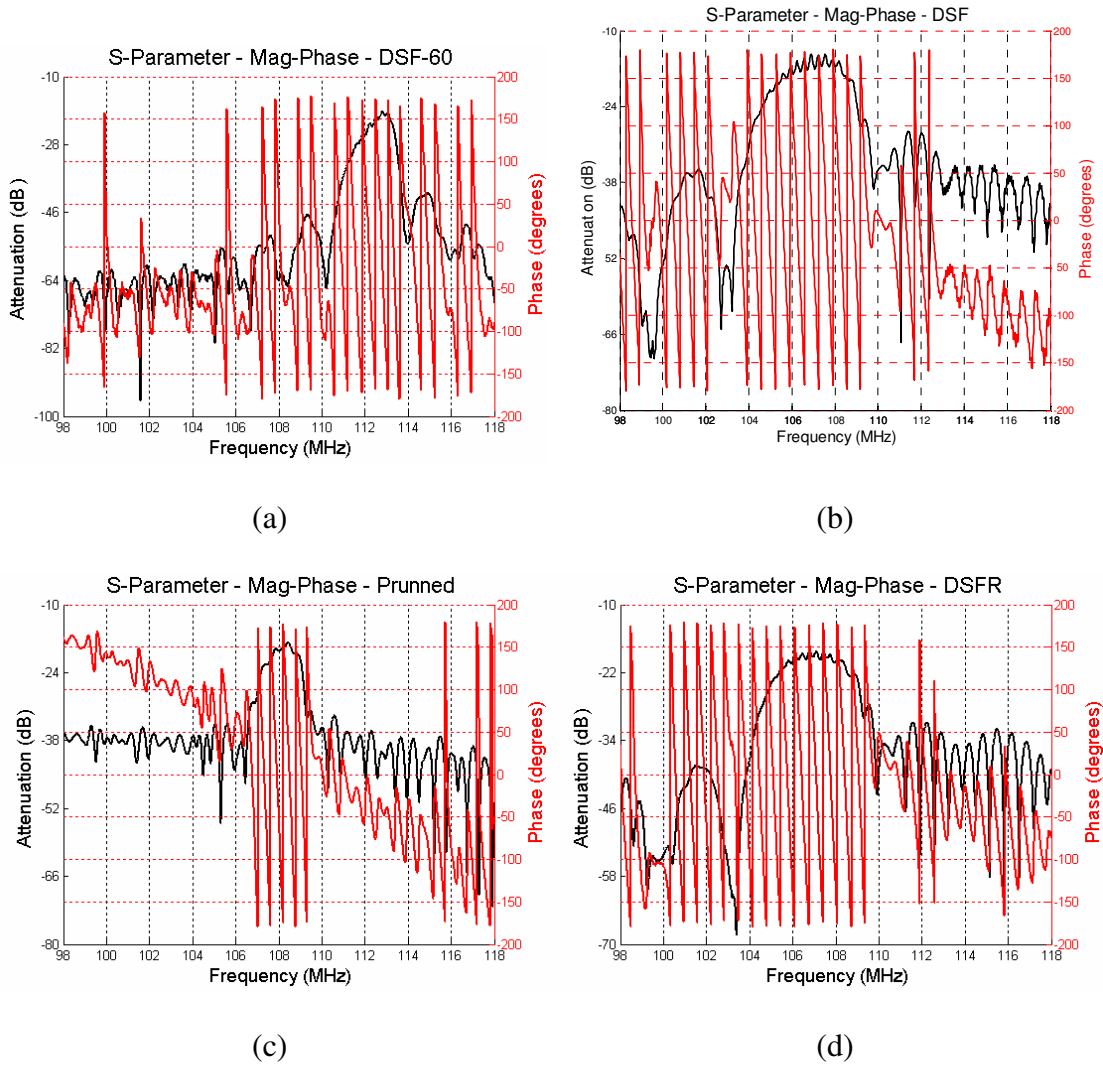
Figure 10  Comparison of in house SAW device designs responses as shown with phase and magnitude measurements.  (a) $S_{21}$ parameters of 60 finger pair double split finger IDT structure.  (b) $S_{21}$ measurements of 30 finger pair double split finger IDT structure. (c) $S_{21}$ measurements of pruned 30 finger pair double split finger IDT structure.  (d) $S_{21}$ measurements of pruned 30 finger pair combined single/double split finger IDT structure.
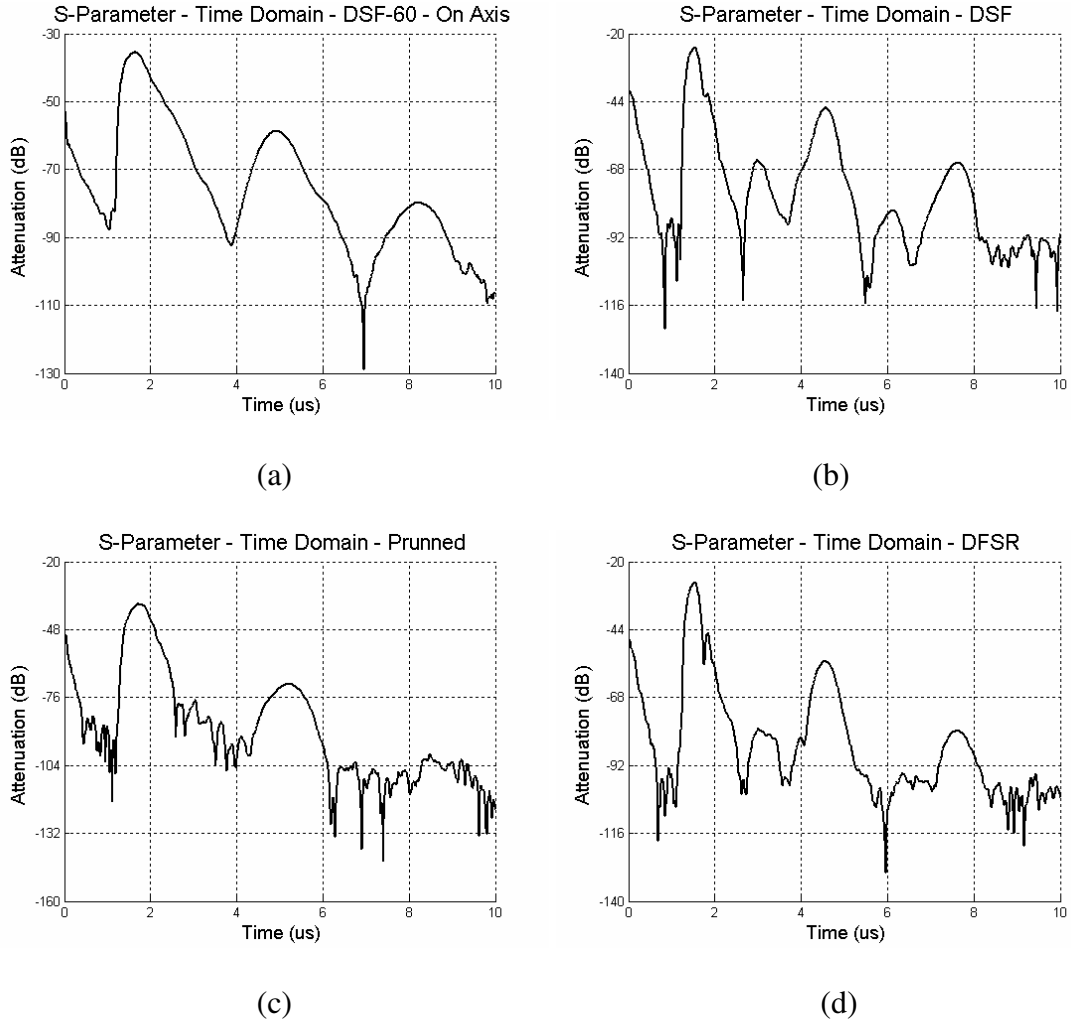
Figure 11 Comparison of fabricated SAW device designs responses as shown in the time domain. (a) $S_{21}$ parameters of 60 finger pair double split finger IDT structure. (b) $S_{21}$ measurement of 30 finger pair double split finger IDT structure. (c) $S_{21}$ measurement of pruned 30 finger pair double split finger IDT structure. (d) $S_{21}$ measurement of pruned 30 finger pair combined single/double split finger IDT structure.

Of the three other designs as illustrated in Figure 11, two of them are direct comparisons to the original 60 finger pair design. First the pruned IDT design is an

interesting modification that has the same length IDT; however, every other finger pair set has been removed. As expected, the response from this design shows much less internal reflection, yet it maintains the desirable narrow pass band. The second direct modification was to remove half of the finger pairs. This design also met expectations with less internal reflections and a wider pass band. Unfortunately, this design shows a triple transient effect that can hinder a sensors signal to noise ratio. The final design as shown in the figure is an advanced design that utilizes non-uniform IDT widths to reduce unwanted effects and better guide the SAW. All of these newer designs have additional features that include aperturization and gratings to further guide the SAW for brevity, these features provide small improvements to wave propagations from the input to output port.

S-Parameter - Mag-Phase - DSF-60 - On Axis

(a)

S-Parameter - Mag-Phase - DSF-60 - Off Axis 1

(b)

S-Parameter - Mag-Phase - DSF-60 - Off Axis 2

(c)
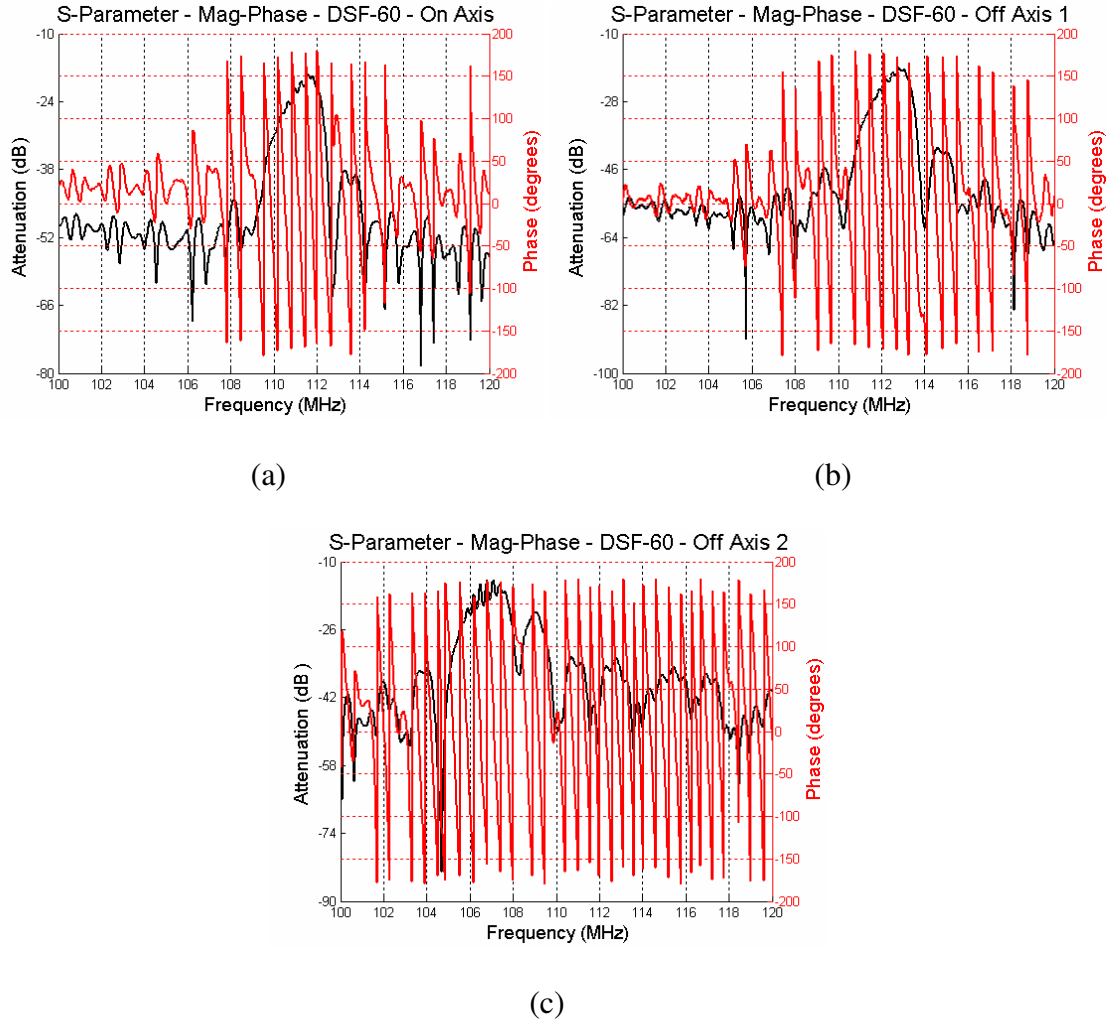
Figure 12  Comparison of one of the fabricated SAW device designs responses as shown as both the Logrithmic Magnitude and Phase of the three delay paths that make up one SAW.  (a) $S_{21}$ parameters of 60 finger pair double split finger IDT structure on axis propagation.  (b) $S_{21}$ parameters of 60 finger pair double split finger IDT structure off axis 1 propagation.  (c) $S_{21}$ parameters of 60 finger pair double split finger IDT structure off axis 2 propagation.
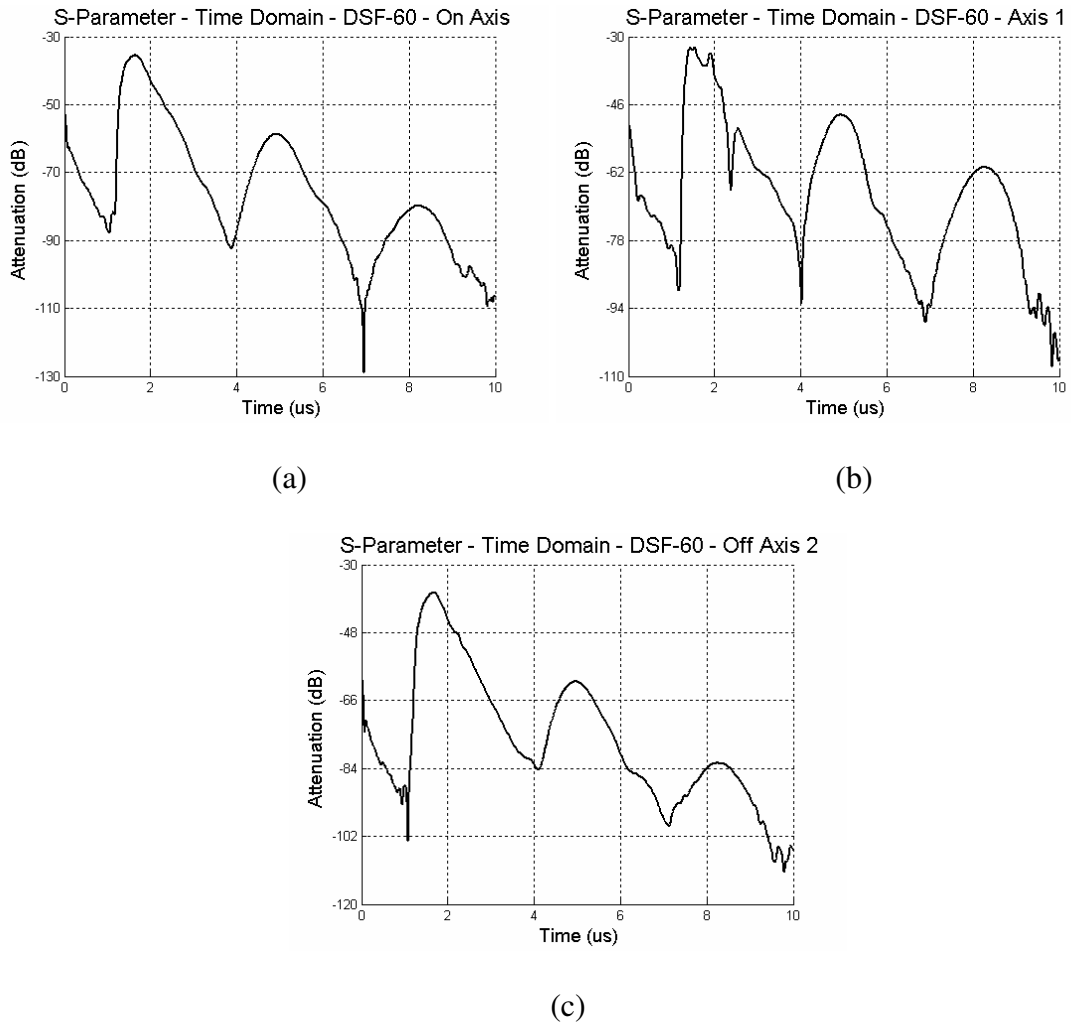
Figure 13  Comparison of one of the fabricated SAW device designs responses as shown as time domain measurements of the three delay paths that make up one SAW device.  (a) $S_{21}$ parameters of 60 finger pair double split finger IDT structure on axis propagation.  (b) $S_{21}$ parameters of 60 finger pair double split finger IDT structure off axis 1 propagation. (c) $S_{21}$ parameters of 60 finger pair double split finger IDT structure off axis 2 propagation.

### 3.3.2   Polymer Solvent Results

The hexagonal SAW device response to varying concentrations of benzene from exposures to the polymer film is shown in Figure 14.   The 500 nm PIB film on the hexagonal SAW responded to benzene at varying concentrations with differing attenuation and phase changes for the three delay paths.   The varying attenuation of the device is an indication that the polymer film was behaving as an acoustically thick film. Upon calculation of $R$ it is found that the film does fit the guideline for a thick film.
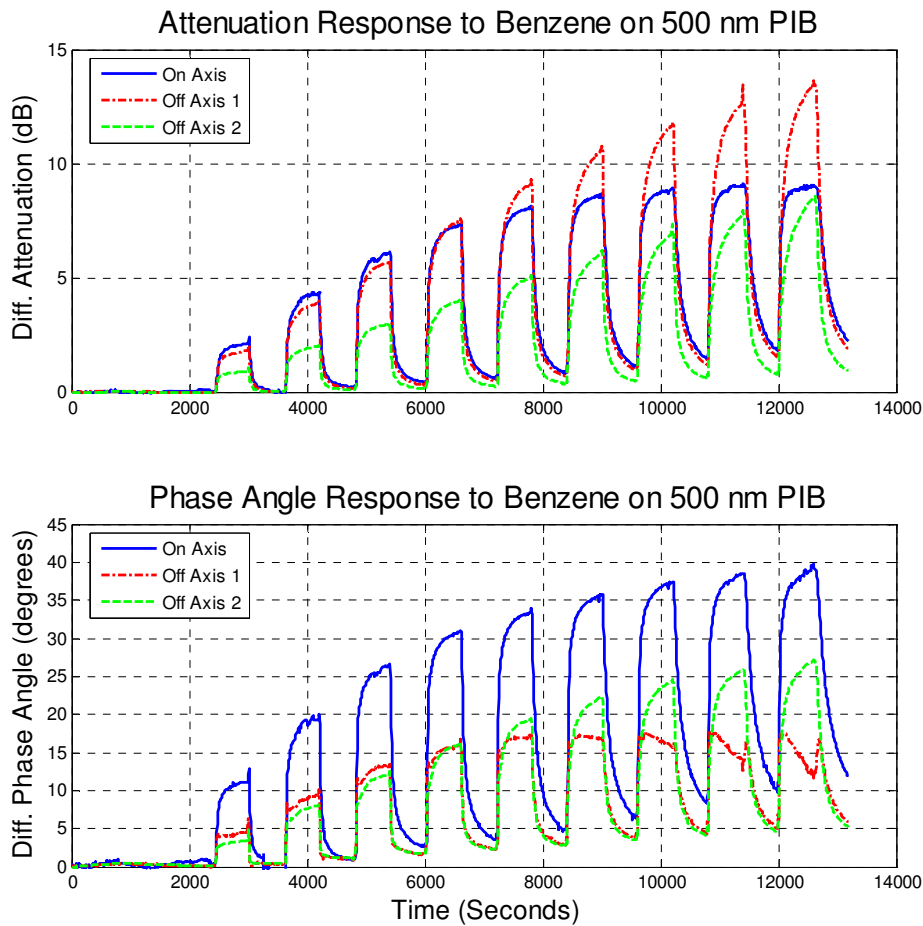
Figure 14  Difference measurements from 500 nm PIB on the hexagonal SAW absorbing benzene in nitrogen at 25 ºC, of volume percentages 0.9-8.0.  Attenuation (top) and phase angle (bottom)


Similar results are shown in Figure 15 for the solvent chloroform.  Notice in this plot the response of the on-axis phase starts to increase, but as the concentration increases, the phase response begins to shift in the opposite direction.  This phenomenon is more apparent in Figure 16 for the solvent hexane. The cause of the change is that the polymer film is acoustically thick and at the higher solvent concentrations, the film moduli actually can change significantly [1].

These vapor sorption data indicate that different wave types are likely propagating in the different delay path directions of the hexagonal device. In this case of YZ lithium niobate substrate, the on-axis wave is predominately a Rayleigh wave, but on rotation about the center origin, different modes of propagation are found. Because each delay path has its own unique frequency and wave type, multiple sets of equations can be solved to extract significantly more information on the coated film than if one device were to be used, providing a fuller picture of the film properties.
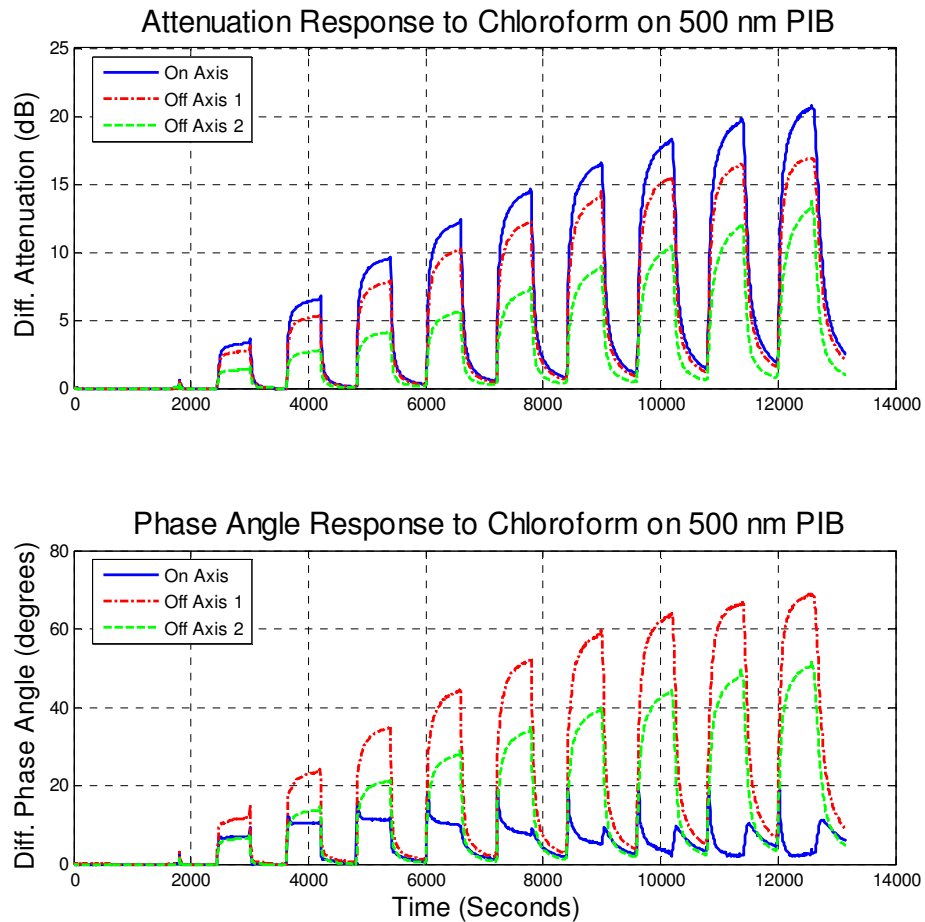


Figure 15  Difference measurements from 500 nm PIB on the hexagonal SAW absorbing chloroform in nitrogen at 25 ºC, of volume percentages 2.0-17.2.
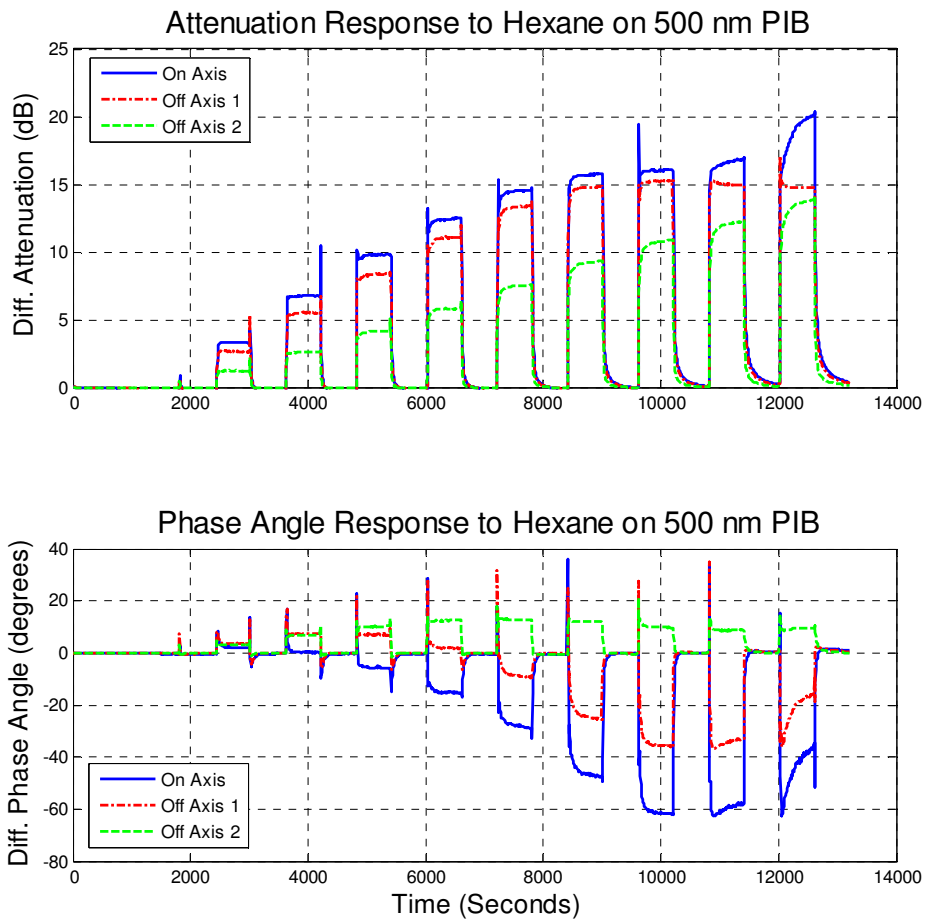
Figure 16  Difference measurements from 500 nm PIB on the hexagonal SAW absorbing

hexane in nitrogen at 25 ºC, of volume percentages 1.5-13.1.


Processed data from Figure 14, Figure 15 and Figure 16 of the extracted and

normalized maximum sensor response value for the three chemicals across the range of

concentrations is given in Figure 17.
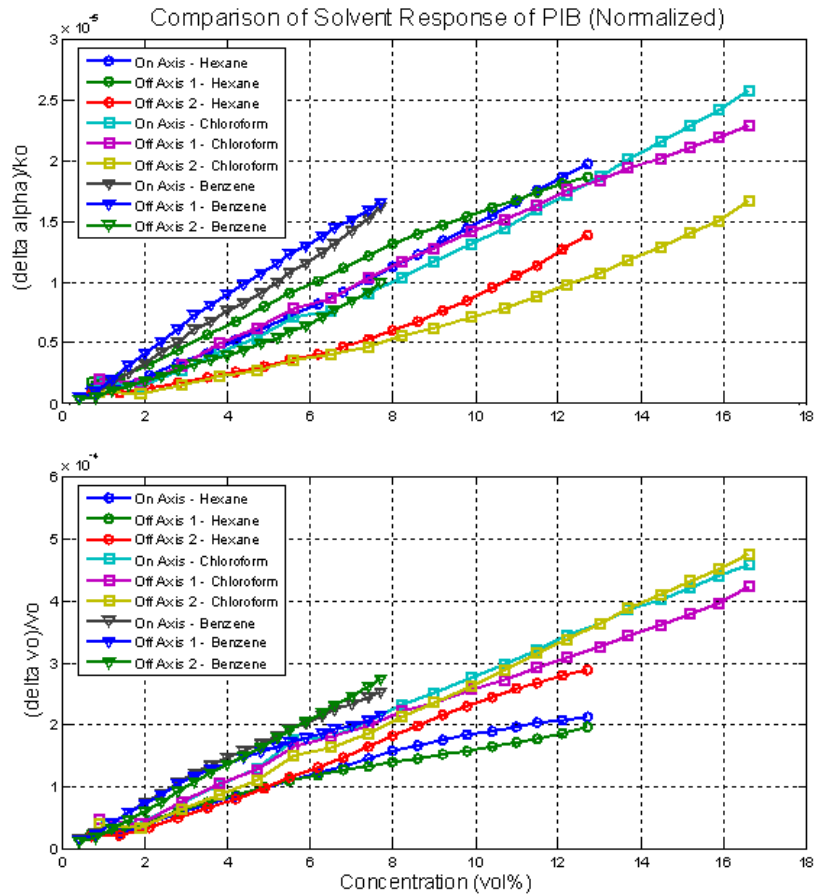
Figure 17  Normalized sensor responses to hexane, chloroform and benzene.

The pre-processed (normalized) data are shown in Figure 18 where the three delay path results for three different solvent vapors are plotted as the normalized change in velocity *versus* the normalized change in attenuation. From these plots, two observations can be made upon inspection. First, the three delay paths of the hexagonal SAW provide unique responses most likely from the variation of wave amplitudes and modes being generated. Second, a complex response of the polymer film is evident by the loops most easily observed in Figure 18(a) for the solvent chloroform. This behavior can be

explained by changes in the viscoelastic properties of the polymer film when exposed to different concentrations of solvent vapor.

The normalized data shown in Figure 18, were processed with the built-in function PRINCOMP in Matlab® version 7.0 [45, 48, 49]. This function centered the data and performed a PCA; a representative analysis is given in Table I. In this table, 98.07% of the data variance from the hexagonal SAW can be represented by the first principal component, and the second principal component is uniquely significant for the concentration of vapor. In effect, the PCA has reduced six independent measures and one control parameter to two components. It should be noted that although the 98.07% variance in the data are found in the first principal component, there are significant contributions to each of the other components by individual variables. This is shown by coefficient being underlined in Table 4 and indicates that the variables are fully independent.
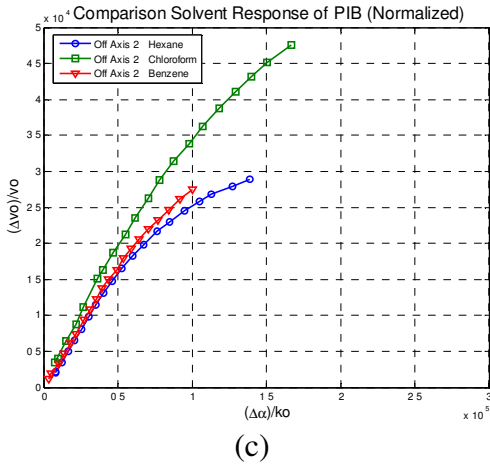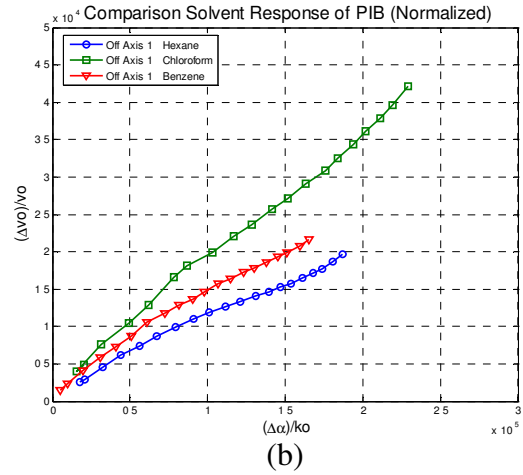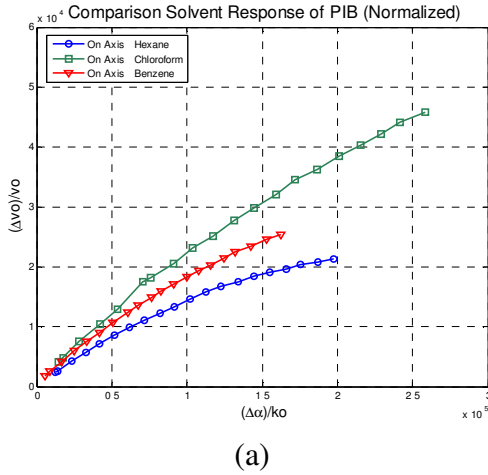
Figure 18  Pre-processed data of the hexagonal SAW response to 20 concentrations of hexane, chloroform, and benzene vapors.  Data are shown as the normalized change in velocity versus the normalized change in attenuation.  Each of the three plots is for a different delay path, (a) on axis, (b) off axis 1, and (c) off axis 2 for the three vapors

Table 4  Principal component analysis results.

| PC | Eigen value | Percent Variance Explained | Conc. | Phase 1 | Mag. 1 | Phase 2 | Mag. 2 | Phase 3 | Mag. 3 |
|---|---|---|---|---|---|---|---|---|---|
| 1 | 0.63 | 98.07 | *0.35* | *0.37* | *0.39* | *0.39* | *0.38* | *0.39* | *0.39* |
| 2 | 0.01 | 1.37 | *0.93* | -0.11 | -0.14 | -0.23 | -0.06 | -0.17 | -0.14 |
| 3 | 0.00 | 0.36 | -0.10 | *0.69* | -0.06 | -0.55 | 0.34 | -0.30 | 0.01 |
| 4 | 0.00 | 0.17 | -0.02 | -0.25 | *0.84* | -0.11 | 0.14 | -0.38 | -0.23 |
| 5 | 0.00 | 0.03 | 0.04 | 0.40 | -0.07 | *0.66* | -0.20 | -0.53 | -0.28 |
| 6 | 0.00 | 0.00 | 0.02 | 0.26 | 0.13 | -0.06 | -0.12 | *0.55* | -0.77 |
| 7 | 0.00 | 0.00 | -0.04 | -0.29 | -0.31 | 0.21 | *0.82* | -0.05 | -0.33 |

Based on this analysis, the principal components can be plotted against one another to show relationships in the lower dimensional space. The first principal component, combined film properties, is plotted against the second, concentration of vapor, in Figure 19. From this representation of the data, differences in the sensor responses between chemicals become easier to see.
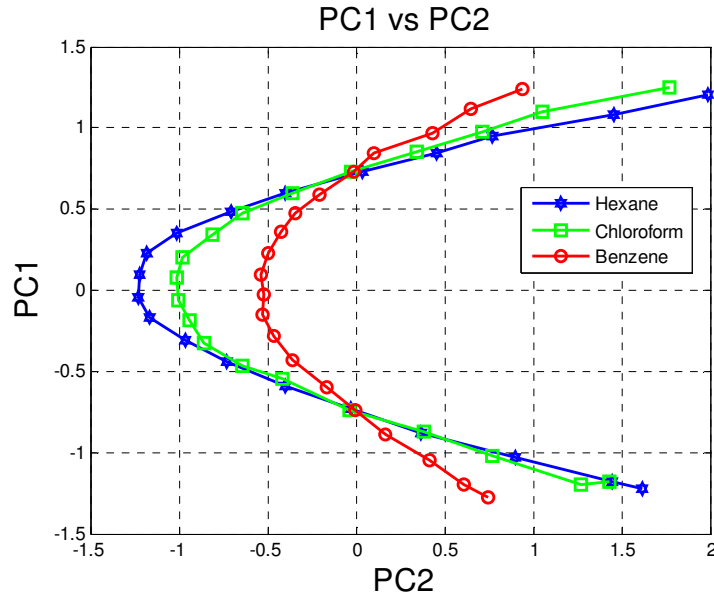
Figure 19 PCA component 1, predominately material properties, versus the PCA component 2, predominately concentration data.

3.4 Conclusions

The use of multiple SAW modes can provide more information about a sensing film as compared to using multiple SAW sensors with a single wave mode. Additional benefits of interrogating one uniform film can be realized, by providing multiple measurements for verification of responses. The use of a hexagonal pattern SAW on LiNbO$_3$ makes efficient use of the substrate, while having the potential to yield a clearer picture of the interactions of the sensing films with an analyte.

PCS was shown for the measurement of the relative measurement of material properties of PIB as it absorbs three solvents. Effectively, the PCA has reduced a six

dimension set of values to a three dimension set that is shown in Figure 19. From this analysis, the three solvents show unique principal components indicating that the data obtained from the hexagonal SAW are independent for the individual three delay paths and provide more information on the polymer film than a single delay line. Additionally, independence of the data is believed to allow one to solve for multiple film parameters simultaneously through the use of perturbation models that account for the viscoelastic effects seen in the film.

Chapter 4

Removal of Nonspecifically Bound Proteins on Micro-arrays Using Surface Acoustic
Waves

Nonspecific binding of proteins is an ongoing problem that dramatically reduces the sensitivity and selectivity of biosensors. Ultrasonic waves are generated by surface acoustic wave (SAW) devices remove nonspecifically bound proteins from the sensing and non-sensing regions of the micro-arrays. The approach for controllably and non-destructively cleaning the micro-array interface was demonstrated. In this work, SAWs were generated using 128º YX lithium niobate, chosen for its high coupling coefficient and efficient power transfer to mechanical motion. These waves propagating along the surface were coupled into specifically bound and nonspecifically bound proteins on a patterned surface of 40 μm feature size. Fluorescence intensity was used to quantify cleaning efficacy of the micro-arrays. The results have shown that excess protein layers and aggregates are removed leaving highly uniform films as evidenced by fluorescence intensity profiles. Selected antigen-receptor interactions remained bound during the acoustic cleaning process when subjected to 11.25 mW of power and retained their efficacy for subsequent antigen capture. Results demonstrate near-complete fluorescence signal recovery for both the sensing and non-sensing regions of the micro-arrays. Of significance is that this approach can be integrated into existing array technologies where

sensing and non-sensing regions are extensively fouled.  This technology will be pivotal in the development and advancement of microsensors and their biological applications.

## 4.1    Background

Current microsensors for protein quantifications rely on optical, acoustic, electrochemical, or thermal principles and techniques [32, 34, 46, 50-52].  Response discrimination from unwanted signal noise is a deficiency common to all of these techniques.    False positive/negative identifications and decreased sensitivity are associated with this lack of discrimination, limiting the usefulness of automation [5]. This is a result of nonspecific binding of proteins over the entire surface of the micro-array [5, 32].  Unlike chemical sensors that are long-lasting and reusable because of known, reversible interactions between the analyte and sensing film, proteomic interactions are not as controllable.  Even though biological sensors have known specific interactions that are relied on in every biosensor to make determinations, they also have nonspecific interactions with nearly every surface.   These nonspecific interactions, termed nonspecific binding, occur from a combination of intermolecular forces such as ionic, hydrophobic, and van der Waals forces and result in large undesirable effects [1, 53].

Beyond nonspecific binding, biological sensors are prone to many challenges, including toxicity and difficulties with binding of desired proteins to appropriate locations.  This has been recognized for some time as one of the most difficult issues

found in protein patterning [54, 55]. As sample volumes decrease, nonspecific binding becomes a more significant problem as typically rare and expensive samples are tested, and statistically valid data are needed. To address this problem, chemical techniques and processes have been developed to reduce nonspecific binding [1, 56]. Another common method is to use micro-patterning followed by applying a blocking agent to the non-patterned regions. This latter method will not only terminate the active surface groups, but also block other proteins from binding where they are desired [56-60].

SAW devices have been used for many years in chemical sensing [1]. Within the past few years, these sensors, and more generally acoustic wave sensors, have been tested for application in biological sensor applications for the same reasons they were chosen for general chemical applications, such as: high sensitivity, ease of integration into electronic circuits, and all around robustness [34, 61]. For instance, SAW sensors have been used for rapid detection of antigens in foods and fluids [1, 18, 55], operating primary as mass sensors. SAW sensors can also be perturbed by temperature, pressure, and electrical properties of the sensing film [1], allowing for the possibility of additional sensing mechanisms.

Surface acoustic wave devices have also been investigated for their ability to launch longitudinal waves into fluids. This phenomena known as acoustic streaming [26] can generate very large nonlinear gradients in fluids [29]. To date, the phenomena of acoustic streaming has been limited to few applications for example in high-efficiency micro-fluidic mixing [4] and in removal of nanoparticles from a surface [28]. Additionally, Cooper *et al* has shown rupture event scanning using a quartz crystal

acoustic wave resonator to break bonds between materials on surfaces. In their work, this technique has been applied to the detection of herpes simplex virus [62, 63].

In this study, SAW devices were evaluated for their ability to remove proteins without disrupting subsequent biological activity for immunoassay applications. Three primary experiments focused on testing the hypotheses that: (1) acoustic waves do not inhibit the activity of the covalently attached antibody receptor layer after acoustic treatment, (2) nonspecifically bound proteins can be removed using surface acoustic waves, and (3) specifically bound proteins can also be removed from their receptors using acoustic waves. Collectively, these experiments were performed to determine whether surface acoustic waves can be used to enhance signal response by removing weakly bound proteins from both the sensing and non-sensing regions for protein micro-array applications.

## 4.2    Materials and Methods

### 4.2.1    SAW Device and RF Design

A Rayleigh SAW device was fabricated in 128º LiNbO$_3$ with an electrode pattern having 40 double split finger pairs per interdigital transducer (IDT). The aperture was 38 $\lambda$ and the center to center IDT separation of the device was 120 $\lambda$ wavelengths. The substrate was chosen for efficient Rayleigh wave generation to produce the acoustic streaming phenomenon. Acoustic wave sensing using Rayleigh wave SAW devices is

not suitable for liquid environments, for which shear-horizontal SAWs have been shown to be effective.

4.2.2    Silanization of Lithium Niobate

A 1 vol% (3-glycidoxypropyl)dimethylethoxysilane (Sigma Aldrich) (3-GPDMS), in toluene for 1 h was used to form the organosilane  film on the lithium niobate surface as shown in Figure 20. Prior to this treatment, the SAW devices were washed with a typical acetone, methanol, de-ionized water cleaning process to remove any photo-resist as well as other surface contaminants.  This general cleaning was followed by 2 minutes of air plasma cleaning in a Harrick plasma cleaning system set on the lowest setting of 6.8 Watts.  Substrates were rinsed in toluene for 1 minute, dried with nitrogen and baked at 125 °C for 1 hour to complete the hydrolysis reaction.
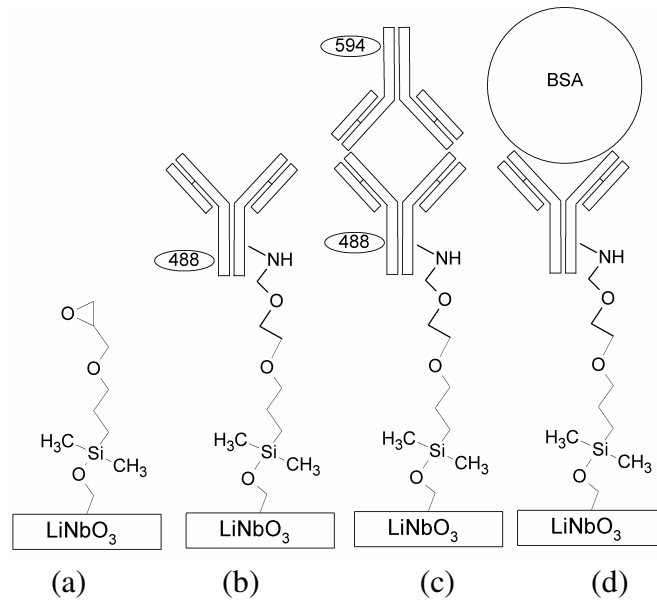
Figure 20  Covalent attachment of IgG and BSA to LiNbO$_3$ substrates via 3-GPDMS.  (a) lithium niobate with organosilane; (b) lithium niobate with organosilane and covalently bound IgG antibody; (c) lithium niobate with organosilane and covalently bound IgG antibody with specifically bound IgG antigen; and (d) lithium niobate with organosilane and covalently bound IgG antibody with nonspecifically bound BSA.

### 4.2.3  Patterning of SAW Devices

To form a representative micro-pattern array of 40 μm squares on the delay path of the SAW devices, a photo-lithographic process was utilized [53].  By patterning the IgG proteins, both sensing and non-sensing regions were defined.  The sensing regions are shown in Figure 20b, and with the specific antigen capture in Figure 20c.  The non-sensing region is passivated using BSA as shown in Figure 20d. To achieve this, devices

were spin coated with AZ5214 photo-resist for 30 seconds at 3000 rpm. This provided a uniform coating of 1.6 µm that was subsequently soft-baked for 20 minutes at 95 ºC. Patterning of the photo-resist was accomplished on the bench top with a long wavelength UV lamp and a dark field emulsion mask. Devices were aligned using a custom fabricated mask aligner, followed by exposure to UV light for an optimized time of 30 seconds. Devices were removed from the aligner and the photo-resist was developed for 1 minute in a 1:5::400K developer:water solution. Immediately following the development, the devices were rinsed for 2 minutes in de-ionized water to terminate the development reaction. This process was used for both non-treated and organosilane treated devices.

4.2.4    Deposition of Protein Films

To assess the impact of nonspecific binding in the sensing and non-sensing regions, proteins were fluorescently labeled with Molecular Probes Alexa Fluor kits (Invitrogen, Carlsbad A). Goat anti-mouse IgG (Pierce Chemical Co., Rockford, IL) was labeled with Alexa-488 (Molecular Probes, Eugene, OR) and covalently attached to the 3-GPDMS film. Mouse anti-rabbit (Pierce Chemical Co., Rockford, IL) was labeled with Alexa-594 (Molecular Probes, Eugene, OR.), acting as the specific capture antigen. To determine the degree of nonspecific interactions of proteins on the IgG films, BSA was labeled with Alexa-488, whereas goat anti-mouse was not labeled in this case.

Following preparation of the 3-GPDMS film (Figure 20a), 6 µl of goat anti-mouse IgG (Pierce, Rockford, IL) 0.1 mg/ml in 1X PBS pH 7.2 was applied to the devices for 20 minutes. The devices were rinsed using 1X PBS. The non-sensing regions were blocked using 1 mg/ml of unlabeled BSA in 1X PBS pH 7.2, applied for 20 minutes. To demonstrate antigen capture on the sensing regions of the array and potential background fouling, mouse anti-rabbit IgG (Pierce, Rockford, IL) 0.1 mg/ml in 1X PBS was applied over the entire array for 20 minutes. Subsequently, the devices were sealed in a humidity chamber to minimize evaporation. Following the incubation period, the devices were rinsed with 1X PBS to remove weakly bound proteins and stored in 1X PBS.

For the first protein layer which was directly patterned with the photo-resist, acetone was used to rinse away the photo-resist. The acetone rinse was followed by a 1X PBS rinse and immersion in 1X PBS buffer while waiting for the next processing step.

### 4.2.5 Ellipsometry and Thickness Measurements

Film quality was assessed by measuring the film thickness of each layer using ellipsometry. To quantify the films, silicon wafers were used as substrates in the covalent attachment procedure. These measurements established the baseline properties of the films prior to acoustic excitation.

Polished silicon (Si) wafers (100, phosphorous doped) were purchased from MEMC Electronic Materials Inc. (Spartanburg, SC). The wafers were cleaned by rinsing with de-ionized water then rinsed with acetone, methanol, isopropanol, and de-ionized

water.    Residual organics were removed using an UV/Ozone Cleaner (UVOCS, Montgomeryville, PA) for 10 minutes.

An automated Microphotonics ellipsometer was used (Model ELX-01R, Microphotonics Corp., Allentown PA), with an incident angle of 70° and a wavelength of 6328 Å.  Using the vendor's software, models were developed to measure the individual film thickness for each layer.  The surface concentration and hence surface coverage of the organosilane and protein films can be calculated from the film's refractive index thickness [64] by:

$$\Gamma(\mu gcm^{-2}) = d\rho_0 = 0.01d\frac{M_w}{A}\frac{n^2-1}{n^2+2} \tag{4}$$

where $\rho_0$ is the bulk density (g/cm$^3$), d is the thickness of the film (Å), Mw is the molecular weight of the substance,  n is the index of refraction, A is the molar refractivity of the material. For the organosilane, the index was taken as n = 1.44.  For protein, Mw/A = 4.12 g/cm$^3$ based on the findings of Vogel et al. [65] and the index of refraction was estimated from atom or atom groups [66] and found to be 1.542.  By knowing the crystallographic dimensions of IgG, the surface coverage can be computed from the cross-sectional area given as 45 nm$^2$ [67].  The estimated cross-sectional area for the organosilane was 25 Å$^2$ [68].

4.2.6    Acoustic Protein Removal

Prepared protein patterns on lithium niobate were placed in a lexan micro-fluidic cell to permit optical interrogation during acoustic excitation.   The protein microarrays were patterned in the central region between the opposing IDTs on the lithium niobate. The SAW devices were driven using a Hewlett Packard 8656B frequency generator and an ENI 420A RF amplifier.  Power delivered to the SAW devices was calculated to make direct comparisons with previous work done with quartz crystal resonators (QCR) for removal of nonspecifically bound proteins [5] and SAW streaming to mix samples [4]. The S-parameters of the SAWs were measured to determine both the return and insertion loss using an Agilent E8358A vector network analyzer.  Experimental data with respect to the removal of proteins were collected in the form of fluorescent images.

4.2.7    Fluorescent Imaging and Processing

Successful formation of the patterns was verified using an Olympus IX-70 microscope configured with a Roper Scientific Cool Snap ES® CCD camera.  Images of the fluorescently labeled devices were taken outside of the micro-fluidic fixture to increase their clarity.   Images were obtained by application of a large drop (~50 µL) of 1X PBS to a cleaned glass slide and inversion of the coated device onto the slide.  The drop of 1X PBS protected the films on the surface of the SAW device.

Images were processed using the MetaMorph® software (Molecular Devices Corp., Sunnyvale, CA). To reduce differences from potential dye photobleaching, fluorescent images were taken before and after acoustic excitation using the same exposure times. Background fluorescence was obtained from regions adjacent to the fluorescently attached protein. To facilitate image clarity, bit thresholding was used remove low and high level intensities in the images. After thresholding, equal area regions were defined to correspond to the sensing and non-sensing regions. Sequential red and green images were placed in stacks and aligned. The region number, pixel area, threshold pixel area, percent threshold area, and average pixel intensity were recorded for analysis.

## 4.3    Results

First the depositions of organosilane film and protein attachment to it were considered. Secondly, two major issues were investigated for the Alexa-488 labeled goat anti-mouse IgG film schematically shown in Figure 20b, first the potential ability of acoustic excitation to remove covalently attached proteins, and second possible acoustic damage to the proteins that would prevent antibody-antigen binding (Figure 20c). Thirdly, for the Alexa-594 labeled mouse anti-rabbit IgG, whether acoustic excitation could remove nonspecifically bound proteins (e.g. fouling by BSA) without removing the bound mouse anti-rabbit antigen were determined. Fourthly, whether acoustic excitation can remove specifically bound Alexa-594 labeled mouse anti-rabbit IgG were

58

determined. Collectively, the experiments conducted in this work and the results allowed: evaluation of the effectiveness of acoustic waves in removing nonspecifically bound proteins, of potentially damaging the desired bonding and attachment of proteins, and the possibility of removing specifically bound proteins. While the objective of this work is to fabricate a device that can remove nonspecifically bound proteins, it is important to know what levels of acoustic energy can affect specific binding; hence this last topic was also investigated.

### 4.3.1 Organosilane and Protein Films

Ellipsometry was used to verify that an adequate amount of organosilane was bound to the lithium niobate substrate (Table 1). The organosilane film resulted in a spacing of 9.4 Å between adjacent molecules. Given that the cross-sectional area of the anti-mouse IgG is around 45 nm$^2$, presence of a sufficient amount of organosilane to permit high surface coverage of antibody in the patterned regions and BSA in the non-patterned regions is suggested.

Prior to measuring the 3-GPDMS and protein film thicknesses using ellipsometry, the complex refractive indices of the bulk silicon and silicon dioxide were determined. This was done by measuring the ellipsometric angles $\Psi$ and $\Delta$ in air and water using the ELX-01R. Using two sets of $\Psi$ and $\Delta$, the bulk silicon index (nSi), the refractive index of $SiO_2$ (nox), and the $SiO_2$ thickness (d$_0$) were determined using a three-layer model. The

values calculated for $n_{Si}$, and $n_{ox}$ were $3.885 - 0.019i$ and $1.459$ at $\lambda = 6328$ Å. The oxide thickness $d_0$ ranged from 12 to 22 Å.

The subsequent 3-GPDMS and protein films were measured using four, five, and six layer models with the vendor's software. After a 1 h application of 3-GPDMS, ellipsometry indicated an average thickness was $4.3 \pm 0.5$ Å (n = 4). This corresponded to a surface coverage of 61.4% or nearly a monolayer of organosilane. The results are shown in Table 5.

Table 5  Ellipsometry determined organosilane and protein film average thickness and surface coverage.

| Film | Average Thickness (Å) | Surface Coverage (%) |
|---|---|---|
| 3-GPDMS | $4.3 \pm 0.5$ | 61.4 |
| Anti-mouse IgG | $33.5 \pm 4.0$ | 70.1 |
| Mouse IgG | $37.3 \pm 5.3$ | 72.3 |

4.3.2    Protein Activity after Acoustic Excitation

Protein activity was determined by measuring the fluorescent intensity of the Alexa-594 labeled mouse anti-rabbit IgG antigens on two samples. Sample one consisted covalently bound Alexa-488 goat anti-mouse IgG pattern, shown schematically in Figure 20b; whereas, sample two consisted of the same pattern which was acoustically driven using 500 mW for 15 minutes. This power was estimated to be several times in excess of that required to remove nonspecifically bound proteins. Alexa-594 labeled mouse anti-

rabbit IgG antigens were specifically bound to both samples. Fluorescence intensity

measurements were then conducted on both samples. As shown in Figure 21b, there is

not a significant decrease in fluorescence intensity for the Alexa-594 mouse anti-rabbit

IgG bound to acoustically treated goat anti-mouse IgG, in comparison to Figure 21a.

Thus, the covalently bound antigens do not lose activity upon acoustic excitation.
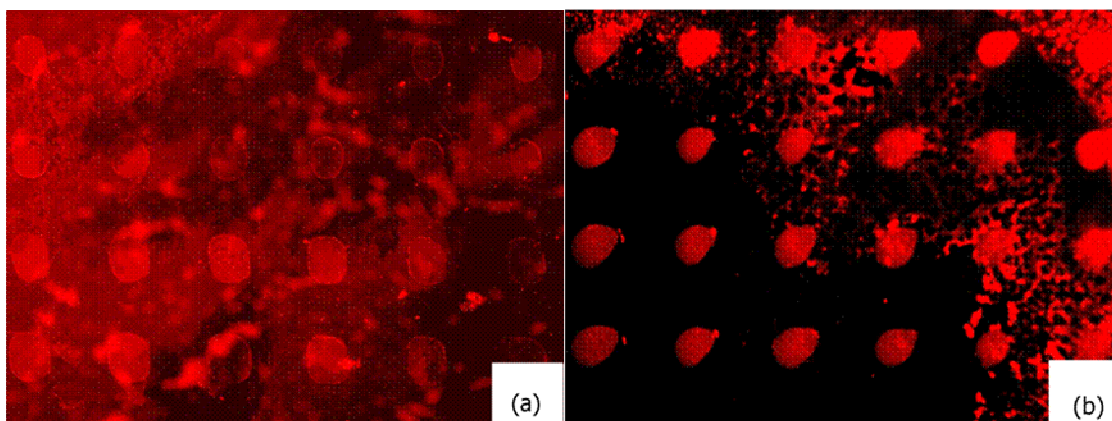


Figure 21   Alexa-594 labeled mouse anti-rabbit IgG binding to goat anti-mouse IgG

without and with acoustic excitation.  Two samples (a) without acoustic excitation and

(b) With acoustic excitation for 15 minutes at 500 mW.

4.3.3   Removal of Nonspecifically Bound Proteins While Retaining the Specifically
        Bound

Nonspecifically bound protein removal, while retaining specifically bound ones,

was shown using covalently bound non-fluorescently labeled goat anti-mouse IgG to the

microarray-surface.  This change in surface preparation allowed for the use of only two

fluorophores in all experiments reported in this work.  The antigen, mouse anti-rabbit

IgG, was labeled with Alexa-594, and BSA, not used as the blocking agent, was labeled with Alexa-488. Consistent deposition procedures were followed in the all experiments. The labeled BSA was applied over the antibody-antigen complex. The result of the nonspecific binding across the entire surface of the sensor was a difficult to distinguish microarray pattern. As the acoustic waves interacted with the protein film, the fluorescent intensity of nonspecifically bound BSA decreased significantly while the fluorescent intensity of the specifically bound proteins only decreased slightly (Fig. 3). This slight decrease in the Alexa-594 intensity is believed to be a result of the reduction in multilayers of antigen-antigen nonspecific binding.
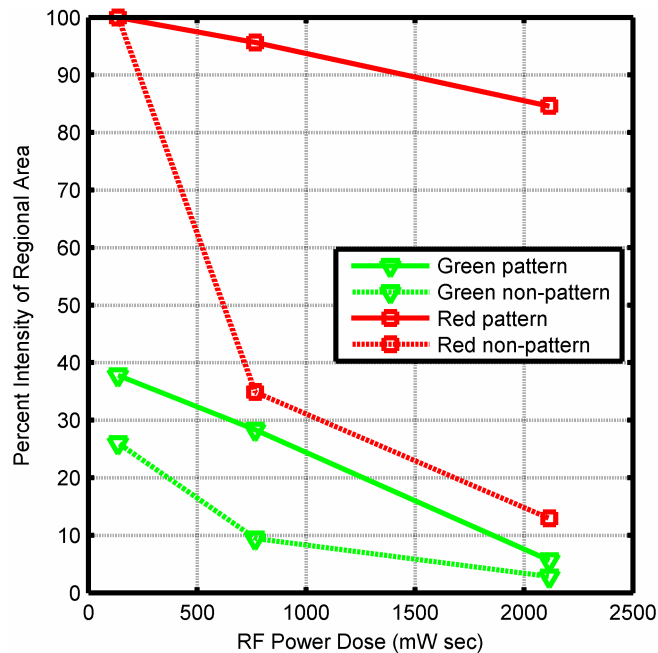


Figure 22  Non-labeled goat anti-mouse IgG was covalently patterned and bound to the 3-GPDMS surface followed by acoustic excitation and application of BSA to terminate non-patterned regions.  Alexa-594 labeled mouse anti-rabbit IgG (Red) was specifically bound.

Figure 23 and Figure 24 indicate nonspecifically bound proteins can be removed by acoustic waves, consistent with the observed general trend of a decrease in fluorescence intensity with increased applied RF power dose. The covalently bound antibodies labeled with the green fluorophore decreased only slightly, whereas, the intensity of the antigen labeled with the red fluorophore decreased from ~65% to ~15%, a level nearly equivalent to that of the green labeled antibody as shown in Figure 23. This quantitative analysis was done from the image sequence represented by Figure 24. In Figure 24d, partial recovery of the Alexa-594 labeled mouse anti-rabbit IgG from the completely obscured pattern in Figure 24a is shown, indicating that blocking agents such as BSA are extremely difficult to remove unless acoustic methods are used. The use of a moderate level (1mg/ml) of BSA to block the un-reacted 3-GPDMS groups, suggests that protocols using higher levels are not suitable for subsequent reaction and hence may suffer from poor detection efficacy in biosensor applications.
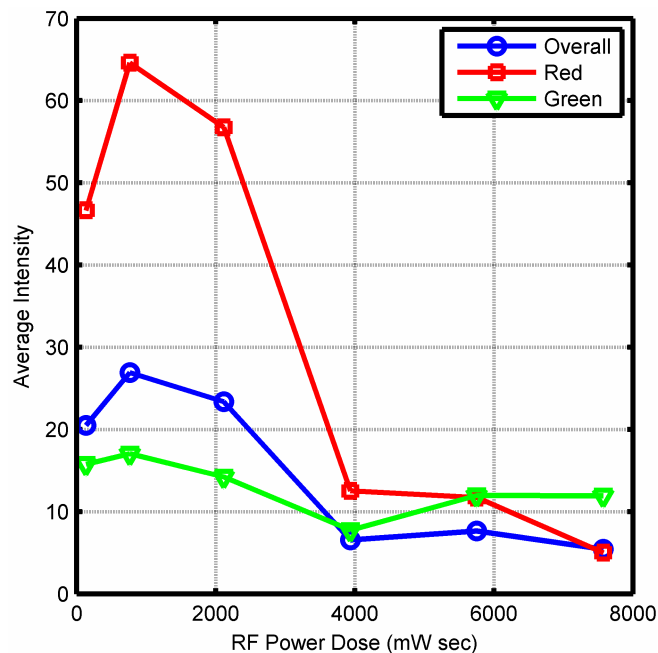
Figure 23 Overall intensities of fluorescently labeled proteins versus RF power dose. The Green and Red labeled data sets represent antibodies covalently bound to surface and the analyte antigens, respectively. The Overall is a combined intensity across the entire surface of the microarray being imaged.
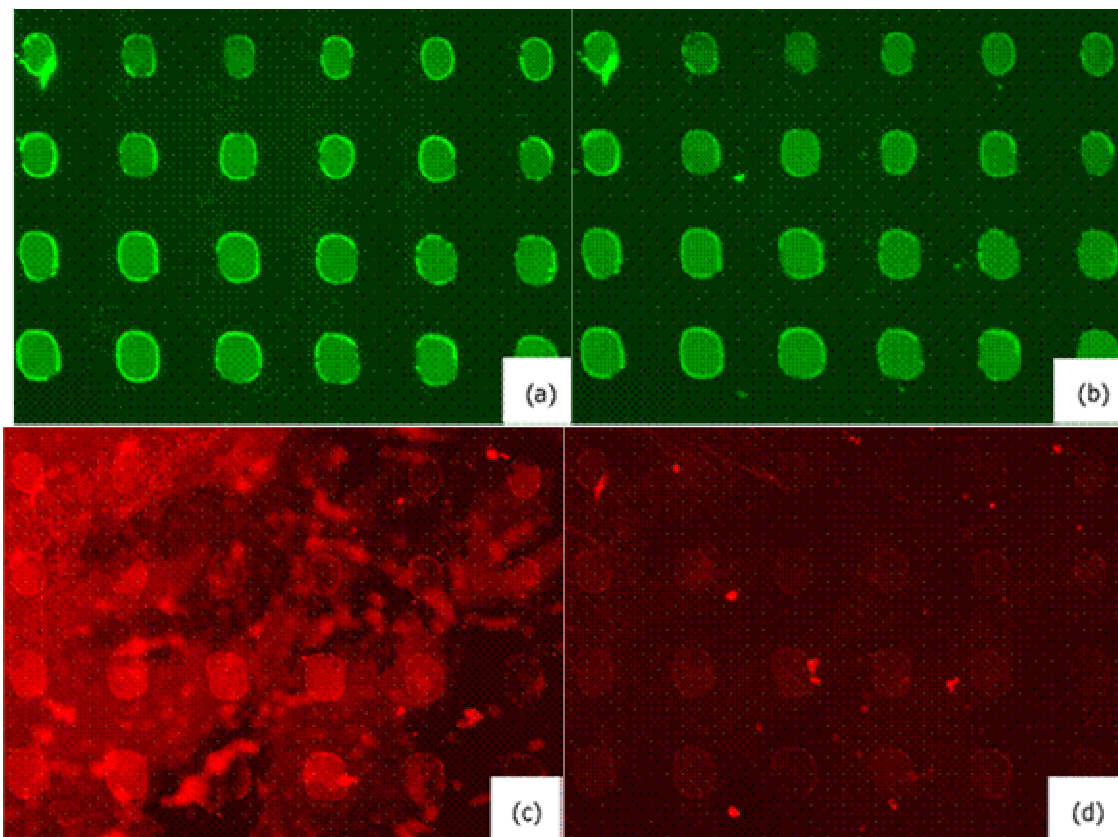
Figure 24  Grayscale images (pseudo-colored) of 40 μm microarray pattern before and after acoustic cleaning.  (a) Antibody covalently bound to the silanized surface prior to the acoustic cleaning.  (b) The result of acoustic cleaning on the pattern from image a. (c) Microarray pattern of antigen specifically and nonspecifically bound to the blocking agent and antibody.  (d) The result of acoustic cleaning showing partial recovery of the pattern.

### 4.3.4  Removal of Nonspecific and Specific Proteins

Previous experiments in this study have shown that it is possible to remove nonspecifically bound proteins easily.  With increased exposure to the acoustic waves, it

is possible to remove specifically bound proteins also.  Figure 25 shows two major steps in the red patterned line.   The first step is believed to indicate the removal of nonspecifically bound proteins and the second step the removal of specifically bound proteins.  These results are valuable for biological sensors because it is possible to make a renewable device with no more than a few minutes of exposure to increased RF power doses.
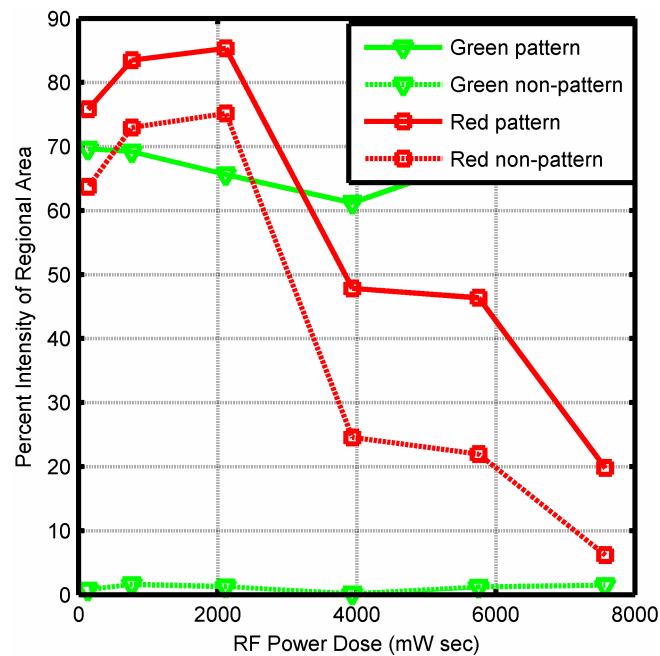


Figure 25  Mouse anti-rabbit IgG (red) and goat anti-mouse IgG (green) pattern and non-patterned intensities versus the RF power dose delivered to the microarray.

4.3.5   The Control Experiments

Control experiments were conducted to represent current practices in microarray analysis. For the controls, substrates were treated identically as the ones tested with acoustic cleaning. The first control experiment was done after the application of the fluorescently labeled antigen by vigorously washing the sample in PBS buffer solution. The results of the washing are shown in Figure 26; there are a few nonspecific attachments of the antigen to the BSA blocking agent in the non-patterned regions that appear to have been removed. Additionally, after the vigorous washing (Figure 26), there was an increase slightly beyond the standard deviation in the non-patterned regions' fluorescence intensity.

Subsequent control experiments were conducted for each of the processing steps and showed similar results.
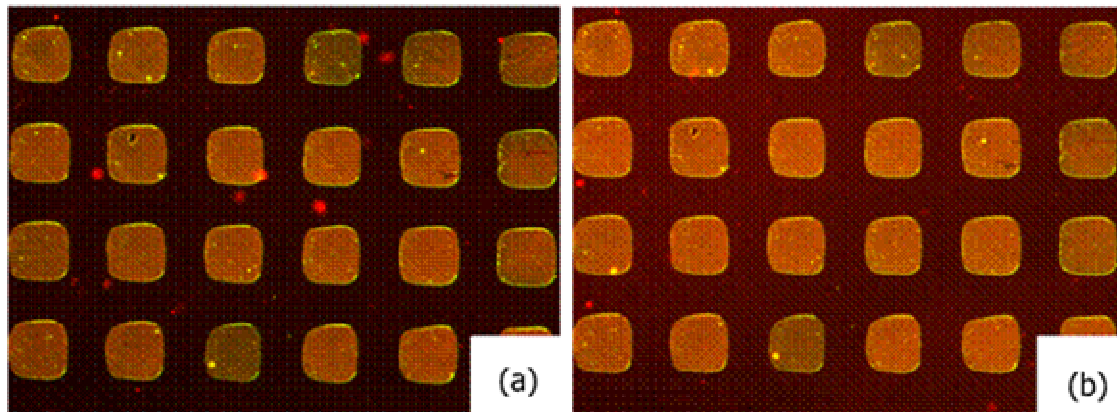


Figure 26   Alexa-594 labeled mouse anti-rabbit IgG bound to goat anti-mouse IgG with (b) and without (a) vigorous washing in PBS solution.

## 4.4    Discussion

One major concern regarding the acoustic cleaning approach was to determine whether the antibody receptor films were damaged by the acoustic waves, resulting in a reduction of antigen binding efficacy.  However, qualitatively this did not occur, as shown in Figure 21.

Direct measurement of the amount of mouse anti-rabbit IgG on the lithium niobate substrates using ellipsometry was not done.  Nonetheless, the end result was the foreground regions showed significant fluorescence from the mouse anti-rabbit IgG. During preparation, BSA was used to minimize covalent attachment of anti-mouse and mouse IgG in the non-patterned regions.  This permitted evaluation of the ability of surface acoustic waves to remove excess mouse-IgG from the non-patterned regions blocked with BSA (Figure 23 and Figure 24).  The removal of covalently attached anti-mouse IgG in the study (Figure 21) was not observed.

Further experiments supported the notion that the acoustic waves at the levels required for the cleaning do not harm the proteins.  To demonstrate this, the SAW device was turned on to stress the specifically bound proteins after each step of the process to remove nonspecifically bound proteins.  After each step of binding the proteins and then running the device in the acoustic cleaning mode, measurements were made to determine whether the proteins were still on the device.  Since the cleanings did not harm the proteins, specific binding was still possible as shown in Figure 21; however, the non-patterned intensity decreased significantly.

The fluorescence measurements in this work demonstrate that it is possible to remove nonspecifically bound proteins from surfaces to desirable levels for micro-array applications. However they are not capable of exposing the detailed mechanisms by which the surface acoustic waves remove the proteins. This is evidenced in inability to account for the sudden drops in intensity at specific power doses seen in Figure 22, Figure 23, and Figure 25. Additional computer simulation and experimental studies are desirable to expose these mechanisms and such work is underway.

Fluorescence assays are widely used in optical detection schemes, for example, in micro-dot arrays. Such arrays represent a large practical application of the device described in this paper. In such cases, this device, fabricated in 128° YX LiNbO3, will be immensely useful for removal of nonspecifically bound proteins to significantly improve determinations. While the relative intensities measured in this work are not quantitative measures of amounts of proteins removed, they quantify the relative amounts of protein removal, which is the level of quantification possible with this device, and is adequate for the intended purpose.

Unlike the Rayleigh waves generated in the lithium niobate device of this work, shear-horizontal SAWs, which can be generated in substrates such as Lithium Tantalate ($LiTaO_3$) and langasite, can be utilized in liquid phase sensing [46]. It is possible to generate both shear-horizontal SAWs and waves with significant shear-vertical components in different directions in such substrates, which opens the possibility of simultaneous removal of nonspecifically bound proteins and sensing in the same device. Encouraging preliminary results have been found using such devices on $LiTaO_3$ [7]. It should be noted that such a device would allow quantification of the protein removal

process via measured attenuation or phase shifts of the shear-horizontal SAW mode. Due to damping of the Rayleigh waves, such quantification was not possible in the device utilized in this work.

Throughout this work, two major challenges were faced. First, leaks in the micro-fluidic test fixture caused protein deposition to occur on the electrodes, reducing the efficacy of the SAW devices. Measurements confirmed that the addition of protein films across the electrodes increased the return loss of the SAW device from approximately -14.0 dBm to -1.4 dBm. The second challenge was establishing a visible pattern from the fluorescent emissions of the labeled proteins. Making a distinguishing measurement by inspection was not possible for all experiments; hence, image processing was used to systematically enhance the images for visual evaluation. This was done through the use of MetaMorph® software.

4.5    Conclusions

In conclusion, the surface acoustic waves were demonstrated to be a powerful tool for the removal of nonspecifically bound proteins on micro-arrays. This removal method has the benefit of reducing background noise attributed to nonspecifically bound proteins, while reducing excessively bound proteins forming multilayers in the foreground. Principal to this method is the application of surface acoustic waves that actuate the interface, thereby permitting selective removal of nonspecifically and specifically bound proteins.

Two primary experiments were focused on testing the hypotheses that: (1) acoustic waves do not inhibit the activity of a bound protein and (2) nonspecifically bound proteins can be removed with surface acoustic waves. Together, these experiments show that surface acoustic waves can be used to enhance sensor response by removing loosely bound proteins from the surface.

Experimental evidence shows that the acoustic waves do not damage the proteins bound to the surface. This can become a valuable tool for increasing the sensitivity and reusability of biological sensors. As shown through these experiments, optical measurements are greatly improved, and the same improvements are expected by applying SAW cleaning technology to other common biological sensors. Additionally, the potential was demonstrated to remove specifically bound proteins at higher input powers for longer exposure times. As a consequence of this potential, it is believed plausible to tune the acoustic waves to selectively remove bound proteins as a tool for interfacial interaction measurements.

Chapter 5

Interdigital Transducer Design for Biosensors


The work presented herein is an experimental and theoretical comparison of surface acoustic wave (SAW) interdigital transducer (IDT) designs used to generate Love-waves for biosensor applications. Three IDT designs were investigated for sensor properties through improvements to electrical characteristics of the SAW devices by reducing second and third order effects. Parameters studied in this work include the attenuation and velocity changes due to the addition of varying thickness of a polystyrene waveguide. Experimental measurements were made using an S-parameter network analyzer with time domain capabilities. Theoretical calculations were conducted using coupled field finite element models. Results from both experimental and theoretical work are used for the optimization of waveguide thickness to produce a biosensor with greater sensitivity and low signal to noise ratio than commonly used designs. The data show the unidirectional IDT design both experimentally and theoretically coupled more efficiently with the polystyrene waveguide to produce the greatest increase of transmitted energy compared with the standard bi-directional IDT designs tested and simulated.

5.1    Introduction

SAW devices are commonly used in communication electronics in the commercial world, and used as a mass sensitive element, mostly in the research laboratories. The fundamental operation of this device is the application of alternating voltage across pairs of IDTs on a piezoelectric substrate. The applied voltage deforms the substrate to launch a mechanical wave. The period and other measures of the wave are determined by the dimensions and layout of the IDTs [1, 2].

Recent work has shown wide application of SAW devices to sensor applications particularly for biological systems [46, 69, 70]. It has been shown that a Love-wave SAW sensor can be 20 times more sensitive to perturbations than a typical shear-horizontal (SH) SAW sensor [46, 71, 72]. Inherent to this great SAW biosensor sensitivity enhancement is the generation of Love-waves through application of an appropriate material and thickness waveguide. Theory dictates that for the generation of Love-waves for the most sensitive sensor 1) the lowest mode wave is required, and 2) a large ratio of substrate to guiding layer shear wave velocity, density, or both is required [73]. Materials tested for Love-wave generation from SH-SAW devices include polymers (polystyrene and polymethyl methacrylate) and oxides such as silicon dioxide. Initially, these materials have been tested for ease of availability, their well-characterized properties, and processing ease. Because the waveguide material for this project is intended for biosensing applications, additional characteristics such as low water permeability, non-toxic nature, and robust structure to withstand multiple tests, are

required [74, 75].  For these reasons, polystyrene was chosen in this work for creating a Love-wave SAW biosensor.

In past literature, the only significant SAW IDT design comparisons have been for telecommunication applications [76-86], with the most current and advanced designs being proprietary information held closely by a few companies.  Fundamental designs that could potentially change sensor characteristics significantly include double split finger design (DSF) [85], pruned double split finger design (PR-DSF) [18], and unidirectional design (U-DSF) [81].  These three designs are illustrated in Figure 3, and are described in detail in the design and fabrication section of this chapter.

The finite element method (FEM) is a powerful tool for problems that require multiple physical sciences to create a full computational solution.  Within this work, current practical limitations exist in creating a full SAW device finite element model that has all the features of one created experimentally [87-89].  Although such limitations might not allow for an exact quantitative comparison of the simulated models with experiments, enough information is generated to create useful data that can guide experimental studies as well as provide a more comprehensive and thorough understanding of the underlying physics [90, 91].  Previous work with FEM of SAW devices indicate that small models, of about one fourth the size  of an experimental device, provide adequate information to reach meaningful conclusions [87, 92].

In the present work, the comparison of voltages and velocities as functions of waveguide thickness of different SAW IDT designs are shown for the generation of Love-waves in biosensor applications.  Based on the experimental and simulated results,

recommendations for using advanced IDT designs are presented to improve SAW biosensor responses.

## 5.2    Materials and Methods

SAW devices are readily available for communication applications packaged and characterized.  For sensor applications, it is necessary to fabricate SAW devices or open packaging.  The former was chosen to permit total control of design.  The materials and methods used in this study are readily available from suppliers.

### 5.2.1    SH-SAW Design and Fabrication

SH-SAW devices were fabricated on single side polished 36° YX LiTaO$_3$ 3" wafers obtained from Sawyer Research.  Wafers were initially cleaned with a solvent rinse consisting of acetone, methanol, isopropanol, and de-ionized water, and subsequently dried with nitrogen.  Wafers were then processed with a standard photolithographic process to pattern the SAW delay lines. A three-layer metallization was done with e-beam evaporation without breaking the vacuum.  The deposited three-layer metal film consisted of a 10 nm titanium adhesion layer, 70 nm gold, and a 10 nm titanium adhesion layer.  Following lift-off processing and quality inspection, wafers

were coated with a protective layer of photo-resist and diced by American Dicing, Inc. (Syracuse, New York) into individual devices.

Delay line SH-SAW devices with a double split interdigital transducer were designed for this project to account for the properties of the substrate [93] and reduce surface wave reflections and bulk wave scattering [84]. Each transducer consisted of 30 finger pairs with an aperture of 47 $\lambda$. The delay line was shorted with a center to center length of 197 $\lambda$. These dimensions were utilized in all three designs to limit design variations and permit testing using standardized probe pattern

The second design tested was the pruned double split finger. This design consisted of a standard DSF 60 finger pair design that had half of the finger pairs removed to create a ladder-like structure. As indicated in literature, this design would maintain the lower insertion loss of a standard 30 finger pair DSF transducer, but have a narrower pass band. Additionally, this design reduces the internal reflections that would occur for a 60 finger DSF design [18].

The final design employed a weighting technique of using one $\lambda/4$ finger followed by a double split finger with each part $\lambda/8$ wide to make up one finger pair [18, 19]. Such a design generates waves that are directional [81], thus more energy sent across the delay path. This design is referred to as a single-phase unidirectional transducer (SPUDT), and it has the advantages of low interfering reflections and low insertion loss. [83]

## 5.2.2  Waveguide Application

Individual devices were washed with solvents to remove the protective photoresist coating.  Devices were then placed in an air plasma cleaner (Harrick Plasma sterilizer/cleaner) for 30 minutes.  The plasma cleaner ensured all organic contaminants were removed to provide the best possible surface for waveguide attachment.  280,000 molecular weight polystyrene (Aldrich) was dissolved in ethyl benzene (Aldrich) to various concentrations giving spin coated thicknesses of 45 – 1,200 nm.  The material properties for the polystyrene used are given in Table 6.  Following the spin coating, devices were cured for 1 hour at 140 °C.  Witness plates were coated and cured in parallel with the devices for additional profilometry measurements.

Table 6  Polystyrene material properties.

| | |
|---|---|
| Typical Molecular Weight | $2.80 \times 10^5$ |
| Glass Temperature | 100.0 °C |
| Modulus of Elasticity | $3.40 \times 10^9$ Pa |
| Poisson Ratio | 0.33 |
| Density | $1.11 \times 10^3$ kg/m$^3$ |

## 5.2.3  Waveguide Measurements

Waveguides were measured for three characteristics: 1) thickness using a Tencor profilometer, 2) insertion loss using an Agilent 8753ES s-parameter network analyzer, and 3) acoustic velocity using a time domain function built into the Agilent 8753ES

network analyzer.  The combinations of these measurements form a complete picture to choose an optimal waveguide thickness.

All RF measurements were automated with LabView 7.0 [®] and recorded on a standard PC through GPIB.  The automation consisted of controlling the network analyzer to scan the s-parameters for signal transmission across 1601 points, followed by the phase.  The system next switched to the time domain using the built-in function and preformed a 1601 point scan of the time domain of transmitted energy to calculate the velocity of the acoustic waves.  Additional analysis, non-automated, of selected devices was done such as applying gating to measure the effect of bulk acoustic waves, triple transit signals, and internal IDT reflections of the different SAW devices while the instrument operated in the time domain.

5.2.4   Finite Element Model Configuration

3-D finite element models were used to evaluate IDT designs and guiding layers. The transient response of the SAW device to an impulse input applied at the transmitting IDT fingers was utilized to study the wave generation and propagation characteristics as well as deduce its frequency response. The developed models consisted of a 36° YX LiTaO$_3$ substrate 40 $\lambda$ long, 5 $\lambda$ wide and 5 $\lambda$ deep with IDT's 2 $\lambda$ long and $\lambda/4$ wide for the split finger design as shown in Figure 27. The periodicity of all IDT designs was 40 μm, while the transducers were considered to be mass-less elements in this work.  The polystyrene waveguide thickness was varied from 0.0 μm to 3.0 μm while using the same

material properties as used in the experimental portion. Tetrahedral elements were used throughout the model with 4 degrees of freedom to account for displacements in the x-, y- and z-directions as well as voltage. Elements were formed to ensure the highest density on the top center surface of the substrate where the most deformation occurs.

The simulations were initiated with an electric impulse of 10 V applied at the transmitting IDT fingers over time steps of 0.95 ns. The simulation was carried out for 190 ns and interpolation between the 0.95 ns time-steps was used on all data. The simulation time and dimensions of the model were chosen to prevent reflected signals from the edges and bottom of the substrate.



(a)                                                        (b)
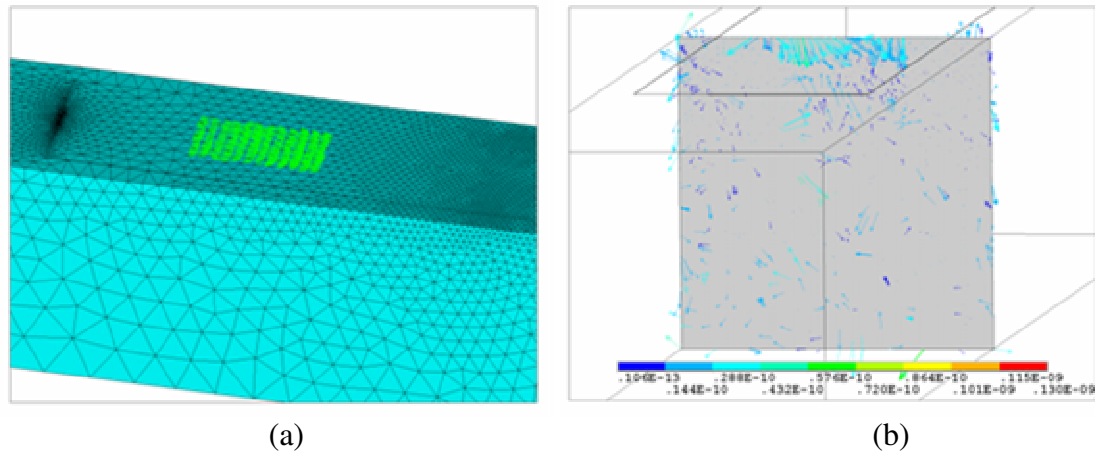
Figure 27  (a) Pre-solution 3d meshed split finger IDT design with highest mesh density at the top and center of delay path (right side of image). (b) Displacement vectors at middle of delay path at time step 75 showing predominately surface parallel wave motion.

5.3    Results and Discussion

Advanced SAW filter design is a technology belonging to the communication industry.  For many years, the industry has developed advanced designs through an iterative process to eliminate the effects that are sometimes needed to make good sensors.  As shown in Figure 28, three SAW IDT designs have been fabricated and tested in this work.  First analyzed were the frequency responses of the devices, followed by a time domain analysis.
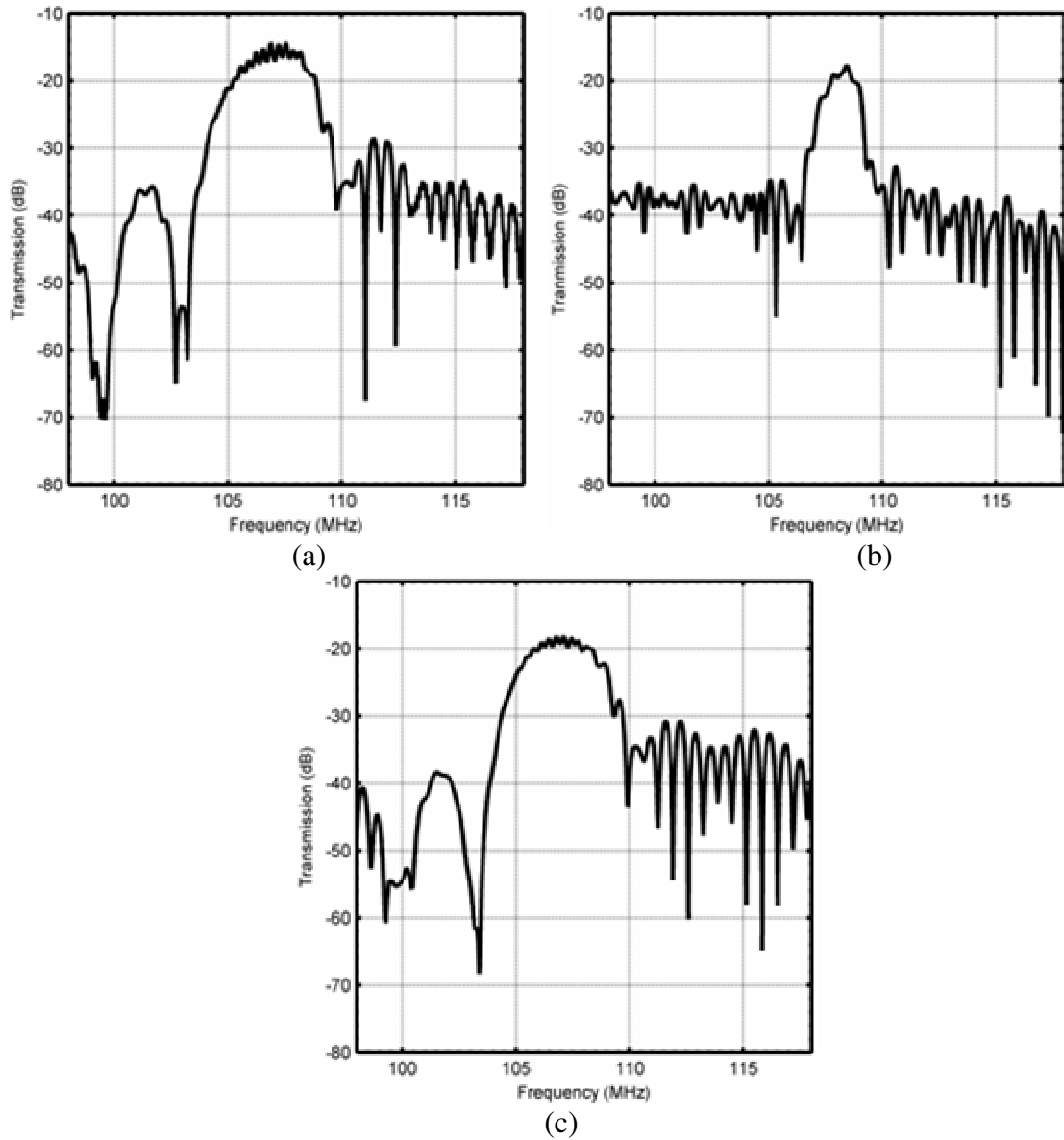
Figure 28  Comparison of fabricated SAW device designs responses as shown magnitude measurements. (a) $S_{21}$ measurements of 30 finger pair DSF IDT structure. (b) $S_{21}$ measurements of 30 finger pair PR-DSF IDT structure. (c) $S_{21}$ measurements of 30 finger pair U-DSF IDT structure.

The first design tested was a standard DSF IDT structure consisting of 30 finger pairs, delay path of 197 λ, and a wavelength of 32 μm. This design was tested as a control and basis for comparison with two more advanced designs. As shown in Figure 28(a), the DSF design on 36° YX LiTaO$_3$ shows a classical band pass filter response with a 4 MHz passband and > 15 dB attenuation for out of band frequencies. The considerable second order effects most likely triple transit effects (TTE) are seen as a couple of dB sized ripple across the pass band, which can lead to erroneous sensor responses. The final general characteristic of importance, *i.e.,* the linearity of the phase within the pass band is not seen in the data presented in Figure 29(a).
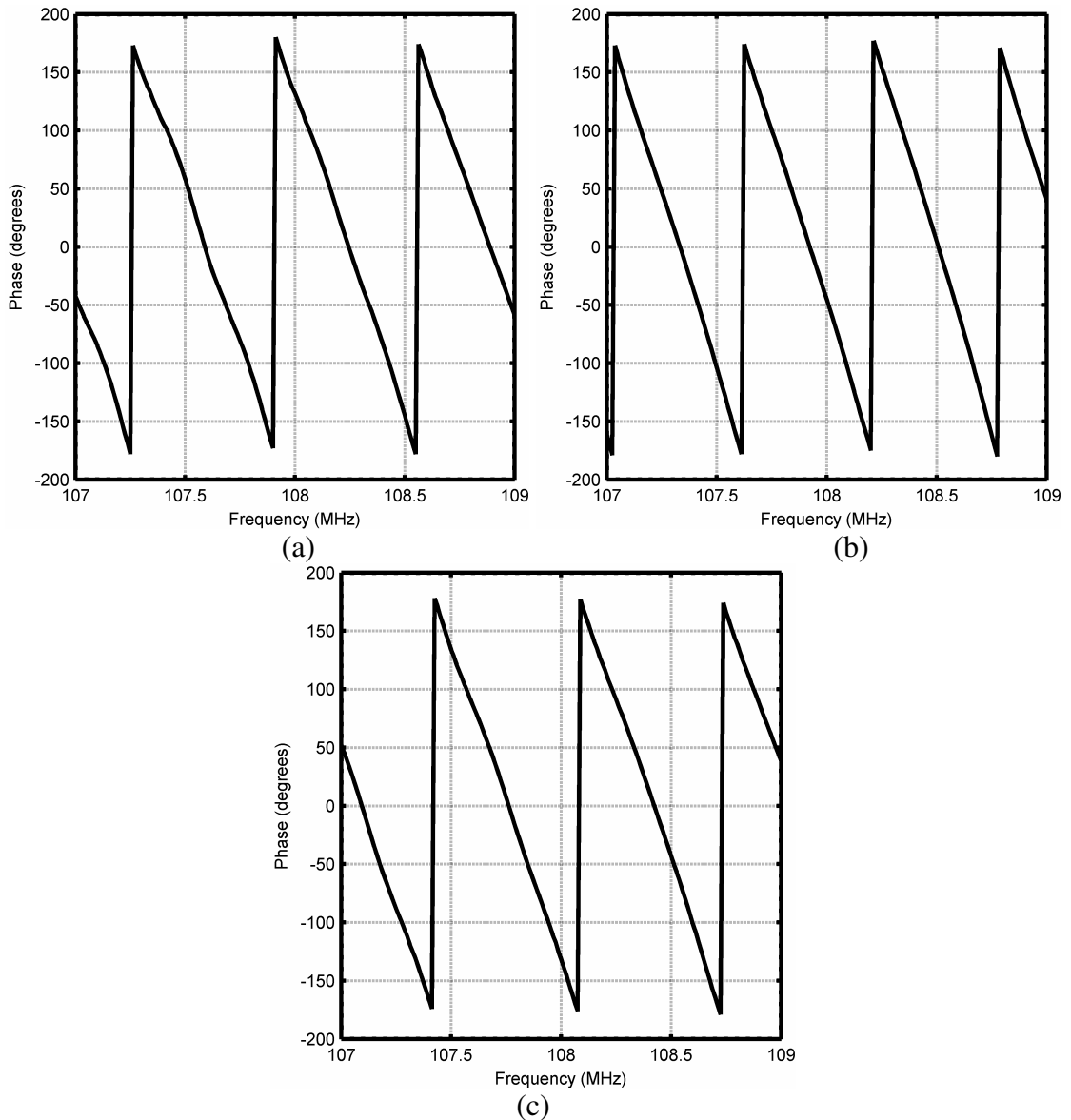
Figure 29   Comparison of fabricated SAW device designs responses as shown with measurements of 3 MHz within the pass band.  (a) 30 finger pair DSF IDT structure.  (b) 30 finger pair PR-DSF IDT structure.  (c) 30 finger pair U-DSF IDT structure.

The second device design shown in Figure 28(b), PR-DSF, is an interesting modification that has the same length IDTs of a 60 finger pair DSF design; however, every other finger pair set has been removed resulting in only 30 finger pairs.  As

expected, the response from this design shows a pass band of only 2 MHz (half the pass band of the DSF design). The attenuation of the out of band frequencies is approximately equal to the standard DSF design. The second order effects in this design were reduced from the DSF design. Additionally, as shown in Figure 29(b), the phase through the pass band is more linear.

The final design as shown in Figure 28(c) is the most advanced design tested in this study that utilizes non-uniform IDT widths to reduce unwanted second order effects and transmit more energy directionally to the output IDT. The U-DSF design is a 30 finger pair design; hence, the expected device response was an improved version of the DSF design. As shown in the Figure 28(c), the U-DSF device frequency response shows the same general characteristics of the DSF design; however, the second order effects reduce as shown by the decreased magnitude of the pass band ripple. The phase linearity as shown in Figure 29(c), is improved from the DSF data; however, it is not as good as the PR-DSF design phase linearity.

The frequency responses of the three tested designs as shown in Figure 28 can be qualitatively compared with the calculated responses of the FEM simulations of the same designs. These data are shown in Figure 30. The simulations only used 3 finger pairs and a much shorter delay path (6 $\lambda$) in comparison to the experimental devices (30 finger pairs and 197 $\lambda$), the data show similar and expected results. These results such as pass band width can be scaled and correlated with the more common experimental type devices. The simulations are simplified through mass-less electrodes and reduced dimensions. This results in the second order effects not appearing predominately in the simulation results. Additionally, the PR-DSF design response does not correlate as well

as the others to the experimental data due to maintaining the same element configuration of the modeled substrate throughout all of the simulations.
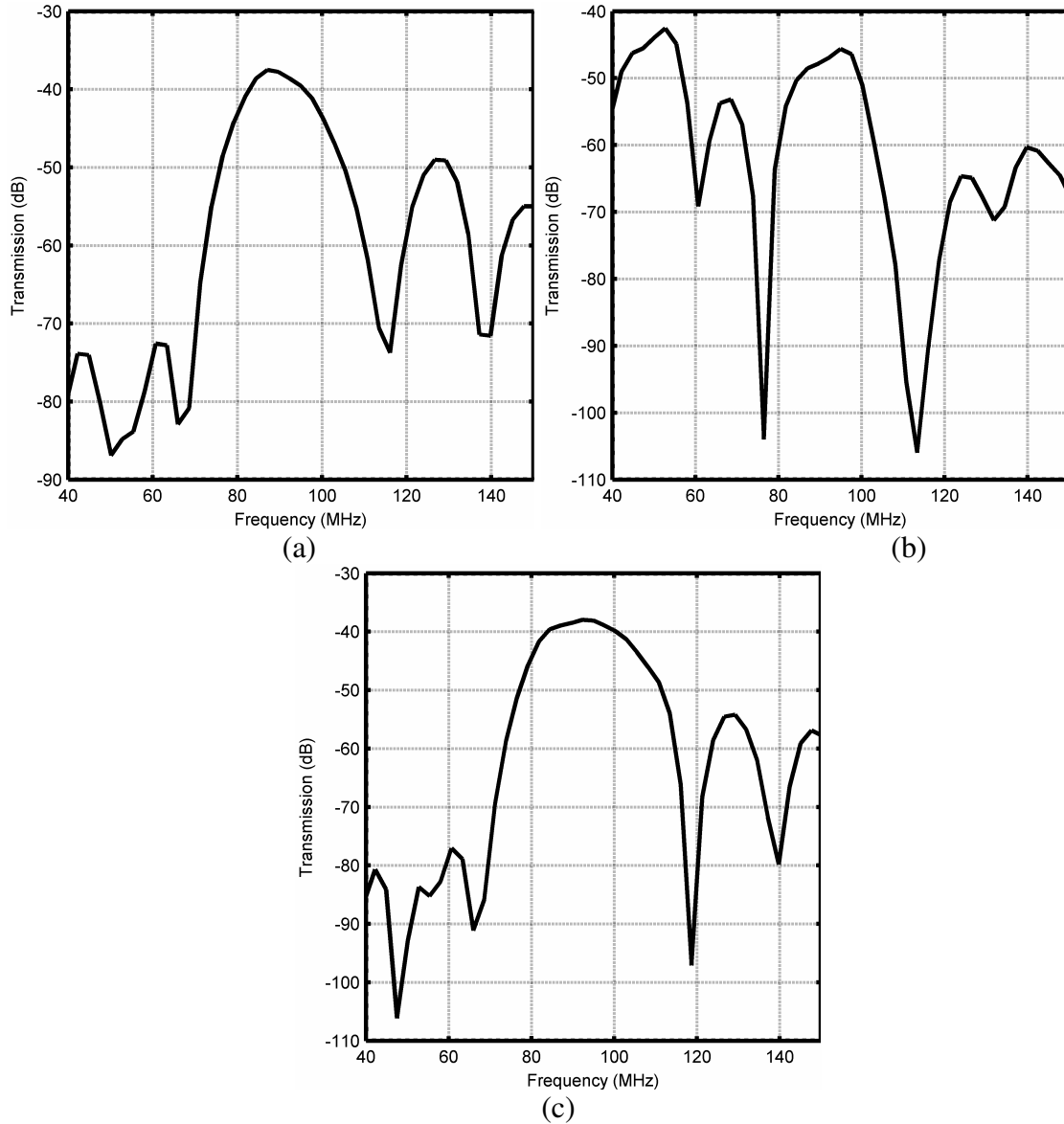
Figure 30   Comparison of simulated SAW device designs responses as shown with magnitude measurements of the power spectrum as simulated with Ansys.  (a) Power spectrum of 3 finger pair double split finger IDT structure.  (b) Power spectrum of pruned 3 finger pair double split finger IDT structure as simulated with Ansys.  (c) Power spectrum of 3 finger pair combined single/double split finger IDT structure as simulated with Ansys.

Further analysis of the devices characteristics were done using a built in transform function of the network analyzer. These data are plotted in Figure 31 for the three designs tested in this study. The primary features examined in these data are the second order effects consisting primarily of reflections. The TTE of all of the device responses appears at ~ 4.8 μs. Clearly as shown in the data, the DSF device response has a significant TTE peak with ~ 21 dB separating it from the primary SAW signal peak. The difference between the TTE peak of the PR-DSF device response is increased to ~ 35 dB, but the primary SAW peak of this device is only at ~ -32 dB. This is a considerable insertion loss for a sensor. The U-DSF device response shows the difference between the primary peak and the TTE peak to be ~ 27 dB.
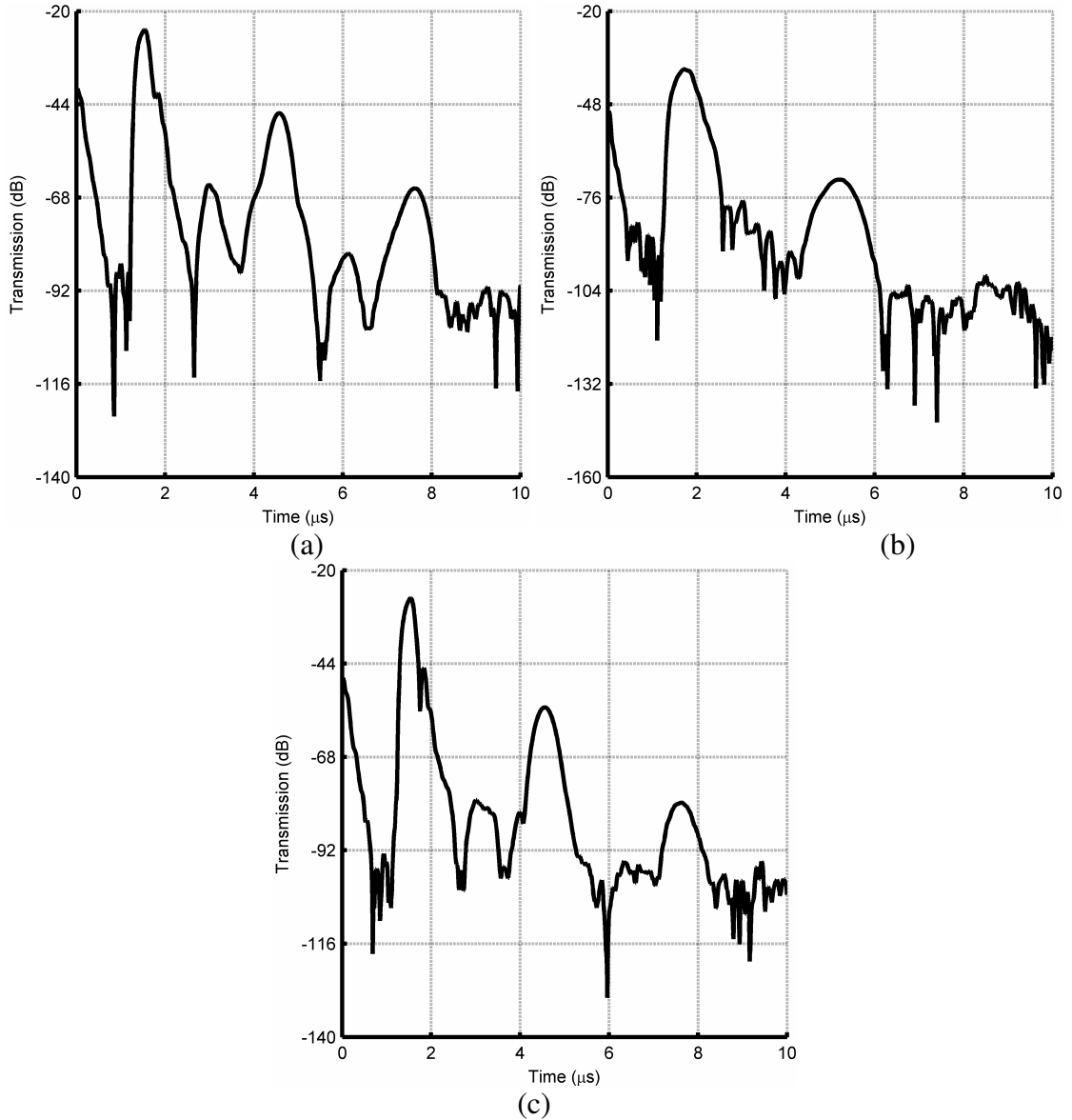
Figure 31 Comparison of fabricated SAW device designs responses as shown in the time domain. (a) $S_{21}$ measurement of 30 finger pair DSF IDT structure. (b) $S_{21}$ measurement of 30 finger pair PR-DSF IDT structure. (c) $S_{21}$ measurement of 30 finger pair U-DSF IDT structure.

88

The data in Figure 32 show three independent responses following the same general trend with the addition of polystyrene. There is an initial increase in attenuation followed by a decrease in attenuation to 2-3 dB less than the bare SH-SAW device. This indicates that leaky wave energy is being trapped in the waveguide instead of being lost to the environment. Following the maxima, the attenuation again increases from mass loading. The U-DSF design shows the greatest improvement which correlates with the fact the design is not bi-directional as are the DSF and PR-DSF designs. This means there is more energy for the waveguide to trap. The simpler DSF design has the next greatest improvement, and lastly, the PR-DSF design shows very little improvement. Other features of the data as shown in the figures include the range of optimal waveguide thickness is broadest and best defined for the case of the U-DSF design.
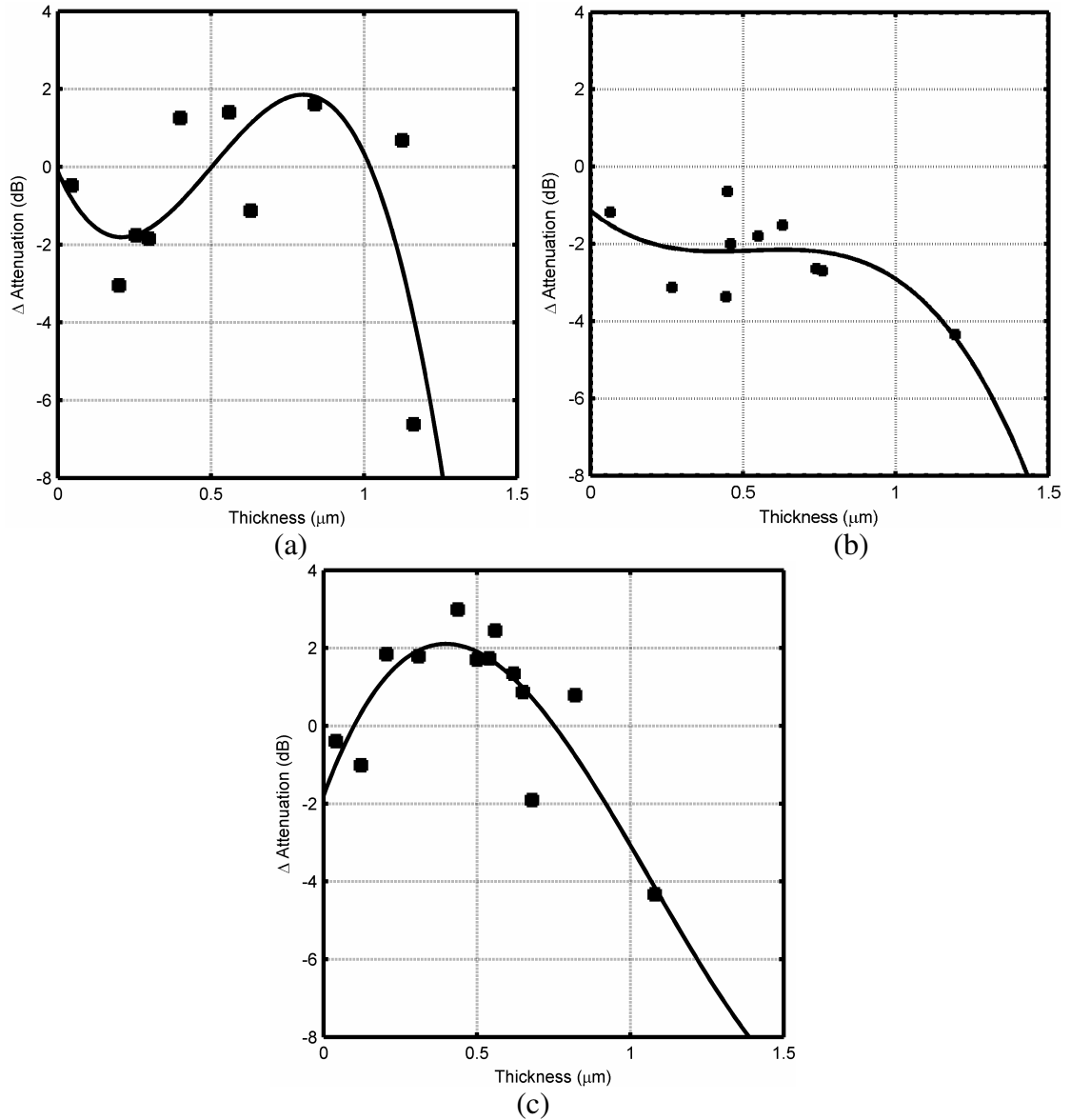
Figure 32 Comparison of fabricated SAW device designs responses to the addition of a polystyrene waveguide. Experimental data of the transmitted power change as a function of polystyrene thickness for three IDT designs. (a) is the DSF design data. (b) is the PR-DSF design data. (c) is the U-DSF design data.

Comparable simulation data as shown in Figure 33 have the same trends as the experimental work shown in Figure 32; however, the value of the optimal waveguide thickness is significantly different. The optimal thickness for the DSFR design found through experiment is ~ 0.50 μm. The value as found from simulation data is ~ 1.50 μm as indicated by the significant increase in transmitted energy followed by a saturation type response from the addition of more mass on the surface in the form of a thicker polystyrene layer. The difference in the value of optimal thickness of a waveguide is a result of the difference in frequency of the experimental and simulated devices as well as the limitations of the model such as size.
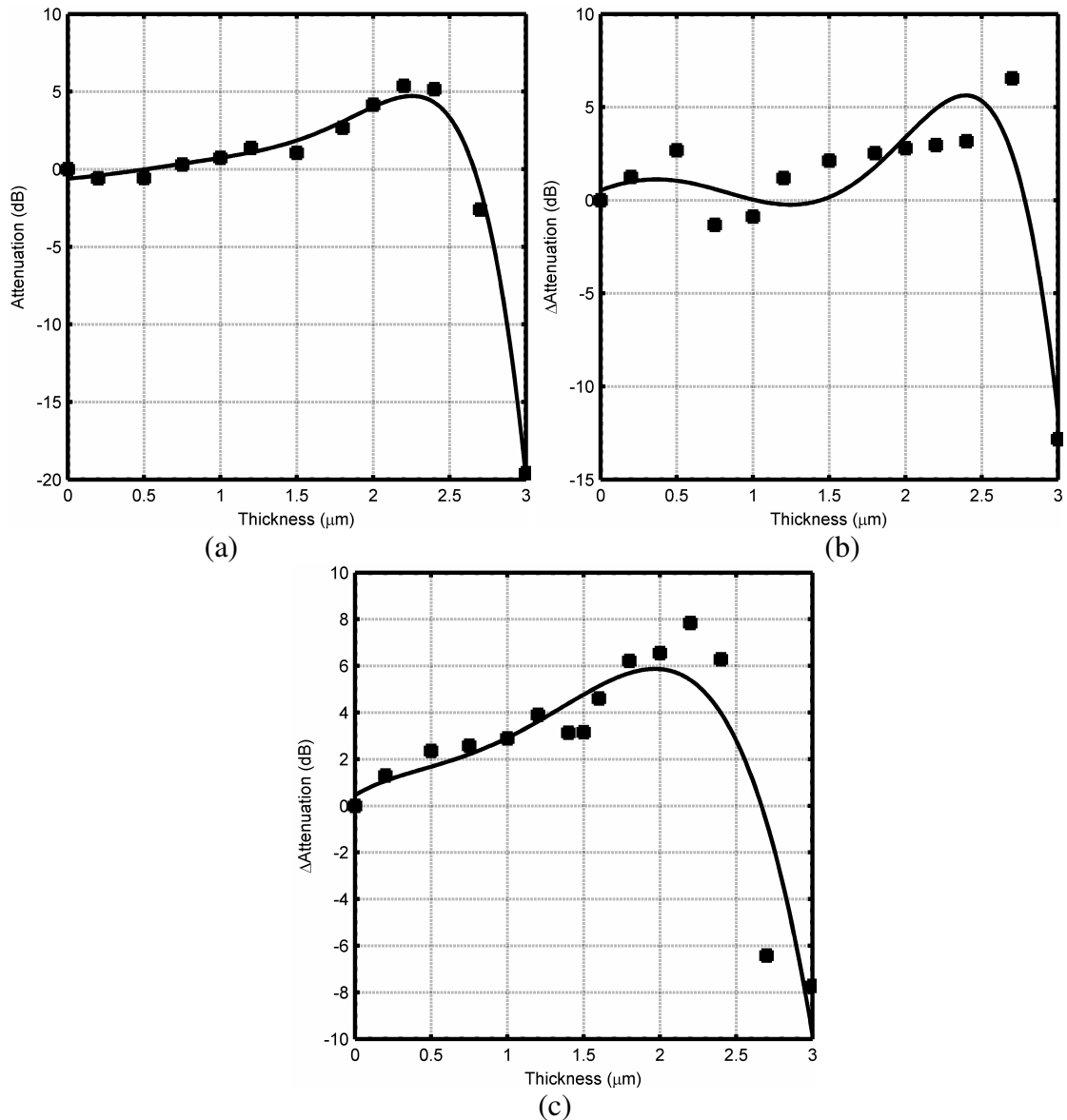
Figure 33  Comparison of simulated SAW device designs responses to the addition of a polystyrene waveguide.  FEM simulation data of the change in attenuation change as a function of polystyrene thickness for three IDT designs.  (a) is the DSF design data.  (b) is the PR-DSF design data.  (c) is the U-DSF design data.


The second measure used to evaluate the designs was the device velocity as a function of the polystyrene thickness.  These data, Figure 34, show trends expected as a

result of the responses in Figure 32. The order of the IDT design efficiencies as determined by the increase of transmitted energy maintained through the velocity measurement data. The U-DSF design developed the most significant dip in device velocity due to the polystyrene guiding layer. The DSF design response shows a decrease in velocity; however, since it is not a dip, it is difficult to identify an optimal thickness. The PR-DSF design response showed a slight increase followed by a decrease. The reason for the velocity increase is not known, but the poor velocity versus thickness response corresponds with the poor attenuation versus thickness measurements of this particular design.

Simulation data for the change in velocity for the different thicknesses of polystyrene are shown in Figure 35. These data, unlike the experimental, do not show a significant change in the velocity across the range of thicknesses studied. The DSF and PR-DSF designs responses show approximately the same decrease in velocity (~ 120 m/s) at 3 μm. The U-DSF design data show a slightly greater decrease of ~ 150 m/s, which correlates to the greater power transmission shown in Figure 33.
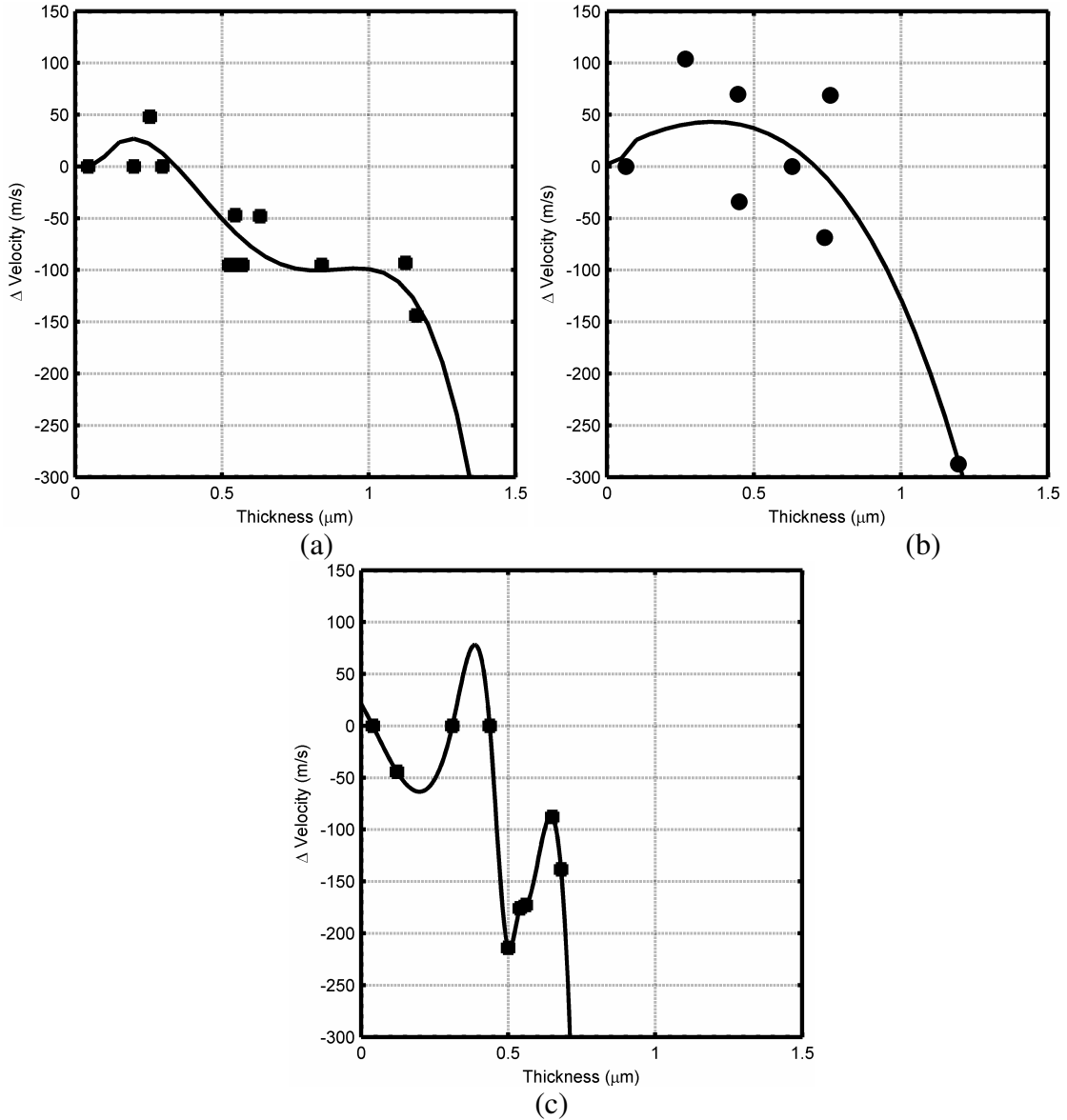
Figure 34  Comparison of fabricated SAW device designs responses to the addition of a polystyrene waveguide.  Change of SAW velocity experimentally obtained as a function of polystyrene thickness for three IDT designs.    (a) is the DSF design data.  (b) is the PR-DSF design data.  (c) is the U-DSF design data.
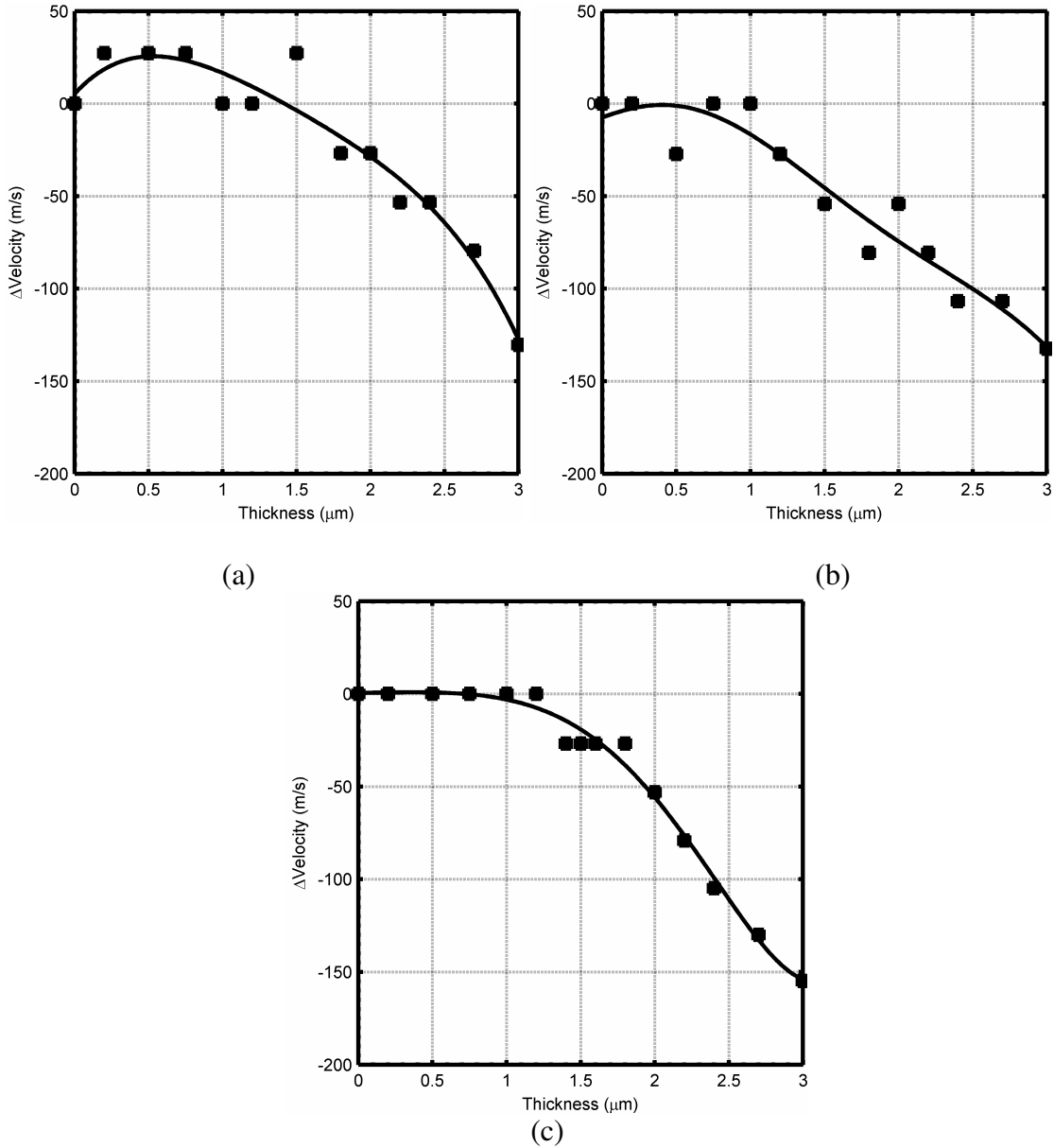
Figure 35  Comparison of simulated SAW device designs responses to the addition of a polystyrene waveguide.  Change of SAW velocity calculated from FEM simulation data shown as a function of polystyrene thickness for the three designs.  (a) is the DSF design data.  (b) is the PR-DSF design data.  (c) is the U-DSF design data.

From the simulation data in Figure 33 and Figure 35, the resulting sensitivities of the different IDT sensor designs have been calculated. The sensitivity is based on the application of a 100 pg ideal mass applied over a 9.6 x $10^{-9}$ $m^2$ area. As shown in Figure 36a, the sensitivity of the standard DSF design is significantly better than the DSF waveguide device as well as the pruned and U-DSF design without waveguide. Only the optimized waveguide U-DSF design has a greater combined sensitivity as defined by the square root of the summation of the squares of the change in velocity and change in voltage. As shown in Figure 36b, the DSF sensor without a waveguide again has a very large response to the 100 pg ideal mass, indicating that the acoustic wave is severely attenuated by several decibels. Further inspection of the data shown in Figure 36, shows the U-DSFR design to not be easily attenuated and still provide a large response to small masses. It is expected the experimental results would follow the same trend if the same precision were possible.
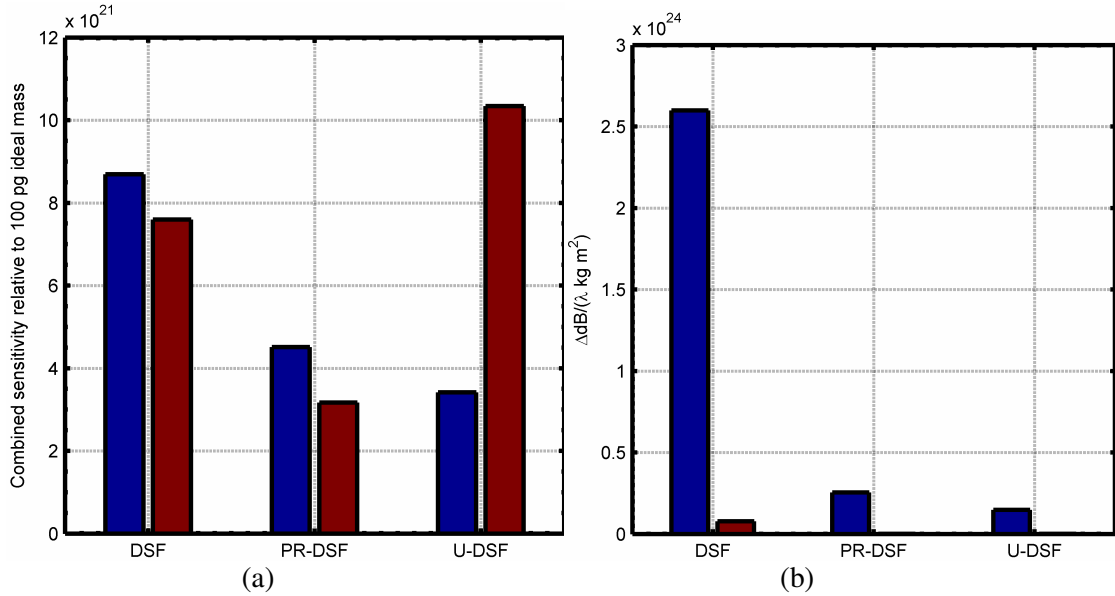
Figure 36  Comparison of in-house SAW device designs responses to the addition of a 100 pg ideal mass across 9.6 x $10^{-9}$ m$^2$ area.  (a) Combined sensitivity as calculated from FEM simulation data for the three designs both without (left bars) and with (right bars) an optimized waveguide.  (b) Attenuation sensitivity as calculated from FEM simulation data for the three designs both without (left bars) and with (right bars) an optimized waveguide.

## 5.4    Conclusion

Measurements from the application of the polystyrene film to the SH-SAW devices show that insertion loss and acoustic velocity were both reduced at the optimal thicknesses.    These two measurements verified the application of the polystyrene waveguide was trapping energy, thus creating Love-waves.

The waveguides were studied based on the three measurements of thickness, insertion loss, and acoustic velocity. The waveguide thickness was used as the reference to compare the insertion loss of the devices as well as the acoustic velocity. The maximum decrease was found in attenuation for the U-DSF design to be at ~ 0.50 μm. This corresponds to the thickness of the acoustic waveguide that is trapping the maximum energy from the LiTaO$_3$ substrate forming the Love-waves. This maximum shows that through the appropriate coating, it is possible to reduce the insertion loss of this SH-SAW sensor system by ~ 3 dB leading to lower power consumption of the system. Through the use of time domain measurements, the velocity of the SAW is calculated. At the optimum waveguide thickness (~ 0.5 μm) a minimum is found. The acoustic velocity minimum verifies that the acoustic wave is being slowed down as a condition of forming Love-waves.

The same IDT designs were simulated using FEM to find the optimal thickness for a guiding layer of polystyrene, and calculated an effective sensitivity of the different designs. The FEM solutions were found to qualitatively agree with experimental data. A significant factor for the differences in data is the slightly different frequencies of the experimental and simulated devices. The simplification from experimental to simulation namely the reduction of IDTs and the use of mass less transducers that does not allow the simulation to account for dispersion associated with the added bulk material is a likely source of the additional differences. Future work is in progress to show the effect of transducer mass on the optimization of waveguides and IDT design.

Finally, from FE simulation data the effective sensitivity was calculated for the different IDT designs tested both with a bare delay path and an optimized waveguide

thickness. Results from the data suggest the efforts applied to advanced IDT designs such as the U-DSF one presented in this paper can lead to sensors with significantly greater sensitivity as well as greatly reduced power requirements.

Chapter 6

Surface Acoustic Wave Biosensor for Interleukin-6


The development of a biosensor for Interleukin-6 at levels required for physiological relevance. Interleukin-6 is a proinflammatory cytokine involved in the body's pathophysiologic response to injury due to various causes, *e.g.* trauma, burns, sepsis, and disease. The sensor configuration was optimized to provide a substantially improved response in comparison with traditional SAW sensors. The SAW biosensor was fabricated in $36°$ YX LiTaO$_3$ to generate shear-horizontal (SH) waves using the high electro-mechanical conversion efficiency of this substrate material. The biosensors were coated with an optimal thickness polystyrene waveguide enabling Love-wave generation and increased sensitivity. The biosensor was fabricated using an anti-human Interleukin-6 biosensor film physically adsorbed to the polystyrene waveguide of the sensor. Data were collected using a homebuilt sensor circuit connected to a multimeter and personal computer for data acquisition, and were verified using fluorescent microscopy. The data result in the conclusion that the Love-wave SAW biosensor developed can be efficiently used for the sensing of human Interleukin-6.

## 6.1    Introduction

There are many types of biosensors that have been used for sensing of biomarkers [9, 10, 13, 51, 69, 94-99].  Surface acoustic wave (SAW) devices are one type that has a proven record to for chemical sensing as well [1, 2, 100-104].  These devices utilize an acoustic wave with most of its energy confined near to the surface as a sensing element. As the wave propagates across the surface of the sensor, small perturbations to the wave can be measured as a change of the acoustic wave's magnitude and velocity.  Although the SAW devices are sensitive to many types of perturbations, the one that is often sought and is predominate is mass change on the surface.  Thus, the detection limit of a typical SAW sensor is a few picograms.  While working with solutions, detection limit is on the order of picograms per milliliter of solution.

Biosensing applications such as the one described here require the consideration of energy loss to viscous environments the sensor is required to operate in.  SAW sensors that can be used in chemical vapor sensing are not viable options for biosensing; therefore, a different type of SAW is needed.  As a solution, shear-horizontal SAW devices have been found to work well.  The SH-SAW does not contain a vertical component of motion, and thus does not lose much energy into viscous fluids that are on the sensors surface.  SH-SAW sensors have been used successfully in the detection of biomarkers [1, 23, 34, 69, 95, 105-109].

Of particular interest to the work described herein is the SH-SAW sensor that uses a thin-film guiding layer to form Love-waves.  The guiding layers commonly used are a polymer, oxide, or a combination of the two materials to achieve a desired property [71,

72, 107, 110]. With the addition of the guiding layer that meets the conditions that for the generation of Love-waves for the most sensitive sensor 1) the lowest mode wave is required, 2) the greater the ratio of substrate to guiding layer shear wave velocity, density, or both is required [73]. The SH-SAW device can become 20 times more sensitive to surface perturbations through the confinement of the wave-energy in the guiding layer [22].

To realize, a Love-wave sensor, first the SAW must be of the shear-horizontal nature. This type of wave is found in many common crystalline cuts including quartz; however, more recently found piezoelectric crystals and cuts provide higher velocities improve sensor characteristics. 36 ° YX LiTaO3 is one such material that produces a suitable wave over 4,000 m/s where as typical quartz velocities are around 3,000 m/s [71, 111, 112]. Not only does this extra velocity give a higher frequency SAW device, but also a greater differential between the velocity of the guiding layer and substrate.

Interleukin-6 has been known for many years to be an agent in the inflammatory process, but until recent studies, the importance and timing of the up-regulation has not been known. Studies both on animal models and human patients show elevated levels of IL-6 indicate traumatic injuries, multiple organ failures and ultimately can be used as an early indicator (3-6 hours from time of injury) of mortality [113-117]. For these reasons, IL-6 was considered to be a good first biomarker to establish a biosensor for cardiac trauma. Healthy adults have IL-6 levels typically < 10 pg/ml and diseased individuals have IL-6 levels up to ng/ml levels [117]. When an otherwise healthy individual is injured, IL-6 levels can reach 250 pg/ml. The increase in IL-6 concentration was seen within 3 hours of trauma and the level peaked 6 hours after the trauma occurred. The fast

response of the IL-6 can be attributed to being part of a larger cytokine proinflammatory response [118].

Although animal models are used to represent human responses, there are some distinct differences that are important to consider in developing a biosensor. Of primary concern are the normal and elevated levels of IL-6 found from traumas. In mice, injuries result in IL-6 levels up to 10,000 pg/ml. Of significance for sensing, mice with IL-6 levels > 3,000 pg/ml typically had a higher 3-day mortality rate than those with < 2,000 pg/ml IL-6 [114, 116]. Throughout the studies, IL-6 was found to have a normal relative molecular mass ranging from 21 kD to 30 kD depending on the source and method used to produce [117], and the assays used in the studies had a sensitivity > 1 pg/ml [117].

## 6.2   Materials and Methods

Love-wave biosensors require different parts to be assembled. The piezoelectric substrate provides the basis of all of the SAW work. In this work, $LiTaO_3$ was used for its unique properties of a high coupling coefficient and a nearly pure shear-horizontal wave when rotated 36 degrees. On the substrate, the SAW interdigital transducers are patterned and deposited using photo-lithography, and the waveguide at an optimal thickness is applied. The final step to create a biosensor is the functionalization of the surface with a biomarker sensitive material. In the case of this paper, the waveguide surface is functionalized with an anti-body.

6.2.1  SAW Device Design and Fabrication

SH-SAW devices were fabricated on single side polished 36° YX LiTaO$_3$ 3"
wafers obtained from Sawyer Research.  Wafers were initially cleaned with a solvent
rinse consisting of acetone, methanol, isopropanol, and de-ionized water, and
subsequently dried with nitrogen.  Wafers were then processed with a standard
photolithographic process to pattern the SAW delay lines. A three-layer metallization was
done with e-beam evaporation without breaking the vacuum.  The deposited three-layer
metal film consisted of a 10 nm titanium adhesion layer, 70 nm gold, and a 10 nm
titanium adhesion layer.  Following lift-off processing and quality inspection, wafers
were coated with a protective layer of photo-resist and diced by American Dicing into
individual devices.

Delay line SH-SAW devices employed a weighting technique of using one $\lambda/4$
finger followed by a double split finger with each part $\lambda/8$ wide to make up one finger
pair [19, 119].  Such a design generates waves that are directional [81], thus more energy
sent across the delay path. This design is referred to as a single-phase unidirectional
transducer (SPUDT), and it has the advantages of low interfering reflections and low
insertion loss [83].  Each transducer consisted of 30 finger pairs and had an aperture of 47
$\lambda$. The delay line was shorted with a center to center length of 197 $\lambda$.

### 6.2.2 Waveguide Application and Measurement

Individual devices were washed with solvents to remove the protective photoresist coating. Devices were then placed in an air plasma cleaner (Harrick Plasma sterilizer/cleaner) for 30 minutes. The plasma cleaner ensured all organic contaminants were removed to provide the best possible surface for waveguide attachment. 280,000 molecular weight polystyrene (Aldrich) was dissolved in ethyl benzene (Aldrich) to various concentrations giving spin coated thicknesses of 45 – 1,200 nm. Following the spin coating, devices were cured for 1 hour at 140 °C. Witness plates were coated and cured in parallel with the devices for additional profilometry measurements.

Waveguides were measured for three characteristics: 1) thickness using a Tencor profilometer, 2) insertion loss using an Agilent 8753ES s-parameter network analyzer, and 3) acoustic velocity using a time domain transform of the Agilent 8753ES network analyzer. The combinations of these measurements form a complete picture to choose an optimal waveguide thickness.

All RF measurements were automated with LabView 7.0 ® and recorded on a standard PC through GPIB. The automation consisted of controlling the network analyzer to scan the s-parameters for signal transmission across 1601 points, followed by the phase. The system next switched to the time domain and preformed a 1601 point scan of the time domain to calculate the velocity of the acoustic waves. Additional analysis, non-automated, of selected devices was done such as applying gating to measure the effect of bulk acoustic waves, triple transient signals, and internal IDT

reflections of the different SAW device designs while the instrument was in the time domain.

### 6.2.3 Antibody Attachment to Waveguide

Love-wave devices were dried with nitrogen then coated with anti-human IL-6 in PBS pH 7.4 and allowed to adsorb the protein for 20 minutes. After the adsorption, the devices were rinsed thoroughly in PBS to remove non-bound proteins. The time between and attachment and use of the sensor was minimized. Additionally between the attachment and use, sensors were kept in a high humidity chamber to prevent degradation and loss of activity of the antibodies.

### 6.2.4 Experimental Setup

Individual biosensors once prepared with the antibody coatings were mounted in a micro-fluidic test fixture. The test fixture served as a union of sensor, analyte solutions, and electrical connections to measure the perturbations to the acoustic wave. All samples were allowed to equilibrate to temperature prior to performing the experiments at a constant temperature.

Love-wave devices were mounted in a micro-fluidic test fixture that had a lexan viewing window, spring loaded contacts, RF connectors, and an aluminum heat sink.

106

The lexan viewing window was used to verify no air bubbles interfered with the sensing, while the aluminum heat sink added to the temperature stability of the device. The spring loaded contacts connected the Love-wave device with the RF connectors through a printed circuit board.

The micro-fluidic fixture was supplied fluid at a constant rate of 150 μl/min via a syringe pump (Harvard Apparatus PHD 2000) and a 6-way multi-port valve (Scivex) used to switch to and from a 0.150 ml injection column. Additionally all fluids were degassed prior to entering the micro-fluidic chamber through the use of a frit (Upchurch Scientific). The sensing chamber has a volume of 6.8 μl.

## 6.2.5   Data Acquisition

Data from the sensor was acquired using a phase comparator circuit connected to a multimeter (Keithley 2010) controlled through a LabView [®] interface. The input signal was generated from a signal generator (Rhode&Swarz SMA100A) and split into a reference line connected directly to the phase comparator circuit and the sensor line that was connect through the Love-wave delay path to the phase comparator. The frequency was chosen to provide a linear phase response close to the design frequency of 130 MHz.

6.3    Results and Discussion

Following the methods described above, the SAW sensors were prepared with a polystyrene guiding layer to produce Love-waves for enhanced sensitivity. Chapter 5 describes the optimization of these layers for use in sensors specifically an IL-6 biosensor described in this chapter. For the purposes of the IL-6 biosensor, the polystyrene wave guide was applied to the SAW sensor slightly thinner than optimal to ensure not overshooting and decreasing the sensitivity when antibodies and antigens are attached to the sensor surface. Verification of the thickness of each layer was done on a silicon (Si) wafer with a native oxide film of $16.48 \pm 3$ Å as given in Table 7 as $\Delta$ and $\Psi$ values from ellipsometer measurements.

Table 7  Ellipsometry data for IL-6 biosensor layers.

| Layer | $\Delta$ | $\Psi$ |
|---|---|---|
| SiO$_2$ | 174.41 | 10.43 |
| PS (2,500 rpm) | 99.20 | 20.14 |
| Biotinylated Anti-Human IL-6 | 110.08 | 18.64 |
| Alexa-488 labeled Human IL-6 | 81.20 | 29.50 |

6.3.1    Sensor Evaluation

To evaluate sensor mass sensitivity, BSA was flowed across the sensor at various levels that would not saturate the surface. From these experiments the sensor and electronics were found to have a noise level of 0.0034° phase with a mass sensitivity of

0.97 to 0.0083 deg. cm$^2$ / µg.  The variation of the mass sensitivity is a result of a large range of concentrations tested (6 ng/ml to 60 µg/ml).   The highest concentrations exceeded the linear regime of the sensor as shown in Figure 37.  In light of the non-linear behavior of the sensor, all responses were repeatable and complete within 20 seconds of injection.  Even this slow response can be attributed to transport and diffusion limitation of the micro-fluidic test system.
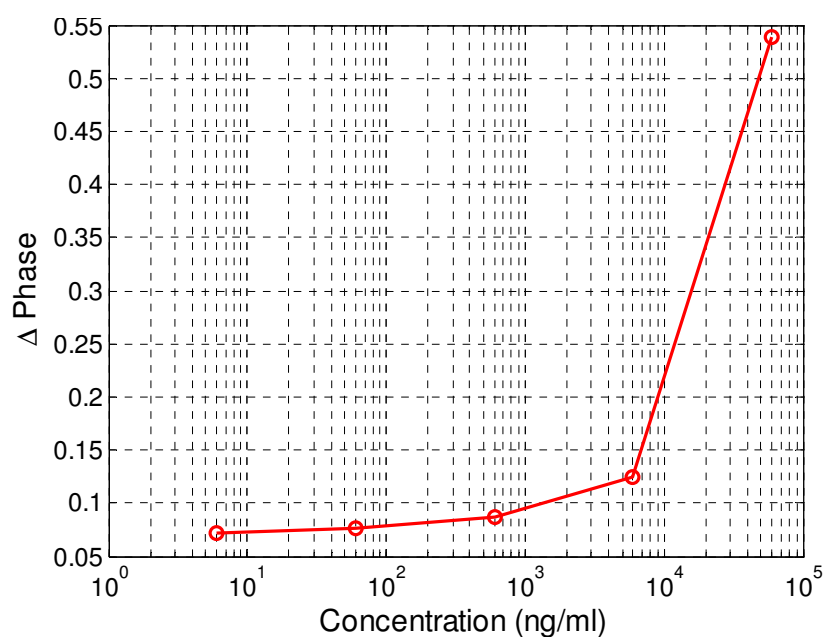


Figure 37  Sensitivity determination using BSA at various concentrations from 6 ng/ml to 60,000 ng/ml.

## 6.3.2  Interleukin-6 Sensing

The polystyrene coated 36° YX LiTaO$_3$ SH-SAW sensors were prepared according to section 6.2.3.  Following the surface attachment, the sensors were inserted into the microfulidic test fixture illustrated in Figure 5.  The sensor was given 4 minutes to equilibrate to conditions of the micro-fluidic test fixture.  PBS pH 7.4 was used as the carrier of antigens.  To control the injections of human IL-6, an injection loop of 0.150 ml was used.

The experimental data shown in Figure 38 is the result of a series of consecutive injections human IL-6 into the micro-fluidic system.  The data shown on the right side of the graph is the total antigen adsorbed to the surface of the sensor.  Approximations of the possible number of antigens able to bond to the antibody surface based on the concentrations of the used antibodies to prepare the surface, theoretically, 23 ng total mass was possible.
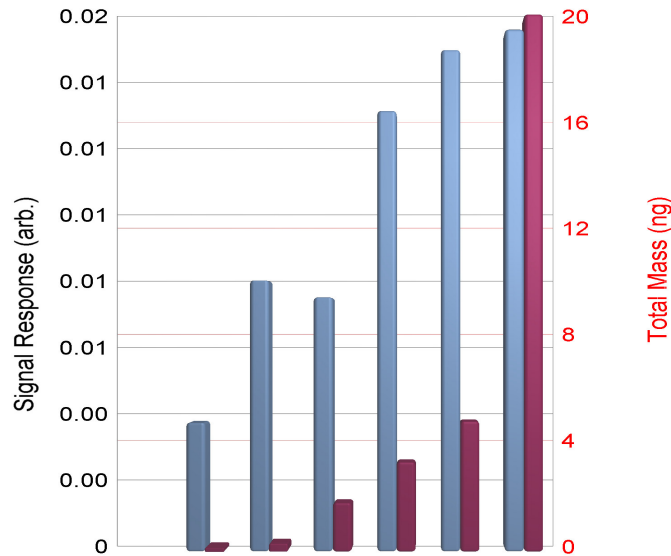
Figure 38  Sensor signal response to a series of human IL-6 injections onto one sensor element.  The total mass accumulated on the surface is given as the right axis.

6.4    Conclusions

In this study the development of a polystyrene Love-wave surface acoustic wave sensor is shown for sensing of interleukin-6 at physiologically relevant concentrations. The sensitivity of the sensor and associate measurement electronics used in this work were tested using various concentration of BSA.  These results gave the necessary parameters to continue the work for IL-6 sensor development.  The finally portion of this study verified the polystyrene Love-wave SAW sensor was sensitive enough for the necessary level of IL-6 to be physiologically important to animal model studies such as mice and can potentially be used in clinical studies.

Further studies are necessary to improve the maximum attachment of antibody and antigen to the sensor. This work can be further expanded to sensing IL-6 in serum.

Chapter 7

Simultaneous Surface Manipulation and Sensing in a Biosensor Using a Hexagonal SAW

Device

Presented is the development of a hexagonal surface acoustic wave (SAW) device to simultaneously manipulate biological films and sense in biosensors. The objective is to improve sensitivity and selectivity. A hexagonal device fabricated in 36° YX LiTaO$_3$ allows for propagation of both Rayleigh and shear-horizontal wave modes simultaneously. The high electro-acoustic coupling in this piezoelectric material allows for efficient transfer of energy from electrical to mechanical form.

The Rayleigh acoustic waves stress the bonds between the sensing film and analyte forcing only the analyte with the highest affinity for the sensing film to stay bound, while the shear-horizontal (SH) waves are used for sensing. Additionally, the acoustic waves work to efficiently mix the liquid samples flowing through the micro-channels of the sensor system, reducing the effects of diffusion-limited processes.

Results from using a sensing film of anti-mouse IgG covalently bound to the sensor-surface and mouse IgG as the analyte in buffer solution have shown improved sensor response, determined using fluorescent microscopy. Manipulation of liquid samples was achieved by strongly exciting the piezoelectric substrate with power levels of ~12 mW which is significantly greater than the 1 mW used for sensing. The larger

113

electrical power creates an acoustic wave *via* piezoelectric coupling that can physically force loosely bound species from binding sites, reducing noise that can lead to inaccurate measurements.

## 7.1 Introduction

Surface acoustic wave (SAW) sensors have now been used in many applications in both gaseous [1, 40, 120] and liquid environments[95, 101, 121]. The use of a SAW as a biosensor implies the device must not inherently be attenuated by the environment it is supposed to operate in. For general purposes, this implication restricts the SAW biosensors to SH and a specialized SH-SAW device that creates a Love mode wave from a thin film deposited on its surface [71, 111].

SAW sensors have been shown to work well as high sensitivity biosensors; however, like all other biosensors nonspecifically bound (NSB) protein interactions can cause a less than ideal sensor response and determination [5, 27]. Some possible responses seen as a result of NSB proteins include: exaggerated response due to multi-layers, false responses due to miscellaneous proteins covering the surface, and no response due to poor alignment of the functional groups. Minor improvements to biosensor responses can be achieved from thoroughly rinsing, use of ultrasonic baths to remove NSB proteins, and pretreatment of the analyte containing fluids. Each one of these processes adds to the complexity and functionality of a biosensor to be operated without specialized training in everyday environments.

Developments in acoustic wave applications have shown the functionality of nonspecific protein removal with relatively low power consumption thus significantly decreasing the uncertainty of the sensors response.

7.2    Materials and Methods

7.2.1    Sensor Device Design

The hexagonal SAW is a composite of three traditional delay line SAW devices rotated about the center of the die, which is approximately 20 x 20 mm.  The individual delay line devices are identical bi-directional interdigital transducers (IDTs) with an aperture of 47 $\lambda$, delay length of 197 $\lambda$, and feature size of 4 $\mu$m.  To eliminate unwanted waves and eliminate the electrical effect the delay path is shorted.   A standard metallization procedure of 100 nm titanium adhesion layer followed by 700 nm gold layer was used.   Figure 8 is an illustration of the hexagonal SAW layout.   The IDT designs tested included design considerations to improve the phase linearity and decrease the phase noise [18, 19].

7.2.2    Micro-fluidic Sensor Fixture and Testbed

The sensitivity required for detection of many biological markers is on the order of a few nano-grams, which is obtainable by many sensors; however, with advances to

SAW sensors they are some of the most sensitive devices [30-32]. The challenge associated with this scale of mass sensitivity becomes largely a fixture and test parameter issue as any variation in fluid flow or pressure will cause a significant sensor response [33]. To address this issue, it was decided to use a precision syringe pump manufactured by Harvard Apparatus which unlike peristaltic pumps provides a smooth continuous flow with no pulses. The equipment shown in the illustration (Figure 5) is highly adaptable for all of required fluid requirements from nano-liters to milli-liters [34]. Additionally, making the configurability and operation of the testbed simple is a LabView virtual instrument interface that controls and records all electronic operations including flow rate, flow direction, and valve sample selection. Due to the design of the hex-a-saw a typical fluidic fixture is not feasible, so an in house design has been designed and fabricated. The test fixture is constructed of polycarbonate, which has low moisture absorption, high strength, no centerline porosity, easily machineable, and can be polished to be optically clear. The micro-fluidic fixture to make electrical connections has a printed circuit board with SMA connectors attached.

7.2.3   Experimental Procedures

Although the sensors were designed for biosensor applications additional preparation of the sensors' surfaces were necessary. Primary to the preparations was to insulate the IDTs from the environment meeting three conditions 1) the insulating material must not attenuate the SH-SAW, 2) the material must not be highly permeable

116

by water, and 3) the material must permit attachment of antibodies. Polystyrene (Sigma Aldrich) was chosen as a solution. Coating the sensor was achieved by dissolving polystyrene in 2-Butoxyethyl acetate (Sigma Aldrich) to 4 weight percent then spin coating to a uniform thickness and annealed at 120 °C for 1 hour. Following the annealing, the sensors where mounted in the micro-fluidic fixture.

From a calculated area of the sensor exposed and cross-sectional areas of the antibodies used, a concentration of proteins was specified to ensure for 100% coverage of the sensor surface without excessive multi-layers of nonspecifically bound proteins. The calculated protein concentration was applied to the surface of the sensor through the micro-fluidic fixture for 1 hour to allow adequate surface adsorption to the polystyrene. Having the sensor functionalized with an antibody, varying concentrations of antigen were flowed across the sensor at a constant 0.15 ml/min. The antigen concentrations were calculated to ensure less than 25 % surface coverage. To further insure a good response of the sensor the pH was maintained at 7.4 through the use of phosphate buffer solution (PBS).

7.3    Surface Manipulation

The second task of this project was the use of high amplitude waves to remove loosely bound materials from the sensors surface thus improving the sensors abilities. The first tests to show the surface was being manipulated were conducted using a Leica DMI4000 fluorescent microscope. With the prepared sensors, fluorescently labeled

proteins were excessively adsorbed onto the surface of the device for 1 hour. Sensors where then flushed with 3 ml of PBS. Following the flushing the devices were subjected to high amplitude waves using 5 watt power amplifier (Mini-Circuits). Calculations were done to find the actual power delivered to the IDT was on the order of milli-watts due to insertion loss of the device and attenuation of the films on the surface.

7.4    Simultaneous Surface Manipulation and Sensing

The final task of these experiments was the combination of the high amplitude waves manipulating the surface and the use of low amplitude waves for sensing the changes of the sensing film simultaneously. The sensors were first prepared with an antibody film as described above, and used to sense a known concentration of antigen in solution. After the sensing test, the sensors were coated with known concentrations of a nonspecific binding protein, Bovine Serum Albumin (BSA). Following the BSA application, the sensors were flushed with 3 ml of PBS then subject to high amplitude waves while monitoring the changes with a different delay path.

7.5    Results and Discussion

The sensor used in this project is theoretically capable of detecting nano-grams of mass change on the surface, the first round of experiments showed that this was the case with the detection of low levels of mouse IgG onto a functionalized surface. A

representative data set of the sensing capability is shown in Figure 39. The first drop on the curve is the result of flushing away the excess antibody from the 1 hour adsorption process. Following the first large drop, the antigen is injected and flushed away. For this there are actually two measurements that are significant. First the phase change while injecting the known concentration, and second the phase change seen remaining on the surface of the device even after an extensive flushing with PBS.
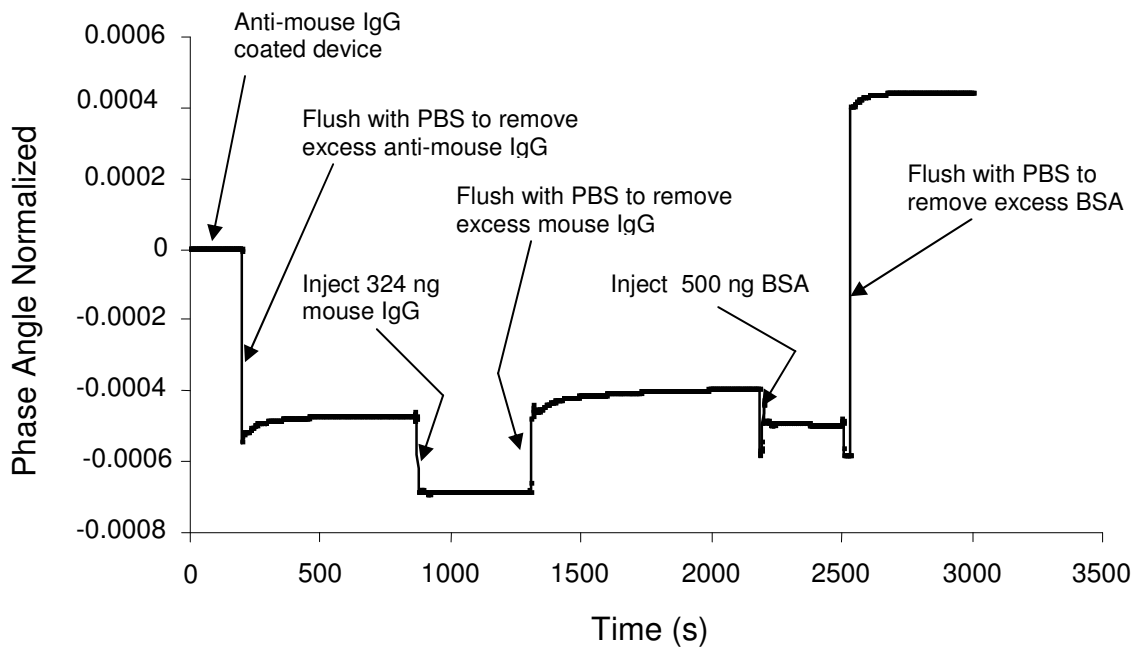


Figure 39 Normalized phase response for the coating of a sensor with anibodies (138 ng/ml anti-mouse IgG in PBS) followed by the detection of of the antigen (324 ng mouse IgG), and the coating of the sensor with nonspecifically binding BSA (500 ng).

The final responses in Figure 39 are from the addition of BSA to completely coat the surface in preparation for testing the removal NSB proteins. Upon first inspection

119

one will note the magnitudes of the two steps are significantly different from the response of the specific antigen. This is the result of leaving the linear response regime of the SAW sensor by applying too much material onto the surface. For many biosensors this would result in discarding the sensor and starting over to make any determination; however, this provides this project with a perfect beginning to test the cleaning functionality of the hexagonal SAW, such a result is shown in Figure 40.

Having coated a sensor's surface beyond its functioning point is often encountered, but more common is not having a pure sample with only one protein. Such a sample requires extensive filtering and/or processing to be able to make a determination on the concentration of the desired protein. The results in Figure 40 address this issue, but more specific to this project show that it is simultaneous operation of crossing delay paths to sense and manipulate the sensing film is feasible. The data show the addition of a high concentration of BSA to the surface of the SAW sensor followed by the removal of some of the BSA remaining on the surface after and extensive flushing with PBS. The removal is achieved through the application of the power amplified signal for 50 seconds on a different SAW delay path from the one doing the sensing. Due to the limitations of the current design of the hexagonal SAW more of the sensing delay line is exposed to the sample solutions than what the second and third delay paths would be able to manipulate.
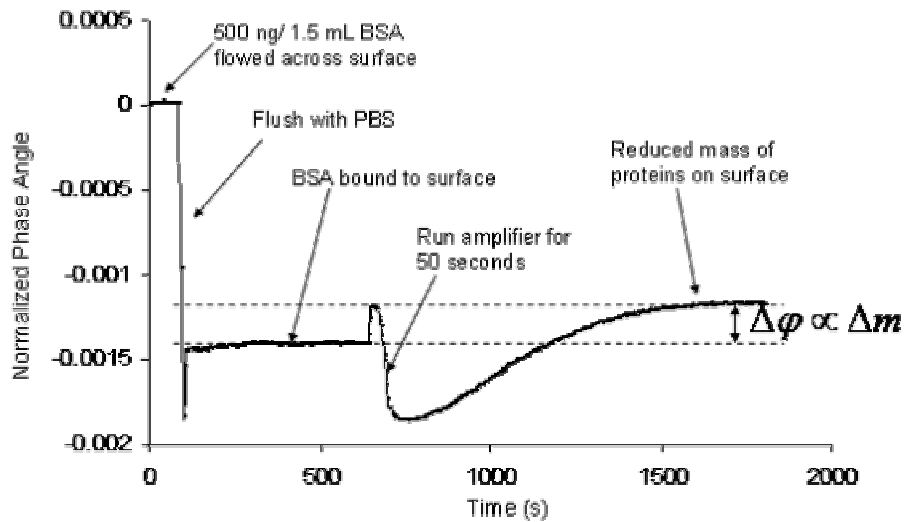
Figure 40  Normalized phase angle response of sensor to the removal of excess BSA with just a flush of PBS followed by the removal of NSB BSA using high amplitude waves of a different delay path.

## 7.6    Conclusion

The development of a hexagonal SAW device was shown to simultaneously manipulate biological films and sense the changes using a different acoustic wave across the same sensing film.  The results have shown both that low level sensing of proteins in solution is possible with this new SAW sensor.   Additionally the sensor has the functionality to reduce error in responses by removing NSB proteins and other loosely bound material that are common in complex samples.  With further design improvements and studies, this device is believed to have wide application to bio-sensing especially

where non-purified samples containing many different proteins need to be analyzed without the use of technicians and laboratory equipment.

Chapter 8

Effects of Micro-cavities on Shear-horizontal Surface Acoustic Wave Sensors:

Theoretical Study

Micro-cavities in delay paths of 36° YX-LiTaO$_3$ surface acoustic wave sensors were studied using finite element methods. Simulation results of $\lambda$/2, $\lambda$/4 and $\lambda$/8 micro-cavities empty and polystyrene filled were compared to standard delay line shear-horizontal SAW, optimized Love-wave, and etched grating sensors. The micro-cavities reduced the insertion loss by 19.25 dB from 33.28 dB with a velocity sensitivity 4.83 times greater than the standard SAW sensor simulated.

8.1   Introduction

Challenges for developing sensors include factors such as sensitivity, power consumption and reproducibility. For surface acoustic wave (SAW) sensors, sensitivity is one of the most critical parameters and is often improved by decreasing the operational wavelength.[1]  Sensitivity can be improved secondly through the addition of a guiding layer to create Love-wave devices.[22, 122]  An analytical solution by Mchale *et al.* showed a theoretical improvement limit to sensitivity of 20 times.[22]  Our finite element

(FE) simulations show an improvement of 5.36 times the velocity sensitivity of the Love-wave sensor over a standard SAW sensor.

Power loss for sensors is a growing issue with the increasing demand for personal and remote sensing applications for these reasons power usage of a sensor is very important. Ideal SAW delay line sensors have an insertion loss of 7 dB and it is not uncommon to work with insertion losses of 20 dB simulated devices had insertion losses from 14.03 to 33.28. Common methods to decrease the insertion loss in SAW devices, not particularly sensors, include reflective gratings[18], grooves and corrugated gratings[19, 123, 124], and wave-guides[72]. The reoccurring methods in these four primary schemes to improve the SAW device power loss is the conversion bulk waves into surface waves and entrapment of energy near the surface that would otherwise be lost to bulk waves.[18, 25]

8.2   Methods

The micro-cavity devices described herein are a combination known methods to improve SAW device characteristics. First etched substrates with square patterns of $\lambda/2$, $\lambda/4$ and $\lambda/8$ dimensions at varying depths to increase the dispersion and bulk to surface wave conversion were studied and compared to etched gratings. The polystyrene was added to the micro-cavity simulations to act as an inhomogeneous waveguide for further entrapment of wave energy near the device surface. Last, the device design that gave the best characteristics was applied to sensing applications through the addition of an ideal

mass to measure sensitivity.  The same mass was added to a standard SAW sensor, an optimized Love-wave sensor, and the best etched grating sensor for comparison using a combined sensitivity term that accounts for both voltage and velocity perturbations.

The base sensor model is 3-D FE model created in ANSYS.  The FE SAW model is used to simulate effect of micro-cavities on sensor sensitivity. The transient response of the SAW sensor to an impulse input applied at the transmitting interdigital transducer (IDT) fingers were utilized to study the wave generation and propagation characteristics as well as deduce its frequency response.  The developed models consisted of a 36° YX LiTaO$_3$ substrate 40 $\lambda$ long, 5 $\lambda$ wide and 5 $\lambda$ deep with IDT's 2 $\lambda$ long and $\lambda/4$ wide with a periodicity of 40 $\mu$m.  For this work, the transducers were considered to be mass-less elements.  Tetrahedral elements were used throughout the model with 4 degrees of freedom to account for voltage and particle displacements in the x-, y- and z-directions. The formation of the elements was done to ensure a highest density on the top center surface of the substrate where the most deformation occurs.  The simulations were initiated with an electric impulse of 10 V applied at the transmitting IDT fingers with time steps of 0.95 ns.  The simulation was carried out for 190 ns and parabolic fitting/interpolation between the 0.95 ns time-steps were used on all data.  The simulation time and dimensions of the model were chosen to prevent reflected signals from the ends and bottom of the substrate.

The models were so configured that the micro-cavities (20 identical per simulation) were located in the center of the delay path forming 4 rows of 5 micro-cavities each as shown in the cross-section of the meshed model in Figure 41.  For comparison, grooves (etched gratings) of length $\lambda/4$ and $\lambda/2$ with width equivalent to the

aperture of the IDT's and depths the same as the cavities have been simulated. For complete details of the models used including example Ansys script files, see Appendix B.

Additionally, the micro-cavities and grooves were filled with polystyrene (PS) to serve as a waveguide and further enhance the sensor characteristics. From the theory of waveguides, the addition of polystyrene, a material with a lower density and lower acoustic velocity than the substrate, was expected to trap more energy at the surface than if the device were bare.[22]
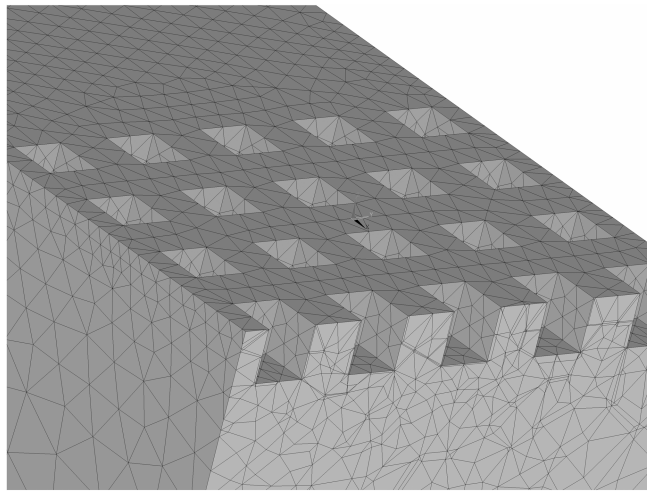


Figure 41  Cross-section of meshed $\lambda/2$ x $\lambda/2$ x $\lambda/2$ micro-cavity SAW device.

8.3    Results

For the $\lambda\backslash4$ design data as shown in Figure 42, the $\lambda\backslash4$ depth filled with PS design have 14.26 dB greater energy transmission across the delay path as compared to a plain

path. This design even has an improvement over the Love-wave (LW) design data by 6.66 dB. Notably, the λ\8 depth not filled with PS is between the λ\4 depth filled with PS and the LW design data. From the λ\2 design data as shown in Figure 43, the λ\8 depth filled with PS design has an increase of 5.35 dB over the λ\4 design data.
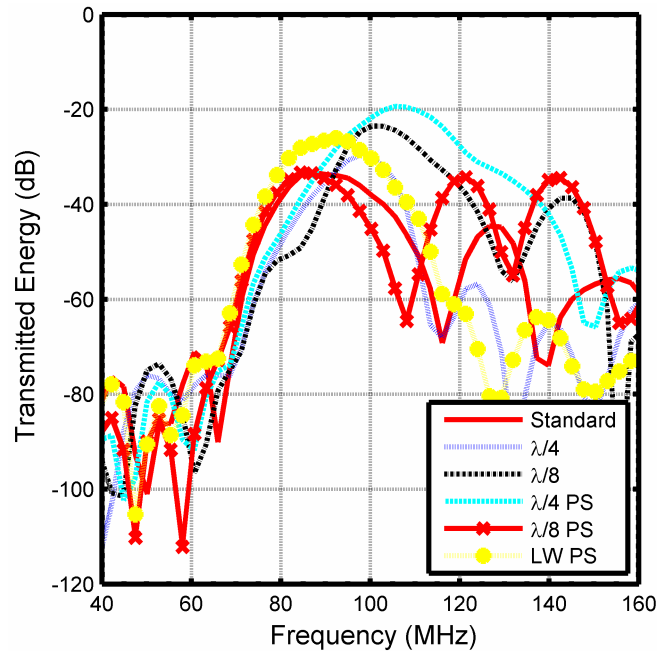


Figure 42  Comparison of transmitted energy of the λ/4 designs λ/4 and λ/8 deep that are both empty and filled with polystyrene to an optimized Love-wave and a standard SAW delay path.
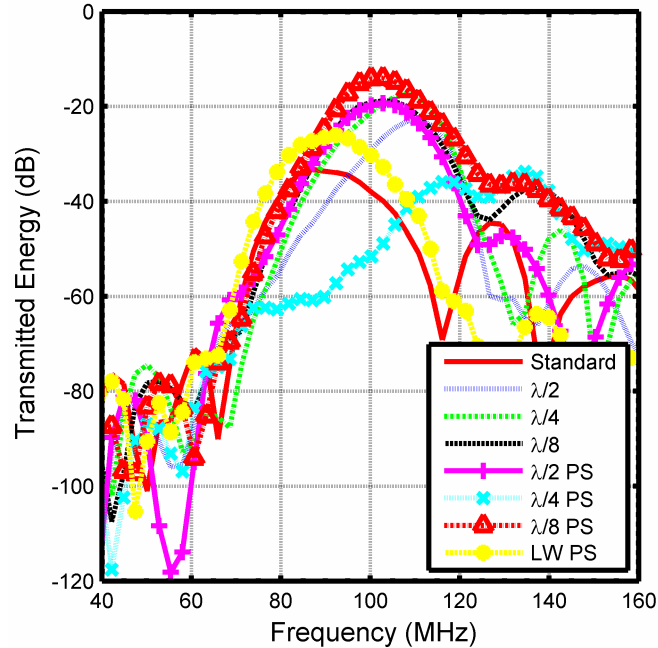
Figure 43  Comparison of transmitted energy of the λ/2 designs λ/2, λ/4 and λ/8 deep that are empty and filled with polystyrene to an optimized Love-wave and a standard SAW delay path.

The λ/2 width by λ/2 length by λ/8 depth micro-cavity filled with polystyrene showed the greatest energy transmission across the delay path and was chosen for comparison to a standard split finger sensor, Love-wave sensor, and λ/2 width by λ/8 depth groove grating filled with polystyrene sensor.  Simulation models were created to apply a 100 pg mass across 9,600 μm$^2$ center in the delay path of the SAW sensor.  The same transient analysis used for initial work was performed on these now ideal-mass-perturbed sensors.  The resulting data are summarized in Figure 44 as the square root of the summation of the squares of velocity and voltage changes as a result of the 100 pg mass perturbation.  The data show the λ/2 width by λ/2 length by λ/8 depth micro-cavity

128

array filled with polystyrene to be 1.38 times more sensitive than a standard split finger SAW sensor and 1.79 times more sensitive than an optimized Love-wave SAW sensor through finite element simulations applying 100 pg ideal mass to the surface of each sensor resulting in both velocity and voltage perturbations. Although the finite element models simulated in this work are limited in comparison to experimental dimensions, previously shown, the results show clear trends that are found in experimental studies.[6, 110]
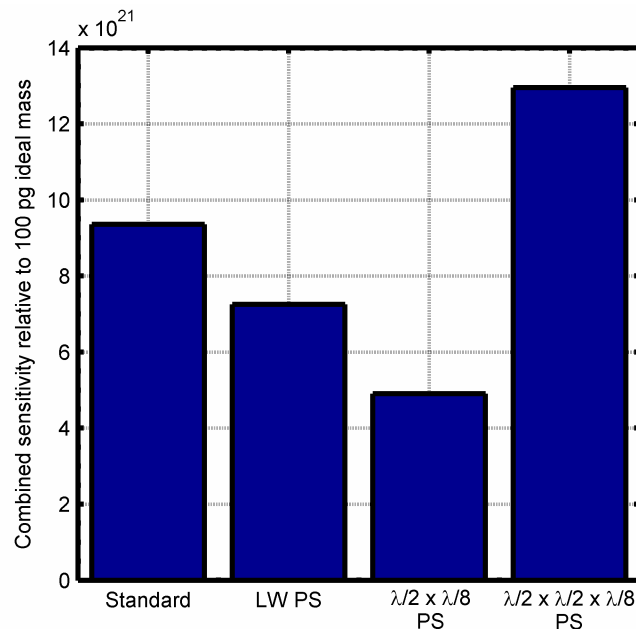


Figure 44  Comparison of combined velocity and voltage mass sensitivities of a plain single split finger SAW sensor, an optimized 2,200 nm polystyrene Love-wave sensor, a $\lambda/2$ length by $\lambda/8$ depth groove grating filled with polystyrene, and a $\lambda/2$ length by $\lambda/2$ width by $\lambda/8$ depth micro-cavity array filled with polystyrene.

## 8.4    Conclusion

In summary, theoretical studies using finite element methods to study the effects of micro-cavities and grooves on SAW propagation were completed for sensor applications. Additionally, the filling of the micro-cavities and grooves with a less dense and lower acoustic velocity material (polystyrene) was studied. The data presented compares micro-cavity structured SAW sensors to traditional designs such as a plain delay path and an optimized waveguide coating. The micro-cavity structure data show significantly greater energy transmission than the other structures presented in this study.

Chapter 9

Conclusions and Points for Future Endeavors


The work presented in the previous chapters covered topics including acoustic wave theory, material characterization, chemical and biological sensing, and removal of nonspecifically bound proteins. As such, these components and applications are the result of research to develop one sensor system that can ultimately be used for the sensing of biological moieties with the capability to be reused either through a sensor self regeneration or the replacement of sensor element. Progress towards this goal was made through contributions to the scientific community as summarized in the following section. Finally with all work, facets of interest for future research are developed. Some of the key points are explained in the final section.


9.1    Summary of Contributions

Across the work that is presented in this dissertation considerable effort has been made to establish a foundation both in available knowledge and physical resources for current and future researchers to build from. Key examples of this work are the

development of designs, scripts, programs, and test fixtures necessary to conduct sensor research from experimentation to data analysis.

A direct contribution resulting in a patent was the development of the hexagonal SAW device. This device was conceived as a new tool for material characterization and sensing application. The device consists of three independent SAW delay paths that intersect. It was shown that the delay paths can operate simultaneous for improved chemical determinations and material characterization as verified through the use of principal component analysis on polymer / organic vapor sorption experiments. The same design was later used for simultaneous sensing of biological moieties while removing nonspecifically bound materials.

Prior to testing the hexagonal SAW device for simultaneous liquid phase sensing and cleaning, experiments were conducted to show the feasibility of using acoustic streaming to remove proteins from surfaces. Additionally in collaboration with Subramanian K.R.S. Sankaranarayanan finite element models created and run to explore the physics of acoustic streaming.

In an effort to have the best sensitivity both experimental and theoretical studies were conducted to find the best IDT design with optimal waveguide thickness to generate Love-waves. IDT designs for sensor applications previously were only very basic due to the range of knowledge necessary to develop sensors. From a thorough search of sensor literature, this type of work had not previously been attempted either through experimental or simulation methods.

A new design approach to increase sensor sensitivity and decrease sensor power consumption was created and studied in this dissertation work through the use of finite

132

element model simulations. The designs simulated based on a microarray etched into the delay path of a SAW sensor took the best of all previously used concepts for efficient surface acoustic wave transmission, and showed the best sensor in terms of energy loss and mass sensitivity. Part of this study compared the use of Love-waves and etched gratings to the etched microarray design proposed. Additionally, it was shown that the use of typical Love-waveguide material to fill the etched patterns further improved the desired sensor properties.

9.2    Points for Future Endeavors

This work has encompassed many different disciplines to set up experimental and theoretical test apparatuses that can be adapted to support many new exciting endeavors. Throughout this work, the designs and equipment used was specified for general use instead of specific one time tasks for this reason there are many worthwhile projects that can be spun from this ground laying work.

9.2.1    SAW IDT Designs

In Chapter 5 three IDT designs were compared both experimentally and through FE simulations. This chapter serves as a basis for this part of the future work. In essence, more IDT designs need to be studied for sensor response to ideal and non-ideal mass

loading. One of the first designs to be studied should be the focused IDT. Other interesting designs worth studying are acoustic horns and variations to unidirectional designs similar to the one discussed in this dissertation. For some of the designs, analytical models can be developed for further comparison.

### 9.2.2 Microcavity Delay Path Experiments

Methods to improve sensitivity and reduce power consumption of sensors are wonderful topics that form a very large project. As shown in Chapter 8 modifications to the delay path of a surface acoustic wave sensor can produce large changes to sensor characteristics. Further work needs to be done on this topic to experimentally verify the findings of the FE simulations. The work involves creating a mask for the microcavities, then etching the pattern into characterized SAW devices. Sensitivity can be accurately determined through the addition of thin metal film experimentally.

### 9.2.3 Simulations of Non-square Microcavities

In the present work only square microcavities have been studied, but there are many designs that can be simulated and experimentally verified. Designs including circles and polygons as the base of the microcavity can be studied with vertical side walls and angled sides to form cone and pyramids. More elaborate designs to reduce

reflections and maximize wave propagation can also be investigated. Designs for such cavities can be adapted from optic and RF waveguide theory.

9.2.4   Combined SAW – Bulk Acoustic Wave Device

New devices are always interesting endeavors to pursue. One such device, proven in concept by Don Malocha and students, is to combine a SAW and bulk acoustic wave (BAW) device in one [125]. The idea behind this is similar to the hexagonal SAW, have more signals thus more information for the sensor. The plan to develop this device is to take the hexagonal SAW and pattern gold electrodes on the back side of the crystal. Due to the thickness, the BAW that can be generated will be about 3 MHZ. (0.5 mm = 20 mils) This will allow the measurement verification of the SAW parameters using the BAW. The BAW can be used for temperature compensation or measurements. Unfortunately, the electrode size is not ideal and the backside of current wafers is not polished.

9.2.5   Combined SAW – Surface Plasmon Resonance Device

Biosensors ultimately need to be sensitive to extremely small concentrations of analytes. For surface acoustic wave sensors, the sensitivity is dependent on the frequency which is a function of the substrate properties. Sometimes one method is not the best for

a task, so the use of another sensor technology is required. The ability to integrate is there for SAW and Surface Plasmon Resonance (SPR). In the combined system, the SAW can be used for sensing or acoustic streaming to move material from the sensor surface.

Surface plasmon resonances are electromagnetic fields generated on the surface of metals through an incident light source. Once the resonance is established, the refractive index can be measured via the angle of the reflected light with a photo-detector. To utilize SPR in a sensor configuration, Figure 45, a thin film of gold is deposited on the top side of a substrate through which the light is transmitted to measure changes occurring in the sample on the gold surface.
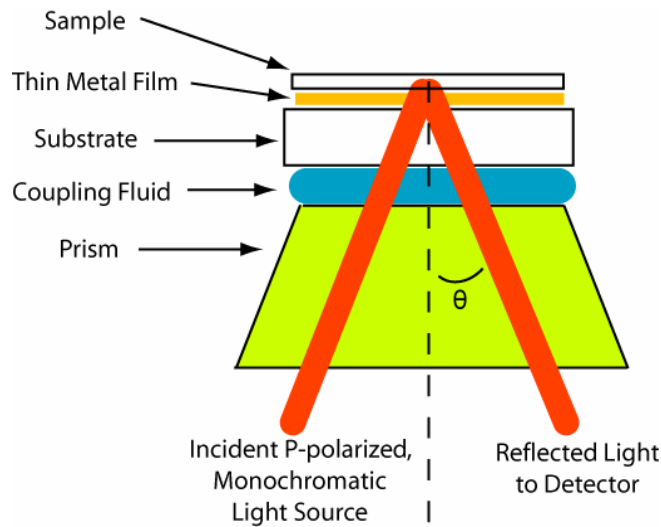


Figure 45  SPR sensor schematic.

SPR is a sensitive measurement for thin films on the nanometer-scale that has been used recently to measure single biomarker levels as well as to determine binding energies of the antibody/antigen interaction involved in such measurements. Sensitivity of SPR is enhanced by selectivity of the sensor film and by the quality of the photo-detector utilized.

The proposed project will integrate SAW and SPR principles on one sensing element to enhance analyte identification and quantification from the orthogonal information afforded by the two sensing and acoustic streaming principles. The SAW sensor component will be based on the hexagonal SAW device. This component of the proposed device is capable of simultaneously transducing the biochemical concentration at the tens of picogram to nanogram/ml levels into a readable signal and of keeping other proteins and biomarkers from interfering with the transduction mechanism. Thus, the proposed sensing element will integrate two sensor principles and selective protein removal on a single area element. Combined, it will allow for differential sensing of multiple biomarkers, when applied in a biosensor format.

The integrated device schematic is shown in Figure 46. The first milestone for the project is the acquisition of theoretical device fundamentals and device fabrication details. This sensor system element will be designed to function on the available microscope platform to facilitate the SPR measurements. SAW sensor measurements and high-energy Rayleigh wave generation will utilize RF electronics and analyzers. Acquisition of these skills and utilization of these techniques will be a second milestone for the project. The third and important milestone will be reached when a successful

sensor system element is fabricated and tested. The fourth milestone is the demonstration of differential detection of multiple biomarkers, including data analysis.
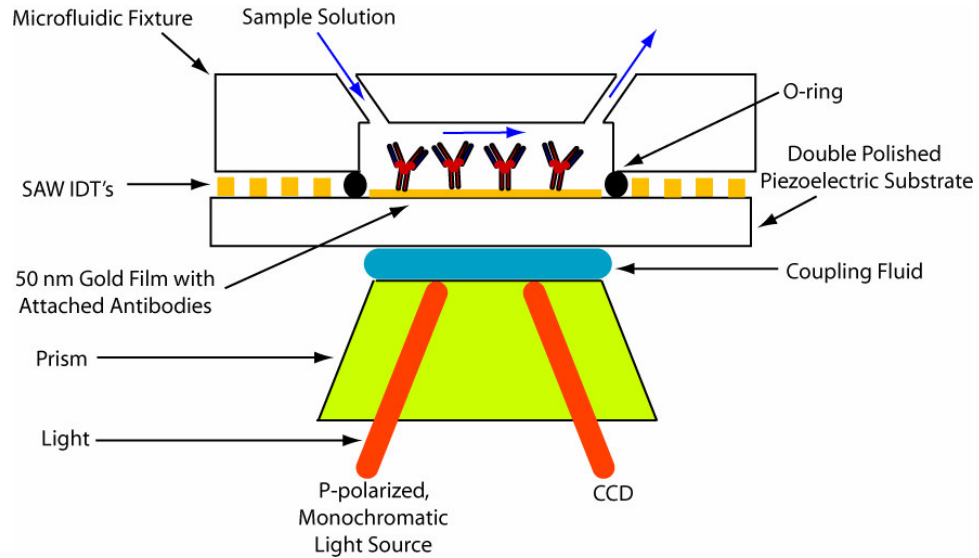


Figure 46  Integrated SAW-SPR sensor schematic.

9.2.6   New Materials:  Langasite and Nano-Crystalline Diamond

New materials provide a range of repetitive type work that needs to be done to characterize the material.  Fortunately, new materials also open new areas of study.  For example, Langasite is a material that maintains its piezoelectricity to a very high temperature enabling sensing at these temperatures has previously been inconceivable. With Langasite sensors need to be made and compared to existing quartz, $LiNbO_3$ and $LiTaO_3$ devices.  Some of this work can be done with FE simulations already configured by simply changing the input material matrices rotated appropriately.

138

Diamond has many fantastic chemical and mechanical properties that are being leveraged in numerous projects. For the proposed biosensor, diamond has a dual role for both enhanced transduction as well as a biofunctionalization. Since diamond is just carbon atoms, it is by itself biocompatible [126, 127]. Polycrystalline diamond in part due to its biocompatibility has been used for biosensors. Typical micron sized grain structured diamond exhibits poor, sluggish sensor responses, while nanocrystalline diamond films exhibit improved sensor responses that are indicative of enhanced selectivity [128]. Slight modifications to the diamond growth conditions and post-growth treatments such as dopping can fine tune the properties of the diamond [129]. Nanocrystalline diamond has been shown to form covalent bonds with proteins that still show full functionality and activity once bound [126, 127, 130].

Nanocrystalline diamond can be plasma treated to increase the surface oxygen and hydroxide terminations. The advantage of this treatment is to be able to choose between hydrophilic and hydrophobic surfaces depending on which will provide the best surface coverage using a set protein. General results confirmed using ELISA show that the immunoglobulins have a higher binding efficacy with a hydrophilic nancrystalline diamond [127, 130]. Once the surface has been modified to be hydrophilic, it is possible to use common silane treatments for creating covalent bonds between the diamond and a chosen protein [27, 131].

From the devices fabricated and characterized, it is possible then to use the devices for an exciting use, namely in-situ material characterization of high growth / deposition temperature materials such as nano-crystalline diamond. The advantage of

this work will be the development of a system that can measure material properties of things that usually require post-operation metrology.

9.2.7   SAW Sensor Circuit Optimization

To be able to produce a device that is feasibly used in the field for testing, the electronics of the sensor described need to be optimized and condensed into a tight package.  The most challenging aspect of the optimization will be the power amplifier integration and condensing.  This RF component is required to be high power to be able to remove materials from the surface of the sensing element.  Typically this component is not packaged tightly with other electronics; however, with known SAW properties, the power amplifier is only required to be operated for a short period of time which makes this a doable task.

9.2.8   Fluid Solid Interaction Simulations

With the available computing resources and developed FE models, the application of these to the different IDT designs is a natural progression of work.  Although only intuitive results are expected, the work is worthy to further understand the methods to tune acoustic streaming for the desired applications of biosensors.

Slightly more complicated to create a model for are the microcavity designs. These structures have the potential to create tremendous forces with acoustic streaming at the boundaries of the microcavities due to the reflections. The devices need to be simulated both without and will the waveguide material in the microcavity.

References Cited

[1].    Ballantine, D.S., R.M. White, S.J. Martin, A.J. Ricco, E.T. Zellers, G.C. Frye, and H. Wohltjen, *Acoustic Wave Sensors: Theory, Design, and Physico-chemical Applications*. Applications of Modern Acoustics. 1997, San Diego: Academic Press. xii, 436.

[2].    Thompson, M. and D.C. Stone, *Surface-Launched Acoustic Wave Sensors: Chemical Sensing and Thin-Film Characterization*. Chemical Analysis, ed. J.D. Winefordner. Vol. 144. 1997, New York: John Wiley & Sons, Inc.

[3].    Cular, S., D.W. Branch, V.R. Bhethanabotla, G.D. Meyer, and H.G. Craighead, *Removal of Nonspecifically Bound Proteins on Microsensors using Surface Acoustic Waves -- Accepted*. IEEE Sensors Journal, 2007.

[4].    Branch, D.W., G.D. Meyer, C.J. Bourdon, and H.G. Craighead, *Active Mixing in Microchannels using Surface Acoustic Wave Streaming on $128^o$ YX LiNbO$_3$*. Submitted JMEMS, 2005.

[5].    Meyer, G.D., J.M. Moran-Mirabal, D.W. Branch, and H.G. Craighead, *Nonspecific Binding Removal from Protein Microassays Using Thickness Shear Mode Resonators*. IEEE Sensors Journal, 2006. 6(2): p. 254-261.

[6].    Sankaranarayanan, S., S. Cular, V.R. Bhethanabotla, and B. Joseph, *Flow Induced by Acoustic Streaming on Surface Acoustic Wave Devices and Its Application in Biofouling Removal: Numerical and Experimental Study*. Physical Review - E -- Accepted, 2007.

[7].    Cular, S., V.R. Bhethanabotla, and D.W. Branch. *Simultaneous Surface Manipulation and Sensing in a Biosensor Using a Hexagonal SAW Device*. in *AIChE Annual Meeting*. 2006. San Francisco, Ca, USA.

[8].    Diamond, D., ed. *Principles of Chemical and Biological Sensors*. Chemical Analysis, ed. J.D. Winefordner. Vol. 150. 1998, John Wiley & Sons, Inc.: New York.

[9].    Eggins, B.R., *Chemical Sensors and Biosensors*. Analytical Techniques in the Sciences, ed. D.J. Ando. 2002, New York: John Wiley & Sons, Inc.

[10].   Cular, S., S. Sankaranarayanan, and V.R. Bhethanabotla. *Improved Love-wave Biosensors Through Advanced Interdigitated Transducer Design*. in *AIChE Annual Meeting*. 2007. Salt Lake City, Utah.

[11].   Cular, S., V.R. Bhethanabotla, and D.W. Branch. *Vapor Discrimination Using a Hexagonal Surface Acoustic Wave Device*. in *IEEE Ultrasonics Symposium*. 2006. Vancouver, CA: IEEE.

[12].   Neuman, M.R. and C.-C. Liu, *Biomedical Sensors in Interventional Systems: Present Problems and Future Strategies*. Proceedings of the IEEE, 1988. 76(9): p. 1218-1225.

[13].   Blum, L.J. and P.R. Coulet, eds. *Biosensor Principles and Applications*. Bioprocess Technology Series, ed. W.C. McGregor. 1991, Marcel Dekker, Inc.: New York.

[14].   Sadana, A., *Engineering Biosensors: Kinetics and Design Applications*. 2002, New York: Academic Press.

[15].   Richardson, A., V.R. Bhethanabotla, and S. Cular. *Determination of the Viscoelastic Shear Modulus of Poly(Isobutylene)/solvent Systems Using Thickness Shear Mode Quartz Resonators*. in *AIChE Annual Meeting*. 2007. Salt Lake City, Utah.

[16].   Wong, H.C., S.W. Campbell, and V.R. Bhethanabotla, *Sorption of Bezene, Tetrahydrofuran and 2-butanone by Poly(vinyl acetate) at 323.15K Using a Quartz Crystal Balance*. Fluid Phase Equilibria, 2000. 179: p. 181-191.

[17].   Michael, F. and J. Hénaff, *Surface Acoustic Waves for Signal Processing*. The Artech House acoustic library. 1989, Boston: Artech House.

[18].    Morgan, D.P., *Surface-Wave Devices for Signal Processing*. Studies in Electrical and Electronic Engineering. Vol. 19. 1991, New York: Elsevier.

[19].    Campbell, C., *Surface Acoustic Wave Devices and Their Signal Processing Applications*. 1989, Boston: Academic Press. xiv, 470.

[20].    Gizeli, E., Bender, F., Rasmusson, A., Saha, K., Josse, F., and Cernosek, R.W., *Sensitivity of the Acoustic Waveguide Biosensor to Protein Binding as a Function of the Waveguide Properties*. Biosensors & Bioelectronics, 2003. 18: p. 1399-1406.

[21].    Josse, F., F. Bender, and R. Cernosek, *Guided Shear Horizontal Surface Acoustic Wave Sensors for Chemical and Biochemical Detection in Liquids*. Analytical Chemistry, 2001. 73: p. 5937-5944.

[22].    McHale, G., M.I. Newton, and F. Martin, *Theoretical Mass Sensitivity of Love Wave and Layer Guided Acoustic Plate Mode Sensors*. Journal of Applied Physics, 2002. 91(12): p. 9701-9710.

[23].    Kovacs, G., G.W. Lubking, M.J. Vellekoop, and A. Venema. *Love Waves for (Bio)chemical Sensing in Liquids*. in *IEEE Ultrasonics Symposium*. 1992: IEEE.

[24].    Rohde, H.J. and H.J. Frohlich, *Investigation of Rayleigh-wave Propagation in XY-quartz with SiO Film Overlays*. Acta Physica Slovaca, 1982. 32(1): p. 85-90.

[25].    Auld, B.A., *Acoustic Fields and Waves in Solids*. 1973, New York: John Wiley & Sons, Inc. 2 v.

[26].    Nyborg, W.L., *Acoustic Streaming due to Attenuated Planes Waves*. The Journal of The Acoustical Society of America, 1953. 25(1): p. 68-75.

[27].    Cular, S., D.W. Branch, V.R. Bhethanabotla, G.D. Meyer, and H.G. Craighead. *Removal of Nonspecific Binding on Microsensors Using Surface Acoustic Waves*. in *AIChE Annual Meeting*. 2005. Cincinnati, OH, USA.

[28].    Bakhtari, K., R. Guldiken, P. Makaram, A.A. Busnaina, and J.-G. Park. *Removal of Nano Scale PSL Particle Using Acoustic Streaming*. in *Annual Meeting of the Adhesion Society*. 2005.

[29]. Miyamto, K., S. Nagatomo, Y. Matsui, and S. Shiokawa, *Nonlinear Vibration of Liquid Droplet by Surface Acoustic Wave Excitation.* Jpn. J. Appl. Phys., 2002. 41: p. 3465-3468.

[30]. Rapp, M., T. Wessa, and H.J. Ache. *Modification of Commercially Available Low-Loss SAW Devices Towards an Immunosensor for in-situ Measurements in Water.* in *IEEE Ultrasonics Symposium.* 1995: IEEE.

[31]. Bender, F., K. Lange, N. Barie, J. Kondoh, and M. Rapp, *On-line monitoring of Polymer Deposition for Tailoring the Waveguide Characteristics of Love-wave Biosensors.* Langmuir, 2004. 20: p. 2315-2319.

[32]. Wessa, T., M. Rapp, and H. Sigrist, *Immunosensing of Photoimmobilized Proteins on Surface Acoustic Wave Sensors.* Colloids and Surfaces, 1999. 15: p. 139-146.

[33]. Barie, N., H. Sigrist, and M. Rapp, *Development of Immunosenors Based on Commercially Available Surface Acoustic Wave (SAW) Devices.* Analusis, 1999. 27(7): p. 622-629.

[34]. Lange, K., F. Bender, A. Voigt, H. Gao, and M. Rapp, *A Surface Acoustic Wave Biosensor Concept with Low Flow Cell Volumes for Label-Free Detection.* Analytical Chemistry, 2003. 75: p. 5561-5566.

[35]. *LF-2.7GHz RF/IF Gain Phase Detector AD8302.* 2002, Analog Devices, Inc.

[36]. Stubbs, D.D., S.-H. Lee, and W.D. Hunt, *Molecular Recognition of for Electronic Noses Using Surface Acoustic Wave Immunoassay Sensors.* IEEE Sensors Journal, 2002. 2(4): p. 294-300.

[37]. Grate, J.W., A. Snow, D.S. Ballantine, H. Wohltjen, M.H. Abraham, R.A. McGill, and P. Sasson, *Determination of Partition Coefficients from Surface Acoustic Wave Vapor Sensor Responses and Correlation with Gas-Liquid Chromatographic Partition Coefficients.* Analytical Chemistry, 1988. 60: p. 869-875.

[38]. Grate, J.W., S.J. Patrash, S.N. Kaganove, M.H. Abraham, B.M. Wise, and N.B. Gallagher, *Inverse Least-squares Modeling of Vapor Descriptors Using Polymer-Coated Surface Acoustic Wave Sensor Array Responses.* Analytical Chemistry, 2001. 73: p. 5247-5259.

[39]. Grate, J.W., B.M. Wise, and N.B. Gallagher, *Classical Least Squares Transformations of Sensor Array Pattern Vectors into Vapor Descriptors. Simulation of Arrays of Polymer-coated Surface Acoustic Wave Sensors with Mass-plus-volume Transduction Mechanisms.* Analytica Chimica Acta, 2003. 490: p. 169-184.

[40]. Grate, J.W., *Acoustic Wave Microsensor Arrays for Vapor Sensing.* Chemical Reviews, 2000. 100: p. 2627-2648.

[41]. Martin, S.J., G.C. Frye, and S.D. Senturia, *Dynamics and Response of Polymer-Coated Surface Acoustic Wave Devices: Effect of Viscoelastic Properties and Film Resonance.* Analytical Chemistry, 1994. 66: p. 2201-2219.

[42]. Grate, J.W., M. Klusty, R.A. McGill, M.H. Abraham, G. Whiting, and J. Andonian-Haftvan, *The Predominant Role of Swelling-Induced Modulus Changes of the Sorbent Phase in Determining the Response of Polymer-Coated Surface Acoustic Wave Vapor Sensors.* Analytical Chemistry, 1992. 64: p. 610-624.

[43]. Gemperline, P., ed. *Practical Guide to Chemometrics.* 2nd ed. 2006, Taylor & Francis Group, LLC: Boca Raton.

[44]. Vernin, G. and M. Chanon, eds. *Computer Aids to Chemistry.* Chemical Science. 1986, Ellis Horwood Limited: Chichester.

[45]. Jackson, J.E., *A User's Guide to Principal Components.* Wiley Series in Probability and Statistics. 1991, New York: John Wiley and Sons, Inc.

[46]. Branch, D.W. and S.M. Brozik, *Low-level Detection of a Bacillus Anthracis Simulant Using Love-wave Biosensors on 36 deg YX LiTaO$_3$.* Biosensors & Bioelectronics, 2004. 19: p. 849-859.

[47]. Müller, C., T. Nirmaier, A. Rügemer, and M.V. Schickfus, *Sensitive NO$_2$ Detection with Surface Acoustic Wave Devices Using a Cyclic Measuring Technique.* Sensors and Actuators B Chemical, 2000. 68: p. 69-73.

[48]. Upadhyayula, A.K., R.D. Williams, and V.R. Bhethanabolta, *High Frequency Thickness Shear Mode Devices for Organic Vapor Sensing.* Sensors and Actuators B Chemical, 2005 *(submitted).*

[49].  *Matlab*, The Mathworks, Inc.

[50].  Narang, U., P.R. Gauger, A.W. Kusterbeck, and F.S. Ligler, *Multianalyte Detection Using a Capillary-Based Flow Immunosensor.* Analytical Biochemistry, 1998. 255: p. 13-19.

[51].  Qiaocui, S., P. Tuzhi, Z. Yunu, and C.F. Yang, *An Electrochemical Biosensor with Cholesterol Oxidase/Sol-Gel Film on a Nanoplatinum/Carbon Nanotube Electrode.* Electroanalysis, 2005. 17(10): p. 857-861.

[52].  Ramanathan, K. and B. Danielsson, *Review: Principles and Applications of Thermal Biosensors.* Biosensors & Bioelectronics, 2001. 16: p. 417-423.

[53].  Blawas, A.S. and W.M. Reichert, *Protein Patterning.* Biomaterials, 1998. 19: p. 595-609.

[54].  Mitchell, P., *A Perspective on Protein Microarrays.* Nature Biotechnology, 2002. 20: p. 225-229.

[55].  Roederer, J.E. and G.J. Bastiaans, *Microgravimetric Immunoassay with Piezoelectric Crystals.* Analytical Chemistry, 1983. 55: p. 2333-2336.

[56].  Lee, S.-H., C.-S. Lee, D.-S. Shin, B.-G. Kim, Y.-S. Lee, and Y.-K. Kim, *Micro protein Patterning Using Lift-off Process with Fluorocarbon Thin Film.* Sensors and Actuators B Chemical, 2004. 99: p. 623-632.

[57].  MacBeath, G. and S.L. Schreiber, *Printing Proteins as Microarrays for High-Throughput Function Determination.* Science, 2000. 289: p. 1760-1763.

[58].  Kenna, J.G., G.N. Major, and R.S. Williams, *Methods for Reducing Non-specific Antibody Binding in Enzyme-Linked Immunosorbent Assays.* Journal of Immunological Methods, 1985. 85: p. 409-419.

[59].  Robert F. Vogt, J., D.L. Phillips, L.O. Henderson, W. Whitfield, and F.W. Spierto, *Quantitative Differences Among Various Proteins as Blocking Agents for ELISA Microtiter Plates.* Journal of Immunological Methods, 1987. 101: p. 43-50.

147

[60]. Schonheyder, H. and P. Anderson, *Effects of Bovine Serum Albumin on Antibody Determination by Enzyme -Linked Immunosorbent Assay.* Journal of Immunological Methods, 1984. 72: p. 251-259.

[61]. Dahint, R., R.R. Seigel, P. Harder, M. Grunze, and F. Josse, *Detection of Non-specific Protein Adsorption at Artificial Surfaces by the Use of Acoustic Plate Mode Sensors.* Sensors and Actuators B Chemical, 1996. 35-36: p. 497-505.

[62]. Cooper, M.A., F.N. Dultsev, T. Minson, V.P. Ostanin, C. Abell, and D. Klenerman, *Direct and Sensitive Detection of Human Virus by Rupture Event Scanning.* Nature Biotechnology, 2001. 19: p. 833-837.

[63]. Cooper, M.A., *Biosensing Using Rupture Event Scanning (REVS)$^{TM}$.* Measurement Science and Technology, 2003. 14: p. 1888-1893.

[64]. Cuypers, P.A., J.W. Corsel, M.P. Janssen, J.M.M. Kop, W.T. Hermens, and H.C. Hemker, *The Adsorption of Prothrombin to Phosphatidylserine Multilayers Quantitated by Ellipsometry.* The Journal of Biological Chemistry, 1983. 258(4): p. 2426-2431.

[65]. Vogel, A.I., W.T. Cresswell, and J. Leicester, *Bond Refractions for Tin, Silicon, Lead, Germanium, and Mercury Compounds.* Journal of Physical Chemistry, 1953. 58: p. 174-177.

[66]. Arwin, H., *Optical Properties of Thin Layers of Bovine Serum Albumin, γ-Globulin, and Hemoglobin.* Applied Spectroscopy, 1986. 40(3): p. 313-318.

[67]. Carrasco, B., J. Garcia de la Torre, K.G. Davis, S. Jones, D. Athwal, C. Walters, D.R. Burton, and S.E. Harding, *Crystallohydrodynamics for Solving the Hydration Problem for Multi-domain Proteins: Open Physiological Conformations for Human IgG.* Biophysical Chemistry, 2001. 93: p. 181-196.

[68]. Stevens, M.J., *Thoughts on the Structure of Alkylsilane Monolayers.* Langmuir, 1999. 15: p. 2772-2778.

[69]. Tamarin, O., S. Comeau, C. Dejous, D. Moynet, D. Rebiere, J. Bezian, and J. Pistre, *Real Time Device for Biosensing: Design of a Bacteriophage Model Using Love Acoustic Waves.* Biosensors & Bioelectronics, 2003. 18: p. 755-763.

[70]. Bender, F., K. Lange, A. Voigt, and M. Rapp, *Improvement of Surface Acoustic Wave Gas and Biosensor Response Characteristics Using a Capacitive Coupling Technique.* Analytical Chemistry, 2004. 76(13): p. 3837-3840.

[71]. Barie, N., T. Wessa, M. Bruns, and M. Rapp, *Love Waves in SiO$_2$ Layers on STW-resonators Based on LiTaO$_3$.* Talanta, 2004. 62: p. 71-79.

[72]. Gizeli, E., C.R. Lowe, M. Liley, and H. Vogel, *Detection of Supported Lipid Layers with the Acoustic Love Waveguide Device: Application to Biosensors.* Sensors and Actuators B, 1996. 34: p. 295-300.

[73]. Wang, Z., J.D.N. Cheeke, and C.K. Jen, *Sensitivity Analysis for Love Mode Acoustic Gravimetric Sensors.* Applied Physics Letters, 1994. 64(22): p. 2940-2942.

[74]. Brandrup, J. and E.H. Immergut, eds. *Polymer Handbook.* 3$^{rd}$ ed. 1989, John Wiley & Sons, Inc.: New York.

[75]. van Kooten, T.G., H.T. Spijker, and H.J. Busscher, *Plasma-treated Polystyrene Surfaces: Model Surfaces for Studying Cell-biomaterial Interactions.* Biomaterials, 2004. 25(10): p. 1735-1747.

[76]. Hunsinger, B.J., N. Gloudemans, and J. Rowe. *Low Resolution Weighted Tap Transducers with Reflection and Diffraction Suppression.* in *IEEE Ultrasonics Symposium.* 1975: IEEE.

[77]. DeVries, A.J., T. Sreenivasan, S. Subramanian, and T.J. Wojcik. *Detailed Description of a Commercial Surface-wave TV IF Filters.* in *IEEE Ultrasonics Symposium.* 1974: IEEE.

[78]. Mader, W.R., C. Ruppel, and E. Ehrmann-Falkenau. *Universal Method for Compensation of SAW Diffraction and Other Second Order Effects.* in *IEEE Ultrasonics Sypmosium.* 1982: IEEE.

[79]. Sittig, E.K. and G.A. Coquin, *Filters and Dispersive Delay Lines Using Repetitively Mismatched Ultrasonic Transmission Lines.* IEEE Transactions on Sonics and Ultrasonics, 1968. su-15(2): p. 111-119.

[80].    Hodé, J.M., J. Desbois, P. Dufilié, M. Solal, and P. Ventura. *SPUDT-Based Filters: Design Principles and Optimization*. in *IEEE Ultrasonics Symposium*. 1995: IEEE.

[81].    Jones, W.S., C.S. Hartmann, and T.D. Sturdivant, *Second Order Effects in Surface Wave Devices*. IEEE Transactions on Sonics and Ultrasonics, 1972. su-19(3): p. 368-384.

[82].    Hartmann, C.S., P.V. Wright, R.J. Kansy, and E.M. Garber. *An Analysis of SAW Interdigital Transducers with Internal Reflections and the Application to the Design of Single-phase Unidirectional Transducers*. in *IEEE Ultrasonics Symposium*. 1982: IEEE.

[83].    Hartmann, C.S. and B.P. Abbott. *Overview of Design Challenges for Single Phase Unidirectional SAW Filters*. in *IEEE Ultrasonics Symposium*. 1989: IEEE.

[84].    Bristol, T.W., W.R. Jones, P.B. Snow, and W.R. Smith. *Application of Double Electrodes in Acoustic Surface Wave Device Design*. in *IEEE Ultrasonics Symposium*. 1972: IEEE.

[85].    Darby, B.J., P.M. Grant, and J.H. Collins. *High Performance Communication Modems Incorporating Surface Acoustic Wave*. in *IEEE Ultrasonics Symposium*. 1973: IEEE.

[86].    Hanma, K. and B.J. Hunsinger. *A Triple Transit Suppression Technique*. in *IEEE Ultrasonics Symposium*. 1974: IEEE.

[87].    Ippolito, S.J., K. Kalantar-Zadeh, D.A. Powell, and W. Wlodarski. *A 3-dimensional Finite Element Approach for Simulating Acoustic Wave Propagation in Layered SAW Devices*. in *IEEE Ultrasonics Symposium*. 2003: IEEE.

[88].    Ippolito, S.J., K. Kalantar-zadeh, D.A. Powell, and W. Wlodarski. *A Finite Element Approach for 3-dimensional Simulation of Layered Acoustic Wave Transducers*. in *Optoelectronic and Microelectronic Materials and Devices*. 2002: IEEE.

[89].    Atashbar, M.Z., K. Kalantar-zadeh, S.J. Ippolitto, and W. Wlodarski. *3-D Finite-Element Simulation Model of SAW Palladium Thin Film Hydrogen Sensor*. in

*IEEE International Ultrasonics, Ferroelectronics, and Frequency Control Joint 50$^{th}$ Anniversary Conference*. 2004: IEEE.


[90].   Lerch, R., *Simulation of Piezoelectric Devices by Two- and Three-dimensional Finite Elements.* IEEE Transactions on Ultrasonics, Ferroelectrics and Frequency Control, 1990. 37(3): p. 233-247.


[91].   Xu, G. *Finite Element Analysis of Second Order Effects on the Frequency Response of a SAW Device*. in *IEEE Ultrasonics Symposium*. 2000: IEEE.


[92].   Sankaranarayanan, K.R.S.S., V.R. Bhethanabotla, and B. Joseph. *3-D Finite Element Model of Surface Acoustic Wave (SAW) Sensor Response*. in *Acoustic Wave Based Sensors and Sensor Systems*. 2006: Electrochemical Society.


[93].   Rösler, U., D. Cohrs, A. Dietz, F. G., W. Ruile, P. Russer, and R. Weigel. *Determination of Leaky SAW Propagation, Reflection and Coupling on LiTaO$_3$*. in *IEEE Ultrasonics Symposium*. 1995: IEEE.


[94].   Laricchia-Robbio, L. and R.P. Rivoltella, *Comparison Between the Surface Plasmon Resonance (SPR) and the Quartz Crystal Microbalance (QCM) Method in a Structural Analysis of Human Endothelin-1*. Biosensors & Bioelectronics, 2004. 19: p. 1753-1758.


[95].   Martin, F., M.I. Newton, G. McHale, K.A. Melzak, and E. Gizeli, *Pulse Mode Shear Horizontal Surface Acoustic Wave (SH-SAW) System for Liquid Based Sensing Applications*. Biosensors & Bioelectronics, 2004. 19: p. 627-632.


[96].   Zhang, B., Q. Mao, X. Zhang, T. Jiang, M. Chen, F. Yu, and W. Fu, *A Novel Piezoelectric Quartz Micro-array Immunosensor Based on Self-assembeld Monolayer for Determination of Human Chorionic Gonadotropin*. Biosensors & Bioelectronics, 2004. 19: p. 711-720.


[97].   Di Natale, C., A. Macagnano, E. Martinelli, R. Paolessee, G. D'Arcangelo, C. Roscioni, A. Finazzi-Agro, and A. D'Amico, *Lung Cancer Identification by the Analysis of Breath by Means of an Array of Non-selective Gas Snsors*. Biosensors & Bioelectronics, 2003. 18: p. 1209-1218.


[98].   Lim, D.V., *Detection of Microorganisms and Toxins with Evanescent Wave, Fiber Optic Biosensors*. Proceedings of the IEEE, 2003. 91: p. 902-907.

[99].   DeMarco, D.R. and D.V. Lim, *Detection of Escherichia Coli O157:H7 in 10- and 25-gram Ground Beef Samples Using an Evanescent Wave Biosensor with Silica and Polystyrene Waveguides.* Journal of Food Protection, 2002. 65: p. 596-602.

[100].  Cui, Y., Q. Wei, H. Park, and C.M. Lieber, *Nanowire Nanosensors for Highly Sensitive and Selective Detection of Biological and Chemical Species.* Science, 2001. 293 (5533): p. 1289-1292.

[101].  Josse, F.J., F. Bender, and R.W. Cernosek, *Guided Shear Horizontal Surface Acoustic Wave Sensors for Chemical and Biochemical Detection in Liquids.* Analytical Chemistry, 2001. 73: p. 5937-5944.

[102].  Grate, J.W., S.N. Kaganove, and V.R. Bhethanabotla, *Comparison of Polymer/Gas Partition Coefficients Calculated from Responses of Thickness Shear Mode and Surface Acoustic Wave Vapor Sensors.* Analytical Chemistry, 1998. 70: p. 199-203.

[103].  Wohltjen, H. and R. Dessy, *Surface Acoustic Wave Probe for Chemical Analysis. I. Introduction and Instrumentation Description.* Analytical Chemistry, 1979. 51(9): p. 1458-1464.

[104].  Wohltjen, H. and R. Dessy, *Surface Acoustic Wave Probes for Chemical Analysis. II. Gas Chromatography.* Analytical Chemistry, 1979. 51(9): p. 1465-1470.

[105].  Cular, S., V.R. Bhethanabotla, D.W. Branch, and J.A. Strom. *Hexagonal SAW Interleukin-6 Biosensor.* in *AIChE Annual Meeting.* 2007. Salt Lake City, Utah.

[106].  Roma, A., S. Cular, and V.R. Bhethanabotla. *SH-SAW Biosensors.* in *USF REU Symposium.* 2006. Tampa, FL, USA.

[107].  Branch, D.W. and S.M. Brozik, *Low-level Detection of a Bacillus Anthracis Simulant Using Love-wave Biosensors on $36^o$ YX LiTaO$_3$.* Biosensors & Bioelectronics, 2004. 19: p. 849-859.

[108].  Gizeli, E., F. Bender, A. Rasmusson, K. Saha, F.J. Josse, and R.W. Cernosek, *Sensitivity of the Acoustic Waveguide Biosenor to Protein Binding as a Function of the Waveguide Properties.* Biosensors & Bioelectronics, 2003. 18: p. 1399-1406.

[109]. Schickfus, M.v., W. Welsch, M. Weib, and S. Hunklinger, *Biosensing with Surface Acoustic Wave Devices*, Institut fur Angewandte Physik. p. 1-5.

[110]. Cular, S., S.K.R.S. Sankaranarayanan, V.R. Bhethanabotla, and D.W. Branch, *Interdigitated Transducer Design for Biosensor Applications Requiring Love-wave Surface Acoustic Waves.* IEEE Transactions on Ultrasonics, Ferroelectrics, and Frequency Control -- In preparation, 2007.

[111]. Branch, D.W. and S.M. Borzik, *Low-level Detection of a Bacillus anthracis Simulant Using Love-wave Biosensors on 36 deg YX LiTaO3.* Biosensors & Bioelectronics, 2004. 19: p. 849-859.

[112]. Kovacs, G., M. Anhorn, H.E. Engan, G. Visintini, and C.C.W. Ruppel. *Improved Material Constants for LiNbO$_3$ and LiTaO$_3$.* in *IEEE Ultrasonics Symposium.* 1990: IEEE.

[113]. Claridge, J.A., A.M. Schulman, and J.S. Young, *Improved Resuscitation Minimizes Respiratory Dysfunction and Blunts Interleukin-6 and Nuclear Factor-κB Activation after Traumatic Hemorrhage.* Critical Care Medicine, 2002. 30(8): p. 1815-1819.

[114]. Remick, D.G., G.R. Bolgos, S. Copeland, and J. Siddiqui, *Role of Interleukin-6 in Mortality from and Physiologic Response to Sepsis.* Infection and Immunity, 2005. 73(5): p. 2751-2757.

[115]. Brundage, S.I., N.A. Sautke, J.B. Holcomb, D.A. Spain, J.C. Lam, M.A. Mastrangelo, J.M. Macaitis, and D.J. Tweardy, *Interleukin-6 Infusion Blunts Proinflammatory Cytokine Production Without Causing Systematic Toxicity in a Swine Model of Uncontrolled Hemorrhagic Shock.* The Journal of Trauma, 2004. 57: p. 970-979.

[116]. Remick, D.G., G.R. Bolgos, J. Siddiqui, J. Shin, and J.A. Nemzek, *Six at Six: Interleukin-6 Measured 6 H After the Initiation of Sepsis Predicts Mortality Over 3 Days.* Shock, 2002. 17(6): p. 463-467.

[117]. Simpson, R.J., A. Hammacher, D.K. Smith, J.M. Matthews, and L.D. Ward, *Review: Interleukin-6: Structure-function Relationships.* Protein Science, 1997. 6: p. 929-955.

[118]. Hensler, T., S. Sauerland, B. Bouillon, M. Raum, D. Rixen, H.-J. Helling, J. Andermahr, and E.A.M. Neugebauer, *Association Between Injury Pattern of Patients with Multiple Injuries and Circulating Levels of Soluble Tumor Necrosis Factor Receptors, Interleukin-6 and Interleukin-10, and Polymorphonuclear Neutrophil Elastase.* The Journal of Trauma, 2002. 52: p. 962-970.

[119]. Morgan, D.P., *Surface-Wave Devices for Signal Processing*. Studies in Electrical and Electronic Engineering 19. 1991, New York: Elsevier.

[120]. Chaudhari, A., D. Srinivasagupta, S. Cular, V.R. Bhethanabotla, and B. Joseph. *Surface Acoustic Wave Sensors Using Nanocrystalline Palladium for Hydrogen Gas Detection.* in *AIChE Annual Meeting*. 2004. Austin, Texas.

[121]. Cunha, M.P.d., D.C. Malocha, D.W. Puccio, J. Thiele, and T.B. Pollard, *LGX Pure Shear Horizontal SAW for Liquid Sensor Applications.* IEEE Sensors Journal, 2003. 3(5): p. 554 – 561.

[122]. Kovacs, G., M.J. Vellekoop, R. Haueis, G.W. Lubking, and A. Venema, *A Love Wave Sensor for (Bio)chemical Sensing in Liquids.* Sensors and Actuators A Mechanical, 1994. 43(1-3): p. 38-43.

[123]. Humphryes, R.F. and E.A. Ash, *Acoustic Bulk-Surface-Wave Transducer.* Electronic Letters, 1969. 5(9): p. 175-176.

[124]. Chen, D.-p., J. Melngailis, and H.A. Haus. *Filters Based on Conversion of Surface Acoustic Waves to Bulk Plate Modes in Gratings*. in *1982 IEEE Ultrasonics Symposium*. 1982: IEEE.

[125]. Lobo, N. and D.C. Malocha. *Novel Dual Mode SAW-BAW Device*. in *IEEE Ultrasonics Symposium*. 2006. Vancouver, BC, Canada: IEEE.

[126]. Hartl, A., E. Schmich, J.A. Garrido, J. Hernando, S.C.R. Catharino, S. Walter, P. Feulner, A. Kromka, D. Steinmuller, and M. Stutzmann, *Protein-modified Nanocrystalline Diamond Thin Films for Biosensor Applications.* Nature Materials, 2004. 3: p. 735-742.

[127]. Hartl, A., S. Nowy, J. Hernando, J.A. Garrido, and M. Stutzmann, *Bio-interfacing of Diamond Films for Sensor Applications.* IEEE, 2005: p. 496-499.

[128]. Siew, P.S., K.P. Loh, W.C. Poh, and H. Zhang, *Biosensing Properties of Nanocrystalline Diamond Electrodes.* Diamond & Related Materials, 2005. 14: p. 426-431.

[129]. Birrell, J., J.E. Gerbi, O. Auciello, J.M. Gibson, D.M. Gruen, and J.A. Carlisle, *Bonding Structure in Nitrogen Doped Ultrananocrystalline Diamond.* Journal of Applied Physics, 2003. 93(9): p. 5606-5612.

[130]. Huang, T.S., Y. Tzeng, Y.K. Liu, Y.C. Chen, K.R. Walker, R. Guntupalli, and C. Liu, *Immobilization of Antibodies and Bacterial Binding on Nanodiamond and Carbon Nanotubes for Biosensor Applications.* Diamond & Related Materials, 2004. 13: p. 1098-1102.

[131]. Matrab, T., M.M. Chehimi, J.P. Boudou, F. Benedic, J. Wang, N.N. Naguib, and J.A. Carlisle, *Surface Functionalization of Ultrananocrystalline Diamond Using Atom Transfer Radical Polymerization (ATRP) Initiated by Electro-grafted Aryldiazonium.* Diamond & Related Materials, 2006. 15: p. 639-644.

[132]. Kondoh, J., S. Shiokawa, M. Rapp, and S. Stier, *Simulation of Viscoelastic effects of Polymer Coatings on Surface Acoustic Wave Gas Sensor under Consideration of Film Thickness.* Japanese Journal of Applied Physics, 1998. 37: p. 2842-2848.

[133]. Li, Z., *Guided Shear-Horizontal Surface Acoustic Wave (SH-SAW) Chemical Sensors for Detection of Organic Contaminants in Aqueous Environments.* 2005, Marquette University: Milwaukee.

Appendices

Appendix A Acoustic Wave Theory

Through out the literature [1, 25, 132, 133] there are a number of variations in nomenclature and coordinate definitions for this reason all derivations have been standardized to conform to a single notation. Figure 49 illustrates the motion of the Rayleigh (Figure 47a) and shear-horizontal waves typically found in SAW sensors. A pure shear wave either horizontal (Figure 47b) or a shear-vertical wave (not illustrated) have only have a particle motion in one direction, for example, the SH wave's particle motion is parallel to the x-axis. Rayleigh waves are distinguished from a shear wave in that the particle motion is elliptical having both a shear vertical and a longitudinal mode. Following the coordinate system in Figure 49 the motion is both in the z- and y-directions for the Rayleigh SAW.



(a)                                        (b)
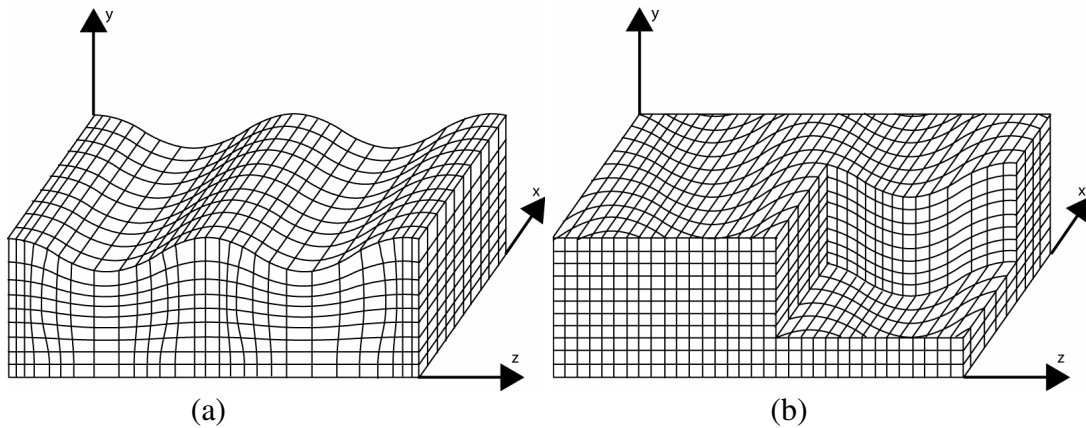
Figure 47  Illustration of Rayleigh (left) and shear-horizontal (right) waves.

Appendix A (Continued)

By following the general perturbation theory given in literature [25], the surface impedance of a SAW can be found from:

$$Z_i = -\frac{\beta_i^f M_i^f}{\omega}\left(\frac{A-B}{A+B}\right) = \frac{\beta_i^f M_i^f}{\omega}\tanh\left(j\beta_i^f h\right) \qquad (A.1)$$

where the variables in the equations are solely physical properties of the materials. Various films and liquid can be coated onto the SAW to make small changes in the propagating wave's properties. Such changes can be recorded and analyzed through the surface impedance when considered as a complex propagation represented by:

$$\frac{\Delta\gamma}{k_0} = \frac{\Delta\alpha}{k_0} - j\frac{\Delta v}{v_0} = \sum_{i=1}^{3} c_i Z_i \qquad (A.2)$$
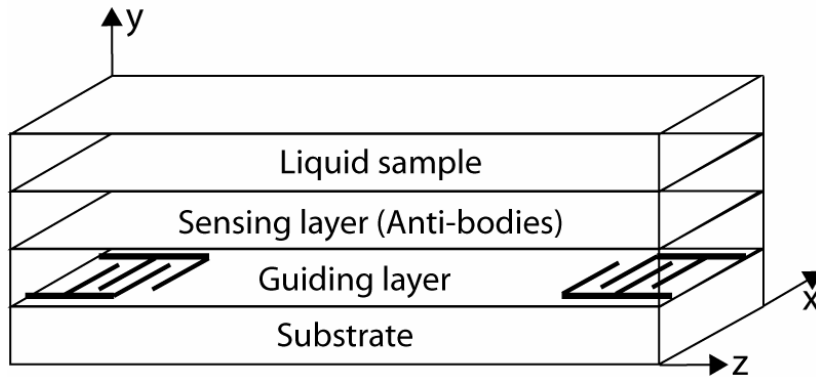


Figure 48  Four layer model diagram of SAW device needed for biological sensing applications in liquid samples while utilizing a guiding layer for enhanced sensitivity.
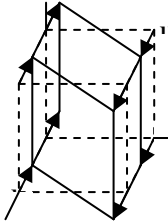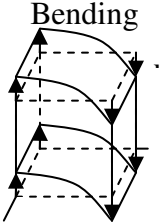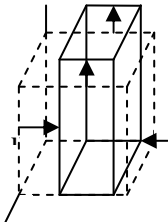
Appendix A (Continued)

This model can be more beneficial than just analyzing the behavior of a SAW device. Built into the model is are material properties such as the Lamé, bulk and shear moduli, that can be extract through further mathematical derivations based on the displacements associated with the different wave modes. A generalized table is given below for an acoustically thin film on a Rayleigh wave device as an example. The definitions of the displacement motions are illustrated in Table 8 as well. This shows the changes in the wave propagation are a result of the changes of the waves in all directions, for the case of a Rayleigh wave this is limited to y- and z-direction motion plane. For shear-horizontal wave, the motion is further limited to the x-direction [1, 132, 133].

Appendix A (Continued)

Table 8  Moduli associated with strain modes generated by SAW  (acoustically thin

film (R<<1) => E(2)≈0)

| Strain mode | Displacement gradient | Modulus definition | In terms of $\lambda$ and $\mu$ | In terms of G and K |
|---|---|---|---|---|
| Transverse shear  | $\dfrac{\partial u_x}{\partial z}$ | $E^{(1)} = \dfrac{T_{13}}{2S_{13}}$ | $\mu$ | G |
| Bending  | $\dfrac{\partial u_y}{\partial z}$ | $E^{(2)} = \dfrac{T_{23}}{2S_{23}}$ | $\dfrac{6\pi\mu(\mu+\lambda)}{14\mu+\lambda}\left(\dfrac{h}{\Lambda}\right)^2$ $\approx 0$ | $\dfrac{2\pi G(G+3K)}{3(4G+K)}\left(\dfrac{h}{\Lambda}\right)^2$ $\approx 0$ |
| Longitudinal compression  | $\dfrac{\partial u_z}{\partial z}$ | $E^{(3)} = \dfrac{T_{33}}{S_{33}}$ | $\dfrac{4\mu(\lambda+\mu)}{\lambda+2\mu}$ | $\dfrac{4G(3K+G)}{3K+4G}$ |

Within the confines of this project, the perturbation model is developed from

the basic SAW device through a four layer device as shown in Figure 48.  From the

substrate up for the biomarker detector the layers are a piezoelectric substrate, an

insulating guiding layer, an analyte specific layer, and finally the carrier fluid of the

analyte.  The model for such a system becomes cumbersome; however, the surface

Appendix A (Continued)

impedance of the differing films remains a function of just the physical properties of

the materials.   One assumption that has been made to simplify the solution was

considering the liquid layer as a solid to avoid the use of the Navier-Stokes equation.

The thought behind this simplification is the liquid flow rate and volume of liquid are

very small as well as being constant.   The complex propagation can thus be

represented as:

$$
\frac{\Delta\gamma}{k_0} = \frac{\Delta\alpha}{k_0} - j\frac{\Delta v}{v_0} = \sum_{i=1}^{3} c_i \left( Z_i^f + Z_i^l \right)
$$

$$
\frac{\Delta\gamma}{k_0} = \sum_{i=1}^{3} c_i \left( \left( \frac{\beta_i^{f_2} M_i^{f_2}}{\omega} \frac{A_2 - B_2}{A_1 + B_1} \right) + \left( \frac{j\beta_i^{f_2} M_i^{f_2}}{\omega} \frac{A_{2l} - B_{2l}}{A_{1l} + B_{1l}} \right) \right)
$$

(A.3)

where the values of the $A$'s and $B$'s are:

$$
A_1 = u_{i0}^{f_1} - (R_1 - R_3)\left( R_1 u_{i0}^{f_1} - \frac{2M_i^{f_1}\beta_i^{f_1} u_{i0}^{f_1}(R_1 R_3 - R_3 R_2)}{M_i^{f_1}\beta_i^{f_1}(R_1 + R_2 + R_3 + R_4) + \beta_i^{f_2} M_i^{f_2}(R_1 - R_2 - R_3 + R_4)} \right)
$$

$$
B_1 = (R_1 - R_3)\left( R_1 u_{i0} - \frac{2M_i^{f_1}\beta_i^{f_1} u_{i0}^{f_1}(R_1 R_3 - R_3 R_2)}{M_1\beta_i^{f_1}(R_1 + R_2 + R_3 + R_4) + \beta_i^{f_2} M_2(R_1 - R_2 - R_3 + R_4)} \right)
$$

$$
A_2 = \left( \begin{array}{l} (R_1 - R_3)\left( R_1 u_{i0} - \dfrac{2M_i^{f_1}\beta_i^{f_1} u_{i0}^{f_1}(R_1 R_3 - R_3 R_2)}{M_i^{f_1}\beta_i^{f_1}(R_1 + R_2 + R_3 + R_4) + \beta_i^{f_2} M_i^{f_2}(R_1 - R_2 - R_3 + R_4)} \right) \\ \left( -e^{j\beta_i^{f_1} h_1} e^{-j\beta_i^{f_1} h_1} \right) \end{array} \right) +
$$

$$
e^{j\beta_i^{f_1} h_1} u_{i0} - \frac{2M_i^{f_1}\beta_i^{f_1} u_{i0}^{f_1} R_3 e^{j\beta_i^{f_1}}}{M_i^{f_1}\beta_i^{f_1}(R_1 + R_2 + R_3 + R_4) + \beta_i^{f_2} M_i^{f_2}(R_1 - R_2 - R_3 + R_4)}
$$

$$
B_2 = \frac{2M_i^{f_1}\beta_i^{f_1} u_{i0}^{f_1} R_3 e^{j\beta_i^{f_1}}}{M_i^{f_1}\beta_i^{f_1}(R_1 + R_2 + R_3 + R_4) + \beta_i^{f_2} M_i^{f_2}(R_1 - R_2 - R_3 + R_4)}
$$

161

Appendix A (Continued)

$$B_{2l} = \cfrac{1}{R_1T_2 - R_3T_2 + R_1T_1 + R_3T_1 - R_2T_1 - R_4T_1 + R_2T_2 - R_4T_2}$$

$$\left( 2R_1 u_{i0}^{f_1} T_1 e^{-j\beta_i^{f_1} h_1} + \cfrac{\left( \begin{array}{c} 4jT_2 R_1 u_{i0} T_1\, R_4\left(T_1 - T_2\right) e^{j\beta_i^{f_1} h_1} + \\ 4jT_2 R_1 u_{i0} T_1\, R_4\left(T_1 + T_2\right) e^{-j\beta_i^{f_1} h_1} \end{array} \right)}{\left( \begin{array}{c} R_1\left(-jT_2^2 - jT_1T_2 + M_i^{f_1} T_2\right) + R_2\left(jT_2^2 - T_1 M_i^{f_1} + jT_1T_2 + T_2 M_i^{f_1}\right) \\ + R_3\left(jT_2^2 T_1 M_i^{f_1} + jT_1T_2 - T_2 M_i^{f_1}\right) + R_4\left(jT_2^2 + jT_1T_2 - T_2 M_i^{f_1}\right) \end{array} \right)} \right)$$

$$B_{1l} = \cfrac{\left(T_1 - T_2 e^{j\beta_i^{f_1} h_1} u_{i0}\right) 2T_2 B_{2l}}{T_1 e^{j\beta_i^{f_1} h_1} + T_1 e^{-j\beta_i^{f_1} h_1} - T_2 e^{j\beta_i^{f_1} h_1} + T_2 e^{-j\beta_i^{f_1} h_1}}$$

$$A_{2l} = \left( u_{i0}^{f_1} - \left( \cfrac{\left(T_1 - T_2 e^{j\beta_i^{f_1} h_1} u_{i0}\right) 2T_2 B_{2l}}{T_1 e^{j\beta_i^{f_1} h_1} + T_1 e^{-j\beta_i^{f_1} h_1} - T_2 e^{j\beta_i^{f_1} h_1} + T_2 e^{-j\beta_i^{f_1} h_1}} \right) \right) e^{j\beta_i^{f_1} h_1}$$

$$+ \left( \cfrac{\left(T_1 - T_2 e^{j\beta_i^{f_1} h_1} u_{i0}\right) 2T_2 B_{2l}^2}{T_1 e^{j\beta_i^{f_1} h_1} + T_1 e^{-j\beta_i^{f_1} h_1} - T_2 e^{j\beta_i^{f_1} h_1} + T_2 e^{-j\beta_i^{f_1} h_1}} \right) e^{-j\beta_i^{f_1} h_1}$$

$$A_{1l} = u_{i0}^{f_1} - \left( \cfrac{\left(T_1 - T_2 e^{j\beta_i^{f_1} h_1} u_{i0}\right) 2T_2 B_{2l}}{T_1 e^{j\beta_i^{f_1} h_1} + T_1 e^{-j\beta_i^{f_1} h_1} - T_2 e^{j\beta_i^{f_1} h_1} + T_2 e^{-j\beta_i^{f_1} h_1}} \right)$$

and

$$R_1 = e^{j\beta_i^{f_1} h_1}\, e^{-j\beta_i^{f_2}(h_1 - h_2)}$$

$$R_2 = e^{j\beta_i^{f_1} h_1}\, e^{j\beta_i^{f_2}(h_1 - h_2)}$$

$$R_3 = e^{-j\beta_i^{f_1} h_1}\, e^{-j\beta_i^{f_2}(h_1 - h_2)}$$

$$R_4 = e^{-j\beta_i^{f_1} h_1}\, e^{j\beta_i^{f_2}(h_1 - h_2)}$$

$$T_1 = \beta_i^{f_1} M_i^{f_1}$$

$$T_2 = \beta_i^{f_2} M_i^{f_2}$$

The first portion of the derivation is general for all waves. Following the generalized derivation, conditions will be applied to constrain the waves to Rayleigh

Appendix A (Continued)

and pure shear-horizontal waves independently. To begin this derivation the equation

of motion is known to be:

$$\nabla \cdot T = \rho \frac{\partial v}{\partial t} \tag{A.4}$$

from which the following expansions are known:

$$\frac{\partial T_{xx}}{\partial x} + \frac{\partial T_{yx}}{\partial y} + \frac{\partial T_{zx}}{\partial z} = \frac{\partial}{\partial t} \rho v_x$$

$$\frac{\partial T_{xy}}{\partial x} + \frac{\partial T_{yy}}{\partial y} + \frac{\partial T_{zy}}{\partial z} = \frac{\partial}{\partial t} \rho v_y \tag{A.5}$$

$$\frac{\partial T_{xz}}{\partial x} + \frac{\partial T_{yz}}{\partial y} + \frac{\partial T_{zz}}{\partial z} = \frac{\partial}{\partial t} \rho v_z$$

Appendix A.1.1 Isotropic Film

For an isotropic film, modifications to these equations can be done where:

$$\frac{\partial}{\partial t} = j\omega \tag{A.6}$$

In plane displacement gradients can be considered as follows:

Appendix A (Continued)

$$[T_{ij}] = \begin{bmatrix} T_{xx} & T_{xy} & T_{xz} \\ T_{yx} & T_{yy} & T_{yz} \\ T_{zx} & T_{zy} & T_{zz} \end{bmatrix} = \begin{bmatrix} \dfrac{T_{xx}}{S_{xx}}\dfrac{\partial u_x}{\partial x} & \dfrac{1}{2}\dfrac{T_{xy}}{S_{xy}}\dfrac{\partial u_x}{\partial y} & \dfrac{1}{2}\dfrac{T_{xz}}{S_{xz}}\dfrac{\partial u_x}{\partial z} \\ \dfrac{1}{2}\dfrac{T_{yx}}{S_{yx}}\dfrac{\partial u_y}{\partial x} & \dfrac{T_{yy}}{S_{yy}}\dfrac{\partial u_y}{\partial y} & \dfrac{1}{2}\dfrac{T_{yz}}{S_{yz}}\dfrac{\partial u_y}{\partial z} \\ \dfrac{1}{2}\dfrac{T_{zz}}{S_{zz}}\dfrac{\partial u_z}{\partial x} & \dfrac{1}{2}\dfrac{T_{zy}}{S_{zy}}\dfrac{\partial u_z}{\partial y} & \dfrac{T_{zz}}{S_{zz}}\dfrac{\partial u_z}{\partial z} \end{bmatrix} \tag{A.7}$$

Cross film displacement gradients can then be defined:

$$[T_{ij}] = \begin{bmatrix} T_{xx} & T_{xy} & T_{xz} \\ T_{yx} & T_{yy} & T_{yz} \\ T_{zx} & T_{zy} & T_{zz} \end{bmatrix} = \begin{bmatrix} K\dfrac{\partial u_x}{\partial x} & G\dfrac{\partial u_x}{\partial y} & G\dfrac{\partial u_x}{\partial z} \\ G\dfrac{\partial u_y}{\partial x} & K\dfrac{\partial u_y}{\partial y} & G\dfrac{\partial u_y}{\partial z} \\ G\dfrac{\partial u_z}{\partial x} & G\dfrac{\partial u_z}{\partial y} & K\dfrac{\partial u_z}{\partial z} \end{bmatrix} \tag{A.8}$$

where $G$ and $K$ are the shear and bulk modulus of the material that are complex numbers whose real portions represent the storage moduli and the imaginary portions represent the loss moduli as shown below:

$$\begin{aligned} K &= K' + jK'' \\ G &= G' + jG'' \end{aligned} \tag{A.9}$$

Additionally, stress and strain are related through the following equations utilizing the material moduli:

Considering the relationships between the stress ($T$) and strain ($S$):

164

Appendix A (Continued)

$$T_{ij} = \lambda(S_{11} + S_{22} + S_{33}) + 2\mu S_{ij} \quad \text{(for i=j)} \tag{A.10}$$

$$T_{ij} = \mu \cdot \frac{S_{ij}}{2} \quad \text{(for } i \neq j) \tag{A.11}$$

where $\lambda$ and $\mu$ are the Lamé constants. Similar relations can be given using the bulk

($K$) and shear ($G$) moduli using the following equations:

$$\lambda = K - \frac{2}{3}G$$
$$\mu = G \tag{A.12}$$

Substituting the displacement gradients into the continuity equation a set of three

dimensional wave equations are found,

$$\frac{T_{xx}}{S_{xx}}\frac{\partial^2 u_x}{\partial x^2} + \frac{1}{2}\frac{T_{yx}}{S_{yx}}\frac{\partial^2 u_y}{\partial y^2} + \frac{1}{2}\frac{T_{zx}}{S_{zx}}\frac{\partial^2 u_z}{\partial z^2} = \frac{\partial}{\partial t}\rho v_x$$

$$\frac{1}{2}\frac{T_{xy}}{S_{xy}}\frac{\partial^2 u_x}{\partial x^2} + \frac{T_{yy}}{S_{yy}}\frac{\partial^2 u_y}{\partial y^2} + \frac{1}{2}\frac{T_{zy}}{S_{zy}}\frac{\partial^2 u_z}{\partial z^2} = \frac{\partial}{\partial t}\rho v_y \tag{A.13}$$

$$\frac{1}{2}\frac{T_{xz}}{S_{xz}}\frac{\partial^2 u_x}{\partial x^2} + \frac{1}{2}\frac{T_{yz}}{S_{yz}}\frac{\partial^2 u_y}{\partial y^2} + \frac{T_{zz}}{S_{zz}}\frac{\partial^2 u_z}{\partial z^2} = \frac{\partial}{\partial t}\rho v_z$$

Into this set of wave equations, the harmonic solution $\vec{u} = \hat{u}(d)e^{j(\omega t - kz)}$ is substituted,

where d is the distance across the film, $\hat{u}(d)$ is the cross-film displacement, $\omega$ is the

angular frequency ($\omega = 2\pi f$), and $k$ is the SAW wave number ($k = 2\pi / \Lambda = \omega / v_o$).

Appendix A (Continued)

$$\frac{T_{xx}}{S_{xx}}\frac{\partial^2 u_x}{\partial x^2} + \frac{1}{2}\frac{T_{yx}}{S_{yx}}\frac{\partial^2 u_y}{\partial y^2} = \rho\omega^2\vec{u} - \frac{1}{2}\frac{T_{zx}}{S_{zx}}k^2\vec{u}$$

$$\frac{1}{2}\frac{T_{xy}}{S_{xy}}\frac{\partial^2 u_x}{\partial x^2} + \frac{T_{yy}}{S_{yy}}\frac{\partial^2 u_y}{\partial y^2} = \rho\omega^2\vec{u} - \frac{1}{2}\frac{T_{zy}}{S_{zy}}k^2\vec{u} \qquad (A.14)$$

$$\frac{1}{2}\frac{T_{xz}}{S_{xz}}\frac{\partial^2 u_x}{\partial x^2} + \frac{1}{2}\frac{T_{yz}}{S_{yz}}\frac{\partial^2 u_y}{\partial y^2} = \rho\omega^2\vec{u} - \frac{T_{zz}}{S_{zz}}k^2\vec{u}$$

Appendix A.1.2 Wave Propagation Limited to Z-direction

At this point the derivation will be constrained to a wave propagating in the z-direction implying, motion in the z-direction is longitudinal and in the x- and y-directions is lateral or shear. These equations can be further simplified by assuming the displacements in a particular direction are zero. In the case of a Rayleigh wave, the displacement in the x-direction is zero thus, $\frac{\partial u_x}{\partial x} = 0$.

$$0 + \frac{1}{2}\frac{T_{yx}}{S_{yx}}\frac{\partial^2 u_y}{\partial y^2} = \rho\omega^2\vec{u} - \frac{1}{2}\frac{T_{zx}}{S_{zx}}k^2\vec{u}$$

$$0 + \frac{T_{yy}}{S_{yy}}\frac{\partial^2 u_y}{\partial y^2} = \rho\omega^2\vec{u} - \frac{1}{2}\frac{T_{zy}}{S_{zy}}k^2\vec{u} \qquad (A.15)$$

$$0 + \frac{1}{2}\frac{T_{yz}}{S_{yz}}\frac{\partial^2 u_y}{\partial y^2} = \rho\omega^2\vec{u} - \frac{T_{zz}}{S_{zz}}k^2\vec{u}$$

166

Appendix A (Continued)

In the case of a shear-horizontal wave, displacements only occur in the x-direction

thus,

$$\frac{\partial u_y}{\partial y} = \frac{\partial u_z}{\partial z} = 0 \tag{A.16}$$

$$\frac{T_{xx}}{S_{xx}} \frac{\partial^2 u_x}{\partial x^2} + 0 = \rho\omega^2 \vec{u} - 0$$

$$\frac{1}{2} \frac{T_{xy}}{S_{xy}} \frac{\partial^2 u_x}{\partial x^2} + 0 = \rho\omega^2 \vec{u} - 0 \tag{A.17}$$

$$\frac{1}{2} \frac{T_{xz}}{S_{xz}} \frac{\partial^2 u_x}{\partial x^2} + 0 = \rho\omega^2 \vec{u} - 0$$

For a Rayleigh SAW coated with a film:

Rearranging the equations yields the displacement profile:

$$u_i(y) = A^f \cdot \sin\left(j\beta_i^f \cdot y\right) + B^f \cdot \cos\left(-j\beta_i^f \cdot y\right) \tag{A.18}$$

where the superscript $f$ indicates variables associated with the film.

The general solution for the displacement profile is:

$$u_i(y) = A^f \cdot \sin\left(j\beta_i^f \cdot y\right) + B^f \cdot \cos\left(-j\beta_i^f \cdot y\right) \tag{A.19}$$

in other terms,

Appendix A (Continued)

$$u_i(y) = A^f \cdot e^{j\beta_i^f y} + B^f \cdot e^{-j\beta_i^f y} \tag{A.20}$$

In order to solve for the constants $A$ and $B$ two boundary conditions needed. The first condition infers the displacements from the crystal into the film are uniform. $u_{i0} = 0^+$ Therefore, $u_{i0} = A^f + B^f$. The second boundary condition is that the film/air interface is stress free. $T_{iy}(h) = 0$. Therefore, $0 = A_0^f e^{j\beta_i^f h} + B^f e^{-j\beta_i^f h}$. Simultaneously solving these boundary conditions,

$$A^f = \frac{u_{i0} e^{-j\beta_i^f h}}{e^{j\beta_i^f h} + e^{-j\beta_i^f h}}$$

$$B^f = \frac{u_{i0} e^{j\beta_i^f h}}{e^{j\beta_i^f h} + e^{-j\beta_i^f h}} \tag{A.21}$$

By substituting $A$ and $B$ into the original equation, and applying the definition of a hyperbolic cosine:

$$u_i(y) = u_{io} \frac{\cosh\left(j\beta_i^f(y-h)\right)}{\cosh\left(j\beta_i^f h\right)} \quad for \ \ 0 \le y \le h \tag{A.22}$$

Now, considering the mechanical surface impedance given for each displacement is described by:

$$Z_i^f = \frac{T_{iy}}{v_i}\bigg|_{y=0} \tag{A.23}$$

168

Appendix A (Continued)

The cross-film gradients give the interfacial shear stress:

$$T_{iy}(0) = \begin{vmatrix} \dfrac{1}{2}\dfrac{T_{xy}}{S_{xy}}\dfrac{\partial u_x}{\partial y} \\[1ex] \dfrac{T_{yy}}{S_{yy}}\dfrac{\partial u_y}{\partial y} \\[1ex] \dfrac{1}{2}\dfrac{T_{zy}}{S_{zy}}\dfrac{\partial u_z}{\partial y} \end{vmatrix}_{y=0} = j\left(A^f - B^f\right)\beta_i^f M_i^f \qquad (A.24)$$

where $M_i^f$ represents the stress gradients of the film.

This leads to the interfacial particle velocity:

$$v_i(0) = \dot{u}_i(0) = j\omega u_i(0) = j\omega u_i\left(A^f + B^f\right) \qquad (A.25)$$

Substituting back,

$$Z_i = -\frac{\beta_i^f M_i^f}{\omega}\left(\frac{A^f - B^f}{A^f + B^f}\right) = \frac{\beta_i^f M_i^f}{\omega}\tanh\left(j\beta_i^f h\right) \qquad (A.26)$$

Finally, the perturbation in SAW propagation arising from changes in film changes can be determined:

$$\frac{\Delta\gamma}{k_0} = \frac{\Delta\alpha}{k_0} - j\frac{\Delta v}{v_0} = \sum_{i=1}^{3} c_i Z_i \qquad (A.27)$$

where $c_i$ is a the SAW film coupling parameter

Appendix A (Continued)
Appendix A.1.3 Liquid loading of the film on the Rayleigh device

Consideration of the film is that it is isotropic non-piezoelectric. For liquid layers, this assumption is carried through as opposed to using the Navier-Stokes relation as during the experiments, the liquid flow rate is very small. With this in mind, the liquid layer in essence is being considered as a solid semi-infinite layer. Therefore the wave equation is follows the same method and close to the same equations as the above derivation.

To begin derivation of the effects of a liquid layer on the SAW, the wave equation is:

$$u_i^l(y) = C_l e^{-\beta_i^l(y-h)}$$
$$\beta_i^l = \frac{1+j}{\delta^l}$$
$$\delta^l = \sqrt{\frac{2\eta^l}{\omega\rho^l}}$$

(A.28)

where $\delta^l$ is the decay length into the liquid, $\eta^l$ is the viscosity of the liquid, and $\rho^l$ is the density of the liquid. Note that the $l$ indicates the liquid layer.

The stress of the liquid layer is represented the same as the film solved previously with the exception of the notation to indicate the layer is indeed liquid. From this point, the mathematics are the same and will not be repeated up to the first difference involving boundary conditions. The boundary conditions in which there are three (1) continuity of particle displacement at the substrate/film interface, (2)

Appendix A (Continued)

continuity of stress as the substrate/film interface, and (3) the film/liquid interface at $y$

$= h$ can be solved straightforward. These can be represented as:

$$u_i^f(0) = u_{i0}$$
$$u_i^f(h) = u_i^l(h) \quad\quad\quad\text{(A.29)}$$
$$T_{iy}^f(h) = T_{iy}^l(h)$$

The boundary conditions lead to three equations with three unknowns:

$$u_{i0} = A^l + B^l$$
$$C^l = A^l e^{j\beta_i^l h} + B^l e^{-j\beta_i^l h} \quad\quad\quad\text{(A.30)}$$
$$M_i^f j\beta^f \left(A^l e^{j\beta h} - B^l e^{-j\beta h}\right) = M_i^l \left(-\beta_i^l C^l\right)$$

Solving for the three unknowns in terms of the layer properties:

$$A^l = \frac{u_{i0} e^{-j\beta_i^f h}\left(jM_i^f \beta_i^f - M_i^l \beta_i^l\right)}{jM_i^f \beta_i^f e^{j\beta_i^f h} + jM_i^f \beta_i^f e^{-j\beta_i^f h} + M_i^l \beta_i^l e^{j\beta_i^l h} - M_i^l \beta_i^l e^{-j\beta_i^l h}}$$

$$B^l = \frac{u_{i0} e^{j\beta_i^f h}\left(jM_i^f \beta_i^f + M_i^l \beta_i^l\right)}{jM_i^f \beta_i^f e^{j\beta_i^f h} + jM_i^f \beta_i^f e^{-j\beta_i^f h} + M_i^l \beta_i^l e^{j\beta_i^l h} - M_i^l \beta_i^l e^{-j\beta_i^l h}} \quad\quad\quad\text{(A.31)}$$

$$C^l = \frac{2u_{i0} M_i^f \beta_i^f}{jM_i^f \beta_i^f e^{j\beta_i^f h} + jM_i^f \beta_i^f e^{-j\beta_i^f h} + M_i^l \beta_i^l e^{j\beta_i^l h} - M_i^l \beta_i^l e^{-j\beta_i^l h}}$$

Appendix A (Continued)

By applying $A^l$ and $B^l$ to the surface mechanical impedance equation from the

derivation involving just the film:

$$
Z_i^f = -\frac{\beta_i^f M_i^f}{\omega}\left(\frac{A^l - B^l}{A^l + B^l}\right) =
$$

$$
-\frac{\beta_i^f M_i^f}{\omega}\left(\frac{e^{-j\beta_i^f h}\left(jM_i^f\beta_i^f - M_i^l\beta_i^l\right) - e^{j\beta_i^f h}\left(jM_i^f\beta_i^f + M_i^l\beta_i^l\right)}{jM_i^f\beta_i^f e^{j\beta_i^f h} + jM_i^f\beta_i^f e^{-j\beta_i^f h} + M_i^l\beta_i^l e^{j\beta_i^l h} - M_i^l\beta_i^l e^{-j\beta_i^l h}}\right)
$$

(A.32)

Finally, by combining the mechanical impedance perturbations from the film and the

liquid into the complex propagating factor,

$$
\frac{\Delta\gamma}{k_0} = \frac{\Delta\alpha}{k_0} - j\frac{\Delta v}{v_0} = \sum_{i=1}^{3} c_i\left(Z_i^f + Z_i^l\right)
$$

$$
\frac{\Delta\gamma}{k_0} = \sum_{i=1}^{3} c_i \left( \begin{array}{l} \dfrac{\beta_i^f M_i^f}{\omega}\tanh\left(j\beta_i^f h\right) - \\[2mm] \dfrac{\beta_i^f M_i^f}{\omega}\left(\dfrac{e^{-j\beta_i^f h}\left(jM_i^f\beta_i^f - M_i^l\beta_i^l\right) - e^{j\beta_i^f h}\left(jM_i^f\beta_i^f + M_i^l\beta_i^l\right)}{jM_i^f\beta_i^f e^{j\beta_i^f h} + jM_i^f\beta_i^f e^{-j\beta_i^f h} + M_i^l\beta_i^l e^{j\beta_i^l h} - M_i^l\beta_i^l e^{-j\beta_i^l h}}\right) \end{array} \right)
$$

(A.33)

Appendix A.1.4 Liquid loading of the film on the Shear-horizontal device

The previous derivation can be applied to shear-horizontal SAW's through

analogy. Since the Rayleigh wave is a composite wave motion consisting of both a

shear and longitudinal components, all that needs to be done is rotate the reference

172

Appendix A (Continued)

coordinate system and negate the longitudinal component of motion. This results in

the following complex propagating factor:

$$\frac{\Delta\gamma}{k_0} = c_x \left( \begin{array}{c} \dfrac{\beta_x^f M_x^f}{\omega} \tanh\!\left(j\beta_x^f h\right) \\[2mm] -\dfrac{\beta_x^f M_x^f}{\omega}\left( \dfrac{e^{-j\beta_x^f h}\left(jM_x^f \beta_x^f - M_x^l \beta_x^l\right) - e^{j\beta_x^f h}\left(jM_x^f \beta_x^f + M_x^l \beta_x^l\right)}{jM_x^f \beta_x^f e^{j\beta_x^f h} + jM_x^f \beta_x^f e^{-j\beta_x^f h} + M_x^l \beta_x^l e^{j\beta_{xi}^l h} - M_x^l \beta_x^l e^{-j\beta_x^l h}}\right) \end{array}\right)$$

(A.34)

Appendix A.1.5 Liquid Loading on the Shear-horizontal Device

One variation that is of some interest is the film on the shear-horizontal SAW

is removed so that it is only exposed to a liquid. Within the terms of the equations,

this means $h = 0$:

$$\frac{\Delta\gamma}{k_0} = c_x \left( -\frac{\beta_x^l M_x^l}{\omega} \right)$$

(A.35)

Appendix A.1.6 Air Loading of the Film on the Shear-horizontal Device

A second variation of the solution for a shear-horizontal SAW is when the

device is coated with a film, the left in a vacuum or even air. This scenario implies

there are no stress gradients exiting the film making $M^l = 0$; under these conditions,

the resulting complex propagation equation is analogous to the one for a Rayleigh,

173

Appendix A (Continued)
with a rotation of the coordinate system with limiting the displacements to only one

shearing motion.

$$\frac{\Delta\gamma}{k_0} = c_x \left( \frac{\beta_x^f M_x^f}{\omega} \tanh\left(j\beta_x^f h\right) \right) \tag{A.36}$$

Appendix A.1.7 Four layers for Biomarker Detection

With the above derivations, it is possible to do some preliminary work with

the shear-horizontal SAW sensor. For example polymer sorption experiments with

first layer as the polymer and the analyte in low concentration in the fluid layer.

Within the scope of this work, an additional layer is needed. From the substrate up

for the biomarker detector the layers are a piezoelectric substrate, an insulating

guiding layer, an analyte specific layer, and finally the carrier fluid of the analyte.

These layers are schematically drawn in Figure 49 and the model will be derived
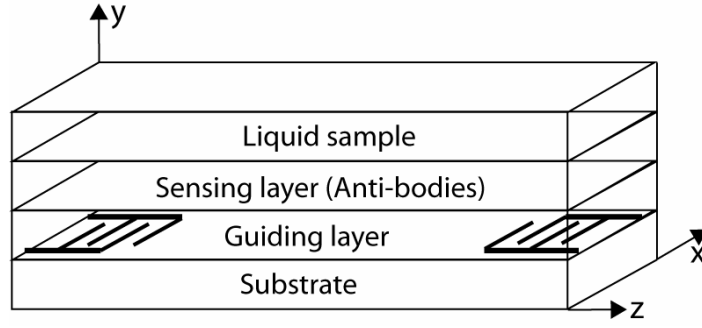
below.

Appendix A (Continued)



Figure 49   Layer model diagram of SAW device needed for biological sensing applications in liquid samples while utilizing a guiding layer for enhanced sensitivity.

The general solution for the displacement profiles in the four layer model is given by:

$$u_i^{f_1}(y) = A_1 e^{j\beta_i^{f_1} y} + B_1 e^{-j\beta_i^{f_1} y}$$
$$u_i^{f_2}(y) = A_2 e^{j\beta_i^{f_2}(y-h_1)} + B_2 e^{-j\beta_i^{f_2}(y-h_1)}$$

(A.37)

The four boundary conditions for the solution of the displacement equations are:

$$at \quad y=0 \quad u_i^{f_1}(0) = u_{i0}$$

$$at \quad y=h_1 \quad u_i^{f_1}(h_1) = u_i^{f_2}(h_1)$$

$$T_{iy}^{f_1}(h_1) = T_{iy}^{f_2}(h_1)$$

(A.38)

$$at \quad y=h_2 \quad T_{iy}^{f_2}(h_2) = 0$$

Appendix A (Continued)
From the four boundary conditions, four equations are developed:

$$u_{i0}^{f_1} = A_1 + B_1$$

$$A_1 e^{j\beta_i^{f_1} h_1} + B_1 e^{-j\beta_i^{f_1} h_1} = A_2 + B_2$$

$$M_i^{f_1} j\beta_i^1 \left( A_1 e^{j\beta_i^{f_1} h_1} + B_1 e^{-j\beta_i^{f_1} h_1} \right) = j\beta_i^{f_2} M_i^{f_2} (A_2 - B_2)$$  (A.39)

$$A_2 e^{j\beta_i^{f_2}(h_2 - h_1)} - B_2 e^{-j\beta_i^{f_2}(h_2 - h_1)} = 0$$

Solving for the constants,

$$A_1 = u_{i0}^{f_1} - (R_1 - R_3) \left( \begin{array}{c} R_1 u_{i0}^{f_1} \\ -\dfrac{2M_i^{f_1}\beta_i^{f_1} u_{i0}^{f_1}(R_1 R_3 - R_3 R_2)}{M_i^{f_1}\beta_i^{f_1}(R_1 + R_2 + R_3 + R_4) + \beta_i^{f_2} M_i^{f_2}(R_1 - R_2 - R_3 + R_4)} \end{array} \right)$$

$$B_1 = (R_1 - R_3) \left( \begin{array}{c} R_1 u_{i0} \\ -\dfrac{2M_i^{f_1}\beta_i^{f_1} u_{i0}^{f_1}(R_1 R_3 - R_3 R_2)}{M_1\beta_i^{f_1}(R_1 + R_2 + R_3 + R_4) + \beta_i^{f_2} M_2(R_1 - R_2 - R_3 + R_4)} \end{array} \right)$$

$$A_2 = \left( \begin{array}{c} (R_1 - R_3) \left( \begin{array}{c} R_1 u_{i0} \\ -\dfrac{2M_i^{f_1}\beta_i^{f_1} u_{i0}^{f_1}(R_1 R_3 - R_3 R_2)}{M_i^{f_1}\beta_i^{f_1}(R_1 + R_2 + R_3 + R_4) + \beta_i^{f_2} M_i^{f_2}(R_1 - R_2 - R_3 + R_4)} \end{array} \right) \\ \left( -e^{j\beta_i^{f_1} h_1} e^{-j\beta_i^{f_1} h_1} \right) \end{array} \right) +$$  (A.40)

$$e^{j\beta_i^{f_1} h_1} u_{i0} - \dfrac{2M_i^{f_1}\beta_i^{f_1} u_{i0}^{f_1} R_3 e^{j\beta_i^{f_1}}}{M_i^{f_1}\beta_i^{f_1}(R_1 + R_2 + R_3 + R_4) + \beta_i^{f_2} M_i^{f_2}(R_1 - R_2 - R_3 + R_4)}$$

$$B_2 = \dfrac{2M_i^{f_1}\beta_i^{f_1} u_{i0}^{f_1} R_3 e^{j\beta_i^{f_1}}}{M_i^{f_1}\beta_i^{f_1}(R_1 + R_2 + R_3 + R_4) + \beta_i^{f_2} M_i^{f_2}(R_1 - R_2 - R_3 + R_4)}$$

Appendix A (Continued)
where

$$R_1 = e^{j\beta_i^{f_1} h_1} e^{-j\beta_i^{f_2}(h_1-h_2)}$$
$$R_2 = e^{j\beta_i^{f_1} h_1} e^{j\beta_i^{f_2}(h_1-h_2)}$$
$$R_3 = e^{-j\beta_i^{f_1} h_1} e^{-j\beta_i^{f_2}(h_1-h_2)}$$
$$R_4 = e^{-j\beta_i^{f_1} h_1} e^{j\beta_i^{f_2}(h_1-h_2)}$$

(A.41)

Following the surface impedance procedure given for the three layer model, the

surface impedance for the four layer geometry is found to be:

$$Z = \frac{j\beta_i^{f_2} M_i^{f_2}(A_2 - B_2)}{j\varpi(A_1 + B_1)}$$

$$Z = \frac{j\beta_i^{f_2} M_i^{f_2}}{j\varpi u_{i0}^{f_1}} \times$$

(A.42)

$$\left( \begin{array}{l} (R_1 - R_3)\left( R_1 u_{i0}^{f_1} - \dfrac{2M_i^{f_1}\beta_i^{f_1} u_{i0}^{f_1}(R_1 R_3 - R_3 R_2)}{M_i^{f_1}\beta_i^{f_1}(R_1 + R_2 + R_3 + R_4) + \beta_i^{f_2} M_i^{f_2}(R_1 - R_2 - R_3 + R_4)} \right) \\ \left( -e^{j\beta_i^{f_1} h_1} e^{-j\beta_i^{f_1} h_1} \right) \\ + e^{j\beta_i^{f_1} h_1} u_{i0}^{f_1} - \dfrac{4M_i^{f_1}\beta_i^{f_1} u_{i0}^{f_1} R_3 e^{j\beta_i^{f_1}}}{M_i^{f_1}\beta_i^{f_1}(R_1 + R_2 + R_3 + R_4) + \beta_i^{f_2} M_i^{f_2}(R_1 - R_2 - R_3 + R_4)} \end{array} \right)$$

Appendix A (Continued)

Appendix A.1.8 Liquid Loading of the Two Film Model

The only changes from the previous derivation to the current needed are changes the boundary conditions for the surface liquid boundary. For this case, the displacement and the stresses are considered to be continuous:

$$u_i^2(h_2) = u_i^3(h_2)$$
$$T_{iy}^2(h_2) = T_{iy}^3(h_2)$$

(A.43)

Applying all five of the boundary conditions, give rise to the following equations:

$$u_{i0l}^{f_1} = A_{1l} + B_{1l}$$

$$A_{1l}e^{j\beta_i^1 h_1} + B_{1l}e^{-j\beta_i^1 h_1} = A_{2l} + B_{2l}$$

$$M_i^{f_1} j\beta_i^{f_1}\left(A_{1l}e^{j\beta_i^{f_1} h_1} - B_{1l}e^{-j\beta_i^{f_1} h_1}\right) = j\beta_i^{f_2} M_i^{f_2}\left(A_{2l} - B_{2l}\right)$$

$$A_{2l}e^{j\beta_i^{f_2}(h_2-h_1)} + B_{2l}e^{-j\beta_i^{f_2}(h_2-h_1)} = C_l$$

$$j\beta_i^{f_2} M_i^{f_2}\left(A_{2l}e^{j\beta_i^{f_2}(h_2-h_1)} - B_{2l}e^{-j\beta_i^{f_2}(h_2-h_1)}\right) = M_i^l C_l$$

(A.44)

Appendix A (Continued)
Solving for the constants,

$$C_l = \frac{4jT_2R_1u_{i0}^{f_1}T_1R_4}{\left(\begin{array}{l}R_1\left(-jT_2^2 - jT_1T_2 + M_i^{f_1}T_2\right) + R_2\left(jT_2^2 - T_1M_i^{f_1} + jT_1T_2 + T_2M_i^{f_1}\right) \\ + R_3\left(jT_2^2T_1M_i^{f_1} + jT_1T_2 - T_2M_i^{f_1}\right) + R_4\left(jT_2^2 + jT_1T_2 - T_2M_i^{f_1}\right)\end{array}\right)}$$

$$B_{2l} = \frac{1}{R_1T_2 - R_3T_2 + R_1T_1 + R_3T_1 - R_2T_1 - R_4T_1 + R_2T_2 - R_4T_2}$$

$$\left(\begin{array}{l}2R_1u_{i0}^{f_1}T_1e^{-j\beta_i^{f_1}h_1} \\ \\ + \dfrac{\left(\begin{array}{l}4jT_2R_1u_{i0}T_1\ R_4\left(T_1 - T_2\right)e^{j\beta_i^{f_1}h_1} + \\ 4jT_2R_1u_{i0}T_1\ R_4\left(T_1 + T_2\right)e^{-j\beta_i^{f_1}h_1}\end{array}\right)}{\left(\begin{array}{l}R_1\left(-jT_2^2 - jT_1T_2 + M_i^{f_1}T_2\right) + R_2\left(jT_2^2 - T_1M_i^{f_1} + jT_1T_2 + T_2M_i^{f_1}\right) \\ + R_3\left(jT_2^2T_1M_i^{f_1} + jT_1T_2 - T_2M_i^{f_1}\right) + R_4\left(jT_2^2 + jT_1T_2 - T_2M_i^{f_1}\right)\end{array}\right)}\end{array}\right)$$

$$B_{1l} = \frac{\left(T_1 - T_2e^{j\beta_i^{f_1}h_1}\right)u_{i0}2T_2B_{2l}}{T_1e^{j\beta_i^{f_1}h_1} + T_1e^{-j\beta_i^{f_1}h_1} - T_2e^{j\beta_i^{f_1}h_1} + T_2e^{-j\beta_i^{f_1}h_1}}$$

$$A_{2l} = \left(u_{i0}^{f_1} - \left(\frac{\left(T_1 - T_2e^{j\beta_i^{f_1}h_1}\right)u_{i0}2T_2B_{2l}}{T_1e^{j\beta_i^{f_1}h_1} + T_1e^{-j\beta_i^{f_1}h_1} - T_2e^{j\beta_i^{f_1}h_1} + T_2e^{-j\beta_i^{f_1}h_1}}\right)\right)e^{j\beta_i^{f_1}h_1}$$

$$\qquad + \left(\frac{\left(T_1 - T_2e^{j\beta_i^{f_1}h_1}\right)u_{i0}2T_2B_{2l}^2}{T_1e^{j\beta_i^{f_1}h_1} + T_1e^{-j\beta_i^{f_1}h_1} - T_2e^{j\beta_i^{f_1}h_1} + T_2e^{-j\beta_i^{f_1}h_1}}\right)e^{-j\beta_i^{f_1}h_1}$$

$$A_{1l} = u_{i0}^{f_1} - \left(\frac{\left(T_1 - T_2e^{j\beta_i^{f_1}h_1}\right)u_{i0}2T_2B_{2l}}{T_1e^{j\beta_i^{f_1}h_1} + T_1e^{-j\beta_i^{f_1}h_1} - T_2e^{j\beta_i^{f_1}h_1} + T_2e^{-j\beta_i^{f_1}h_1}}\right) \qquad (A.45)$$

where

$$T_1 = \beta_i^{f_1}M_i^{f_1}$$
$$T_2 = \beta_i^{f_2}M_i^{f_2} \qquad (A.46)$$

Appendix A (Continued)

Following the surface impedance procedure given for the three layer model, the surface impedance for the four layer geometry is found to be the same as before with the constants solved for with the variation given for the liquid loading:

$$Z_l = \frac{j\beta_i^{f_2} M_i^{f_2}(A_{2l} - B_{2l})}{j\varpi(A_{1l} + B_{1l})} \tag{A.47}$$

Substituting back the complex propagation becomes:

$$\frac{\Delta\gamma}{k_0} = \frac{\Delta\alpha}{k_0} - j\frac{\Delta v}{v_0} = \sum_{i=1}^{3} c_i \left( Z_i^f + Z_i^l \right)$$

$$\frac{\Delta\gamma}{k_0} = \sum_{i=1}^{3} c_i \left( \left( \frac{\beta_i^{f_2} M_i^{f_2}}{\omega} \frac{A_2 - B_2}{A_1 + B_1} \right) + \left( \frac{\beta_i^{f_2} M_i^{f_2}}{\omega} \frac{A_{2l} - B_{2l}}{A_{1l} + B_{1l}} \right) \right) \tag{A.48}$$

Appendix A.1.9 Liquid Loading of the Film on the Shear-horizontal Device

Applying the above complex propagating factor to the shear-horizontal SAW:

$$\frac{\Delta\gamma}{k_0} = \sum_{i=1}^{1} c_i \left( \left( \frac{\beta_i^f M_i^f}{\omega} \frac{A_2 - B_2}{A_1 + B_1} \right) + \left( \frac{\beta_i^f M_i^f}{\omega} \frac{A_{2l} - B_{2l}}{A_{1l} + B_{1l}} \right) \right) \tag{A.49}$$

Appendix B Ansys Simulations Inputs

Many script files have been used for the studies presented in this dissertation. This appendix is merely a compilation of sample scripts for the different aspects involved with simulation an acoustic wave device. The commands given here were developed with Ansys versions 8 through 11. Note there are small deviations for the different versions for the commands, and deviations also arise from using the software on different operation systems, *i.e.* Solaris and Windows. Much of this work has been adapted from the work of Subramanian K. R. S. Sankaranarayanan.

Appendix B.1 Piezoelectric Material Data

The material data used in these simulations can be found in many sources then rotated accordingly for the appropriate cut angles. Throughout the data, SI units have been used, but in some instances particular Ansys units have been utilized. The material data matrices given in the following sections have been converted to an IEEE format that Ansys uses.

Appendix B (Continued)

First, the full 6 x 3 piezoelectric matrix relative terms x, y, z, xy, yz, xz

to x, y, z via 18 constants as shown:


e11 e12 e13

e21 e22 e23

e31 e32 e33

e41 e42 e43

e51 e52 e53

e61 e62 e63


The full 6 x 6 elastic coefficient matrix [D] relates terms ordered x,

y, z, xy, yz, xz via 21 constants as shown below:


C1-C6Terms D11, D21, D31, D41, D51, D61

C7-C12Terms D22, D32, D42, D52, D62, D33

C13-C18Terms D43, D53, D63, D44, D54, D64

C19-C21Terms D55, D65, D66


Appendix B.1.1 36° YX LiTaO3

```
/COM,ANSYS RELEASE   10.0
/NOP
/COM,Internal UNITS set at file creation time = SI    (MKS)
TBDEL,ALL,_MATL
```

Appendix B (Continued)

```
MPDEL,ALL,_MATL


MPTEMP,R5.0, 1, 1,  0.00000000    ,
MPDATA,R5.0, 1,ALPX,_MATL   , 1,  23.0000000    ,
MPTEMP,R5.0, 1, 1,  0.00000000    ,
MPDATA,R5.0, 1,DENS,_MATL   , 1,  7450.00000    ,
MPTEMP,R5.0, 1, 1,  0.00000000    ,
MPDATA,R5.0, 1,PERX,_MATL   , 1, 3.641000000E-10,
MPTEMP,R5.0, 1, 1,  0.00000000    ,
MPDATA,R5.0, 1,PERY,_MATL   , 1, 3.796000000E-10,
MPTEMP,R5.0, 1, 1,  0.00000000    ,
MPDATA,R5.0, 1,PERZ,_MATL   , 1, 3.633000000E-10,
MPTEMP,R5.0, 1, 1,  0.00000000    ,
MPDATA,R5.0, 1,SONC,_MATL   , 1,  4160.10000    ,


TB,PIEZ,_MATL   ,,,   0
TBDAT,  1,  1.4147        ,  -0.4271       ,    1.4487
TBDAT,  4,  -0.6449       ,   2.0329       ,   -0.3232
TBDAT,  7,  -0.3039       ,   0.2214       ,   -0.8920
TBDAT, 10,   2.0732       ,  -0.0073       ,   -0.4340
TBDAT, 13,  -0.4340       ,  -0.0036       ,    2.7216
TBDAT, 16,   1.7683       ,  -0.4340       ,    0.3337


TB,ANEL,_MATL    ,   1,,   0
TBTEM,  0.00000000    ,   1
TBDAT,   1, 2.315200000E+11, 0.7447200000E+11, 0.492400000E+11
TBDAT,   4,-0.044400000E+11, 0.0591000000E+11, 0.051800000E+11
TBDAT,   7, 2.737900000E+11, 0.8110000000E+11, 0.028900000E+11
TBDAT,  10, 0.014500000E+11,-0.0444000000E+11, 2.284600000E+11
TBDAT,  13, 0.025300000E+11,-0.0687000000E+11,-0.031300000E+11
TBDAT,  16, 0.935900000E+11,-0.0307000000E+11, 0.094100000E+11
TBDAT,  19, 0.981900000E+11,-0.0136000000E+11, 0.928300000E+11
/GO
/NOP
/GO
```

```
/NOP
/COM,Internal UNITS set at file creation time = SI   (MKS)
TBDEL,ALL,_MATL
MPDEL,ALL,_MATL


MPTEMP,R5.0, 1, 1,  0.00000000    ,
MPDATA,R5.0, 1,DENS,_MATL   , 1,  2675.00000    ,
MPTEMP,R5.0, 1, 1,  0.00000000    ,
MPDATA,R5.0, 1,PERX,_MATL   , 1, 4.43,
MPTEMP,R5.0, 1, 1,  0.00000000    ,
MPDATA,R5.0, 1,PERY,_MATL   , 1, 4.43,
MPTEMP,R5.0, 1, 1,  0.00000000    ,
MPDATA,R5.0, 1,PERZ,_MATL   , 1, 4.63,


TB,PIEZ,_MATL   ,,,   0
TBDAT,   1,  0.17100000   ,  0.00000000   , 0.000000000
TBDAT,   4, -0.01870000   ,  0.00000000   , 0.000000000
TBDAT,   7, -0.15200000   ,  0.00000000   , 0.000000000
TBDAT,  10,  0.00000000   , -0.07610000   , 0.067000000
TBDAT,  13,  0.06700000   ,  0.00000000   , 0.000000000
TBDAT,  16,  0.00000000   ,  0.06700000   ,-0.095000000


TB,ANEL,_MATL    ,   1,,   0
TBTEM,  0.00000000    ,   1
TBDAT,   1, 86.74e9, 27.15e9, -8.25e9
TBDAT,   4, 0,  -3.66e9,  0.00000000
TBDAT,   7, 102.83e9, -7.42e9,0
TBDAT,  10,  9.92e9,  0.00000000    , 129.77e9
TBDAT,  13,  0,  5.70,  0.00000000
TBDAT,  16, 68.81e9,  0.00000000    ,  2.53e9
TBDAT,  19, 38.61e9, 0.000000, 29.01e9
/GO
/NOP
/GO
```

Appendix B (Continued)
Appendix B.2 SAW Configuration

Common to all simulations described in this dissertation is the general SAW

configuration. This consists of a substrate rectangular solid divided into multiple

pieces and a polymer rectangular solid. Minor variations of the mesh density were

necessary for some of the simulations. These variations were necessary were

considering advanced IDT and delay path designs.

Appendix B.2.1 Common SAW Configuration

```
/COM ! Set graphic options.

/PNUM,KP,0
/PNUM,LINE,1
/PNUM,AREA,1
/PNUM,VOLU,0
/PNUM,NODE,0
/PNUM,TABN,0
/PNUM,SVAL,0
/NUMBER,0
!*
/PNUM,ELEM,0
/REPLOT
/PREP7
!*
ET,1,SOLID98
!*
KEYOPT,1,1,3
KEYOPT,1,3,0
KEYOPT,1,5,0
```

```
MAT,1,
MPREAD,'MATLAB_LiTaO3','SI_MPL','',LIB
MPLIST,1
TBLIST,ALL,1
ET,2,SOLID98
KEYOPT,2,1,3
KEYOPT,2,3,0
KEYOPT,2,5,0
!*
!*
MP,EX,2,3400e6      ! POLYMER MODULUS OF ELASTICITY
MP,NUXY,2,.33    ! POLYMER POISSON RATIO
MP,DENS,2,1110   ! POLYMER DENSITY


*SET,Substrate_Height , 200e-6
*SET,Substrate_Length , 1600e-6
*SET,Substrate_Depth  , 200e-6


*SET,POLYMER_Height ,  0.500e-6
*SET,POLYMER_Length , 800.0e-6
*SET,POLYMER_Depth  , 150e-6


*SET,IDT_Width , 10e-6
*SET,IDT_Length , 75e-6
*SET,IDT_Z , 0e-6
*SET,IDT_Offset , 120e-6


BLOCK, -Substrate_Length / 2, Substrate_Length / 2, -
Substrate_Depth / 2, Substrate_Depth / 2, -Substrate_Height,
0e-6


BLOCK,-POLYMER_Length/2 , POLYMER_Length/2,-
POLYMER_Depth/2,POLYMER_Depth/2,0e-6,POLYMER_Height
ALLSEL
VGLUE,ALL
```

Appendix B (Continued)

```
/VIEW,  1, 0.601671205170, -0.757983672401, 0.251897823021

/DIST,  1,  0.388832652656E-03

/ANG,   1,  -89.0496187725

/REPLO


LDIV,18,,,2,0

LDIV,6,,,2,0

LDIV,20,,,2,0

LDIV,8,,,2,0


LDIV,17,,,2,0

LDIV,5,,,2,0

LDIV,7,,,2,0

LDIV,19,,,2,0


LDIV,1,,,2,0

LDIV,2,,,2,0

LDIV,3,,,2,0

LDIV,4,,,2,0


LDIV,13,,,2,0

LDIV,14,,,2,0

LDIV,15,,,2,0

LDIV,16,,,2,0


/COM ! POLYMER LAYER DIVISION


LSEL,S,LINE,,20

LSEL,A,LINE,,18

LSEL,A,LINE,,15

LSEL,A,LINE,,13

CM,_Y1,LINE

CMSEL,,_Y1

LESIZE,_Y1, , ,40,0.2, , , ,0


LSEL,NONE
```

```
LSEL,S,LINE,,19

LSEL,A,LINE,,14

LSEL,A,LINE,,17

LSEL,A,LINE,,16

CM,_Y1,LINE

CMSEL,,_Y1

LESIZE,_Y1, , ,40,0.2, , , ,0


LSEL,NONE

LSEL,S,LINE,,29

LSEL,A,LINE,,25

LSEL,A,LINE,,39

LSEL,A,LINE,,40

CM,_Y1,LINE

CMSEL,,_Y1

LESIZE,_Y1, , ,40,5, , , ,0


LSEL,NONE

LSEL,S,LINE,,32

LSEL,A,LINE,,38

LSEL,A,LINE,,27

LSEL,A,LINE,,37

CM,_Y1,LINE

CMSEL,,_Y1

LESIZE,_Y1, , ,40,5, , , ,0


/COM PIEZO TOP SURFACE


LSEL,NONE

LSEL,S,LINE,,5

LSEL,A,LINE,,7

CM,_Y1,LINE

CMSEL,,_Y1

LESIZE,_Y1, , ,60,0.2, , , ,0


LSEL,NONE
```

```
LSEL,S,LINE,,6

LSEL,A,LINE,,8

CM,_Y1,LINE

CMSEL,,_Y1

LESIZE,_Y1, , ,45,0.2, , , ,0


LSEL,NONE

LSEL,S,LINE,,28

LSEL,A,LINE,,26

CM,_Y1,LINE

CMSEL,,_Y1

LESIZE,_Y1, , ,45,5, , , ,0


LSEL,NONE

LSEL,S,LINE,,30

LSEL,A,LINE,,31

CM,_Y1,LINE

CMSEL,,_Y1

LESIZE,_Y1, , ,60,5, , , ,0


! BOT

LSEL,NONE

LSEL,S,LINE,,3

LSEL,A,LINE,,1

CM,_Y1,LINE

CMSEL,,_Y1

LESIZE,_Y1, , ,20,0.4, , , ,0


LSEL,NONE

LSEL,S,LINE,,2

LSEL,A,LINE,,4

CM,_Y1,LINE

CMSEL,,_Y1

LESIZE,_Y1, , ,20,0.4, , , ,0


LSEL,NONE
```

189

Appendix B (Continued)

```
LSEL,S,LINE,,34

LSEL,A,LINE,,36

CM,_Y1,LINE

CMSEL,,_Y1

LESIZE,_Y1, , ,20,2.5, , , ,0


LSEL,NONE

LSEL,S,LINE,,33

LSEL,A,LINE,,35

CM,_Y1,LINE

CMSEL,,_Y1

LESIZE,_Y1, , ,20,2.5, , , ,0


LSEL,NONE

LSEL,S,LINE,,10

LSEL,A,LINE,,11

CM,_Y1,LINE

CMSEL,,_Y1

LESIZE,_Y1, , ,20,0.2, , , ,0


LSEL,NONE

LSEL,S,LINE,,9

LSEL,A,LINE,,12

CM,_Y1,LINE

CMSEL,,_Y1

LESIZE,_Y1, , ,20,5.0, , , ,0


!LSEL,NONE

!LSEL,S,LINE,,21

!LSEL,A,LINE,,24

!CM,_Y1,LINE

!CMSEL,,_Y1

!LESIZE,_Y1, , ,4,, , , , ,0


!LSEL,NONE

!LSEL,S,LINE,,22
```

190

Appendix B (Continued)

```
!LSEL,A,LINE,,23
!CM,_Y1,LINE
!CMSEL,,_Y1
!LESIZE,_Y1, , ,4,, , , ,0


ALLSEL


!*
CM,_Y,VOLU
VSEL, , , ,         3
CM,_Y1,VOLU
CMSEL,S,_Y
!*
CMSEL,S,_Y1
VATT,         1, ,   1,         0
CMSEL,S,_Y
CMDELE,_Y
CMDELE,_Y1
!*
M,_Y,VOLU
VSEL, , , ,         2
CM,_Y1,VOLU
CMSEL,S,_Y
!*
CMSEL,S,_Y1
VATT,         2, ,   2,         0
CMSEL,S,_Y
CMDELE,_Y
CMDELE,_Y1
!*
ALLSEL
MSHK,0
VMESH,ALL
```

Appendix B (Continued)
Appendix B.2.2 λ/4 Non-filled Resonant Cavity Design


Although similar to the generalized SAW model, the resonant cavity work described in the body of this dissertation has enough differences to warrant the addition of this section. Primary to the differences is the addition of the resonant cavities.

```
/PNUM,KP,0
/PNUM,LINE,1
/PNUM,AREA,1
/PNUM,VOLU,0
/PNUM,NODE,0
/PNUM,TABN,0
/PNUM,SVAL,0
/NUMBER,0
!*
/PNUM,ELEM,0
/REPLOT
/PREP7
!*
ET,1,SOLID98
!*
KEYOPT,1,1,3
KEYOPT,1,3,0
KEYOPT,1,5,0
MAT,1,
MPREAD,'MATLAB_LiTaO3','SI_MPL','',LIB
MPLIST,1
TBLIST,ALL,1
MP,EX,2,3400e6          ! POLYMER MODULUS OF ELASTICITY
MP,NUXY,2,.33              ! POLYMER POISSON RATIO
MP,DENS,2,1110            ! POLYMER DENSITY
```

```
MP,EX,3,82.737e9           ! IDT MODULUS OF ELASTICITY  (Pa)

MP,NUXY,3,.44                    ! IDT POISSON RATIO

MP,DENS,3,19300                  ! IDT DENSITY (kg/m3)

MP,SONC,3,2030                   ! IDT Sonic Velocity (m/s)


*SET,Cav_depth , -10e-6


*SET,Substrate_Height , 200e-6

*SET,Substrate_Length , 1600e-6

*SET,Substrate_Depth  , 200e-6

*SET,POLYMER_Height ,  0e-6

*SET,POLYMER_Length , 800.0e-6

*SET,POLYMER_Depth  , 150e-6

*SET,IDT_Width , 10e-6

*SET,IDT_Length , 80e-6

*SET,IDT_Z , 0e-6

*SET,IDT_Height , 1.0e-6

*SET,IDT_Offset , 120e-6


BLOCK, -Substrate_Length / 2, Substrate_Length / 2, -
Substrate_Depth / 2, Substrate_Depth / 2, -Substrate_Height,
0e-6


/COM ! Resonant cavities
BLOCK,15e-6,5e-6,-5e-6,5e-6,0,Cav_depth
BLOCK,35e-6,25e-6,-5e-6,5e-6,0,Cav_depth
BLOCK,-5e-6,-15e-6,-5e-6,5e-6,0,Cav_depth
BLOCK,-25e-6,-35e-6,-5e-6,5e-6,0,Cav_depth

BLOCK,15e-6,5e-6,15e-6,25e-6,0,Cav_depth
BLOCK,35e-6,25e-6,15e-6,25e-6,0,Cav_depth
BLOCK,-5e-6,-15e-6,15e-6,25e-6,0,Cav_depth
BLOCK,-25e-6,-35e-6,15e-6,25e-6,0,Cav_depth

BLOCK,15e-6,5e-6,-15e-6,-25e-6,0,Cav_depth
BLOCK,35e-6,25e-6,-15e-6,-25e-6,0,Cav_depth
```

Appendix B (Continued)

```
BLOCK,-5e-6,-15e-6,-15e-6,-25e-6,0,Cav_depth
BLOCK,-25e-6,-35e-6,-15e-6,-25e-6,0,Cav_depth

BLOCK,15e-6,5e-6,35e-6,45e-6,0,Cav_depth
BLOCK,35e-6,25e-6,35e-6,45e-6,0,Cav_depth
BLOCK,-5e-6,-15e-6,35e-6,45e-6,0,Cav_depth
BLOCK,-25e-6,-35e-6,35e-6,45e-6,0,Cav_depth

BLOCK,15e-6,5e-6,-35e-6,-45e-6,0,Cav_depth
BLOCK,35e-6,25e-6,-35e-6,-45e-6,0,Cav_depth
BLOCK,-5e-6,-15e-6,-35e-6,-45e-6,0,Cav_depth
BLOCK,-25e-6,-35e-6,-35e-6,-45e-6,0,Cav_depth

/COM ! Resonant cavities volume delete from the substrate
VSBV,1,2,SEPO,delete,KEEP
VSBV,22,3,SEPO,delete,KEEP
VSBV,1,4,SEPO,delete,KEEP
VSBV,2,5,SEPO,delete,KEEP
VSBV,1,6,SEPO,delete,KEEP
VSBV,2,7,SEPO,delete,KEEP
VSBV,1,8,SEPO,delete,KEEP
VSBV,2,9,SEPO,delete,KEEP
VSBV,1,10,SEPO,delete,KEEP

VSBV,2,11,SEPO,delete,KEEP
VSBV,1,12,SEPO,delete,KEEP
VSBV,2,13,SEPO,delete,KEEP
VSBV,1,14,SEPO,delete,KEEP
VSBV,2,15,SEPO,delete,KEEP
VSBV,1,16,SEPO,delete,KEEP
VSBV,2,17,SEPO,delete,KEEP
VSBV,1,18,SEPO,delete,KEEP
VSBV,2,19,SEPO,delete,KEEP
VSBV,1,20,SEPO,delete,KEEP
VSBV,2,21,SEPO,delete,KEEP
```

```
ALLSEL

Vovlap,ALL


/VIEW,  1,  0.601671205170    , -0.757983672401    ,
0.251897823021
/DIST,  1,  0.388832652656E-03
/ANG,   1,  -89.0496187725
/REPLO
LDIV,265,,,2,0
LDIV,266,,,2,0
LDIV,267,,,2,0
LDIV,268,,,2,0


LDIV,312,,,2,0
LDIV,305,,,2,0
LDIV,306,,,2,0
LDIV,307,,,2,0


LDIV,308,,,2,0
LDIV,309,,,2,0
LDIV,310,,,2,0
LDIV,311,,,2,0


/COM ! Begin with divisions in X


/COM PIEZO TOP SURFACE


LSEL,NONE
LSEL,S,LINE,,310
LSEL,A,LINE,,307
CM,_Y1,LINE
CMSEL,,_Y1
LESIZE,_Y1, , ,60,0.2, , , ,0


LSEL,NONE
LSEL,S,LINE,,311
```

195

Appendix B (Continued)

```
LSEL,A,LINE,,312

CM,_Y1,LINE

CMSEL,,_Y1

LESIZE,_Y1, , ,20,0.2, , , ,0


LSEL,NONE

LSEL,S,LINE,,17

LSEL,A,LINE,,24

CM,_Y1,LINE

CMSEL,,_Y1

LESIZE,_Y1, , ,20,5, , , ,0


LSEL,NONE

LSEL,S,LINE,,23

LSEL,A,LINE,,20

CM,_Y1,LINE

CMSEL,,_Y1

LESIZE,_Y1, , ,60,5, , , ,0


LSEL,NONE

LSEL,S,LINE,,18

LSEL,A,LINE,,19

CM,_Y1,LINE

CMSEL,,_Y1

LESIZE,_Y1, , ,10,.2, , , ,0

LSEL,NONE

LSEL,S,LINE,,21

LSEL,A,LINE,,22

CM,_Y1,LINE

CMSEL,,_Y1

LESIZE,_Y1, , ,10,.2, , , ,0


! BOT

LSEL,NONE

LSEL,S,LINE,,266

LSEL,A,LINE,,268
```

```
CM,_Y1,LINE
CMSEL,,_Y1
LESIZE,_Y1, , ,10,0.4, , , ,0


LSEL,NONE
LSEL,S,LINE,,267
LSEL,A,LINE,,265
CM,_Y1,LINE
CMSEL,,_Y1
LESIZE,_Y1, , ,10,0.4, , , ,0


LSEL,NONE
LSEL,S,LINE,,13
LSEL,A,LINE,,15
CM,_Y1,LINE
CMSEL,,_Y1
LESIZE,_Y1, , ,10,2.5, , , ,0


LSEL,NONE
LSEL,S,LINE,,305
LSEL,A,LINE,,306
CM,_Y1,LINE
CMSEL,,_Y1
LESIZE,_Y1, , ,10,.4, , , ,0


LSEL,NONE
LSEL,S,LINE,,308
LSEL,A,LINE,,309
CM,_Y1,LINE
CMSEL,,_Y1
LESIZE,_Y1, , ,10,0.2, , , ,0


LSEL,NONE
LSEL,S,LINE,,14
LSEL,A,LINE,,16
CM,_Y1,LINE
```

197

```
CMSEL,,_Y1
LESIZE,_Y1, , ,10,5.0, , , ,0

ALLSEL

!*
CM,_Y,VOLU
VSEL, , , ,        2
CM,_Y1,VOLU
CMSEL,S,_Y
!*
CMSEL,S,_Y1
VATT,        1, ,    1,        0
CMSEL,S,_Y
CMDELE,_Y
CMDELE,_Y1
!*
!*
CM,_Y,VOLU
VSEL, , , ,3,21,1,0
CM,_Y1,VOLU
CMSEL,S,_Y
!*
CMSEL,S,_Y1
VATT,        2, ,    1,        0
CMSEL,S,_Y
CMDELE,_Y
CMDELE,_Y1
!*
!*
CM,_Y,VOLU
VSEL, , , ,1
CM,_Y1,VOLU
CMSEL,S,_Y
!*
CMSEL,S,_Y1
```

198

Appendix B (Continued)

```
VATT,          2, ,    1,          0
CMSEL,S,_Y
CMDELE,_Y
CMDELE,_Y1
!*


ALLSEL


MSHK,0
VMESH,ALL
```

Appendix B.2.3 λ/2 PS Filled Resonant Cavity Design

Particular to this example is the λ/2 cavity placement and the cavities have

been filled with polystyrene.

```
/PNUM,KP,0
/PNUM,LINE,1
/PNUM,AREA,1
/PNUM,VOLU,0
/PNUM,NODE,0
/PNUM,TABN,0
/PNUM,SVAL,0
/NUMBER,0
!*
/PNUM,ELEM,0
/REPLOT
/PREP7
!*
ET,1,SOLID98
!*
KEYOPT,1,1,3
```

```
KEYOPT,1,3,0

KEYOPT,1,5,0

MAT,1,

MPREAD,'MATLAB_LiTaO3','SI_MPL','',LIB

MPLIST,1

TBLIST,ALL,1

!*

!*

MP,EX,2,3400e6                  ! POLYMER MODULUS OF
ELASTICITY

MP,NUXY,2,.33                   ! POLYMER POISSON RATIO

MP,DENS,2,1110                  ! POLYMER DENSITY


MP,EX,3,82.737e9               ! IDT MODULUS OF ELASTICITY
(Pa)

MP,NUXY,3,.44                   ! IDT POISSON RATIO

MP,DENS,3,19300                ! IDT DENSITY (kg/m3)

MP,SONC,3,2030                 ! IDT Sonic Velocity (m/s)


*SET,Cav_depth, -5e-6


*SET,Substrate_Height , 200e-6

*SET,Substrate_Length , 1600e-6

*SET,Substrate_Depth  , 200e-6

*SET,POLYMER_Height ,  0.500e-6

*SET,POLYMER_Length , 800.0e-6

*SET,POLYMER_Depth  , 150e-6

*SET,IDT_Width , 10e-6

*SET,IDT_Length , 80e-6

*SET,IDT_Z , 0e-6

*SET,IDT_Height , 1.0e-6

*SET,IDT_Offset , 120e-6


BLOCK, -Substrate_Length / 2, Substrate_Length / 2, -
Substrate_Depth / 2, Substrate_Depth / 2, -Substrate_Height,
0e-6
```

200

Appendix B (Continued)

```
/COM ! Resonant cavities
BLOCK,30e-6,10e-6,-10e-6,10e-6,0,Cav_depth
BLOCK,70e-6,50e-6,-10e-6,10e-6,0,Cav_depth
BLOCK,-10e-6,-30e-6,-10e-6,10e-6,0,Cav_depth
BLOCK,-50e-6,-70e-6,-10e-6,10e-6,0,Cav_depth

BLOCK,30e-6,10e-6,30e-6,50e-6,0,Cav_depth
BLOCK,70e-6,50e-6,30e-6,50e-6,0,Cav_depth
BLOCK,-10e-6,-30e-6,30e-6,50e-6,0,Cav_depth
BLOCK,-50e-6,-70e-6,30e-6,50e-6,0,Cav_depth

BLOCK,30e-6,10e-6,-30e-6,-50e-6,0,Cav_depth
BLOCK,70e-6,50e-6,-30e-6,-50e-6,0,Cav_depth
BLOCK,-10e-6,-30e-6,-30e-6,-50e-6,0,Cav_depth
BLOCK,-50e-6,-70e-6,-30e-6,-50e-6,0,Cav_depth

BLOCK,30e-6,10e-6,-70e-6,-90e-6,0,Cav_depth
BLOCK,70e-6,50e-6,-70e-6,-90e-6,0,Cav_depth
BLOCK,-10e-6,-30e-6,-70e-6,-90e-6,0,Cav_depth
BLOCK,-50e-6,-70e-6,-70e-6,-90e-6,0,Cav_depth

BLOCK,30e-6,10e-6,70e-6,90e-6,0,Cav_depth
BLOCK,70e-6,50e-6,70e-6,90e-6,0,Cav_depth
BLOCK,-10e-6,-30e-6,70e-6,90e-6,0,Cav_depth
BLOCK,-50e-6,-70e-6,70e-6,90e-6,0,Cav_depth

/COM ! Resonant cavities volume delete from the substrate
VSBV,1,2,SEPO,delete,KEEP
VSBV,22,3,SEPO,delete,KEEP
VSBV,1,4,SEPO,delete,KEEP
VSBV,2,5,SEPO,delete,KEEP
VSBV,1,6,SEPO,delete,KEEP
VSBV,2,7,SEPO,delete,KEEP
VSBV,1,8,SEPO,delete,KEEP
VSBV,2,9,SEPO,delete,KEEP
VSBV,1,10,SEPO,delete,KEEP
```

```
VSBV,2,11,SEPO,delete,KEEP
VSBV,1,12,SEPO,delete,KEEP
VSBV,2,13,SEPO,delete,KEEP
VSBV,1,14,SEPO,delete,KEEP
VSBV,2,15,SEPO,delete,KEEP
VSBV,1,16,SEPO,delete,KEEP
VSBV,2,17,SEPO,delete,KEEP
VSBV,1,18,SEPO,delete,KEEP
VSBV,2,19,SEPO,delete,KEEP
VSBV,1,20,SEPO,delete,KEEP
VSBV,2,21,SEPO,delete,KEEP


ALLSEL
Vovlap,ALL


/VIEW,  1,  0.601671205170    , -0.757983672401    ,
0.251897823021
/DIST,  1,  0.388832652656E-03
/ANG,   1,  -89.0496187725
/REPLO
LDIV,265,,,2,0
LDIV,266,,,2,0
LDIV,267,,,2,0
LDIV,268,,,2,0

LDIV,312,,,2,0
LDIV,305,,,2,0
LDIV,306,,,2,0
LDIV,307,,,2,0

LDIV,308,,,2,0
LDIV,309,,,2,0
LDIV,310,,,2,0
LDIV,311,,,2,0
```

Appendix B (Continued)

```
/COM ! Begin with divisions in X


/COM PIEZO TOP SURFACE


LSEL,NONE
LSEL,S,LINE,,310
LSEL,A,LINE,,307
CM,_Y1,LINE
CMSEL,,_Y1
LESIZE,_Y1, , ,60,0.2, , , ,0


LSEL,NONE
LSEL,S,LINE,,311
LSEL,A,LINE,,312
CM,_Y1,LINE
CMSEL,,_Y1
LESIZE,_Y1, , ,25,0.2, , , ,0


LSEL,NONE
LSEL,S,LINE,,17
LSEL,A,LINE,,24
CM,_Y1,LINE
CMSEL,,_Y1
LESIZE,_Y1, , ,25,5, , , ,0


LSEL,NONE
LSEL,S,LINE,,23
LSEL,A,LINE,,20
CM,_Y1,LINE
CMSEL,,_Y1
LESIZE,_Y1, , ,60,5, , , ,0


LSEL,NONE
LSEL,S,LINE,,18
LSEL,A,LINE,,19
CM,_Y1,LINE
```

Appendix B (Continued)

```
CMSEL,,_Y1
LESIZE,_Y1, , ,10,.2, , , ,0


LSEL,NONE
LSEL,S,LINE,,21
LSEL,A,LINE,,22
CM,_Y1,LINE
CMSEL,,_Y1
LESIZE,_Y1, , ,10,.2, , , ,0


! BOT
LSEL,NONE
LSEL,S,LINE,,266
LSEL,A,LINE,,268
CM,_Y1,LINE
CMSEL,,_Y1
LESIZE,_Y1, , ,10,0.4, , , ,0


LSEL,NONE
LSEL,S,LINE,,267
LSEL,A,LINE,,265
CM,_Y1,LINE
CMSEL,,_Y1
LESIZE,_Y1, , ,10,0.4, , , ,0


LSEL,NONE
LSEL,S,LINE,,13
LSEL,A,LINE,,15
CM,_Y1,LINE
CMSEL,,_Y1
LESIZE,_Y1, , ,10,2.5, , , ,0


LSEL,NONE
LSEL,S,LINE,,305
LSEL,A,LINE,,306
CM,_Y1,LINE
```

204

```
CMSEL,,_Y1

LESIZE,_Y1, , ,10,.4, , , ,0


LSEL,NONE

LSEL,S,LINE,,308

LSEL,A,LINE,,309

CM,_Y1,LINE

CMSEL,,_Y1

LESIZE,_Y1, , ,10,0.2, , , ,0


LSEL,NONE

LSEL,S,LINE,,14

LSEL,A,LINE,,16

CM,_Y1,LINE

CMSEL,,_Y1

LESIZE,_Y1, , ,10,5.0, , , ,0


ALLSEL


!*

CM,_Y,VOLU

VSEL, , , ,          2

CM,_Y1,VOLU

CMSEL,S,_Y

!*

CMSEL,S,_Y1

VATT,        1, ,    1,         0

CMSEL,S,_Y

CMDELE,_Y

CMDELE,_Y1

!*

!*

CM,_Y,VOLU

VSEL, , , ,3,21,1,0

CM,_Y1,VOLU

CMSEL,S,_Y
```

205

Appendix B (Continued)

```
!*
CMSEL,S,_Y1
VATT,       2, ,   1,       0
CMSEL,S,_Y
CMDELE,_Y
CMDELE,_Y1
!*
CM,_Y,VOLU
VSEL, , , ,1
CM,_Y1,VOLU
CMSEL,S,_Y
!*
CMSEL,S,_Y1
VATT,       2, ,   1,       0
CMSEL,S,_Y
CMDELE,_Y
CMDELE,_Y1
!*

ALLSEL

MSHK,0
VMESH,ALL
```

## Appendix B.2.4 Single Split Finger Electrode Design

```
/COM !INPUT IDTs
NSEL,S,LOC,Z,IDT_Z,IDT_Z
NSEL,R,LOC,Y,-IDT_Length/2, IDT_Length/2
NSEL,R,LOC,X,-155E-6 - IDT_Offset,-145E-6 - IDT_Offset
CP,1,VOLT,ALL
NLIST,ALL, , , ,NODE,NODE,NODE
*GET,N1,NODE,,NUM,MIN
```

Appendix B (Continued)

```
NSEL,S,LOC,Z,IDT_Z,IDT_Z
NSEL,R,LOC,Y,-IDT_Length/2, IDT_Length/2
NSEL,R,LOC,X,-135E-6 - IDT_Offset,-125E-6 - IDT_Offset
CP,2,VOLT,ALL
NLIST,ALL, , , ,NODE,NODE,NODE
*GET,N2,NODE,,NUM,MIN


NSEL,S,LOC,Z,IDT_Z,IDT_Z
NSEL,R,LOC,Y,-IDT_Length/2, IDT_Length/2
NSEL,R,LOC,X,-115E-6 - IDT_Offset,-105E-6 - IDT_Offset
CP,1,VOLT,ALL
NLIST,ALL, , , ,NODE,NODE,NODE
*GET,N3,NODE,,NUM,MIN


NSEL,S,LOC,Z,IDT_Z,IDT_Z
NSEL,R,LOC,Y,-IDT_Length/2, IDT_Length/2
NSEL,R,LOC,X,-95E-6 - IDT_Offset,-85E-6 - IDT_Offset
CP,2,VOLT,ALL
NLIST,ALL, , , ,NODE,NODE,NODE
*GET,N4,NODE,,NUM,MIN


NSEL,S,LOC,Z,IDT_Z,IDT_Z
NSEL,R,LOC,Y,-IDT_Length/2, IDT_Length/2
NSEL,R,LOC,X,-75E-6 - IDT_Offset,-65E-6 - IDT_Offset
CP,1,VOLT,ALL
NLIST,ALL, , , ,NODE,NODE,NODE
*GET,N5,NODE,,NUM,MIN


NSEL,S,LOC,Z,IDT_Z,IDT_Z
NSEL,R,LOC,Y,-IDT_Length/2, IDT_Length/2
NSEL,R,LOC,X,-55E-6 - IDT_Offset,-45E-6 - IDT_Offset
CP,2,VOLT,ALL
NLIST,ALL, , , ,NODE,NODE,NODE
*GET,N6,NODE,,NUM,MIN
```

Appendix B (Continued)

```
/COM !Output IDTs


NSEL,S,LOC,Z,IDT_Z,IDT_Z
NSEL,R,LOC,Y,-IDT_Length/2, IDT_Length/2
NSEL,R,LOC,X,45e-6 + IDT_Offset,55e-6 + IDT_Offset
CP,3,VOLT,ALL
NLIST,ALL, , , ,NODE,NODE,NODE
*GET,N7,NODE,,NUM,MIN


NSEL,S,LOC,Z,IDT_Z,IDT_Z
NSEL,R,LOC,Y,-IDT_Length/2, IDT_Length/2
NSEL,R,LOC,X,65e-6 + IDT_Offset,75e-6 + IDT_Offset
CP,4,VOLT,ALL
NLIST,ALL, , , ,NODE,NODE,NODE
*GET,N8,NODE,,NUM,MIN


NSEL,S,LOC,Z,IDT_Z,IDT_Z
NSEL,R,LOC,Y,-IDT_Length/2, IDT_Length/2
NSEL,R,LOC,X,85e-6 + IDT_Offset,95e-6 + IDT_Offset
CP,3,VOLT,ALL
NLIST,ALL, , , ,NODE,NODE,NODE
*GET,N9,NODE,,NUM,MIN


NSEL,S,LOC,Z,IDT_Z,IDT_Z
NSEL,R,LOC,Y,-IDT_Length/2, IDT_Length/2
NSEL,R,LOC,X,105e-6 + IDT_Offset,115e-6 + IDT_Offset
CP,4,VOLT,ALL
NLIST,ALL, , , ,NODE,NODE,NODE
*GET,N10,NODE,,NUM,MIN


NSEL,S,LOC,Z,IDT_Z,IDT_Z
NSEL,R,LOC,Y,-IDT_Length/2, IDT_Length/2
NSEL,R,LOC,X,125e-6 + IDT_Offset,135e-6 + IDT_Offset
CP,3,VOLT,ALL
NLIST,ALL, , , ,NODE,NODE,NODE
*GET,N11,NODE,,NUM,MIN
```

Appendix B (Continued)

```
NSEL,S,LOC,Z,IDT_Z,IDT_Z
NSEL,R,LOC,Y,-IDT_Length/2, IDT_Length/2
NSEL,R,LOC,X,145e-6 + IDT_Offset,155e-6 + IDT_Offset
CP,4,VOLT,ALL
NLIST,ALL, , , ,NODE,NODE,NODE
*GET,N12,NODE,,NUM,MIN


ALLSEL
CPLIST,ALL,,,ANY
```

## Appendix B.2.5 Double Split Finger Electrode Design

```
/COM !INPUT IDTs
NSEL,S,LOC,Z,IDT_Z,IDT_Z
NSEL,R,LOC,Y,-IDT_Length/2, IDT_Length/2
NSEL,R,LOC,X,-155E-6 - IDT_Offset,-150E-6 - IDT_Offset
CP,1,VOLT,ALL
NLIST,ALL, , , ,NODE,NODE,NODE
*GET,N1,NODE,,NUM,MIN


NSEL,S,LOC,Z,IDT_Z,IDT_Z
NSEL,R,LOC,Y,-IDT_Length/2, IDT_Length/2
NSEL,R,LOC,X,-145E-6 - IDT_Offset,-140E-6 - IDT_Offset
CP,1,VOLT,ALL
NLIST,ALL, , , ,NODE,NODE,NODE
*GET,N2,NODE,,NUM,MIN


NSEL,S,LOC,Z,IDT_Z,IDT_Z
NSEL,R,LOC,Y,-IDT_Length/2, IDT_Length/2
NSEL,R,LOC,X,-135E-6 - IDT_Offset,-130E-6 - IDT_Offset
CP,2,VOLT,ALL
NLIST,ALL, , , ,NODE,NODE,NODE
*GET,N3,NODE,,NUM,MIN
```

209

```
NSEL,S,LOC,Z,IDT_Z,IDT_Z
NSEL,R,LOC,Y,-IDT_Length/2, IDT_Length/2
NSEL,R,LOC,X,-125E-6 - IDT_Offset,-120E-6 - IDT_Offset
CP,2,VOLT,ALL
NLIST,ALL, , , ,NODE,NODE,NODE
*GET,N4,NODE,,NUM,MIN


NSEL,S,LOC,Z,IDT_Z,IDT_Z
NSEL,R,LOC,Y,-IDT_Length/2, IDT_Length/2
NSEL,R,LOC,X,-115E-6 - IDT_Offset,-110E-6 - IDT_Offset
CP,1,VOLT,ALL
NLIST,ALL, , , ,NODE,NODE,NODE
*GET,N5,NODE,,NUM,MIN


NSEL,S,LOC,Z,IDT_Z,IDT_Z
NSEL,R,LOC,Y,-IDT_Length/2, IDT_Length/2
NSEL,R,LOC,X,-105E-6 - IDT_Offset,-100E-6 - IDT_Offset
CP,1,VOLT,ALL
NLIST,ALL, , , ,NODE,NODE,NODE
*GET,N6,NODE,,NUM,MIN


NSEL,S,LOC,Z,IDT_Z,IDT_Z
NSEL,R,LOC,Y,-IDT_Length/2, IDT_Length/2
NSEL,R,LOC,X,-95E-6 - IDT_Offset,-90E-6 - IDT_Offset
CP,2,VOLT,ALL
NLIST,ALL, , , ,NODE,NODE,NODE
*GET,N7,NODE,,NUM,MIN


NSEL,S,LOC,Z,IDT_Z,IDT_Z
NSEL,R,LOC,Y,-IDT_Length/2, IDT_Length/2
NSEL,R,LOC,X,-85E-6 - IDT_Offset,-80E-6 - IDT_Offset
CP,2,VOLT,ALL
NLIST,ALL, , , ,NODE,NODE,NODE
*GET,N8,NODE,,NUM,MIN


NSEL,S,LOC,Z,IDT_Z,IDT_Z
```

```
NSEL,R,LOC,Y,-IDT_Length/2, IDT_Length/2
NSEL,R,LOC,X,-75E-6 - IDT_Offset,-70E-6 - IDT_Offset
CP,1,VOLT,ALL
NLIST,ALL, , , ,NODE,NODE,NODE
*GET,N9,NODE,,NUM,MIN


NSEL,S,LOC,Z,IDT_Z,IDT_Z
NSEL,R,LOC,Y,-IDT_Length/2, IDT_Length/2
NSEL,R,LOC,X,-65E-6 - IDT_Offset,-60E-6 - IDT_Offset
CP,1,VOLT,ALL
NLIST,ALL, , , ,NODE,NODE,NODE
*GET,N10,NODE,,NUM,MIN


NSEL,S,LOC,Z,IDT_Z,IDT_Z
NSEL,R,LOC,Y,-IDT_Length/2, IDT_Length/2
NSEL,R,LOC,X,-55E-6 - IDT_Offset,-50E-6 - IDT_Offset
CP,2,VOLT,ALL
NLIST,ALL, , , ,NODE,NODE,NODE
*GET,N11,NODE,,NUM,MIN


NSEL,S,LOC,Z,IDT_Z,IDT_Z
NSEL,R,LOC,Y,-IDT_Length/2, IDT_Length/2
NSEL,R,LOC,X,-45E-6 - IDT_Offset,-40E-6 - IDT_Offset
CP,2,VOLT,ALL
NLIST,ALL, , , ,NODE,NODE,NODE
*GET,N12,NODE,,NUM,MIN


/COM !Output IDTs


NSEL,S,LOC,Z,IDT_Z,IDT_Z
NSEL,R,LOC,Y,-IDT_Length/2, IDT_Length/2
NSEL,R,LOC,X,40e-6 + IDT_Offset,45e-6 + IDT_Offset
CP,3,VOLT,ALL
NLIST,ALL, , , ,NODE,NODE,NODE
*GET,N13,NODE,,NUM,MIN
```

211

Appendix B (Continued)

```
NSEL,S,LOC,Z,IDT_Z,IDT_Z
NSEL,R,LOC,Y,-IDT_Length/2, IDT_Length/2
NSEL,R,LOC,X,50e-6 + IDT_Offset,55e-6 + IDT_Offset
CP,3,VOLT,ALL
NLIST,ALL, , , ,NODE,NODE,NODE
*GET,N14,NODE,,NUM,MIN


NSEL,S,LOC,Z,IDT_Z,IDT_Z
NSEL,R,LOC,Y,-IDT_Length/2, IDT_Length/2
NSEL,R,LOC,X,60e-6 + IDT_Offset,65e-6 + IDT_Offset
CP,4,VOLT,ALL
NLIST,ALL, , , ,NODE,NODE,NODE
*GET,N15,NODE,,NUM,MIN


NSEL,S,LOC,Z,IDT_Z,IDT_Z
NSEL,R,LOC,Y,-IDT_Length/2, IDT_Length/2
NSEL,R,LOC,X,70e-6 + IDT_Offset,75e-6 + IDT_Offset
CP,4,VOLT,ALL
NLIST,ALL, , , ,NODE,NODE,NODE
*GET,N16,NODE,,NUM,MIN


NSEL,S,LOC,Z,IDT_Z,IDT_Z
NSEL,R,LOC,Y,-IDT_Length/2, IDT_Length/2
NSEL,R,LOC,X,80e-6 + IDT_Offset,85e-6 + IDT_Offset
CP,3,VOLT,ALL
NLIST,ALL, , , ,NODE,NODE,NODE
*GET,N17,NODE,,NUM,MIN


NSEL,S,LOC,Z,IDT_Z,IDT_Z
NSEL,R,LOC,Y,-IDT_Length/2, IDT_Length/2
NSEL,R,LOC,X,90e-6 + IDT_Offset,95e-6 + IDT_Offset
CP,3,VOLT,ALL
NLIST,ALL, , , ,NODE,NODE,NODE
*GET,N18,NODE,,NUM,MIN
```

Appendix B (Continued)

```
NSEL,S,LOC,Z,IDT_Z,IDT_Z
NSEL,R,LOC,Y,-IDT_Length/2, IDT_Length/2
NSEL,R,LOC,X,100e-6 + IDT_Offset,105e-6 + IDT_Offset
CP,4,VOLT,ALL
NLIST,ALL, , , ,NODE,NODE,NODE
*GET,N19,NODE,,NUM,MIN


NSEL,S,LOC,Z,IDT_Z,IDT_Z
NSEL,R,LOC,Y,-IDT_Length/2, IDT_Length/2
NSEL,R,LOC,X,110e-6 + IDT_Offset,115e-6 + IDT_Offset
CP,4,VOLT,ALL
NLIST,ALL, , , ,NODE,NODE,NODE
*GET,N20,NODE,,NUM,MIN


NSEL,S,LOC,Z,IDT_Z,IDT_Z
NSEL,R,LOC,Y,-IDT_Length/2, IDT_Length/2
NSEL,R,LOC,X,120e-6 + IDT_Offset,125e-6 + IDT_Offset
CP,3,VOLT,ALL
NLIST,ALL, , , ,NODE,NODE,NODE
*GET,N21,NODE,,NUM,MIN


NSEL,S,LOC,Z,IDT_Z,IDT_Z
NSEL,R,LOC,Y,-IDT_Length/2, IDT_Length/2
NSEL,R,LOC,X,130e-6 + IDT_Offset,135e-6 + IDT_Offset
CP,3,VOLT,ALL
NLIST,ALL, , , ,NODE,NODE,NODE
*GET,N22,NODE,,NUM,MIN


NSEL,S,LOC,Z,IDT_Z,IDT_Z
NSEL,R,LOC,Y,-IDT_Length/2, IDT_Length/2
NSEL,R,LOC,X,140e-6 + IDT_Offset,145e-6 + IDT_Offset
CP,4,VOLT,ALL
NLIST,ALL, , , ,NODE,NODE,NODE
*GET,N23,NODE,,NUM,MIN
```

Appendix B (Continued)

```
NSEL,S,LOC,Z,IDT_Z,IDT_Z
NSEL,R,LOC,Y,-IDT_Length/2, IDT_Length/2
NSEL,R,LOC,X,150e-6 + IDT_Offset,155e-6 + IDT_Offset
CP,4,VOLT,ALL
NLIST,ALL, , , ,NODE,NODE,NODE
*GET,N24,NODE,,NUM,MIN


ALLSEL
CPLIST,ALL,,,ANY
```

## Appendix B.2.6 Pruned Double Split Finger Electrode Design

```
/COM !INPUT IDTs
NSEL,S,LOC,Z,IDT_Z,IDT_Z
NSEL,R,LOC,Y,-IDT_Length/2, IDT_Length/2
NSEL,R,LOC,X,-235E-6 - IDT_Offset,-230E-6 - IDT_Offset
CP,1,VOLT,ALL
NLIST,ALL, , , ,NODE,NODE,NODE
*GET,N1,NODE,,NUM,MIN


NSEL,S,LOC,Z,IDT_Z,IDT_Z
NSEL,R,LOC,Y,-IDT_Length/2, IDT_Length/2
NSEL,R,LOC,X,-225E-6 - IDT_Offset,-220E-6 - IDT_Offset
CP,1,VOLT,ALL
NLIST,ALL, , , ,NODE,NODE,NODE
*GET,N2,NODE,,NUM,MIN


NSEL,S,LOC,Z,IDT_Z,IDT_Z
NSEL,R,LOC,Y,-IDT_Length/2, IDT_Length/2
NSEL,R,LOC,X,-215E-6 - IDT_Offset,-210E-6 - IDT_Offset
CP,2,VOLT,ALL
NLIST,ALL, , , ,NODE,NODE,NODE
*GET,N3,NODE,,NUM,MIN
```

Appendix B (Continued)

```
NSEL,S,LOC,Z,IDT_Z,IDT_Z
NSEL,R,LOC,Y,-IDT_Length/2, IDT_Length/2
NSEL,R,LOC,X,-205E-6 - IDT_Offset,-200E-6 - IDT_Offset
CP,2,VOLT,ALL
NLIST,ALL, , , ,NODE,NODE,NODE
*GET,N4,NODE,,NUM,MIN


NSEL,S,LOC,Z,IDT_Z,IDT_Z
NSEL,R,LOC,Y,-IDT_Length/2, IDT_Length/2
NSEL,R,LOC,X,-155E-6 - IDT_Offset,-150E-6 - IDT_Offset
CP,1,VOLT,ALL
NLIST,ALL, , , ,NODE,NODE,NODE
*GET,N5,NODE,,NUM,MIN


NSEL,S,LOC,Z,IDT_Z,IDT_Z
NSEL,R,LOC,Y,-IDT_Length/2, IDT_Length/2
NSEL,R,LOC,X,-145E-6 - IDT_Offset,-140E-6 - IDT_Offset
CP,1,VOLT,ALL
NLIST,ALL, , , ,NODE,NODE,NODE
*GET,N6,NODE,,NUM,MIN


NSEL,S,LOC,Z,IDT_Z,IDT_Z
NSEL,R,LOC,Y,-IDT_Length/2, IDT_Length/2
NSEL,R,LOC,X,-135E-6 - IDT_Offset,-130E-6 - IDT_Offset
CP,2,VOLT,ALL
NLIST,ALL, , , ,NODE,NODE,NODE
*GET,N7,NODE,,NUM,MIN


NSEL,S,LOC,Z,IDT_Z,IDT_Z
NSEL,R,LOC,Y,-IDT_Length/2, IDT_Length/2
NSEL,R,LOC,X,-125E-6 - IDT_Offset,-120E-6 - IDT_Offset
CP,2,VOLT,ALL
NLIST,ALL, , , ,NODE,NODE,NODE
*GET,N8,NODE,,NUM,MIN
```

```
NSEL,S,LOC,Z,IDT_Z,IDT_Z
NSEL,R,LOC,Y,-IDT_Length/2, IDT_Length/2
NSEL,R,LOC,X,-75E-6 - IDT_Offset,-70E-6 - IDT_Offset
CP,1,VOLT,ALL
NLIST,ALL, , , ,NODE,NODE,NODE
*GET,N9,NODE,,NUM,MIN


NSEL,S,LOC,Z,IDT_Z,IDT_Z
NSEL,R,LOC,Y,-IDT_Length/2, IDT_Length/2
NSEL,R,LOC,X,-65E-6 - IDT_Offset,-60E-6 - IDT_Offset
CP,1,VOLT,ALL
NLIST,ALL, , , ,NODE,NODE,NODE
*GET,N10,NODE,,NUM,MIN


NSEL,S,LOC,Z,IDT_Z,IDT_Z
NSEL,R,LOC,Y,-IDT_Length/2, IDT_Length/2
NSEL,R,LOC,X,-55E-6 - IDT_Offset,-50E-6 - IDT_Offset
CP,2,VOLT,ALL
NLIST,ALL, , , ,NODE,NODE,NODE
*GET,N11,NODE,,NUM,MIN
NSEL,S,LOC,Z,IDT_Z,IDT_Z
NSEL,R,LOC,Y,-IDT_Length/2, IDT_Length/2
NSEL,R,LOC,X,-45E-6 - IDT_Offset,-40E-6 - IDT_Offset
CP,2,VOLT,ALL
NLIST,ALL, , , ,NODE,NODE,NODE
*GET,N12,NODE,,NUM,MIN


/COM !Output IDTs


NSEL,S,LOC,Z,IDT_Z,IDT_Z
NSEL,R,LOC,Y,-IDT_Length/2, IDT_Length/2
NSEL,R,LOC,X,40e-6 + IDT_Offset,45e-6 + IDT_Offset
CP,3,VOLT,ALL
NLIST,ALL, , , ,NODE,NODE,NODE
*GET,N13,NODE,,NUM,MIN
```

```
NSEL,S,LOC,Z,IDT_Z,IDT_Z

NSEL,R,LOC,Y,-IDT_Length/2, IDT_Length/2

NSEL,R,LOC,X,50e-6 + IDT_Offset,55e-6 + IDT_Offset

CP,3,VOLT,ALL

NLIST,ALL, , , ,NODE,NODE,NODE

*GET,N14,NODE,,NUM,MIN


NSEL,S,LOC,Z,IDT_Z,IDT_Z

NSEL,R,LOC,Y,-IDT_Length/2, IDT_Length/2

NSEL,R,LOC,X,60e-6 + IDT_Offset,65e-6 + IDT_Offset

CP,4,VOLT,ALL

NLIST,ALL, , , ,NODE,NODE,NODE

*GET,N15,NODE,,NUM,MIN


NSEL,S,LOC,Z,IDT_Z,IDT_Z

NSEL,R,LOC,Y,-IDT_Length/2, IDT_Length/2

NSEL,R,LOC,X,70e-6 + IDT_Offset,75e-6 + IDT_Offset

CP,4,VOLT,ALL

NLIST,ALL, , , ,NODE,NODE,NODE

*GET,N16,NODE,,NUM,MIN


NSEL,S,LOC,Z,IDT_Z,IDT_Z

NSEL,R,LOC,Y,-IDT_Length/2, IDT_Length/2

NSEL,R,LOC,X,120e-6 + IDT_Offset,125e-6 + IDT_Offset

CP,3,VOLT,ALL

NLIST,ALL, , , ,NODE,NODE,NODE

*GET,N17,NODE,,NUM,MIN


NSEL,S,LOC,Z,IDT_Z,IDT_Z

NSEL,R,LOC,Y,-IDT_Length/2, IDT_Length/2

NSEL,R,LOC,X,130e-6 + IDT_Offset,135e-6 + IDT_Offset

CP,3,VOLT,ALL

NLIST,ALL, , , ,NODE,NODE,NODE

*GET,N18,NODE,,NUM,MIN
```

Appendix B (Continued)

```
NSEL,S,LOC,Z,IDT_Z,IDT_Z
NSEL,R,LOC,Y,-IDT_Length/2, IDT_Length/2
NSEL,R,LOC,X,140e-6 + IDT_Offset,145e-6 + IDT_Offset
CP,4,VOLT,ALL
NLIST,ALL, , , ,NODE,NODE,NODE
*GET,N19,NODE,,NUM,MIN


NSEL,S,LOC,Z,IDT_Z,IDT_Z
NSEL,R,LOC,Y,-IDT_Length/2, IDT_Length/2
NSEL,R,LOC,X,150e-6 + IDT_Offset,155e-6 + IDT_Offset
CP,4,VOLT,ALL
NLIST,ALL, , , ,NODE,NODE,NODE
*GET,N20,NODE,,NUM,MIN


NSEL,S,LOC,Z,IDT_Z,IDT_Z
NSEL,R,LOC,Y,-IDT_Length/2, IDT_Length/2
NSEL,R,LOC,X,200e-6 + IDT_Offset,205e-6 + IDT_Offset
CP,3,VOLT,ALL
NLIST,ALL, , , ,NODE,NODE,NODE
*GET,N21,NODE,,NUM,MIN


NSEL,S,LOC,Z,IDT_Z,IDT_Z
NSEL,R,LOC,Y,-IDT_Length/2, IDT_Length/2
NSEL,R,LOC,X,210e-6 + IDT_Offset,215e-6 + IDT_Offset
CP,3,VOLT,ALL
NLIST,ALL, , , ,NODE,NODE,NODE
*GET,N22,NODE,,NUM,MIN


NSEL,S,LOC,Z,IDT_Z,IDT_Z
NSEL,R,LOC,Y,-IDT_Length/2, IDT_Length/2
NSEL,R,LOC,X,220e-6 + IDT_Offset,225e-6 + IDT_Offset
CP,4,VOLT,ALL
NLIST,ALL, , , ,NODE,NODE,NODE
*GET,N23,NODE,,NUM,MIN
```

```
      NSEL,S,LOC,Z,IDT_Z,IDT_Z
      NSEL,R,LOC,Y,-IDT_Length/2, IDT_Length/2
      NSEL,R,LOC,X,230e-6 + IDT_Offset,235e-6 + IDT_Offset
      CP,4,VOLT,ALL
      NLIST,ALL, , , ,NODE,NODE,NODE
      *GET,N24,NODE,,NUM,MIN


      ALLSEL
      CPLIST,ALL,,,ANY
```

## Appendix B.2.7 Unidirectional Electrode Design

```
      /COM !INPUT IDTs


      NSEL,S,LOC,Z,IDT_Z,IDT_Z
      NSEL,R,LOC,Y,-IDT_Length/2, IDT_Length/2
      NSEL,R,LOC,X,-155E-6 - IDT_Offset,-145E-6 - IDT_Offset
      CP,1,VOLT,ALL
      NLIST,ALL, , , ,NODE,NODE,NODE
      *GET,N1,NODE,,NUM,MIN


      NSEL,S,LOC,Z,IDT_Z,IDT_Z
      NSEL,R,LOC,Y,-IDT_Length/2, IDT_Length/2
      NSEL,R,LOC,X,-138.333E-6 - IDT_Offset,-133.333E-6 - IDT_Offset
      CP,2,VOLT,ALL
      NLIST,ALL, , , ,NODE,NODE,NODE
      *GET,N2,NODE,,NUM,MIN


      NSEL,S,LOC,Z,IDT_Z,IDT_Z
      NSEL,R,LOC,Y,-IDT_Length/2, IDT_Length/2
      NSEL,R,LOC,X,-128.333E-6 - IDT_Offset,-123.333E-6 - IDT_Offset
      CP,2,VOLT,ALL
      NLIST,ALL, , , ,NODE,NODE,NODE
      *GET,N3,NODE,,NUM,MIN
```
219

Appendix B (Continued)

```
NSEL,S,LOC,Z,IDT_Z,IDT_Z
NSEL,R,LOC,Y,-IDT_Length/2, IDT_Length/2
NSEL,R,LOC,X,-116.666E-6 - IDT_Offset,-106.666E-6 - IDT_Offset
CP,1,VOLT,ALL
NLIST,ALL, , , ,NODE,NODE,NODE
*GET,N4,NODE,,NUM,MIN


NSEL,S,LOC,Z,IDT_Z,IDT_Z
NSEL,R,LOC,Y,-IDT_Length/2, IDT_Length/2
NSEL,R,LOC,X,-99.999E-6 - IDT_Offset,-94.999E-6 - IDT_Offset
CP,2,VOLT,ALL
NLIST,ALL, , , ,NODE,NODE,NODE
*GET,N5,NODE,,NUM,MIN


NSEL,S,LOC,Z,IDT_Z,IDT_Z
NSEL,R,LOC,Y,-IDT_Length/2, IDT_Length/2
NSEL,R,LOC,X,-89.999E-6 - IDT_Offset,-84.999E-6 - IDT_Offset
CP,2,VOLT,ALL
NLIST,ALL, , , ,NODE,NODE,NODE
*GET,N6,NODE,,NUM,MIN


NSEL,S,LOC,Z,IDT_Z,IDT_Z
NSEL,R,LOC,Y,-IDT_Length/2, IDT_Length/2
NSEL,R,LOC,X,-78.332E-6 - IDT_Offset,-68.332E-6 - IDT_Offset
CP,1,VOLT,ALL
NLIST,ALL, , , ,NODE,NODE,NODE
*GET,N7,NODE,,NUM,MIN


NSEL,S,LOC,Z,IDT_Z,IDT_Z
NSEL,R,LOC,Y,-IDT_Length/2, IDT_Length/2
NSEL,R,LOC,X,-61.665E-6 - IDT_Offset,-56.665E-6 - IDT_Offset
CP,2,VOLT,ALL
NLIST,ALL, , , ,NODE,NODE,NODE
*GET,N8,NODE,,NUM,MIN
```

```
NSEL,S,LOC,Z,IDT_Z,IDT_Z
NSEL,R,LOC,Y,-IDT_Length/2, IDT_Length/2
NSEL,R,LOC,X,-51.665E-6 - IDT_Offset,-46.665E-6 - IDT_Offset
CP,2,VOLT,ALL
NLIST,ALL, , , ,NODE,NODE,NODE
*GET,N9,NODE,,NUM,MIN


/COM !Output IDTs


NSEL,S,LOC,Z,IDT_Z,IDT_Z
NSEL,R,LOC,Y,-IDT_Length/2, IDT_Length/2
NSEL,R,LOC,X,46.665e-6 + IDT_Offset,51.665e-6 + IDT_Offset
CP,3,VOLT,ALL
NLIST,ALL, , , ,NODE,NODE,NODE
*GET,N10,NODE,,NUM,MIN


NSEL,S,LOC,Z,IDT_Z,IDT_Z
NSEL,R,LOC,Y,-IDT_Length/2, IDT_Length/2
NSEL,R,LOC,X,56.665e-6 + IDT_Offset,61.665e-6 + IDT_Offset
CP,3,VOLT,ALL
NLIST,ALL, , , ,NODE,NODE,NODE
*GET,N11,NODE,,NUM,MIN


NSEL,S,LOC,Z,IDT_Z,IDT_Z
NSEL,R,LOC,Y,-IDT_Length/2, IDT_Length/2
NSEL,R,LOC,X,68.332e-6 + IDT_Offset,78.332e-6 + IDT_Offset
CP,4,VOLT,ALL
NLIST,ALL, , , ,NODE,NODE,NODE
*GET,N12,NODE,,NUM,MIN


NSEL,S,LOC,Z,IDT_Z,IDT_Z
NSEL,R,LOC,Y,-IDT_Length/2, IDT_Length/2
NSEL,R,LOC,X,84.999e-6 + IDT_Offset,89.999e-6 + IDT_Offset
CP,3,VOLT,ALL
NLIST,ALL, , , ,NODE,NODE,NODE
*GET,N13,NODE,,NUM,MIN
```

```
NSEL,S,LOC,Z,IDT_Z,IDT_Z
NSEL,R,LOC,Y,-IDT_Length/2, IDT_Length/2
NSEL,R,LOC,X,94.999e-6 + IDT_Offset,99.999e-6 + IDT_Offset
CP,3,VOLT,ALL
NLIST,ALL, , , ,NODE,NODE,NODE
*GET,N14,NODE,,NUM,MIN


NSEL,S,LOC,Z,IDT_Z,IDT_Z
NSEL,R,LOC,Y,-IDT_Length/2, IDT_Length/2
NSEL,R,LOC,X,106.666e-6 + IDT_Offset,116.666e-6 + IDT_Offset
CP,4,VOLT,ALL
NLIST,ALL, , , ,NODE,NODE,NODE
*GET,N15,NODE,,NUM,MIN


NSEL,S,LOC,Z,IDT_Z,IDT_Z
NSEL,R,LOC,Y,-IDT_Length/2, IDT_Length/2
NSEL,R,LOC,X,123.333e-6 + IDT_Offset,128.333e-6 + IDT_Offset
CP,3,VOLT,ALL
NLIST,ALL, , , ,NODE,NODE,NODE
*GET,N16,NODE,,NUM,MIN


NSEL,S,LOC,Z,IDT_Z,IDT_Z
NSEL,R,LOC,Y,-IDT_Length/2, IDT_Length/2
NSEL,R,LOC,X,133.333e-6 + IDT_Offset,138.333e-6 + IDT_Offset
CP,3,VOLT,ALL
NLIST,ALL, , , ,NODE,NODE,NODE
*GET,N17,NODE,,NUM,MIN


NSEL,S,LOC,Z,IDT_Z,IDT_Z
NSEL,R,LOC,Y,-IDT_Length/2, IDT_Length/2
NSEL,R,LOC,X,145e-6 + IDT_Offset,155e-6 + IDT_Offset
CP,4,VOLT,ALL
NLIST,ALL, , , ,NODE,NODE,NODE
*GET,N18,NODE,,NUM,MIN
ALLSEL
CPLIST,ALL,,,ANY
```

Appendix B (Continued)
Appendix B.2.8 Surface Load Applied for Sensitivity Calculation


The importance of sensor sensitivity can be calculated many ways indirectly; however, with the power and ease of simulations available at this time, the addition of an ideal mass was added to various Ansys simulations for direct calculations of wave perturbation due to an exact mass.

```
NSEL,S,LOC,Z,0,0
NSEL,R,LOC,Y,-IDT_Length/2, IDT_Length/2
NSEL,R,LOC,X,-IDT_Offset/2, IDT_Offset/2

F,ALL,FZ,-9.81e-13,,,    ! This 100 pg over the area of 9600e-
12 m^2
```


Appendix B.2.9 Impulse Function Applied to IDTs


This script applies a voltage impulse to the IDTs and must be configured appropriately to apply the load to the proper IDT groups.

```
/PREP7

*DEL,_FNCNAME
*DEL,_FNCMTID
*SET,_FNCNAME,'IMP95'
! /INPUT,..\Ansys\Imp1e-9.func
*DIM,%_FNCNAME%,TABLE,6,3,3
!
! Begin of equation: (TIME)
%_FNCNAME%(0,0,1)= 0.0, -999
%_FNCNAME%(2,0,1)= 0.0
%_FNCNAME%(3,0,1)= 0.0
```

```
%_FNCNAME%(4,0,1)= 0.0

%_FNCNAME%(5,0,1)= 0.0

%_FNCNAME%(6,0,1)= 0.0

%_FNCNAME%(0,1,1)= 1.0, 99, 0, 1, 1, 0, 0

%_FNCNAME%(0,2,1)=   0

%_FNCNAME%(0,3,1)=   0

! End of equation: (TIME)

!

! Begin of equation: 100

%_FNCNAME%(0,0,2)= 1.0e-9, -999

%_FNCNAME%(2,0,2)= 0.0

%_FNCNAME%(3,0,2)= 0.0

%_FNCNAME%(4,0,2)= 0.0

%_FNCNAME%(5,0,2)= 0.0

%_FNCNAME%(6,0,2)= 0.0

%_FNCNAME%(0,1,2)= 1.0, 99, 0, 100, 0, 0, 0

%_FNCNAME%(0,2,2)=   0

%_FNCNAME%(0,3,2)=   0

! End of equation: 100

!

! Begin of equation: 0

%_FNCNAME%(0,0,3)= 1, -999

%_FNCNAME%(2,0,3)= 0.0

%_FNCNAME%(3,0,3)= 0.0

%_FNCNAME%(4,0,3)= 0.0

%_FNCNAME%(5,0,3)= 0.0

%_FNCNAME%(6,0,3)= 0.0

%_FNCNAME%(0,1,3)= 1.0, 99, 0, 0, 0, 0, 0

%_FNCNAME%(0,2,3)=   0

%_FNCNAME%(0,3,3)=   0

! End of equation: 0

!-->


/COM ! Apply the loads.

D,N1,VOLT,0

D,N2,VOLT,0
```

Appendix B (Continued)

```
D,N3,VOLT, %IMP95%

D,N4,VOLT, %IMP95%

D,N13,VOLT,0

D,N14,VOLT,0
```

Appendix B.2.10 Analysis Configuration and Run

The analysis used in these simulation is a full transient one with x, y and z-displacements along with voltage as variables. The below script configures and runs this simulation with a time step of 0.95 ns for a total of 190 ns.

```
!/GRA,POWER

!/GST,ON

!/PLO,INFO,3

!/COL,PBAK,ON,1,BLUE

!/REPLOT,RESIZE

/FILNAME,saw,0

/SOLU

!*

ANTYPE,4

!*

TRNOPT,FULL

LUMPM,0

!*

NLGEOM,0

SSTIF,0

NROPT,AUTO, ,

EQSLV, , ,0,

PRECISION,0

MSAVE,0

TOFFST,300,

!*
```

Appendix B (Continued)

```
!*
OUTPR,BASIC,NONE,
/GST,1,0
!*
OUTRES,NSOL,ALL,
ERESX,DEFA
!*
SOLCONTROL,ON,1,
!*
!*
TIME,190.0e-9
AUTOTS,-1
DELTIM,0.95E-9, , ,1
KBC,1
!*
TSRES,ERASE
!*
TIME,190.0e-9
AUTOTS,-1
NSUBST,200, , ,1
KBC,1
!*
TSRES,ERASE
TIMINT,1,STRUCT
TIMINT,1,ELECT
!*
TINTP, ,0.25,0.5,0.5,0.5,-1
NEQIT,25,
/STATUS,SOLU
SOLVE
SAVE
FINISH
```

Appendix C Experimental Control and Data Collection and Analysis

The construction of a sensor testbed was a time consuming effort necessary for the development of this dissertation. In this appendix, the automation of the equipment used will be described with the intent to not teach LabView and or instrument automation, but rather to illustrate key principles required for a successful development.

Appendix C.1 LabView

LabView is an object oriented programming environment that allows for easy creation and modification of instrument control programs. This software and type of programming is ideally suited for research environments with multiple persons using one setup. LabView allows one to go from editing a program to running it without the need for debugging or compiling. This greatly accelerates the development time and allows for programs to be quickly modified for new test parameters without having to learn hundreds of lines of code.

Every operation in LabView is represented by a different block that has inputs and or outputs as shown in Figure 50. Operations include everything from basic mathematics and logic to complex operations such as instrument communication. Often times the more complex operations have been developed and embedded into blocks that have multiple inputs and outputs. That can easily be connected to other operating blocks.
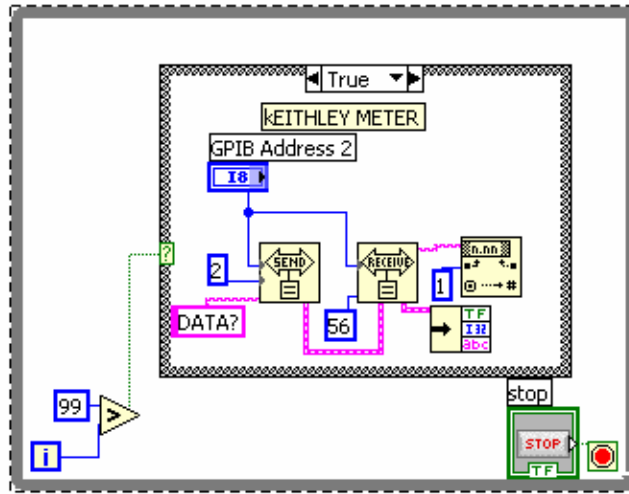
Figure 50   Example LabView program illustrating case structures and operation blocks.

The structure of these programs is intuitive in that case structures (for and while loops, and sequences) appear as boxes.  Every operation contained within the case structure will run the number of times as defined by the case structure argument. The case structures as in any programming language can be placed inside one another allowing for complex programs to be written as shown in Figure 50.

Appendix C.1.1 File preparation for Data Collection

As important as data collection is, it is difficult to keep track of numerous files and continually develop name schemes for experiment data.  To make life simple, it is possible with LabView to program a routine to save data based on the time and date.

Appendix C (Continued)

An example of this is shown in Figure 51 in which the time is taken from the computer, formatted appropriately, then sent inside a case structure where column labels are added and the file is saved. Through this simple process, every time the program is run, a new uniquely named file is generated with appropriately labeled data. The data collected from the instruments is saved to the same file that was uniquely generated with the same set of block shown in Figure 51 on the right side (inside the case structure).
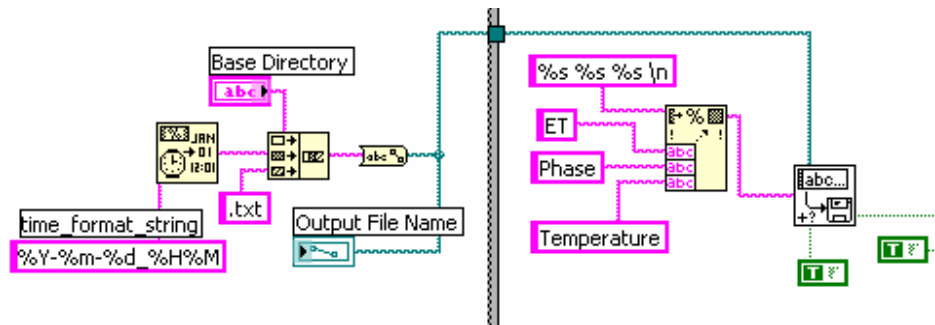


Figure 51  Example of automated file naming and labeling of data labels.

Appendix C.1.2 Instrument Control

The development of controls for each instrument follows the same procedure. The instrument functions and controls first need to be understood, which allow for easy programming, and second the device control code needs to be integrated with the data processing and saving. At this point, knowledge of the instruments and the command sets supplied by the manufacturer is assumed to be the case.

229

Appendix C (Continued)

As shown in Figure 50 a Keithley meter is the instrument that is communicating with the LabView program. The operation is as follows:

1. The instrument address and the data query command are sent to the send command.

2. The instrument address, number of bits of data to collect, and a no error signal are sent to the receive command.

3. The data returned from the receive command is sent to processing where tags are removed.

This general process is done for each instrument that is involved with a particular experiment. As mentioned previously, command blocks can be grouped inside case structures and these will then run simultaneously. Data collected from the individual instruments can be displayed through graphs or text outputs, and or the data can be stored in the fore mentioned formatted text file. An important note for displaying and recording data is to ensure the data is in the proper format throughout all of the operations. A simple check for this is to look at the style of the connecting lines for uniformity.

Appendix C.2 Matlab Analysis of Data

The extracted voltage time data from the Ansys simulations was used for many different calculations including sensitivity calculations. The data from Anys is

Appendix C (Continued)

in the form of a tab delimited text file with time and voltage data as measured on the

output IDTs.  This data was imported into Matlab for all calculations.

Experimental data was measured using an Agilent 8753ES and stored directly

to space delimited text files for processing.  The 8753ES had the time domain option

installed, so no post-processing was necessary to convert to the time domain.

Appendix C.2.1 Finding Maximum Voltage

Following the data import into Matlab, the voltage was plotted against time,

Figure 52.  From this graph, it is possible to determine the peak of maximum voltage;

however, due to the rather large time step used in the simulation, the data points are

too sparse to pick just one.  As a result parabolic fitting was used as shown in the

below example:

```
parabolicfitting(DSFBare(116:120,2))
x = 1:0.01:5;
y = a_0 + a_1 .* x + a_2 .* x .^ 2;
[maxDSFBare,I] = max(y)
IDSFBare = (116 + I*.01)
```
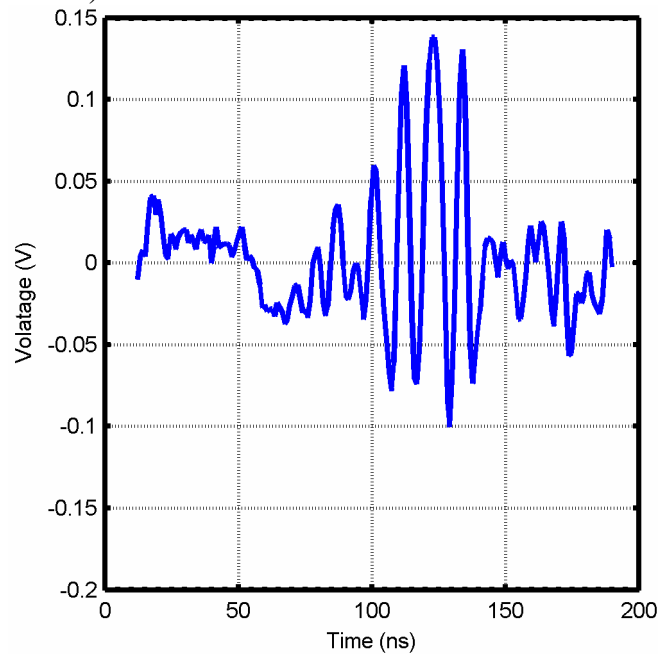
Figure 52  Example of time domain simulation data.

Appendix C.2.2 Finding Wave Velocity

Velocity of the wave can be found through a simple calculation that is dependent on the IDT structure for dimensions.  The following example code is for the determination of the velocity of the double split finger design:

```
veloDSFBare = veloc(DSFBare,IDSFBare);
```

which runs the following function:

Appendix C (Continued)

```
function [veloc] = veloc(data,I)


IR = round(I)
if IR == I
    veloc = (100e-6 + 120e-6 + 120e-6 + 100e-6) / data(I,1);
elseif IR <= I
    veloc = (100e-6 + 120e-6 + 120e-6 + 100e-6) / data(IR,1);
    velocp1 = (100e-6 + 120e-6 + 120e-6 + 100e-6) /
data(IR+1,1);
    veloc = veloc + (velocp1 - veloc) * (I - IR);
else
    veloc = (100e-6 + 120e-6 + 120e-6 + 100e-6) / data(IR,1);
    velocm1 = (100e-6 + 120e-6 + 120e-6 + 100e-6) / data(IR-
1,1);
    veloc = veloc - (veloc - velocm1) * (IR - I);
end
```

Appendix C.2.3 Time Domain to Frequency Domain Conversion

The analysis of all data can be done with only time domain data; it is convenient for discussions to display the data in the frequency domain, Figure 53. The conversion of the data was done with a Fast Fourier Transform (FFT). The following code is an example of what was used to call the FFT for the double split finger design:

```
[dBFreqDSFBare,f2DSFBare,SubstepsDSFBare,fftvoltDSF,ivoltDSF]=
freqconverter(DSFBare);
```

which calls the frequency converter function given below:

233

Appendix C (Continued)

```
function [Db_power_spectrum,f2,Substeps,fftVoltage,ivolt] =
freqconverter(data)

SystemVoltage = data(:,2);
TIME = data(:,1);
srate = 1/TIME(1);
Substeps = size(TIME,1);
f = srate*(0:((Substeps/2)-1))/Substeps;
MSystemVoltage = fft(SystemVoltage,Substeps*5);
PMSystemVoltage = MSystemVoltage.* conj(MSystemVoltage) /
Substeps;
fftVoltage = fft(SystemVoltage.*hanning(Substeps),2 *
Substeps);
f2 = [0:2 * Substeps-1]*srate/(2 * Substeps-1);
Power_spectrum = fftVoltage .* conj(fftVoltage)/ Substeps;
Db_power_spectrum = 20*log10(abs(Power_spectrum(1:Substeps)));
fftvoltshort = fftVoltage(1:175);
ivolt = ifft(fftvoltshort);
ivolt = ivolt(1:175) ./ hanning(175);
```

Appendix C (Continued)
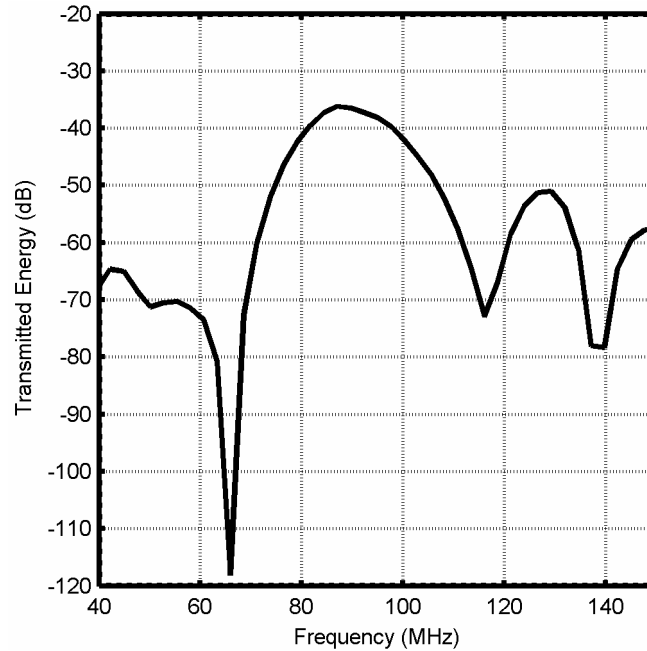


Figure 53  Example of time domain data converted with FFT.

Appendix C.2.4 Finding the Minimum Insertion Loss

Having converted the time domain data into the frequency data, the same calculations can be redone in this new domain.  The first of which is the locating of the minimum of insertion loss.  Like the time domain data, this data is sparse and selecting one of the direct values produces poor results.  The data is thus fitted parabolically as shown in the example below:

```
parabolicfitting(dBFreqDSFBare(30:36,1))
x = 1:0.01:7;
y = a_0 + a_1 .* x + a_2 .* x .^ 2;
[maxdBFreqDSFBare,IFDSFBare] = max(y)
```

235

Appendix D Schematics

Appendix D.1 Device Designs
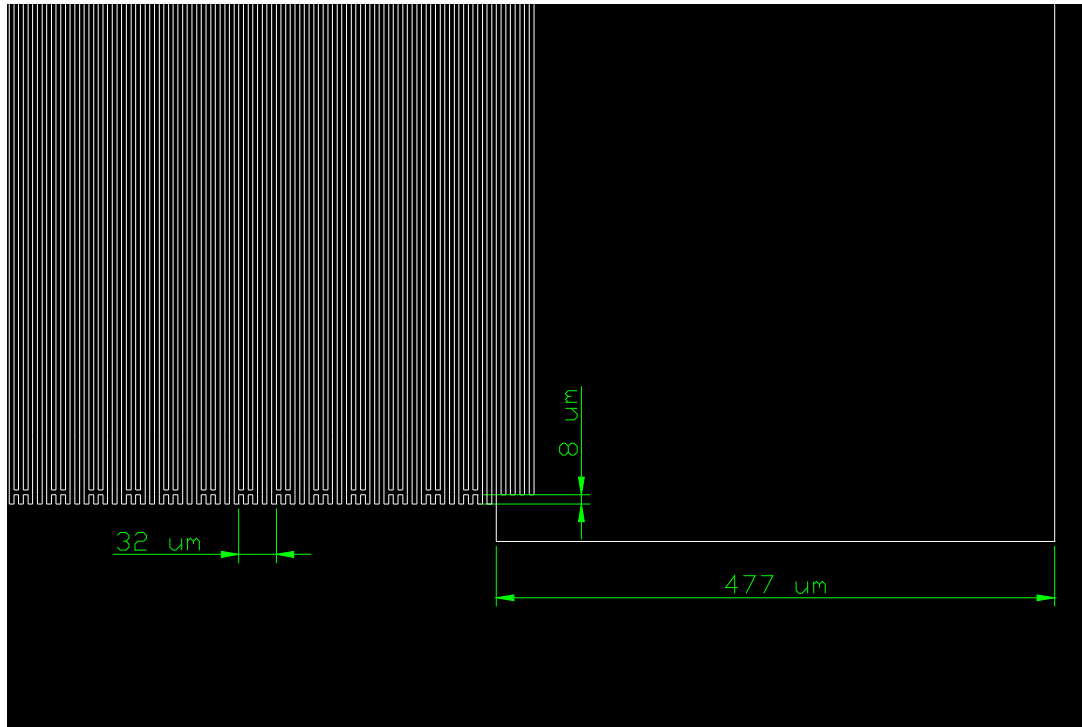


Figure 54  Double split finger IDT design for 32 μm λ with a metalized / shorted

delay path.

Figure 55  Pruned double split finger IDT design for 32 μm λ with a metalized / shorted delay path.

Figure 56  Unidirectional IDT design for 32 μm λ with a metalized / shorted delay path.
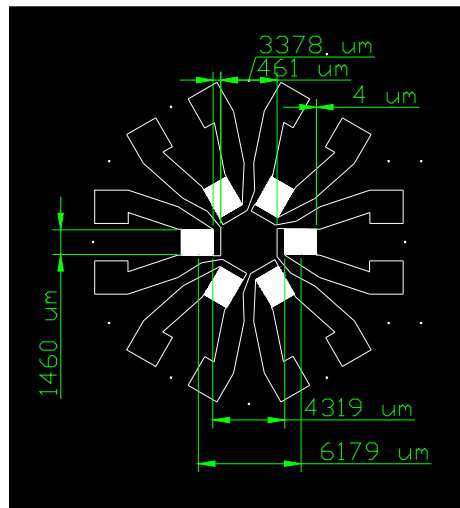


Figure 57  General hexagonal SAW layout for 32 μm λ with a metalized / shorted 197 λ delay path.
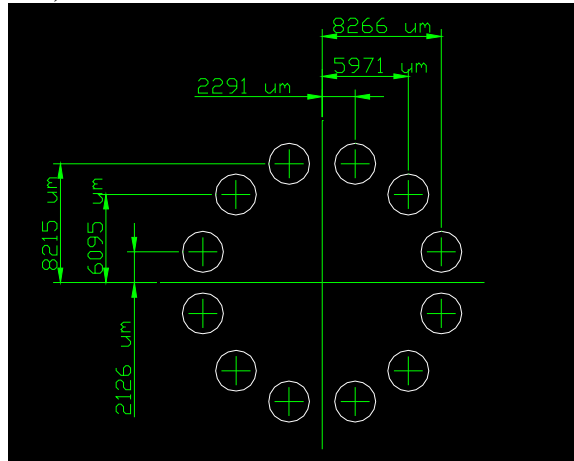
Appendix D (Continued)



Figure 58  General hexagonal SAW bond pad center locations using symmetry.
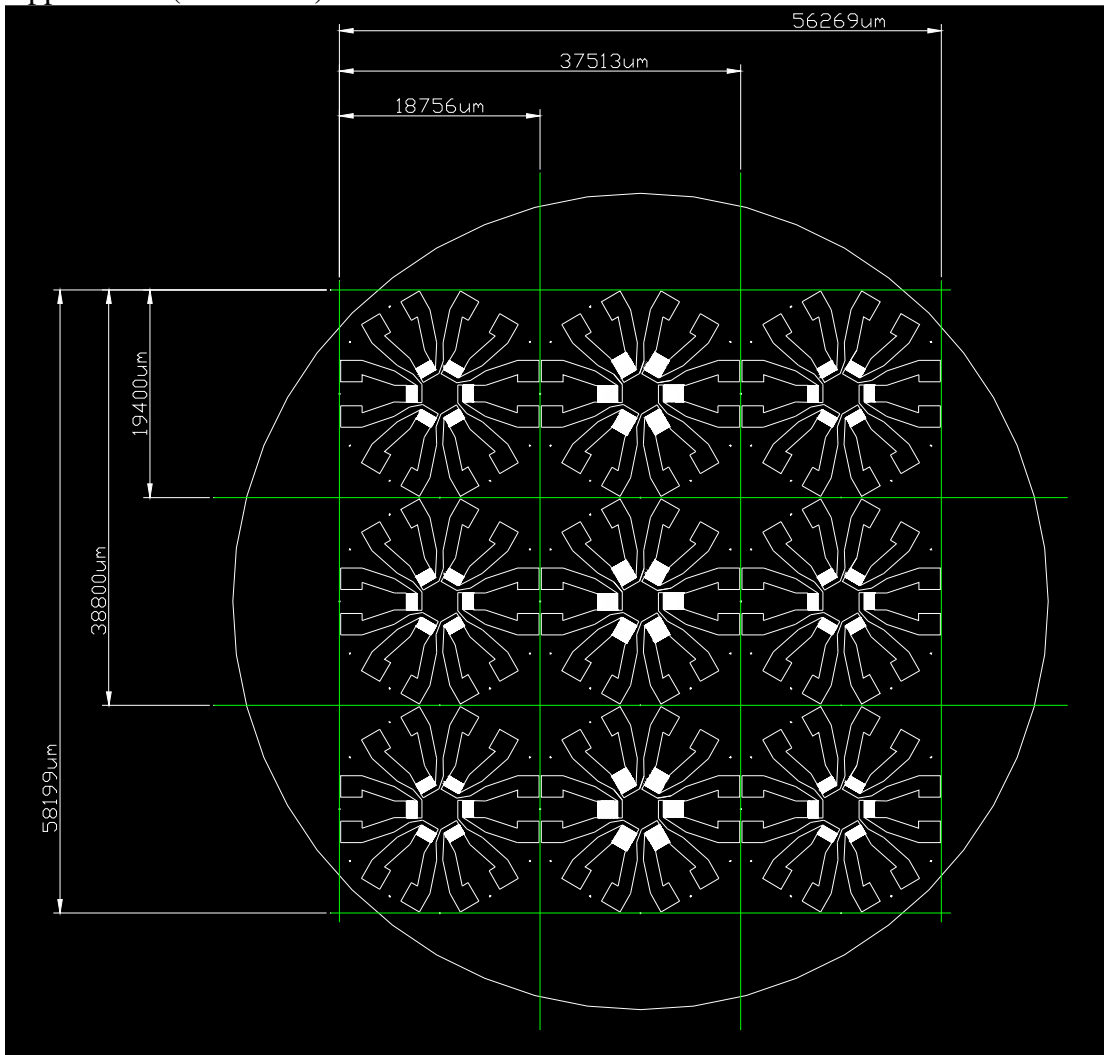
Figure 59  3" hexagonal SAW wafer cut paths.
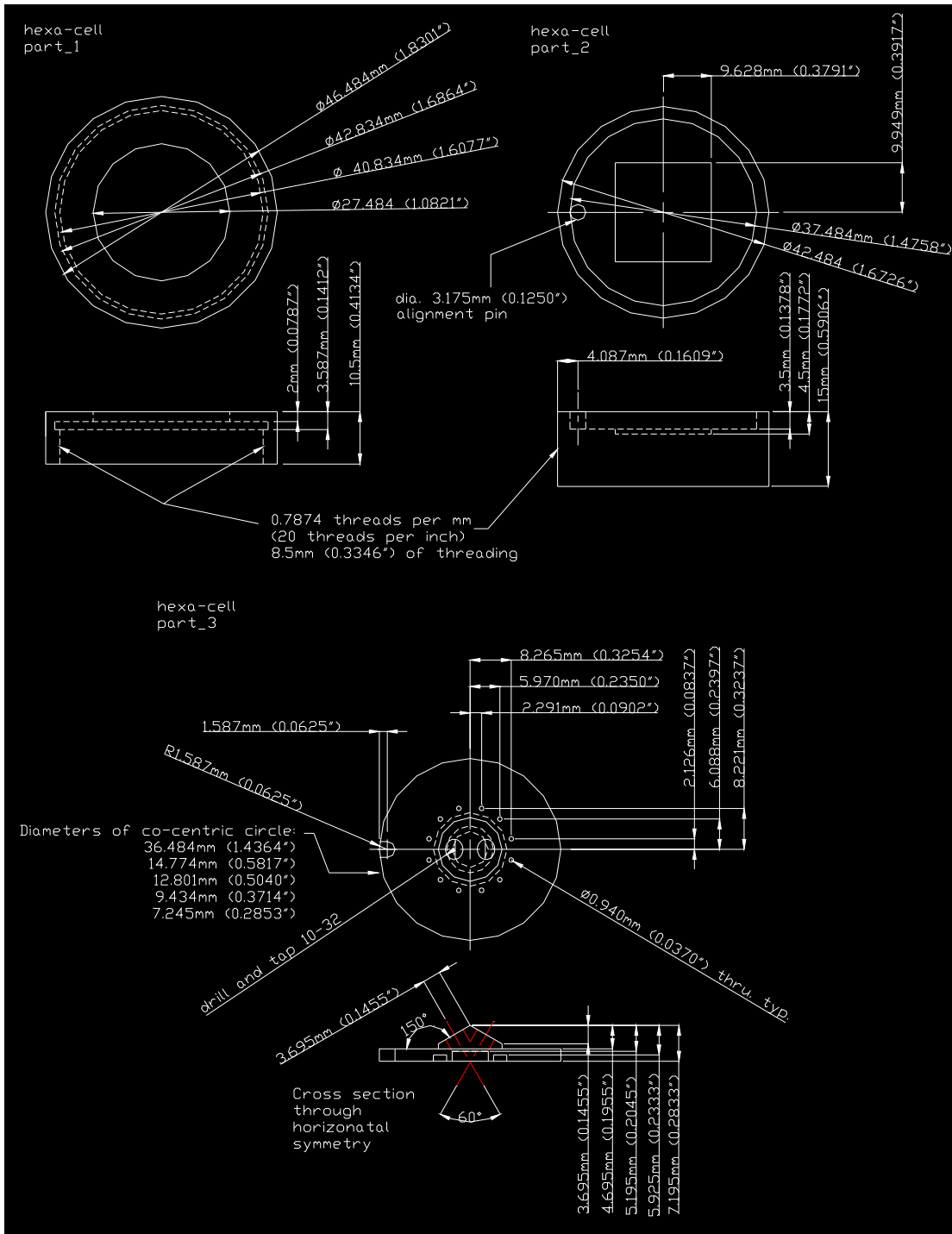
Figure 60  Hexagonal SAW layout pill box test fixture.
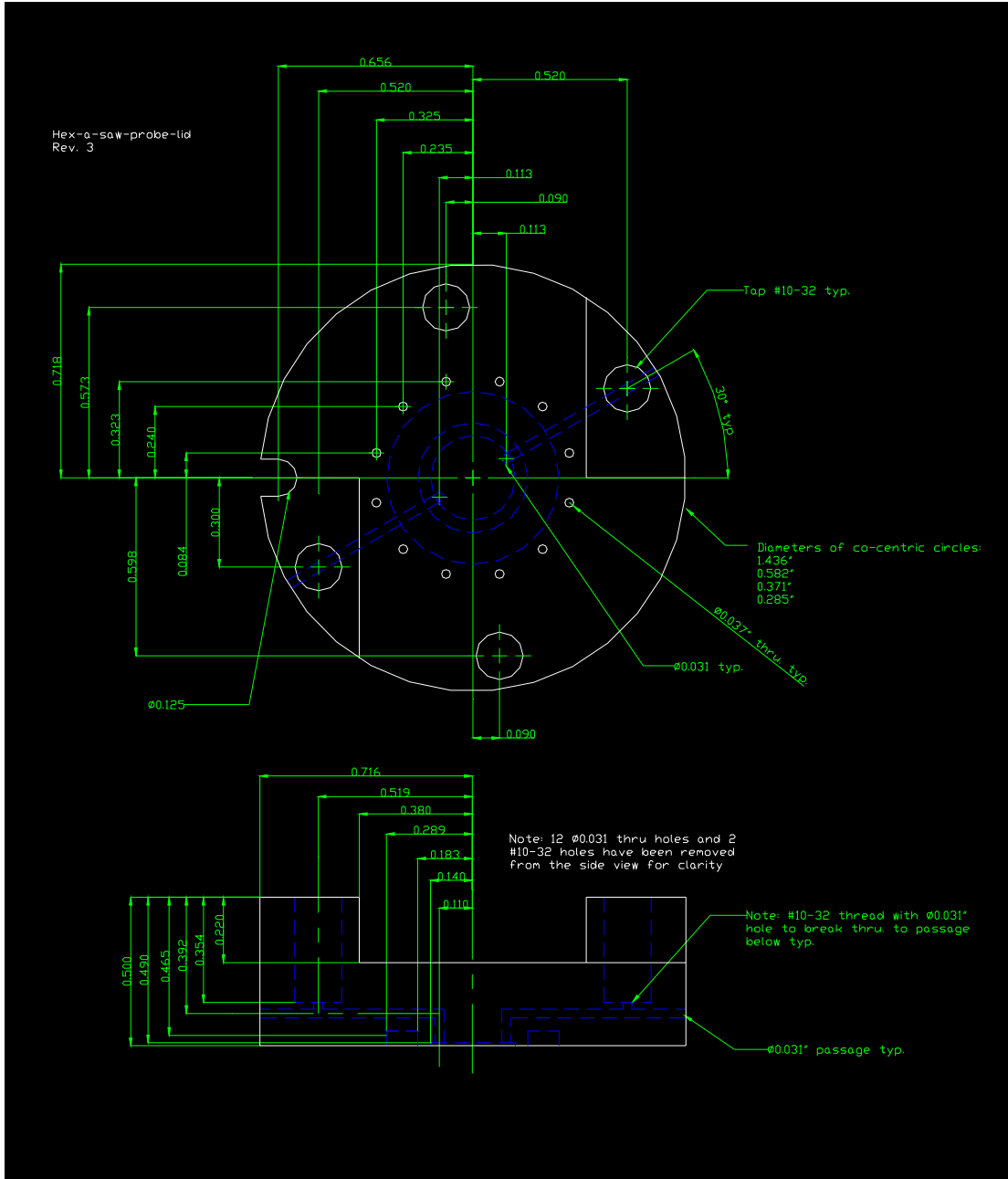
Figure 61  Hexagonal SAW probing lid for micro-fluidic applications.
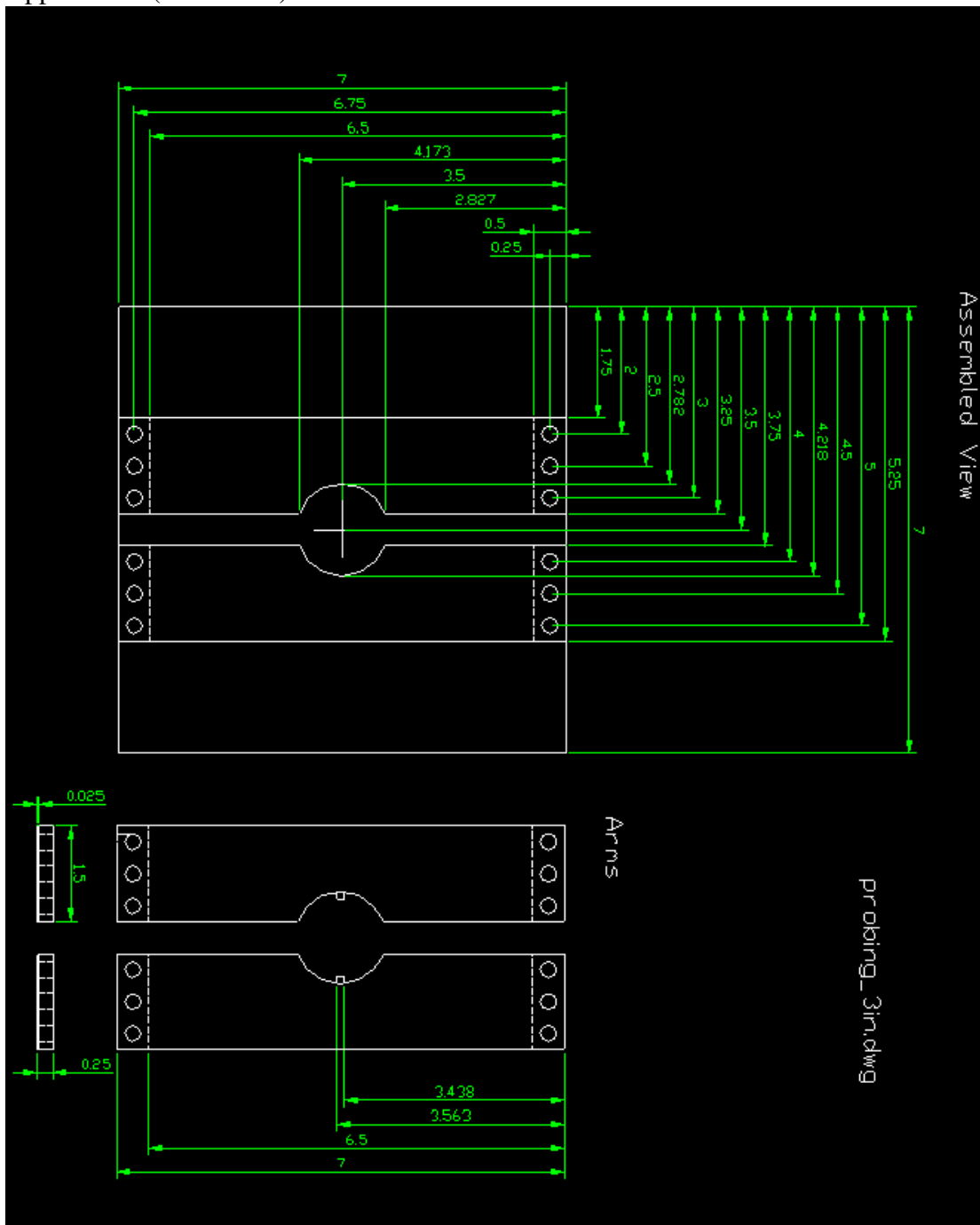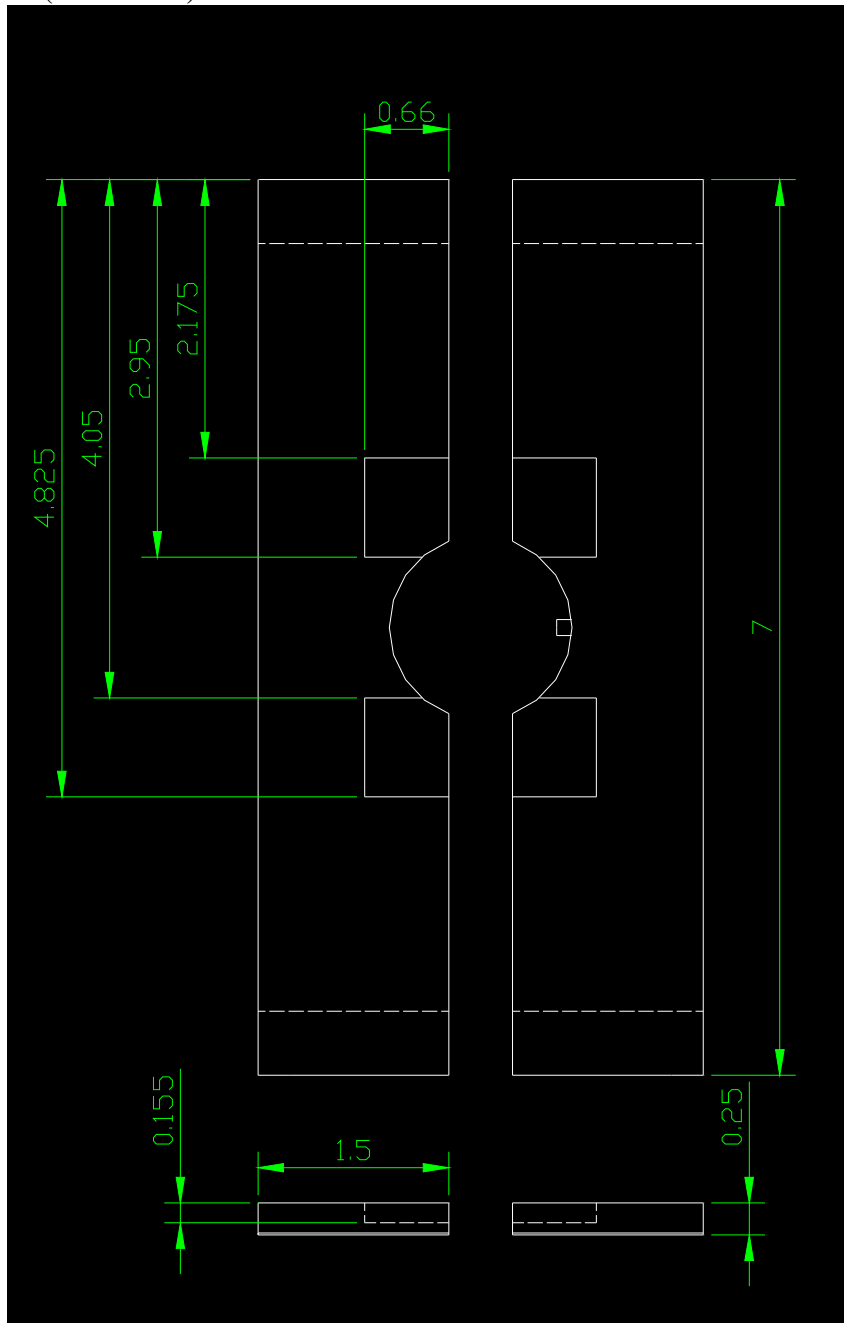
Figure 62  3" wafer probing fixture.

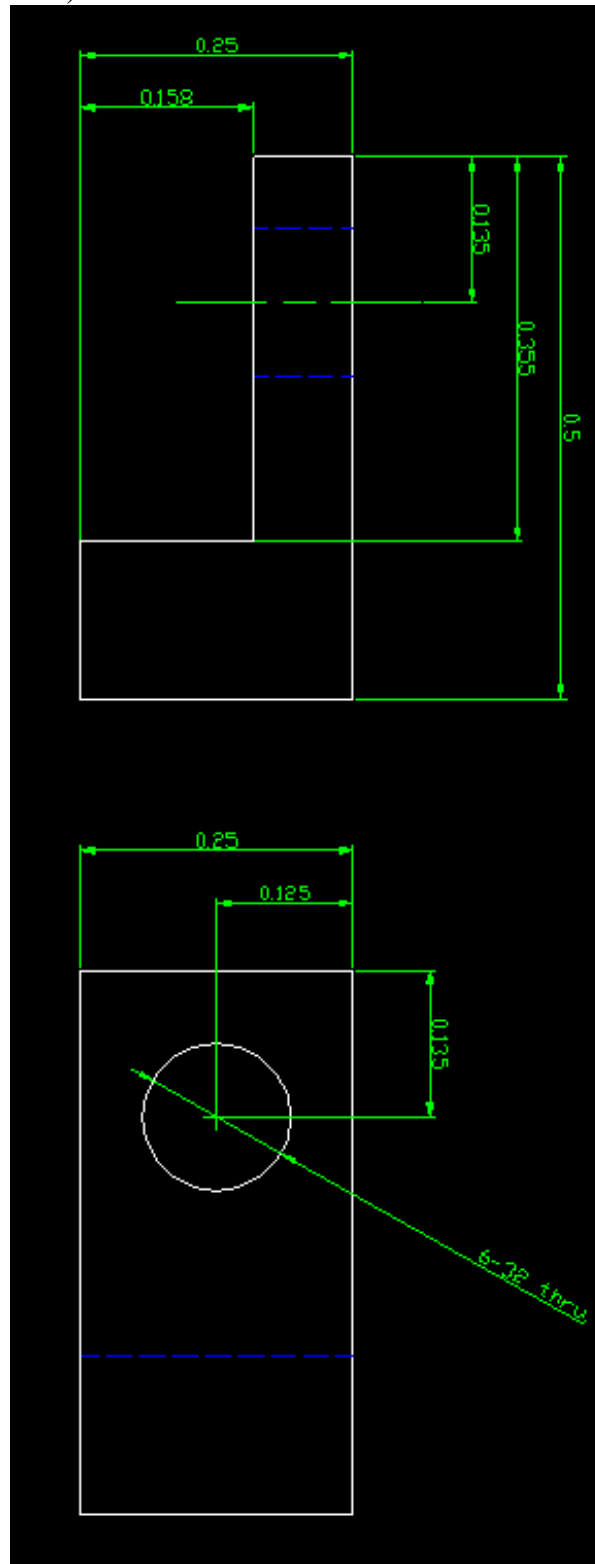Figure 63  Modified probing fixture arms accounting for circuit board.

Figure 64  Wafer probe fixture lid clamps.

Appendix D (Continued)
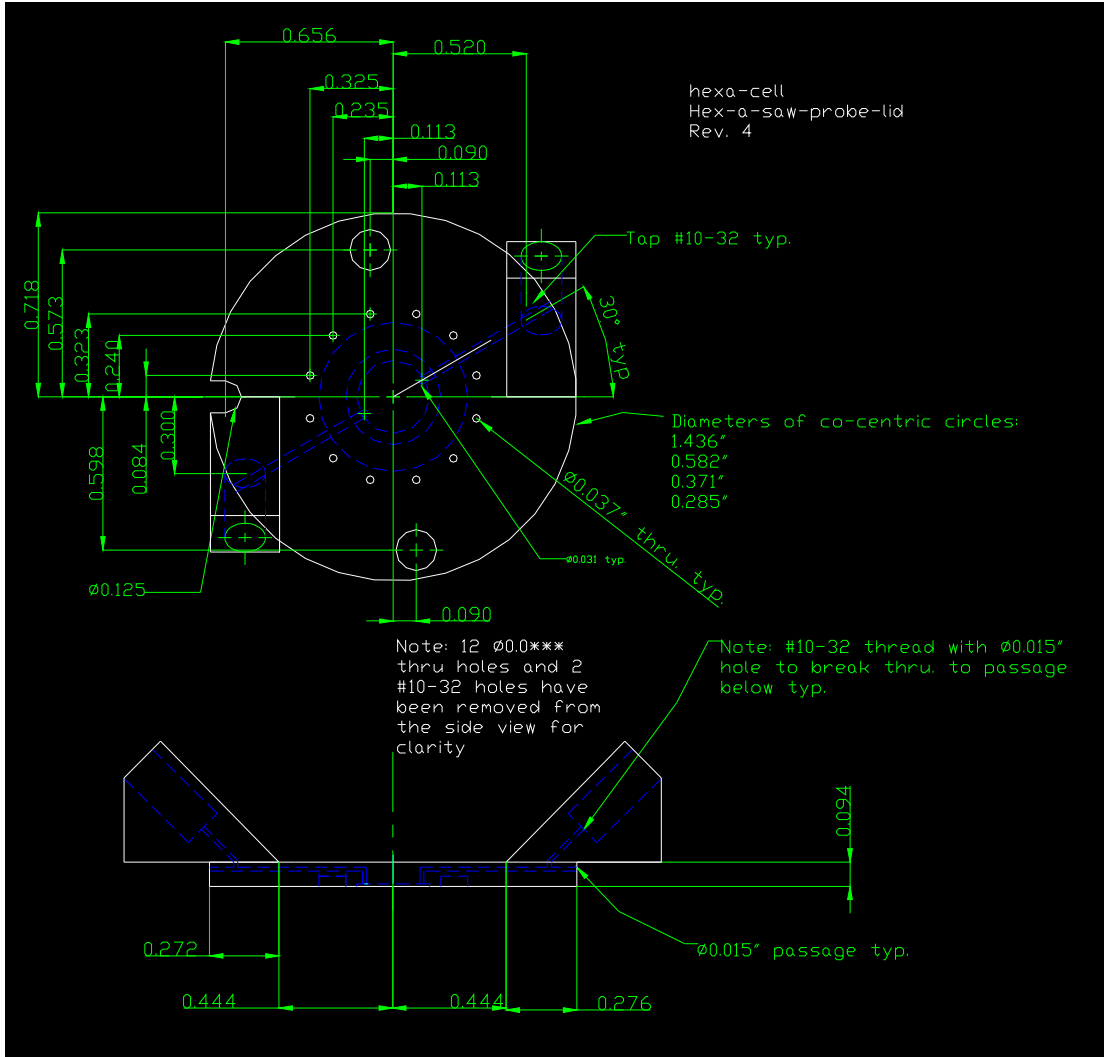


Figure 65  Probe lid for easier microscopy.

Appendix E Photolithography Recipes

Appendix E.1 4 μm Features Using Negative Photoresist

This recipe utilizes Shipley NR9-1500PY photoresist.

1. Turn on oven and set to 120 °C

   a. Turn on nitrogen, vacuum pump and lamp of mask aligner.

   b. Turn on the controller for mask aligner

2. Solvent clean wafers

   a. Acetone, methanol, isopropanol, DI, nitrogen dry

3. Dehydration bake at 120 ° C for 20 minutes

   a. Avoid metal contact with wafers after heated.

4. Allow wafers to cool.

5. Spin wafers 4,000 rpm for 40 seconds

Table 9  Configuration of spin coater #2.

| Recipe #3 | | | |
|---|---|---|---|
| RPM1 – 500 | RPM2 - 4000 | RPM3 - 4000 | RPM4 - 4 |
| Ramp1 – 10 | Ramp2 - 5 | Ramp3 – 1 | Ramp4 - |
| Time1 – 10 | Time2 - 40 | Time3 - 0 | Time4 - |

6. Bake the wafers at 120 °C for 20 minutes

Appendix E (Continued)

    a.  Avoid metal contact with wafers after heated.

7. Set oven to 100 °C

8. Immerse wafers in DI to discharge electric build up 30 seconds

9. Dry wafers with nitrogen

    a.  Wafers may now be handled with metal

10. Clean mask with solvent rinse, if resist does not come off use RD6 for 15 minutes.

11. Align major wafer flat so that it is parallel to one set of IDT's

12. Expose to pattern with mask aligner

    a.  Karl Suss MA56 mask aligner parameters:

- Constant power source 275 watts => 6.5 mW/cm$^2$

- Program #6

- Hard Contact

- Negative resist

- Prealignment – single

- First mask – no

- Alignment gap – 50 μm

- Number of contacts – 1

- Alignment check – no

- Exposure time – 5.3 seconds

- Hard contact delay – 5 seconds

- Wedge error compensation – 3 point

Appendix E (Continued)

13. Bake the wafers at 100 °C for 30 minutes

    a. If last batch of wafers turn off lamp and mask aligner when placing

       wafers into the oven.  When wafers are pulled out of the oven turn off

       nitrogen to mask aligner.

14. Allow wafers to cool

15. Develop photoresist in RD6 for 20 seconds

    a. Remove from solution at t = 15 seconds

    b. Immerse wafers in DI for 1 minute

    c. Rinse wafer with flowing DI

    d. Use fresh developer for each wafer

16. Oxygen plasma clean wafers for 5 minutes on low power setting in Harrick

    plasma cleaner/sterilizer.

17. Deposit 100 Å Ti, 800 Å Au, 100 Å Ti

18. Lift off in acetone.

    a. Use ultrasonic bath to enhance lift off.

19. Solvent rinse

20. Oxygen plasma clean wafers for 5 minutes on low power setting in Harrick

    plasma cleaner/sterilizer.

21. Test for shorts.  If they exist repeat lift off, solvent rinse, and oxygen plasma

    clean.

Appendix E (Continued)
Appendix E.2 4 μm Features Using Positive Photoresist

1. Clean with acetone, methanol, isopropanol, and water.

2. Dry wafer baking in oven (15-30 minutes) or on hot plate (1-2 minutes).

3. Set spinner to 30 seconds at 3500-4000 rpm with a ramp of 500rpm/sec.

4. Coat with HMDS to help adhesion.  This may not be needed if really clean and dry.

5. Spin coat at set time.

6. Let stand for about 1 minute.

7. Puddle photoresist in the center of the wafer covering about ½ the total surface area.  Shipley 1813 will give approximately 1.3 um thickness.  Be sure not to pipette the resist from close to the bottom or edges.

8. Spin at the set time.

9. Inspect for any flaws due to dust, moisture, old photo resist.

    a.  If flaws are discovered rinse with acetone, DI water.

    b.  Dry and bake 15-30 minutes $90^{o}$C in oven.

10. Soft-bake 90-110$^{o}$C for 10-20 minutes in oven or 1-2 minutes on hotplate.  It is crucial to remove all of the solvent.

11. Expose to mask.  Approximately 8 seconds for Shipley 1813 1.3 um thick.

12. Place in chlorobenzene for 1 minute.  This should create a 300-500 nm overhang to be taken advantage of in liftoff processing.

13. Blow dry with nitrogen.  Do not use water!

14. Develop in MF-319 with agitation for 30-45 seconds.

Appendix E (Continued)

15. Rinse with DI water for 2 minutes.

16. Dry with nitrogen.

17. For lift off skip the hardbake.

18. Deposit metal 100 Å of titanium followed by 800 Å of gold.

19. Liftoff in acetone for 5 minutes or longer and use ultrasonic bath if necessary.

20. Rinse with acetone, methanol, isopropanol and DI water.

21. Blow dry with nitrogen

About the Author

Stefan Cular was born in Point Pleasant, NJ, in 1982. In the summer of 1989, his family relocated to Southwestern Florida where he spent his youth. In 2000, he received dual degrees: high school diploma as the salutatorian from North Fort Myers High School and an Associates of Arts degree from Edison College. He continued his studies at the University of South Florida where he received dual degrees again: Bachelor and Master of Science degrees in chemical engineering in 2005. During his Ph.D education, he was fortunate to travel to multiple international and domestic conferences to present his research and learn what others were doing. He also was an NSF – IGERT – Fellow for two years, and received two consecutive summer appoints to Sandia National Laboratories in Albuquerque, NM. In addition to his doctoral studies, Stefan co-founded two companies to utilize his engineering knowledge and develop products from fundamental university research.